TRANSPORT IN FUEL CELLS:

ELECTROCHEMICAL IMPEDANCE SPECTROSCOPY

AND NEUTRON IMAGING STUDIES

A dissertation
Presented to
The Academic Faculty

By

Douglas Scott Aaron

In Partial Fulfillment
of the Requirements for the Degree
Doctor of Philosophy in the
School of Civil and Environmental Engineering

Georgia Institute of Technology

May, 2010

TRANSPORT IN FUEL CELLS:

ELECTROCHEMICAL IMPEDANCE SPECTROSCOPY

AND NEUTRON IMAGING STUDIES

Approved by:

Dr. Sotira Yiacoumi, Advisor
School of Civil and Environmental Engineering
Georgia Institute of Technology

Dr. Costas Tsouris, Advisor
School of Civil and Environmental Engineering
Georgia Institute of Technology

Dr. Spyros Pavlostathis
School of Civil and Environmental Engineering
Georgia Institute of Technology

Dr. Tom Fuller
School of Chemical and Biomolecular Engineering
Georgia Institute of Technology

Dr. Abhijeet Borole
Biosciences Division
Oak Ridge National Laboratory

Date Approved: May 20, 2010

For my family, friends and neighbors everywhere.

ACKNOWLEDGEMENTS

I would like to give thanks to God for the opportunity to perform the work described here and, especially, the people who supported me during these efforts. My advisors at Georia Tech, Dr. Costas Tsouris and Dr. Sotira Yiacoumi, have given me considerable guidance, insight, support, and the occasional course-correction during this endeavor. I thank Dr. Abhijeet Borole for introducing me to the exciting field of biofuel cells and providing much help as we studied them together, as well as serving on my committee. Dr. Tsouris and Dr. Borole have also enriched my life personally through their companionship at Oak Ridge National Laboratory and during trips to the National Institute of Standards and Technology. I also thank my committee members, Dr. Tom Fuller and Dr. Spyros Pavlostathis, for their comments and suggestions while planning the work in this thesis.

I give thanks for the invaluable contributions to various aspects of my research from other colleagues. Mrs. Choo Hamilton was of tremendous help while studying microbial fuel cells. Dr. Daniel Hussey, Dr. David Jacobson, and Eli Baltic were informative and provided great assistance in the neutron imaging aspects of this work. Dr. Kent Williams was an excellent source of information regarding nuclear power economics that comprised work done at ORNL. Chia-Hung, Patricia, Hyojin, Ketke, and Eunhyea were excellent research group companions while I was in Atlanta. I also appreciate Stephanie and Ana Maria for their friendship at Georgia Tech.

I would especially like to acknowledge and give thanks for the support of my wife, Elissa. She is my joy and has encouraged me throughout my life with her. My parents, Ann and Scott Aaron, and sister Lynn have inspired, taught, and unconditionally loved me for over 27 years. A thousand thanks for their support in my life.

FUNDING ACKNOWLEDGEMENT

I would like to thank the Georgia Institute of Technology for funding provided through the Presidential Fellowship. Funding provided by the American Chemical Society, Petroleum Research Fund, Green Chemistry Initiative through a grant to the Georgia Institute of Technology is gratefully acknowledged. Also, partial funding was provided by the Office of Basic Energy Sciences of the U.S. Department of Energy through the grant DE-FG02-05ER15723 to the University of Tennessee. Work conducted at Oak Ridge National Laboratory (ORNL) was sponsored by the Laboratory Directed Research and Development Program of ORNL.

TABLE OF CONTENTS

LIST OF TABLES

LIST OF FIGURES

LIST OF SYMBOLS AND ABBREVIATIONS

ABTS	Mediator - 2,2'-azinobis(3-ethylbenzothiazoline-6-sulfonate)
"A" factor	Empirical factor that indicates non-ideality of a constant phase element
AC	Alternating current
CCS	Carbon capture and storage
CF	Carbon felt
CPE	Constant phase element
CTR	Charge transfer resistance
ΔH^f	Enthalpy of formation
ECM	Equivalent circuit model
EDL	Electrical double layer
EFC	Enzyme fuel cell
EIS	Electrochemical impedance spectroscopy
ESP	Electrostatic precipitation
FeCN	Ferricyanide
FGC	Flue gas desulferization
GDL	Gaseous diffusion layer
HTC	Hydrotalcite
I	Current (in fuel cell output) or neutron intensity (for neutron imaging)
IGCC	Integrated gasification combined cycle
MEA	Membrane-electrode assembly (for fuel cells) or monoethanolamine (for CCS)
MFC	Microbial fuel cell
NIF	Neutron Imaging Facility
NIST	National Institute of Standards and Technology
O&M	Operations and maintenance
ORR	Oxygen reduction reaction
PEM	Polymer electrolyte membrane or proton exchange membrane
PEMFC	Polymer electrolyte membrane fuel cell (or proton exchange membrane fuel cell)
PSA	Pressure swing adsorption
ϕ	Phase shift
Q	Heat
R_{An}	Resistance (subscript generally denotes anode, solution or cathode)
RH	Relative humidity
sccm	Standard cubic centimeters per minute
THF	Tetrahydrofuran
TSA	Temperature swing adsorption
U	Units of laccase enzyme
Y_o	Coefficient for constant phase element
Z	Impedance

SUMMARY

Current environmental and energy sustainability trends have instigated considerable interest in alternative energy technologies that exhibit reduced dependence on fossil fuels. The advantages of such a direction are two-fold: reduced greenhouse gas emissions (notably CO_2) and improved energy sustainability. The work in this dissertation is largely focused on the use of analytical tools for the study of transport in fuel cells. Fuel cells are recognized as a potential technology that achieves both goals described above.

Fuel cells are a field of energy conversion technology that is currently of considerable interest. Such interest is warranted, considering their potential for highly efficient, low emissions energy production. Fuel cells utilize a wide range of fuels, materials, operating conditions and, consequently, can fill a variety of niche energy conversion applications. In an effort to improve the energy density afforded by fuel cells, analytical techniques must be developed that provide detailed information on the state of an operating fuel cell and allow diagnosis of any problems. This dissertation focuses on two powerful methods of performing in-situ studies of transport limitations in fuel cells. The first is electrochemical impedance spectroscopy (EIS) while the second is neutron imaging. Three fuel cell systems are studied in this work: polymer electrolyte membrane fuel cells (PEMFCs), microbial fuel cells (MFCs) and enzyme fuel cells (EFCs).

The first experimental section of this dissertation focuses on application of EIS and neutron imaging to an operating PEMFC. The effects of cathode-side humidity and flow rate, as well as cell temperature and a transient response to cathode-side humidity,

were studied for a PEMFC via EIS. It was found that increased air humidity in the cathode resulted in greatly reduced cathode resistance as well as a significant reduction in membrane resistance. The anode resistance was only slightly reduced in this case. Increased air flow rate was observed to have little effect on any resistance in the PEMFC, though slight reductions in both the anode and the cathode were observed. Increased cell temperature resulted in decreased cathode and anode resistances. Finally, the transient response to increased humidity exhibited unstable behavior for both the anode and the cathode resistances and the PEMFC power output. Neutron imaging allowed the calculation of water content throughout the PEMFC, showing a maximum in water content at the cathode gas diffusion layer – membrane interface.

The second experimental section of this dissertation delves into the world of microbial fuel cells. This work was done on MFCs developed under Dr. Borole and Mrs. Hamilton at Oak Ridge National Laboratory. A variety of experimental parameters were studied through the lens of EIS to understand what transport limitations were present in the MFC and, with this improved understanding, identify conditions that can lead to better MFCs. Multiple long-term observations of changes in internal resistances were performed and illustrated the reduction in anode resistance as the bacterial community was established. Over this same time period, the cathode resistance was observed to have increased; these two phenomena suggest that the anode improved over time while the cathode suffered from degradation. Increased anode fluid ionic strength and flow rate both led to significant reductions in cathode resistance, while the anode resistance was relatively unchanged. Improvement of the cathode after changes effected in the anode

led to the conclusion that proton transport to and in the cathode limited the MFC, not the bioanode. The experiments performed over time and on the MFC anode demonstrate how the limiting resistance in an MFC can change and that some alterations to the MFC can reduce those limitations. EIS was also used to observe the response of the MFC to such material changes as replacing the membrane and cathode. It was found that increased concentration of carbon source to the bioanode had little effect on the MFC resistances. This suggested that the bioanode had a maximum loading of carbon that it could process and further carbon source was excessive. Neutron imaging was not used in this section because interaction between neutrons and bacteria would be deleterious to the bacterial community's health.

The third experimental section involves enzyme fuel cells. EIS was utilized to study the response of the EFC to such operating changes as increased cathode humidity, enzyme loading, air flow rate, and temperature. This work was instigated by a desire to understand the transport limitations in EFCs and then improve power output by minimizing those limitations. It was expected that the enzymatic cathode of the EFC was limiting the EFC power output. It was found that the resistance in the cathode dominated the EFC resistances but it decreased markedly as the enzyme loading increased. The effect of cathode flow rate was relatively small on all internal resistances as long as the flow rate was maintained above a minimum level needed for operation. In addition, changes in cathode humidification temperature resulted in a small reduction in resistances throughout the EFC. This suggested that water content in the EFC did not greatly affect internal resistances or power output on a new EFC. Time had a very strong influence on

internal resistance and power density; however, power output decreased by 95% after ~20 hours of operation while internal resistance went up by a factor of 10 over the same period. This drastic increase in resistance, with an attendant loss of power output, was attributed both to enzyme/mediator degradation and water loss. To explore water loss from the EFC cathode, neutron imaging was performed on a working EFC. These studies allowed quantification of the water loss rate from the enzymatic cathode. It was found that increasing the air-side humidity and cathode solution salt content contributed to water retention in the cathode, which resulted in more stable power output over time. However, even saturated air in the cathode resulted in water loss. It was hypothesized that heating due to the cathode reaction in the EFC warmed the cathode and imposed an unsaturated state. Mass and energy balances were performed that support this hypothesis.

The results and observations from the material included in this dissertation contribute to the body of knowledge regarding the use of EIS and neutron imaging to understand fuel cells. Specifically, it was found via neutron imaging that, in a PEMFC, a peak in water content at the interface between the cathode catalyst layer and polymer membrane was likely. Also, the resistances in various regions of a fuel cell were interrelated and changes in one region can significantly affect transport processes in another region; this finding was consistent for all fuel cell types studied in this work. Novel observations of MFC behavior resulted from EIS studies, especially regarding the phenomenon of the dominating resistance changing when the bioanode exhibited less resistance than a platinum-catalyzed air cathode. EIS has only barely been applied to EFCs so the work performed here was early in using EIS as a tool for EFC studies. It

was found that a maximum useful enzyme loading could be reached, at which point increased enzyme loading didn't contribute to significantly increased power output. In addition, neutron imaging was used for the first time to quantify water loss rates in an operating EFC and explore a quantitative explanation for water loss observed in the EFC cathode.

The appendix to this work deals with a techno-economic evaluation of carbon capture and storage (CCS), a study that was conducted in parallel to the fuel cells work. Both CCS and fuel cell technologies are important for energy sustainability and environmental stewardship. CCS is widely considered a promising method for reducing anthropogenic CO_2 emissions to the atmosphere in an attempt to slow global warming due to the greenhouse effect. However, despite this feature of CCS, it does not address energy sustainability issues. Thus, calculations were performed to compare the carbon avoidance of CCS with that of alternative energy technologies. In the appendix, a literature review and summary of carbon capture technologies is presented. Following this, an economic comparison of the carbon avoidance, per dollar, between CCS and alternative energy is presented. The results of this work have important implications on how viable CCS is (relative to alternative energy technologies) and whether it deserves a prominent place in the landscape of future energy production.

CHAPTER 1

INTRODUCTION

1.1 Fuel cells and environmental stewardship

Much of the research performed by environmental engineers today focuses on various aspects of improvement of our environment, either by solving legacy issues or preventing future damage. Fuel cell development falls into the category of "preventing future damage" since this technology is attractive due to many environmentally-promising features. Relatively high efficiency, reduced harmful emissions, and potential reduced dependence on fossil fuels are among the reasons for studying this field. Fuel cells are not a new technology; the first fuel cell was demonstrated by Sir William Grove in 1839 using a Pt catalyst. Ostwald (1896) was an early advocate of fuel cell technology because he recognized the potential increase in efficiency that electrochemical reactions afforded compared to combustion. Subsequent interest in fuel cells has waxed and waned as other energy technologies were comparatively less or more attractive. Since that time, fuel cells utilizing various materials of construction, fuel sources, and operating conditions have been developed for many stationary and mobile applications (EG&G Services, Inc., 2004).

Fuel cells all share a common theme: electrochemical oxidation of a fuel. This scheme, as opposed to combustion, generally yields higher efficiency because less energy is lost to heat. In other words, direct production of electricity from chemical energy minimizes conversion losses. For example, the following steps in the case of a coal

power plant result in observed efficiencies of roughly 35%: chemical (coal) to thermal (steam) to kinetic (turbine) to electrical (generator) energy. Such an energy conversion scheme can be compared to that of a fuel cell in which the chemical energy to electrical energy conversion is direct with some heat loss. Fuel cell electrical efficiency can be as high as 50%, and above 80% with co-generation or heat capture (Carette et al, 2001). Indeed, the First National Bank of Omaha utilizes an 800 kW phosphoric acid fuel cell plant with efficiency above 80% as a result of using waste heat for space heating the building (Perry and Fuller, 2002). A similar installation operates at the U.S. Post Office in Anchorage, Alaska.

The losses experienced with fuel cells are the result of multiple transport inefficiencies. An early study of PEMFC water and heat transport was presented by Fuller and Newman (1993). In this study, PEMFC features such as water distribution from cathode to anode, water flux, and temperature profiles along the distribution channels, among others, were calculated. A recent thermodynamic study of fuel cell processes by Rasmousse et al. (2009) included such considerations as half reaction thermodynamics, electrochemical activation, water sorption and desorption in the gas diffusion layers and membrane interfaces, and others. These calculations are designed to better understand the processes that limit output of fuel cells. It should be noted that, of the three fuel cell systems considered in this work, such in-depth calculations have focused on PEMFCs since they are the most mature technology of the three. MFCs and EFCs are relatively new fuel cell types and have been treated less thoroughly via calculations.

A complement to such modeling efforts is electrochemical impedance spectroscopy (EIS). This analytical technique allows transport inefficiencies to be determined in operating fuel cell systems (Srinivasan, 2006; Bard and Faulkner, 2001). These inefficiencies are initially measured as impedance to a small signal that is passed through the fuel cell. However, the impedances can be related to such features as charge transfer resistance (CTR), diffusion resistance, electrical double layer (EDL) capacitance or more complex phenomena. An understanding of these contributions to fuel cell inefficiency can guide further improvement to fuel cell designs, overcoming such current obstacles as low power density and short lifespans (for some fuel cell types).

Water management is an important aspect of fuel cell operation, especially for PEMFCs and EFCs since it significantly affects catalyst utilization and transport throughout the fuel cells. As evidenced by PEMFC modeling efforts (Fuller and Newman, 1993; Rowe and Li, 2001; Djilali and Lu, 2002), water content and distribution are of great interest for improvement of fuel cell design and operation. With this being the case, another analytical technique of great interest for fuel cell studies is neutron imaging. Because the hydrogen in water attenuates neutrons strongly, imaging can allow quantification of water content and distribution in fuel cells (Satija et al., 2004). The design of an MFC typically causes water management to not be an issue. Combination of EIS and neutron imaging offers the opportunity to delineate internal resistance mechanisms in the context of water content and distribution. Fuel cells are, because of their environmentally-beneficial nature and incorporation of basic environmental engineering principles, of considerable interest to an environmental engineer.

1.2 Objectives of this work

This research primarily focuses on the application of EIS and neutron imaging to study various transport phenomena in three types of fuel cells. This dissertation involves much experimental work as well as modeling of the fuel cell systems. EIS has been performed on a PEMFC, multiple configurations of MFCs, and two different EFCs. The spectra from these measurements are studied via Bode and Nyquist plots, as well as utilization of a common ECM. Results from such modeling allow delineation of charge transfer and diffusive resistances at the anode, membrane (and the solution, in the case of MFCs), and cathode. In addition, electrical double layer capacitance was also included in these models. These calculations allow identification of transport inefficiencies and diagnosis of multiple problems that may develop in the fuel cells. Neutron imaging was utilized to study water distribution in an operating PEMFC and two different EFCs. MFCs were not studied with neutron imaging because they generally don't have water management issues and because the neutron beam would be unhealthy for the bacteria present in the anode. Included as an appendix to this work are a discussion of various CO_2 capture technologies and a comparison of carbon capture and storage (CCS) and alternative energy technologies with respect to avoidance of CO_2 emissions and economic burdens or benefits.

Both EIS and neutron imaging are powerful methods to guide improvement of fuel cell designs and operating conditions; such improvements can lead to higher power density fuel cells for future applications. Specific objectives in this work are as follows:

1) Develop an improved understanding of transport limitations in an operating PEMFC. This will involve the use EIS to observe the effects of operating conditions such as air humidity, air flow rate, and cell temperature on internal resistances in a PEMFC. Reduction of internal resistances is expected to result in improved power production. In addition, because water balance is possibly the most important aspect of operating a PEMFC at maximum power, another objective is to use neutron imaging to quantify the water distribution in an operating PEMFC. These studies are important since PEMFC power output is expected to be significantly affected by water content and other operational parameters.
2) Improve understanding of MFC transport limitations. Since bacteria are living creatures, changes to the environment are expected to have potentially significant impacts on their behavior and, ultimately, power output. Recent studies have identified that limitation in MFCs can be in the anode, solution or cathode and can change over time or with changing experimental conditions. To identify transport limitations, EIS will be used to quantify the response of the bacterial community to such operating conditions as anode fluid flow rate, ionic strength, and carbon loading. Other operating parameters including changes to the membrane and cathode configuration will be considered to further explore the behavior of MFCs. Also, observations of how the bioanode changes over time will lead to insights regarding the maturation of an exoelectrogenic microbial community.
3) Study EFC behavior with EIS and how internal resistances change with different operating conditions. This is important because EFCs are a new biofuel cell

technology and need to be characterized according to transport limitations so that better EFCs can be built. The effects of enzyme/mediator degradation and enzyme electrode dehydration are negative for power output but are poorly understood. To explore these effects, parameters such as enzyme loading, cathode humidity, and cathode air flow rate are of interest. Reduction in internal resistances can lead to higher power density EFC operation and design, as well as improved longevity.

4) In addition to enzyme/mediator degradation, because water loss has been observed in the literature, another objective is to explore the use of neutron imaging to track changes in water content in an EFC. This work has never been performed before, but such information would be greatly beneficial to understanding the behavior of an operating EFC.

5) Review CCS technology with an emphasis on economic aspects and implications. Current interest in CCS warrants a critical review of the feasibility and benefits of this technology. To accomplish this objective, an economic analysis will be performed that compares the carbon avoidance of CCS with that of alternative energy technologies such as wind and nuclear power. Such an analysis can provide perspective on whether CCS affords enough promise to warrant extensive development.

1.3 A note on dissertation organization

Chapter 1 of this document provides an overview of general fuel cell technology, as well as what aspects of these devices lend themselves to study via EIS and neutron

imaging. The objectives of this work are also included in Chapter 1. A literature review specific to PEMFC, MFC, and EFC development follows in Chapter 2. Also covered in the literature review is a brief history of EIS and neutron imaging, especially for fuel cell studies.

Chapter 3 begins discussion of experimental and modeling results obtained in this work. EIS was performed to evaluate the response of internal resistances in an operating PEMFC to changes in operating parameters. These internal resistances were calculated via comparison between an ECM and the experimentally-obtained spectra. Specifically, the operating parameters considered were air flow rate, air humidification, and cell temperature. An important finding of these EIS studies was the interrelated nature of the components of the PEMFC. In addition, neutron imaging was performed on the operating PEMFC to calculate the distribution of water between the anode, PEM, and cathode. Effects of water content on internal resistances are considered via the crossover between these two analytical techniques.

Chapter 4 is the opening of the section on MFCs. This chapter includes EIS studies of the effects of anode fluid ionic strength and anode flow rate on MFC behavior and internal resistances. Ionic strength was expected to affect not only the solution resistance by changing its conductivity, but potentially the behavior of the bioanode. Since bacteria respond to the environment in which they live, an environmental parameter like ionic strength may have important effects on the MFC. The anode flow rate was expected to affect transport of the feed and products in the anode. Included in

this chapter is a brief study of how the resistances in the MFC changed over the course of establishing the MFC bioanode using an already-optimized bacterial inoculum (from a previous MFC).

Chapter 5 is a detailed observation of how the MFC changed over time via power density and EIS experiments. Of special interest was the resistance of the bioanode since the inoculum for this MFC was from a municipal anaerobic digester. In addition to the anode resistance, solution (including the anode fluid, membrane, and cathode water layer) resistance, and cathode resistance were tracked. The capacitances measured in the anode and cathode were also considered in this chapter. The implications and effects of these capacitances are not as well-understood as the transport resistances in MFCs.

Chapter 6 returns to the effects of experimental parameters. In this chapter, carbon loading to the anode was considered. This is in an effort to understand the limits of carbon loading that can be handled by the bioanode. In addition, a comparison between an air cathode MFC and ferricyanide-based cathode is attempted. Various concentrations of ferricyanide were included in this part. A control cathode solution with just phosphate buffer in the absence of ferricyanide is also analyzed in this chapter. The anode and cathode of the MFCs, in all three of these chapters, were observed to have considerable interrelated dependence on changes to operating conditions.

Chapter 7 introduces the EFC component of this work. The first part focused on EIS studies of how construction and operating conditions affect the internal resistances

and power output of a laccase enzyme-based EFC. A three-dimensional cathode that utilized the laccase enzyme in a buffered, mediated solution was coupled with a traditional Pt-on-carbon anode and Nafion PEM. EIS measurements were performed for varying conditions that included enzyme loading, air flow rate to the cathode, and air humidity. In addition, the concentration of citrate buffer salt in the cathode was varied and observed via EIS. EIS was also used to track changes in internal resistances over time as the cathode dried out and the enzyme/mediator degraded.

Chapter 8 deals with neutron imaging of the EFC. Such work was of considerable interest since water loss in the EFC cathode had been observed by us and others. The capacity of neutron imaging to quantify water content, especially in the cathode, without interruption of operation made it an ideal technique for this study. Previous experiments only allowed measurements of water content at the start and termination of experiments, thus interrupting operation. The effects of cathode feed (air or oxygen), cathode feed flow rate, cathode feed humidity, and cathode solution salt concentration were all studied in terms of water loss rate via neutron imaging. It was found that, despite high feed humidity, low flow rate, and high concentration of buffer salt, water loss was still observed. Such behavior has important implications on EFC stability over time.

Chapter 9 includes a summary of major conclusions from this study. In addition, recommendations for further work are made based on the conclusions. Appendix I offers a literature review of carbon capture and storage technologies along with an economic analysis that compares CCS against alternative energy technologies.

CHAPTER 2

BACKGROUND

2.1 Fuel cell technology

Fuel cells have become a widely studied energy conversion technology due to their high efficiency; simplicity in terms of moving parts; and wide-ranging array of configurations, fuels, and applications. Low-temperature, proton-exchange membrane fuel cells (PEMFCs) are of special interest for automobiles and other portable energy applications. These fuel cells can be designed to operate at temperatures ranging from 0^{o}C to roughly 80^{o}C, have very rapid startup times, and, if protected from poisoning agents, can exhibit long lifetimes (EG&G Services, 2004). A primary drawback, however, is cost, especially in the form of expensive precious-metal catalysts. Because of the high cost, optimal catalyst utilization and transport conditions are desired to increase the power output per unit cost. Another exciting fuel cell technology is the microbial fuel cell (MFC), which uses a bacterial catalyst. In addition, the "fuel" for an MFC can include carbon-containing waste streams such as municipal and industrial (breweries and dairies, for example) wastewaters (Logan et al., 2006). While MFCs are generally not considered suitable for mobile applications, flexible fuel utilization and reduced need for a precious metal catalyst make them promising for stationary applications, especially for wastewater treatment. A third type of fuel cell is the enzyme fuel cell (EFC). This fuel cell design utilizes biologically-produced enzymes to catalyze fuel cell reactions instead of precious metal catalysts. In addition to reduced cost, EFCs

also exhibit flexibility in fuel utilization with alcohols, sugars, pyruvate and hydrogen as examples (Borole et al., 2009a; Ivanov et al., 2010). All three types of fuel cells can be schematically represented as shown in Figure 2.1.

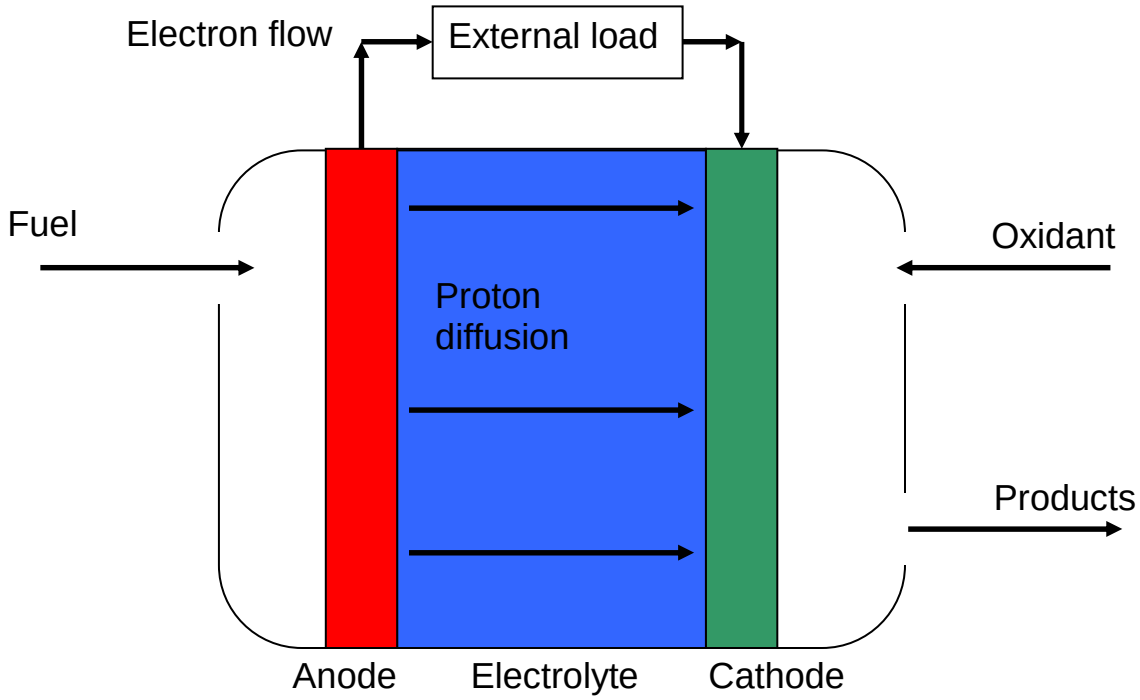

Figure 2.1. General fuel cell schematic. Fuel is oxidized at the anode, producing electrons and protons. The electrons are used for electrical work while the protons diffuse through an electrolyte. At the cathode, protons, electrons and some oxidant combine, producing the potential gradient that drives the fuel cell.

The fuel cells considered in this work include the PEMFC, MFC and EFC. In all three designs, a fuel is oxidized at the anode on a catalyst. For the PEMFC and EFC, this fuel is hydrogen and the catalyst is typically platinum or some other precious metal for low temperature fuel cells. Other metals can be used as catalysts, but operating temperatures must generally be increased, which can pose problems for a polymeric membrane. The protons generated at the anode travel through a water network and PEM

to the cathode. It is in this region that water balance is typically an issue. As shown in Figure 2.2, a film of water is needed to connect catalyst particles to the PEM. If too much water is present (flooding), the catalyst can be covered over, severely impeding contact between gaseous H_2 and the catalyst surface. However, if too little water is present (drying), there is no pathway for protons to travel from the catalyst to the PEM as the hydronium ion. A similar situation exists in the cathode: flooding inhibits oxygen reaching the catalyst surface while drying prevents hydronium ions leaving the PEM from reaching the catalyst sites. In either case, water balance is integral to providing optimal catalyst utilization.

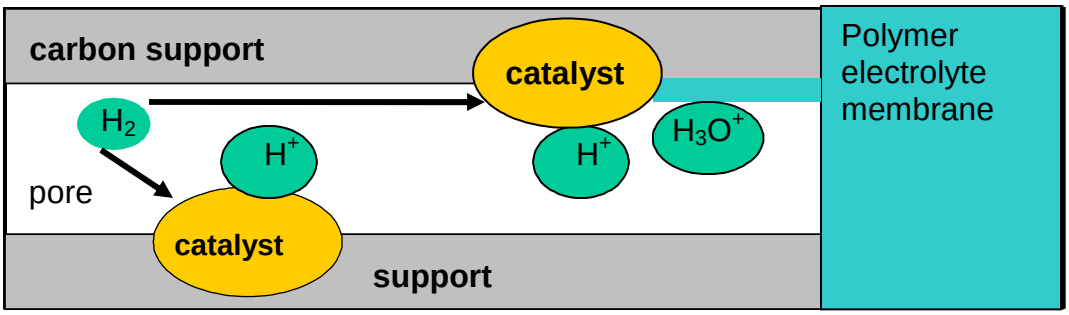

Figure 2.2. Conceptual summary of interfaces in the anode catalyst layer (amended from Liu et al., 2008).

Transport phenomena at the catalyst-electrolyte-gas interface is critical and, as of yet, still not understood (Liu et al., 2008). However, efforts to understand this region are often reported in the literature and incorporate such techniques as Monte-Carlo simulations and other molecular dynamics studies, as well as experiments (Cheng et al., 1999; Biyikoglu, 2005; Jinnouchi and Okazaki, 2003; Kreuer, 2001). Following fuel oxidation at the anode, electrons travel around the external electrical circuit, providing electrical energy. At the cathode, protons and electrons combine with oxygen to form

water. In the case of the MFC, dissolved carbon (in the form of organic compounds such as sugars or acids) is metabolized by bacteria, releasing protons, electrons and other metabolic products. The protons then diffuse through the anode growth medium and a PEM to the cathode.

PEMFCs are the most mature of the three fuel cell technologies included in this work. Much of the current research on PEMFCs focuses on alternative materials that can be used to improve longevity and reduce cost (Rikukawa and Sanui, 2000). Improved construction is also of interest to promote better transport, increase catalyst utilization, prevent flooding issues and avoid other operating complications (Litster and McLean, 2004; Secanell et al., 2008). For example, stainless steel electrodes with ZrB_2 particles were fabricated that exhibited reduced contact resistance between the electrode and gas diffusion layer by Choi et al. (2008). Such an improvement in PEMFC electrode design allowed greater power density and catalyst utilization, both of which would improve the economic potential of the PEMFC.

Microbial fuel cells (MFCs) have been demonstrated to generate electricity from a variety of carbon sources used as electron donors. Major efforts in MFC development are aimed at improving power density (Borole et al., 2009b; Borole et al., 2008a) and investigating issues associated with scale-up operations. The primary drawback of MFCs is relatively low power density, even for small cells. Such issues generally become more pronounced as designs are scaled up to provide greater power. An example of scale-up issues might include long-distance diffusion paths for protons generated far from the

PEM and cathode of an MFC. Early MFCs consisted of the H-cell design, which involved two beakers connected by a channel and a membrane or other separator that prevented the anode and cathode electrolytes from mixing. Such a separator is often necessary because the anode and cathode are typically anaerobic and aerobic, respectively. This design, while it demonstrated the concept of an MFC, suffered from exceptionally high solution or electrolyte resistance; for the case of Min et al. (2005), both PEM and salt bridge separators exhibited kΩ-order solution resistances. A schematic of this early design can be seen in Figure 2.3, below.

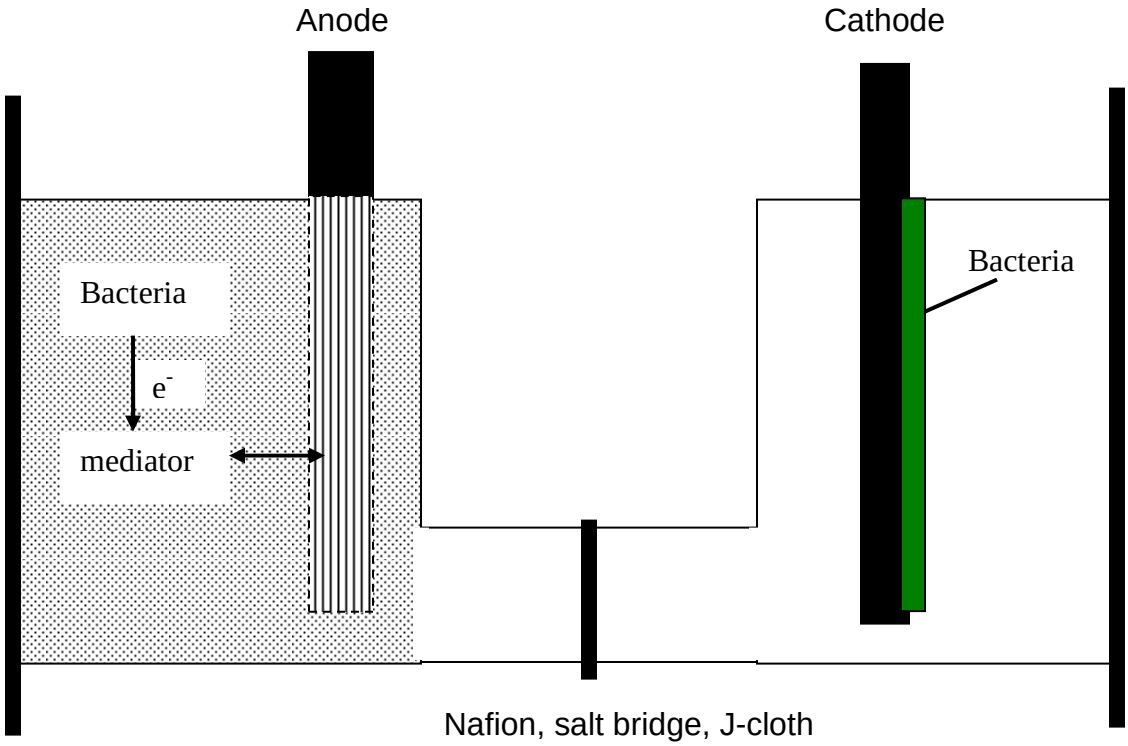

Figure 2.3. Schematic of early MFC design. High internal resistance was a product of large electrode separation. Bacteria could be planktonic (in the anode) or anchored on an electrode (cathode).

Two main types of bacterial communities have been used at the anode and cathode of a MFC: those that use mediated electron transfer (as indicated in Figure 2.3)

or mediatorless transfer (Lovley, 2006). These designations refer to the mechanism by which electrons are transferred between the bacteria and the electrodes. Early designs had free-floating, or planktonic, bacteria that utilized mediators to shuttle electrons to the anode of the MFC. This was the case for both anaerobic anode bacteria as well as aerobic cathode bacteria. Allen and Bennetto (1993) immobilized bacteria on the anode of an MFC and observed increased fuel efficiency as well as more rapid responses to addition of food for the microbes. Such improvements were attributed to the reduced distance that the mediator had to travel between the electrode and bacteria. The current highest-output design exhibits improved power density resulting from using direct electron transfer bacteria and minimizing the distance between electrodes of the MFC. The bioanode bacteria in this design generally form a biofilm on the surface of the anode; this biofilm protects the bacteria from being shorn off the anode and provides close contact to the electrode. Such close contact allows the formation of nanowires that facilitate direct electron transfer from the bacterial cells to the electrode without the need for a mediator. A schematic of the air cathode design is included in Figure 2.4A. Figure 2.4B is a similar schematic for the MFC design that utilizes an aqueous cathode.

(a)

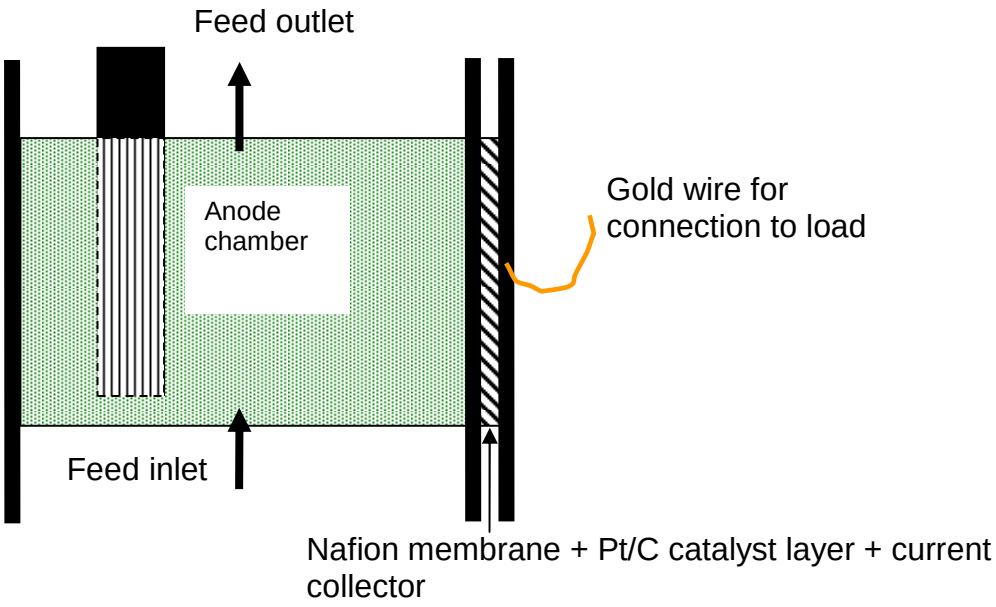

(b)

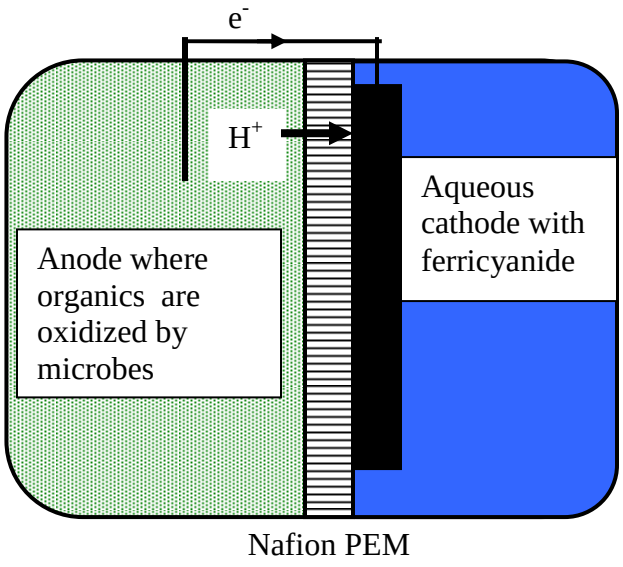

Figure 2.4. (a) Schematic of single-chamber MFC. Connections between the MFC and circuit are made at the anode carbon electrode and the cathode wire (gold in the above example). (b) Schematic of two-chamber MFC with minimal electrode spacing. Note that both anode and cathode materials are in contact with the Nafion PEM.

A popular bioanode bacterial culture was *Shewanella oneidensis* grown in an anaerobic environment to facilitate exoelectrogenesis; many early MFC reports utilized these bacteria. Recently, anaerobic digester inocula, from wastewater treatment plants, have also used in the bioanode of MFCs. The reason for such a shift is illustrated in a recent comparison by Watson and Logan (2010). It was found that the power production of mixed anaerobic cultures (such as those taken from an anaerobic digester) was 70 – 480% greater than that of *Shewanella oneidensis* MR-1, depending on MFC configuration.

In addition to exploring new bacteria to act as catalysts, other studies have dealt with cost and scale-up issues. Removal of the membrane separating the anode and cathode of an MFC has been performed to explore techniques that can reduce MFC cost (Fan et al., 2007; Liu et al., 2008). Multiple techniques have been employed to glean information regarding the processes that occur while an MFC generates electricity. For example, the current interrupt method was employed by Liang et al. (2007) to estimate the internal resistance for MFCs of various designs. This technique was also utilized to study the internal resistance for stacked MFCs, with a total internal resistance as low as $3.9 \pm 0.5\ \Omega$ (Aelterman et al., 2006). However, a more detailed understanding of the MFC, especially of the phenomena occurring at the electrodes, is desirable to allow improvements in MFC design and operation.

Finally, the third type of fuel cell explored in this work is the enzyme fuel cell (EFC). These systems utilize purified enzymes from some biological source (bacteria or fungi, for example) at one or both of the electrodes. Because enzymes are used, a variety of fuels and oxidizers are available to be used as feeds. If enzymes are used on both sides of the EFC, the specificity of the enzymes allows minimal use of a traditional separator such as Nafion. In addition, low temperature applications are the target for EFCs, since enzymes typically denature at elevated temperature. Geometry of EFCs is generally similar to that of a PEMFC; however, since the feeds can be liquid or gaseous, an EFC can look similar to the MFC schematics presented in Figure 2.4, as well. A key difference is that an electrode separator (such as Nafion) can be omitted if enzymes are used at both electrodes, as described later. Such an improvement avoids the cost of Nafion in EFCs, further driving down the cost.

One application for EFCs is in-vivo power production to power such devices as pacemakers or sensors (Amir et al., 2001). Recent efforts to improve EFC power density have included enzyme immobilization techniques (Willner et al., 2009). Since many EFCs feature enzymes in solution, transport limitations are often experienced when providing electrons to the enzymes. Mediators are often used, but present the limitation of diffusion between the electrode and enzymes. Thus, immobilization of the enzymes on the electrodes could reduce the distance traveled by mediators, improving reaction speeds. In contrast to this finding, however, is a study performed by Zhao et al. (2009) that utilized glucose oxidase immobilized on carbon nanotubes. It was found that enzyme utilization of ~40% occurred in the EFC, suggesting that it was actually proton or

electron transfer resistances that limited EFC power production, not necessarily enzyme contact with the electrode. Another observation was that the Nafion membrane actually entrapped some of the enzymes, reducing the catalyst available for oxidation of glucose.

Other alterations besides enzyme immobilization are currently under investigation, as well. Another potential improvement to EFC design is using enzymes in microfluidic EFCs. In this configuration, demonstrated by Zebda et al. (2009), glucose oxidase was immobilized on a gold anode while laccase was immobilized on a gold cathode. Aqueous streams of a glucose solution and oxygenated water flowed laminarly over the electrodes, with no convective mixing, supplying the fuel and oxidant. Power density as high as 70 mW/cm^2 was achieved with this design. For reference, typical PEMFCs can reach power densities on the order of 1 W/cm^2. A review by Minteer et al. (2007) recommended that air-cathode EFCs have three-dimensional cathode designs to improve transport of oxygen to the enzymes. This improved transport can result from utilizing more surface area and by providing more omni-directional flow (due to convective flow around the support electrode). Another improvement mimics biological processes by integrating a chain or cascade of enzymes to perform the electrode reactions. Such a scheme would utilize multiple different enzymes in an effort to extract more useful energy from a substrate by more completely oxidizing it (Arning et al., 2004).

2.2 Electrochemical impedance spectroscopy

Electrochemical impedance spectroscopy has been utilized to characterize internal resistance mechanisms that limit fuel cell power production. Early studies with PEMFCs focused on the effects of catalyst layer support of a PEMFC on internal resistance (Springer et al., 1996; Gerteisen, 2007). Important among these mechanisms are charge transfer resistance, electrical double layer capacitance, and diffusion resistances. Resistances to transport can be thought of in terms of an electrical circuit, where flow is inhibited by impedances. The definition of impedance, as used in EIS, is given by Equation 2.1:

$$Z = \frac{V_o \sin(\omega t)}{I_o \sin(\omega t + \phi)} = Z_o \frac{\sin(\omega t)}{\sin(\omega t + \phi)} \tag{2.1}$$

Current (I_o) and ϕ (phase shift) can be measured as a function of an applied AC signal (V_o), allowing the determination of impedance, Z (Gamry, 2006). By applying this signal over a spectrum of frequency, the magnitudes of various resistances and capacitances can be determined via an equivalent circuit model. It is expected that operating conditions, geometries, materials of construction, feed types and a variety of other fuel cell parameters will affect these impedances, just as they often affect cell power production. As an example, current density has been previously shown to greatly affect EIS results (Wiezell et al., 2006).

The two primary regions of resistance in most fuel cells are at the electrode-electrolyte interfaces and in the electrolyte or compartment-separating material (Liang et al., 2007). The resistances in these regions are typically termed charge transfer resistance and solution resistance, respectively. Another common name for the solution resistance can be ohmic resistance; this resistance can be used to determine conductivity and diffusion of a charged species through the electrolyte. Charge transfer resistance yields important information about exchange current and electrode polarization (Bard and Faulkner, 2001). In addition to the resistances in these regions, EDLs form between a charged electrode and surrounding electrolyte. Accumulation of counter-ions near the electrodes gives rise to an electrochemical capacitance at the solid-liquid interface. However, the capacitive behavior is usually not ideal and this non-ideality is attributed to such factors as non-uniform reaction rates on the electrode surface (Kim et al., 2003) and electrode surface roughness. EDL capacitance is exhibited by phase shift of the signal when performing EIS.

In addition to PEMFC studies via EIS, MFCs and EFCs are also suitable for EIS analyses. Gomadam and Widner (2005) have provided a summary of EIS techniques, including modeling approaches. He and Mansfeld (2009) have described EIS analysis specifically for MFCs and how it can be used to understand the effects of various MFC parameters. EIS measurements allow the study of phenomena happening at the electrodes and within the membrane-solution region. Specific parameters related to mass transfer, charge transfer and reaction kinetics can be evaluated using the technique. EIS has been demonstrated to provide insight regarding the total internal resistance of an

MFC (He and Mansfeld, 2009; Manohar and Mansfeld, 2009; He et al., 2008). Only two studies were found that utilized EIS to evaluate resistances in EFCs. A study by Hudak et al. (2009) found that internal resistance increased over time as water was lost from the EFC cathode. Johnston et al. (2005) utilized EIS, among other electrochemical techniques, to evaluate how immobilization of enzymes affected limiting steps in an operating EFC. It was found that enzyme loading and utilization limited EFC output, while mass transfer also contributed significantly to output limitation.

Bode plots and Nyquist plots are both popular forms of displaying EIS results, especially to make estimates of the internal resistance. The Bode plot simply displays impedance and phase shift as functions of frequency. Such information is useful for estimating ECM parameters, considering behavior in the Bode plots can be associated with either resistive or capacitive elements in an ECM. In general, impedance at very low phase shift (near 0^{o}) is associated with resistances such as charge transfer and ohmic resistances. For fuel cells, these low phase shift regions often occur at very high and very low frequencies. In the mid-frequency range (1000 Hz to 1 Hz, for example), fuel cell impedance responses are often dominated by high phase shift. This generally indicates capacitive behavior (Gamry, 2006). The Nyquist plot is an excellent tool for interpreting EIS results since it directly gives such results as ohmic/solution resistance and total resistance in a cell. Imaginary impedance (as a result of the AC signal) is plotted against real impedance in a Nyquist plot. An example Nyquist plot is included Figure 2.5. Many MFC EIS studies focus on the effects of materials (Manohar and Mansfeld, 2009; Ouitrakul et al., 2007), operating conditions (Torres et al., 2008), or geometry (Manohar

et al., 2008; He et al., 2006; You et al., 2008) on impedance parameters as measured by EIS and on power density. EIS has also been demonstrated by Ramasamy et al. (2009) as a useful tool for the detection of extra-cellular mediators for bacteria that perform mediator-assisted electron transfer to the anode. These studies allow the relationship between power output and chemical, biological and physical processes to be studied. Such knowledge guides optimization efforts to improve MFC performance.

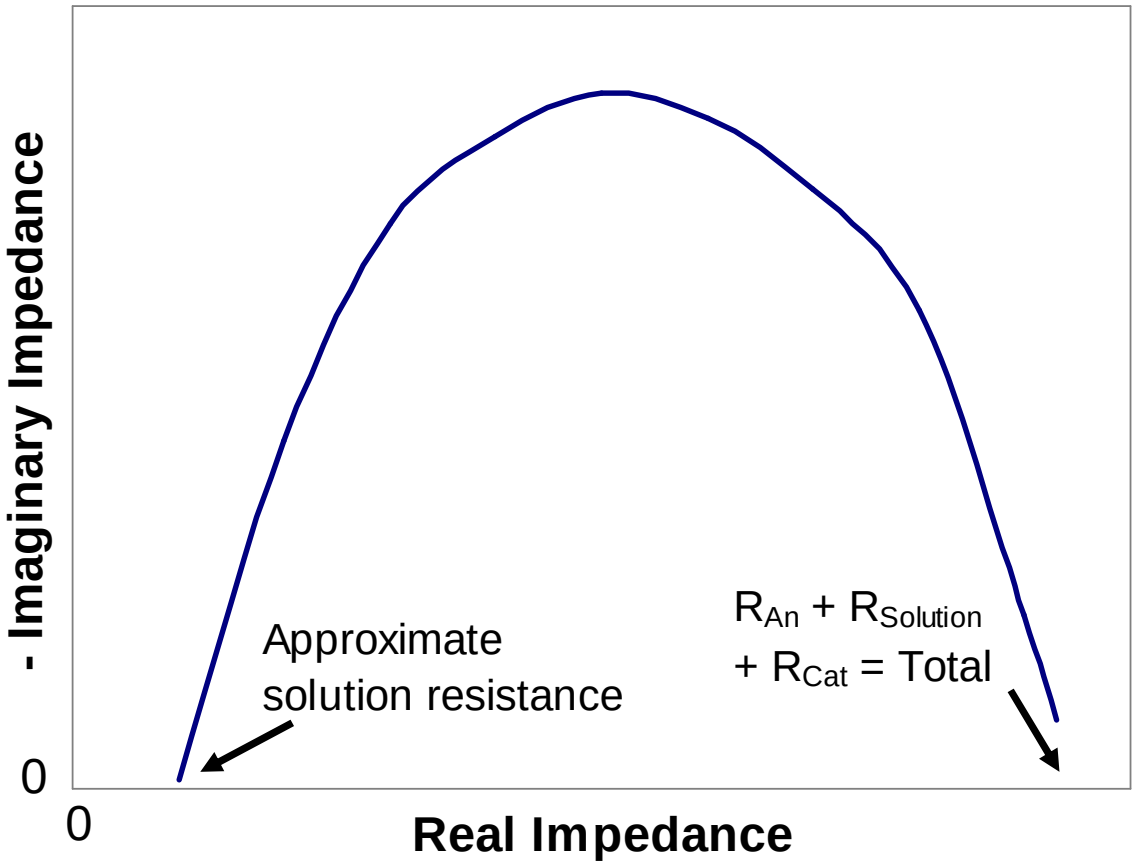

Figure 2.5. Typical Nyquist plot for an MFC. Notations indicate points for estimation of $R_{Solution}$ and total resistance.

2.3. Equivalent circuit model

The ECM used primarily in this work was comprised of two electrodes, each represented as a parallel resistor and constant phase element (CPE). These electrodes are separated by a resistor which represents a "solution resistance." In the PEMFC, the solution resistance was primarily dependent upon the PEM. In the MFC, the solution resistance (termed $R_{solution}$) includes the anode medium, PEM and cathode liquid film and is lumped together as a single parameter. The resistances at the electrodes represent a combined impedance (designated as R_{An} and R_{Cat} for anode and cathode, respectively) at the electrode surface. This resistance can include charge transfer resistance, pore diffusion resistance, and polarization resistance, depending on how the fuel cell is operated. However, for the whole cell measurements that make up the bulk of measurements taken here, those impedances were not broken down into individual impedances. Single electrode measurements are required to understand such detail, and are attempted in the MFC section. The CPE in each electrode represents electrical double layer capacitance that is the result of charged electrolyte species that accumulate near the charged surface of the electrode. Non-idealities, such as charge leakage, non-parallel plates and a non-planar electrode surface, have been proposed as reasons to use CPEs in place of capacitors (Gamry, 2006). Each CPE is comprised of two variable elements: a coefficient that represents capacitance and an exponent that empirically accounts for the aforementioned non-idealities. An inductor is also included in the ECM in Figure 2.6. This inductor is considered a stray inductance resulting from the arrangement of the cable connecting the potentiostat to the MFC, thus not related to phenomena occurring within the MFC.

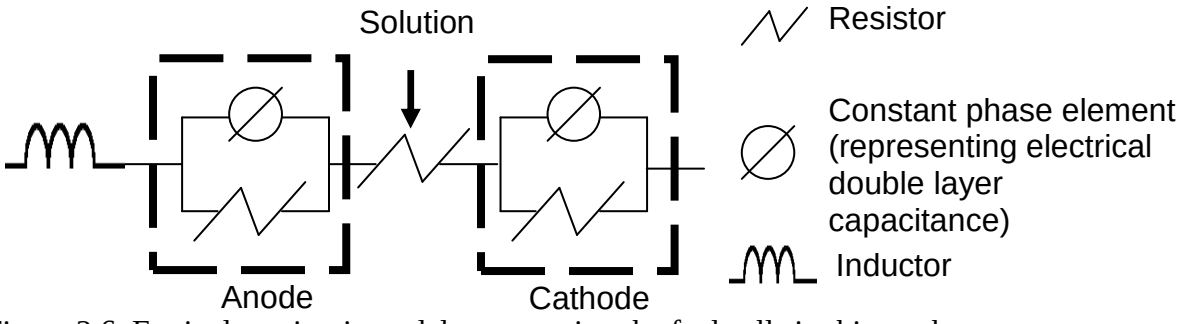

Figure 2.6. Equivalent circuit model representing the fuel cells in this work.

2.4 Neutron imaging

Neutron imaging has been demonstrated as useful for studying water evolution and distribution in PEMFCs without disturbing the fuel cell operation (Satija et al., 2004). Hydrogen has a relatively large neutron cross section when compared to other fuel cell materials (e.g., carbon, oxygen, and aluminum); a qualitative comparison of cross sections is show in Figure 2.7. In addition to illustrating the relatively large cross section of hydrogen, Figure 2.7 also shows why neutron imaging is more suitable for fuel cell water content studies than x-ray imaging. Early experiments oriented the fuel cell plane normal to the neutron beam, resulting in a "face-on" view that allowed quantification of total water content; however, this approach could not distinguish anode water from cathode water (Satija et al., 2004; Chen et al., 2007). As shown in Figure 2.8 below, measurement of water content in the flow fields of the PEMFC was possible with this technique. This was helpful in identifying flooding issues, especially since flooding of the flow fields could cause large pressure swings in the feed delivered to the GDL. The face-view orientation was primarily made necessary by the relatively low resolution (i.e., 130 μm) detectors available at the time.

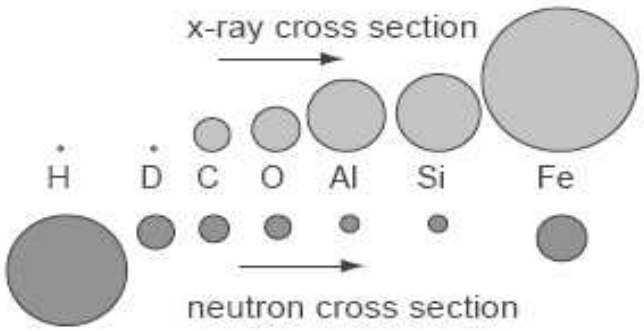

Figure 2.7. This figure from Satija et al (2004) illustrates the relative cross-sections of common elements for x-rays and neutrons.

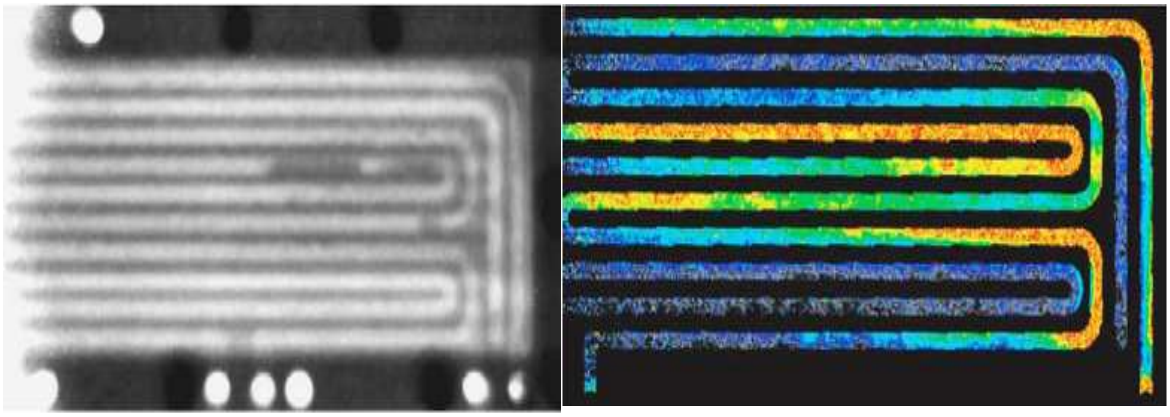

Figure 2.8. The above images are from Satija et al (2004). The left image shows an actual neutron radiograph; darker areas indicate the presence of bulk water in the flow channels. The right image is a computer-enhanced radiograph masked only to show the cathode-side flow field; orange indicates higher water content while blue indicates little water content.

High-resolution neutron imaging (approximately 25-μm resolution) allowed the water content in the anode, PEM, and cathode of a PEMFC to be resolved separately and monitored over time during operation. This was achieved by orienting the fuel cell for an "edge-on" view with respect to the beam (Hussey et al., 2007). The water content in each region of the operating PEMFC could be studied in the context of operating conditions, including current density, to provide a better understanding of the link between local heating, current output, and water content (Hickner et al., 2008). For example, the

competitive effect of increased current density resulting in greater osmotic drag (which dries out the anode) versus increased water production at the cathode could be explored. In addition, edge-on orientation of the fuel cell allowed the water distribution in the PEM to be calculated. Such observations of the trans-membrane water distribution are valuable since many modeling studies of fuel cells calculate this water distribution.

Like in PEMFCs, water management is important to the performance of EFCs. The anode of an EFC can be exactly similar to that of a PEMFC: Pt-deposited carbon cloth pressed against a PEM to provide good contact between the catalyst layer and electrolyte. The membrane used in an EFC is often Nafion, as well, which is identical to many PEMFCs. The difference between a laccase-cathode EFC and a PEMFC is in the cathode, where enzymes and mediators replace platinum. As mentioned previously, water loss in the cathode has been observed by Hudak et al. (2009). This generally leads to reduced power output because enzyme utilization decreases; such losses can be due to enzymes drying onto the carbon felt with no water to allow mediators and protons to diffuse to the enzyme. In addition, pockets of enzyme solution can be left isolated due to drying; this also would result in reduced utilization because protons cannot get to the enzymes (but electrons could). Neutron imaging is an ideal technique to monitor water content in the cathode over time without disturbing the EFC operation.

All of the neutron imaging experiments in this work were performed at the National Institute of Standards and Technology (NIST) Neutron Imaging Facility (NIF) in Gaithersburg, MD. Figure 2.9 below is a representation of the NIF setup. This facility

included a full suite of fuel cell control equipment so that all experimental parameters could be controlled during experiments. The parameters of interest generally included feed flow rates, feed humidity, and cell temperature (in the case of the PEMFC).

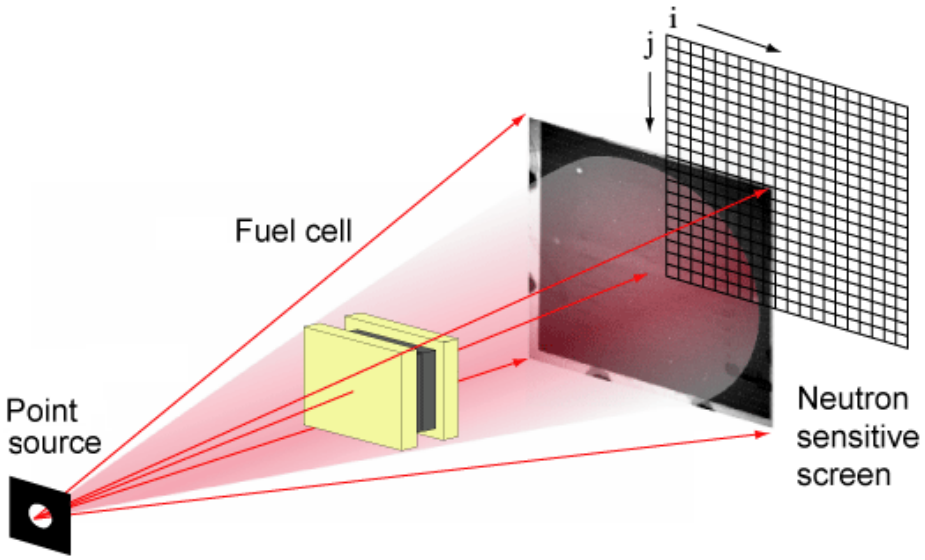

Figure 2.9 Setup for neutron imaging at the NIST NIF. In the experiments presented in this work, the fuel cell is actually oriented such that the layers of the membrane electrode assembly (anode, PEM, cathode) are parallel to the beam, rather than normal to the beam as shown. Image supplied by David Jacobson (http://physics.nist.gov/MajResFac/NIF/radiography.html).

From Figure 2.9, it can be seen that the objective of neutron imaging was to measure the "shadow" that is cast by water contained in a sample (specifically, a fuel cell). As the neutron beam passed through a fuel cell, water in the fuel cell attenuated the neutrons, as well as caused some scattering. The detector positioned behind the fuel cell then measured the intensity of neutrons that have passed through the sample by measuring how many neutrons strike the detector over time. For each exposure, the number of neutrons striking the collector/detector was counted. This neutron intensity was then converted into a depth of water based on internal calibrations performed at the NIST NIF. In general, this calibration was performed by placing a varying-thickness

cuvette of water in the beam path. Neutron intensity was measured for known thicknesses of water, allowing the correlation of water thickness and neutron intensity for a sample. This calibration also allowed calculation of the neutron attenuation coefficient for water, μ.

Attenuation was measured according to Beer's Law, shown in Equation 2.2. It can be seen that neutron intensity (I) is proportional to the original neutron intensity the resulted from passage of the beam through the filter (I_o) and inversely proportional to the water thickness (t). The term "μ" is the attenuation coefficient for water and was measured separately in a calibration experiment, described briefly above.

$$I = I_0 * e^{-\mu * t} \tag{2.2}$$

Since I_o was known as a constant at the facility, μ was determined via calibration and I was measured in the experiments, water thickness (t) could be calculated. This operation was performed for each pixel of the detector to form the image in gray scale.

To aid in understanding the results from neutron imaging of an operating fuel cell, dry images were taken. As can be seen in Figure 2.7, the other materials in a fuel cell do attenuate neutrons (albeit to a less degree than the hydrogen in water). This would cause problems when analyzing a neutron image if all attenuation was attributed to water. The water content would be overestimated because of the contributions to neutron attenuation

from the other fuel cell materials. To mitigate this problem, dry images of a sample were taken. For example, a PEMFC was imaged after dry N_2 was passed through the system, which was expected to remove most water (some residual water probably remained in the Nafion membrane because Nafion is highly hygroscopic). For an EFC, dry images were taken prior to injection of the enzyme solution, since this was when the cathode chamber was completely dry. Dry images were then subtracted from the neutron intensity results for wet, operating fuel cells. This removed all contributions to neutron attenuation that resulted from fuel cell materials, beam fluctuations, etc. Upon subtraction of the dry image, neutron attenuation attributable to the presence of water was left over; these results ware then correlated with water thickness.

In addition to neutrons, a small amount of gamma radiation struck the neutron detector, which could have skewed results. To reduce the impact of gamma rays hitting the detector, an image was acquired when the neutron beam shutter was closed and no sample was in the beam path. The shutter can stop nearly all neutrons from striking the detector, but gamma rays pass through the shutter to hit the detector. Thus, when this image was taken, the impact of gamma rays on the neutron detector was quantified. Results from this image were then subtracted from a wet, operating fuel cell image to improve accuracy. As a result of acquiring dry images and the gamma beam "image," an accurate measurement of water thickness was achieved since all other effects that were measured by the detector during an experiment were subtracted out.

CHAPTER 3

POLYMER ELECTROLYTE MEMBRANE FUEL CELLS

3.1 Introduction

The PEMFC can be readily divided into three distinct regions, each with its own interfaces, transport processes, and electrochemical reactions that should be understood and optimized. As hydrogen is introduced into the fuel cell, the first region is the anode. Outside of the catalyst layer, transport occurs by bulk fluid flow in the flow channels and gas diffusion layer (GDL). In the catalyst layer, hydrogen adsorbs onto a catalyst (Pt in most low-temperature cases) and the resultant protons must follow a continuous channel of water from the catalyst to the membrane to continue through the PEMFC. In this three-phase region (gaseous water and hydrogen, solid catalyst, and liquid water), transport is not well-understood and the catalyst utilization efficiency is affected by humidity and temperature. Many interfaces are important in this region: membrane-catalyst-gas, membrane-support-gas, membrane-gas, and catalyst-gas (see Figure 2.2). Transport may occur across all of these interfaces, but possibly the most important interface is membrane-catalyst-gas. This is the interface where catalyst efficiency is determined, a major cost factor for fuel cells. After hydrogen dissociates into protons and electrons in the anode catalyst layer, the protons must diffuse to, and then through, the proton-exchange membrane (PEM). While there are no chemical reactions for protons occurring in the PEM, resistances to ionic transport are present and can contribute to cell power loss. After protons diffuse through the PEM, they come to the cathode catalyst

layer. It is in this region that protons and electrons (from the feed hydrogen) combine with oxygen to form water. This water can then diffuse back through the membrane or evaporate and exhaust from the system.

Two very important parameters in each of the three regions are water content and temperature. Temperature is controlled externally while water content is controlled by feed humidity and electrical current. Temperature affects catalytic reaction rates and transport of protons through the PEM (Andreaus et al., 2002; Cui et al., 2002). Water is the medium for proton transport in a PEMFC, thus there must be a continuous path of water from the anode catalyst to the cathode catalyst. Too little water in the anode catalyst layer may result in no path for protons to enter the PEM; too much water can cover the catalyst, making hydrogen contact with catalyst difficult. In the PEM, there must be enough water to form pathways connecting the two electrode catalyst layers.

3.2 Experimental

3.2.1 Fuel cell design

A 25 cm^2 active area PEMFC was utilized in these studies. This fuel cell has gold-plated aluminum endplates, graphite current collectors with four-channel serpentine feed distributors, and a membrane-electrode assembly (MEA) with carbon/platinum catalyst layers and a Nafion 117 PEM (made by Asia Pacific Fuel Cells, Taiwan). The MEA was also made by Asia Pacific Fuel Cells, via hot pressing the layers together. A test stand with temperature, feed pressure, feed humidification, and feed flow rate controls was used. A schematic of this fuel cell design is presented in Figure 2.1.

3.2.2 Electrochemical impedance spectroscopy

EIS data were generated and taken by a Gamry Instruments series 750G Galvanostat/potentiostat/zero-resistance ammeter. Equivalent circuit models (ECMs) were constructed and tested using Gamry EChem Analyst software. This package utilizes a least-squares optimization routine to determine impedances in an ECM. The ECM that was used in these studies is shown in Figure 2.6, as described in previous work performed by Page et al. (2007). Various ECMs have been proposed, but the ECM employed here is very common in the literature. Other ECMs include a model with a resistor in series with a parallel resistor-capacitor component and various models that expand the electrodes to include other circuit elements to describe diffusion resistances. These alternative models were tested and found to not offer significantly better fits to the experimental results. Ultimately, it is desirable to use the simplest ECM that physically describes the system. From the anode side to the cathode, there is a high frequency resistance, a parallel component with a charge transfer resistance and electrical double layer capacitance, a resistor for the PEM, and another parallel component similar to the anode to represent the cathode electrode.

To maintain a linear response between the applied AC potential and current (see Equation 2.1), a 10 mV signal was applied to the fuel cell at all frequencies. The frequency range was from 100 mHz to 100 kHz with 10 measurements per decade. Each 10 decade scan required approximately 2.5 minutes; cell voltage was monitored during scans to verify that no noticeable drift was occurring. This determination was qualitative

since the cell output potential was slightly affected by the signal, most noticeably at low frequencies.

3.2.3 Experimental parameters

The goal of these experiments was to measure the effects of operational parameters on internal charge transfer resistances. The effects of cell temperature, air feed humidity, and air feed flow rate were investigated. The matrix of conditions for experiments is shown in Table 3.1. As a summary, the control conditions were 50^{o}C, 98% humidity for both feeds, 20 sccm hydrogen and 45.1 sccm air feed. As one operating parameter was adjusted, the others were maintained at the control conditions. In addition to these experiments, the transient response of the fuel cell to a stepwise increase in air-side humidity from 0% to 98% RH was measured by EIS. In this experiment, the cell was allowed to operate with 0% air-side RH for approximately 30 minutes. Then the air-side humidity was quickly increased to 98% and EIS performed during the response period until steady state was achieved. Since the change in cell voltage was slow over time (1 mV/min) during this response, fast EIS measurements could be completed without significant changes in the performance of the fuel cell. Also, the cell was allowed to run for approximately 30 minutes before performing EIS, as there is a quick startup period and then a slow increase in power over time until steady power output is achieved.

In all the experiments performed, the hydrogen flow rate was maintained between 19.9 and 20.3 sccm; this flow rate corresponds to a stoichiometric ratio of approximately

4.3 since the cell consumes approximately 4.7 sccm of hydrogen. It should be mentioned here that the stoichiometric ratio is defined as the ratio of reactant flow rate fed to the minimum flow rate for stable operation. A hydrogen feed of 20 sccm was chosen to correspond to a 1:1 ratio with the minimum air flow rate for cell operation. Below 20 sccm air flow, the cell was unsteady; below 15 sccm air flow, the cell did not produce power. Also, the humidification columns were maintained at a temperature 10^{o}C warmer than the cell temperature. Both air and hydrogen feed channels were open to the atmosphere at the outlet, so no back pressure was applied to either side. The load in all experiments was set at 5 Ω and resulted in current density ranging from 34 to 50 W/m^{2}.

Table 3.1. Matrix of experiments exploring temperature, air humidity, and air flow rate.

Temperature (^{o}C)	Air humidity (%RH)	Air flow (sccm)
31	98	45
40	98	45
51	98	45
51	20	45
51	63	45
50	98	20
50	98	30

Each effect (temperature, humidity, air flow rate, and transient humidity response) was investigated after completely drying out and cooling the fuel cell. The same startup procedure was followed for each series of experiments, except for the transient humidity response. For temperature, humidity and air flow rate, the feed gas humidifiers were heated to 10^{o}C above the desired fuel cell temperature. Once the humidifiers were

thermally stable, feed gases were turned on to stoichiometric ratios of approximately 4.0. When the feed gases began passing through the cell, the cell was heated to the experimental temperature. The high feed rate of air was maintained for approximately 30 minutes to hydrate the MEA. After this 30 minute period, the air feed rate was set to the experimental rate and the cell allowed to equilibrate. The hydrogen feed rate was maintained at a stoichiometric ratio of 4.0. The cell was then left at the experimental conditions for approximately one hour for stabilization; steady state was confirmed by monitoring the output voltage. Once the output voltage was stable (varying by no more than 1 mV/min), EIS was performed. No experiments changing the condition of the hydrogen feed were conducted because it was found that the cell was unsteady at low hydrogen humidity and low feed rate. Thus, variations in the air feed were explored as they allowed steady cell operation, yet still had appreciable effects on charge transfer resistances throughout the PEMFC.

3.2.4 Neutron imaging and PEMFC control

Neutron imaging studies were conducted at the National Institute of Standards and Technology (NIST) Neutron Imaging Facility (NIF) in Gaithersburg, MD. This facility has been built and designed with the intention of providing control over all aspects of fuel cell operation while simultaneously acquiring neutron images of the operating fuel cell. The test stand at the NIF was capable of controlling feed flow rates, humidities, composition, and temperatures, in addition to fuel cell temperature. An electronic load was normally used, but the fuel cell in this work was too small to provide enough current for the electronic load (the NIF can accommodate vehicle-scale fuel

cells); thus, a variable resistor was used, similar to work performed in our lab. The lines between the humidifiers and PEMFC were heated to mitigate condensation in the feed lines. The beam had a post-filter fluence rate of approximately 5.1×10^7 neutrons $cm^{-1} s^{-1}$. The detector used in this work was a cross-delay line detector with a 20 μm resolution. Exposure time for each image was five minutes.

3.3 Results

3.3.1 Temperature effects on internal resistances

As the cell temperature increased, an increase in cell power output was observed. At the same time, charge transfer resistances in the anode, PEM, and cathode all decreased. The anode and cathode resistances both decreased by approximately 10% while the PEM resistance decreased by approximately 5% over the range of temperature studied. The greater decrease in the electrodes (compared to the PEM) is believed to be due to faster reactions at higher temperature, e.g., higher collision rate of reactant molecules with the catalyst (see Figure 2.2). The results for analysis of the impedance data via ECM are shown in Figure 3.1. Figure 3.2 is the Nyquist plot of the impedance data. The Nyquist plot is useful for identifying resistances in the cell at both the high frequency (to the left of the curve) and low frequency (to the right of the curve) intercepts on the Z_{Real} axis. These resistances are helpful for obtaining initial guesses used in the ECM optimization. The high frequency intercept of the Nyquist plot corresponds to the solution resistance in a fuel cell. In the case of a PEMFC, this resistance is dominated by the PEM. The low frequency resistance corresponds to the total internal impedance of the PEMFC, comprised of the sum of the anode, PEM, and cathode resistances. It can be

seen in Figure 3.1 that the total resistance for the 31^{o}C experiment was higher than that for the higher temperature experiments. Since the Nyquist plot contains no real frequency data, it was only used to provide the initial guesses for the ECM fit optimization.

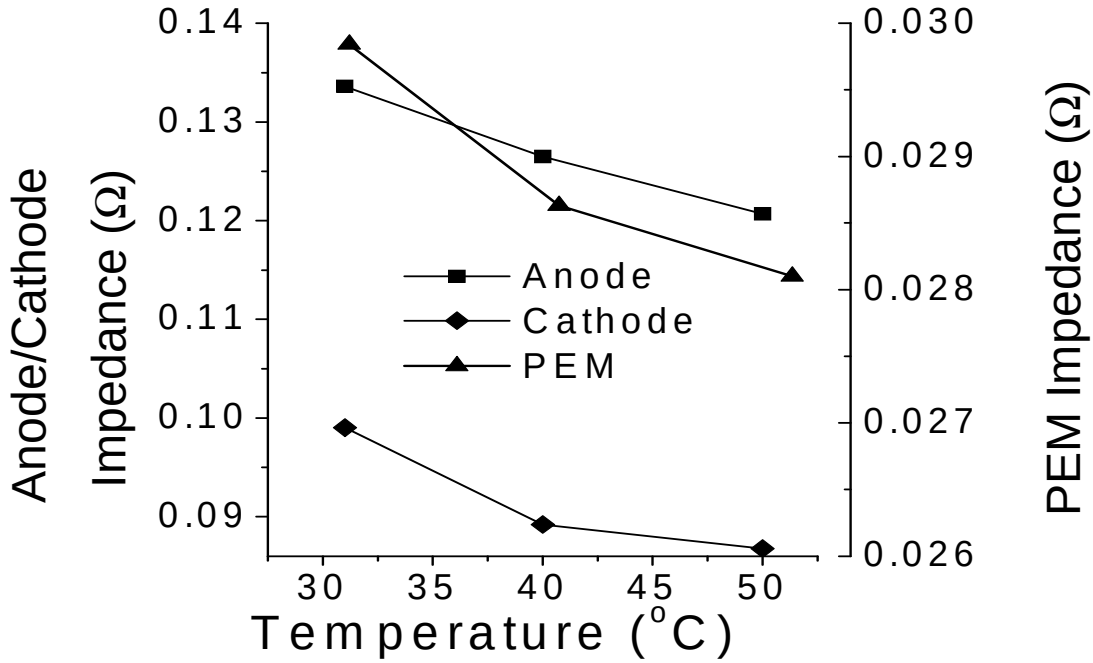

Figure 3.1. Anode, PEM, and cathode charge transfer resistances as a function of temperature. Hydrogen flow: 20.1 sccm (98% RH), air flow: 45.1 sccm; 98% RH for both feed streams.

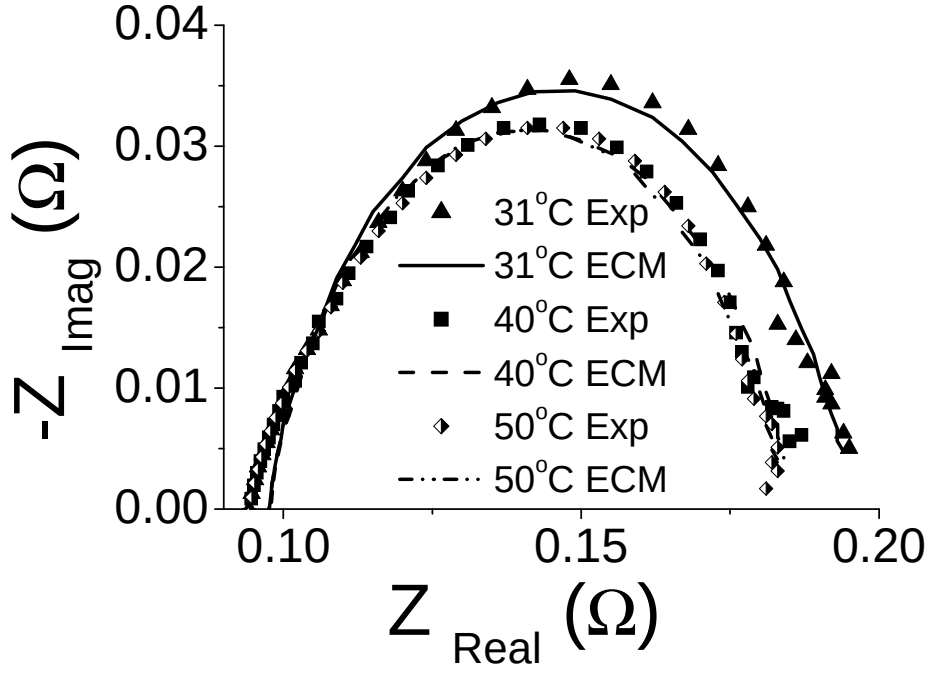

Figure 3.2. Nyquist plot for the PEMFC at 31, 40, and 50°C showing the imaginary impedance as a function of real impedance. Frequency increases from right to left on the curve. Hydrogen flow: 20.1 sccm (98% RH), air flow: 45.1 sccm; 98% RH for both feed streams.

On the Nyquist plot, the imaginary component ($-Z_{Imag}$) is a result of the phase shift while the real component (Z_{Real}) is based on the magnitude of impedance measured in EIS. In this case, charge transfer resistances, in which protons are transferred from the electrode to the electrolyte, decreased with increasing power production. This is reasonable, since decreasing transport resistances in the fuel cell should allow greater throughput of protons and electrons. Indeed, a good first indicator of decreased charge transfer resistances is increased power production. It should be noted that the anode provided the greatest resistance over the whole temperature range studied. The anode resistance was consistently approximately 35 mΩ greater than the cathode resistance and 100 mΩ greater than the PEM resistance.

3.3.2 Effects of air-side humidity on internal resistances

Presented in Figure 3.3 are the responses of anode, PEM, and cathode charge transfer resistances to air-side humidity. Experiments in which the hydrogen feed humidity was varied over a large range could not be carried out because the cell either did not produce power or was too unstable for EIS analysis at low humidification. Thus, experiments were performed where hydrogen humidification was held constant at 98%. It can be seen in Figure 3.3 that resistances in all three regions decreased as humidity increased, especially in the PEM. At the same time, the cell power output increased. All of the experiments were performed at 50^{o}C because the cooler temperatures eventually resulted in suspected flooding of flow channels in the anode, as indicated by short disruptions in power output.

Figures 3.4 and 3.5 show the Bode and Nyquist plots, respectively, of the data collected in these air-side humidity experiments. It can be seen in Figure 3.4 that very slight oscillations in phase shift and impedance occur in the low frequency region. While these can be the signature of flooding conditions, it is not believed that flooding occurred because the cell power output did not drop or oscillate, as would be expected with a flooding event (Le Canut et al., 2006). Flooding occurs in a PEMFC when liquid water builds up in the catalyst layer, GDL, or flow channels and blocks the flow of gas. Also, flooding is expected to cause much larger oscillations in power output, impedance, and phase shift due to unstable performance. At low signal frequency, oscillations in cell potential were observed with a multimeter, but these oscillations were a result of the EIS signal passing through the cell, as determined by comparing the signal generation and

multimeter reading. Thus, slightly unsteady behavior of the PEMFC is expected to have contributed to these results.

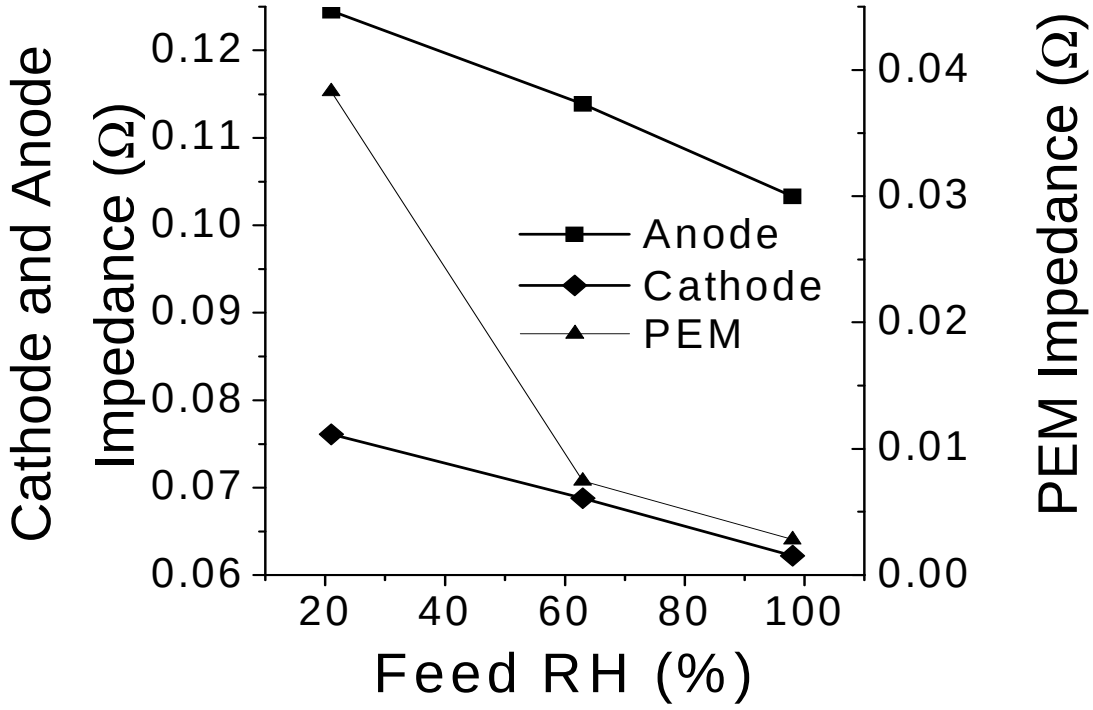

Figure 3.3. Anode, PEM, and cathode charge transfer resistances as a function of air-side humidity. Hydrogen flow: 20.0 sccm (98% RH), air flow: 45.1 sccm; T_{Cell} was maintained at 51°C.

It is difficult, when looking at Figure 3.4, to see a large change in impedance between the various air-side humidification levels. Above 5 Hz, there is significant overlap between the three different series of impedances. However, when analyzing the data via the ECM, it is observed that all of the charge transfer resistances decrease, and power measurements indicate increased power production at greater humidification. The Nyquist plot in Figure 3.5 supports this result, as seen where the low frequency data show a decrease of the summed resistances. While there is scatter in the data, the increase in

power production with increased humidity supports the model results showing decreased resistance at higher air-side humidity.

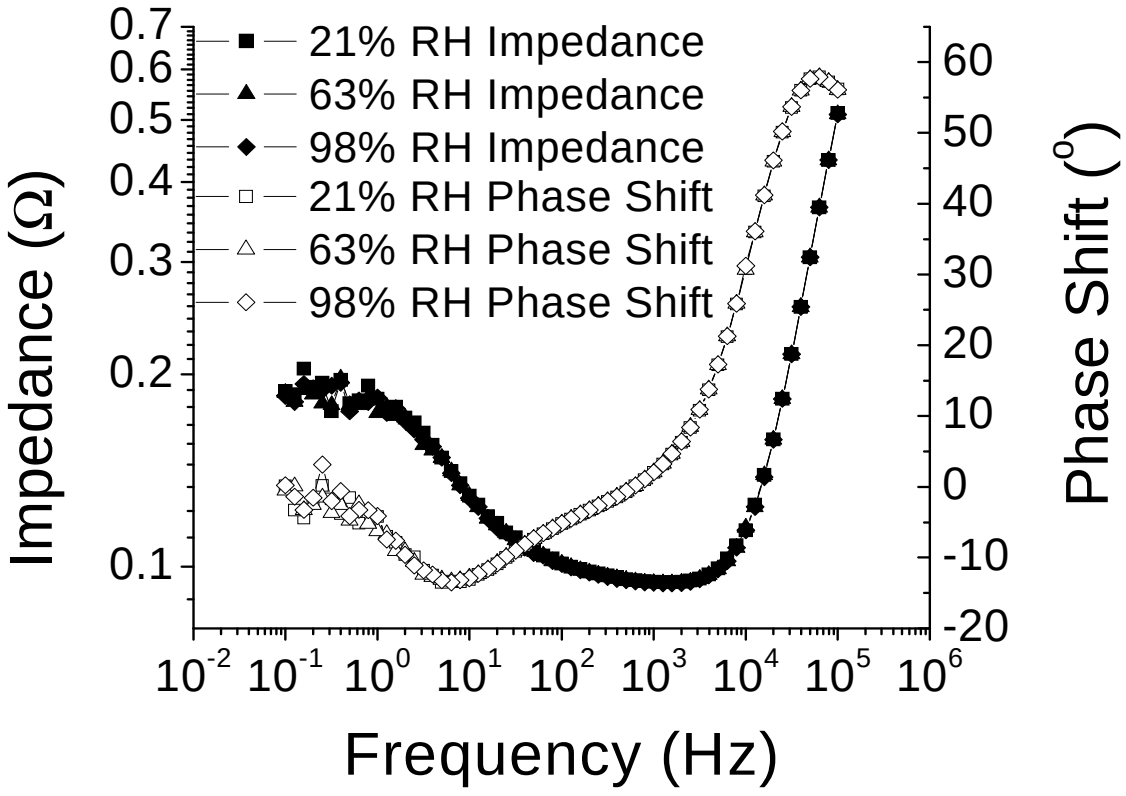

Figure 3.4. Bode plot showing impedance and phase shift for the PEMFC at multiple air-side humidity settings. Hydrogen flow: 20.2 sccm (98% RH), air flow: 45.1 sccm; cell temperature was held constant at 50°C.

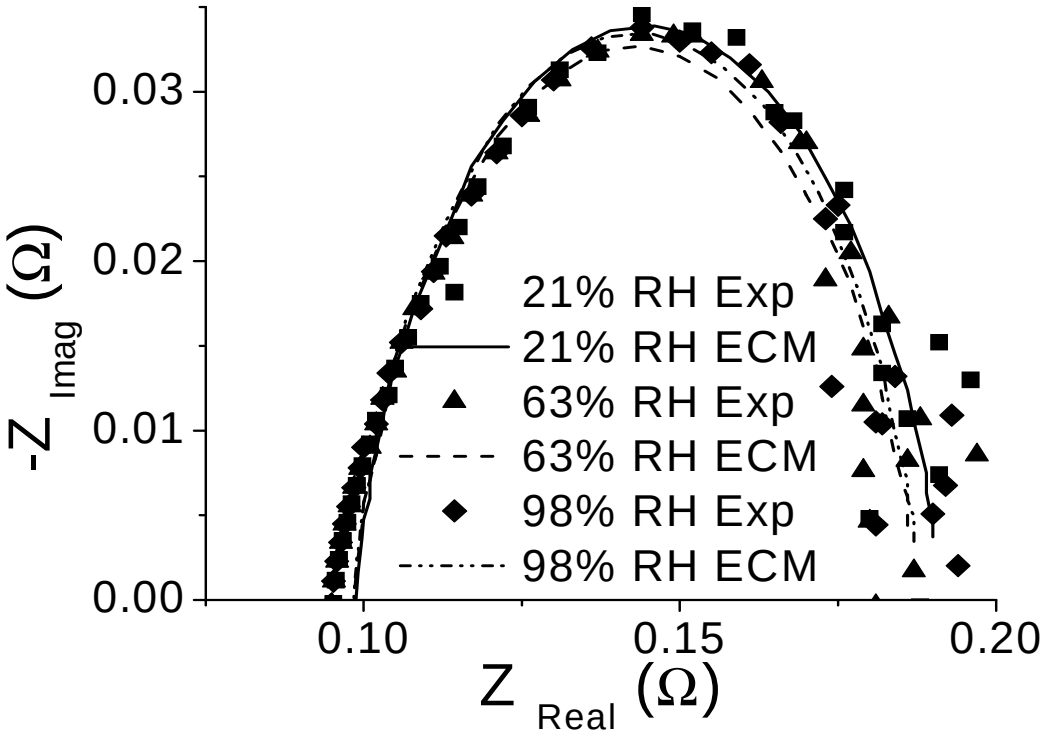

Figure 3.5. Nyquist plot for the PEMFC at multiple air-side humidity settings. Hydrogen flow: 20.2 sccm (98% RH), air flow: 45.1 sccm; cell temperature was held constant at 50^{o}C.

3.3.3 Effects of air flow rate on internal resistances

The effect of air flow rate on the three resistances was also explored; these results are illustrated in Figure 3.6. All three resistances decreased slightly: 3.3% for the anode and approximately 6% for both the PEM and cathode. Since the air flow rate was adjusted on the cathode side, it is reasonable for the cathode side to be affected more than the anode. Similar to the results from the temperature experiments, the anode has the greatest impedance: approximately 35 mΩ greater than the cathode and 90 mΩ greater than the PEM. It can be seen that the air flow rate had little effect on the transport resistances in the fuel cell, as long as it was greater than the minimum flow rate for cell

operation (which was found to be approximately 15 sccm). Additionally, the cell power output changed very little between the three air flow rates, from 40.0 W/m^2 at 20 sccm to 41.0 W/m^2 at 40 sccm. However, even though the air flow rate had little effect on the charge transfer resistances and power output, it is still vital to maintain air flow above a stoichiometric air ratio of one or the cell ceases operation very quickly.

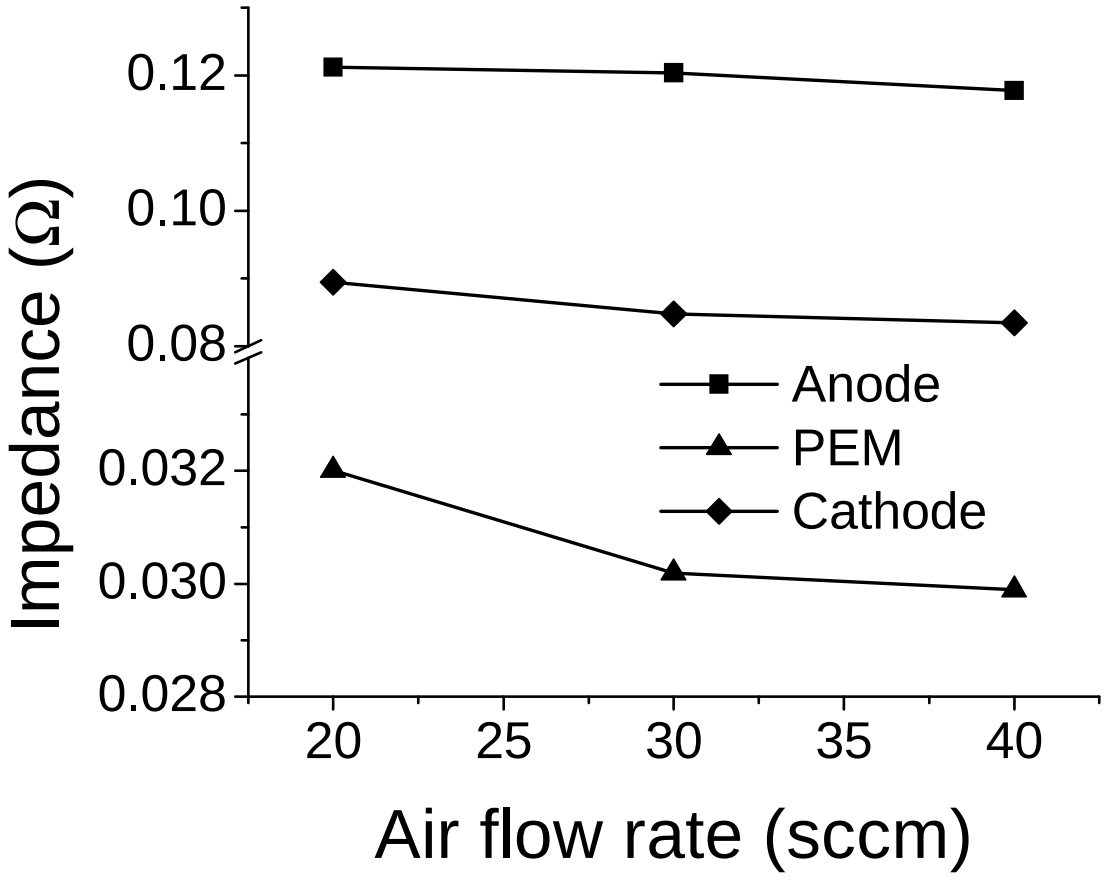

Figure 3.6. Anode, PEM, and cathode charge transfer resistances as a function of air flow rate. Hydrogen flow rate was held at 20 sccm (stoichiometric ratio of ~4.3); cell temperature was constant at 50^{o}C and both feed streams were at 98% RH.

3.3.4 Transient response to an increase in air-side humidity

Finally, a transient response of the fuel cell impedances to a step-wise increase in air humidity was measured at a cell temperature of 51^{o}C. These results can be seen in Figure 3.7. Counter to what was expected, both the anode and cathode charge transfer resistances increased over time; the cell power output steadily increased over this entire time period. Thus, despite the increases in charge transfer resistance for these two regions, the overall cell power increased over time. Upon further review of the data, it was found that the electrical double layer capacitance impedances decreased over time; thus, the overall impedance decreased, but this is not seen when only considering the charge transfer resistances. Even though the two charge transfer resistances did not become steady over time, the power output of the fuel cell became steady within 20 minutes of applying air-side humidification. At this point, the experiment was terminated. EIS experiments measuring the transient response of the cell to a reduction in air-side humidity were not performed, though may be of interest in the future.

It was also observed in these experiments that impedance is not a state function based on operating conditions of the steady-state PEMFC. A repeat of the transient response showed the same trend for charge transfer resistance, but values were approximately 8% greater than in the first experiment. Experiments to establish a reliable standard deviation were not performed; however, the model results fit well the experimental data so that the differences in impedance are not believed to be due to poor model fit. It is believed that the startup of the fuel cell affects impedance values, possibly because some conformational changes that occur during startup persist after steady state

is achieved. For example, the distribution of water channels linking the anode-PEM interface may form uniquely during each startup. In addition to the impedances behaving this way, the cell power output is not always constant from one experiment to another; each startup resulted in different cell potential (and, consequently, power production) at steady state, on the order of 10 mV out of 750 mV.

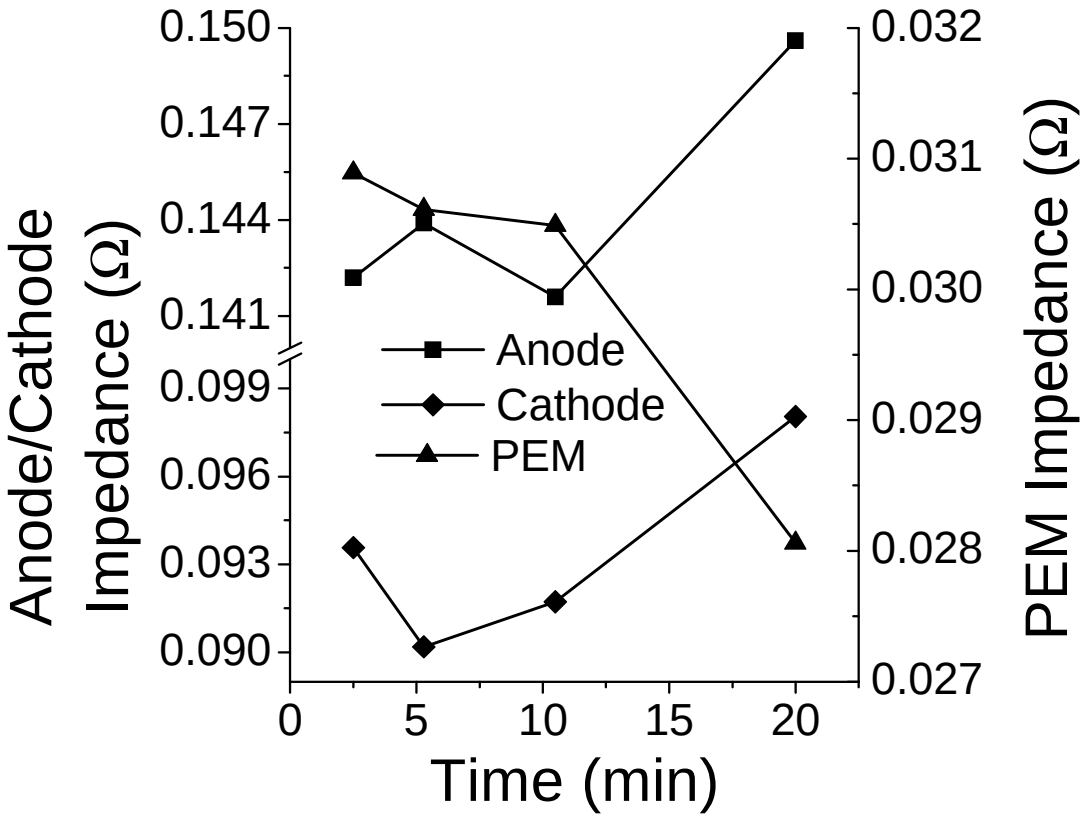

Figure 3.7. Response of anode, PEM, and cathode charge transfer resistances as a function of time after stepping air-side humidity from 0% to 98% RH. Hydrogen flow: 19.9 sccm (98% RH), air flow: 45.1 sccm; cell temperature was 51^{o}C.

3.4 Neutron imaging of the PEMFC

3.4.1 PEMFC design and operation

Neutron imaging experiments were performed on a small PEMFC that had been constructed for use in the NIF beam. A picture and schematic of this smaller PEMFC is shown in Figure 3.8. The photograph shows the PEMFC as it was oriented in the beam line, thus all images showed water content between the anode and cathode via an edge-on view, rather than a face-view. Also shown in the photograph is the heating tape (covered by white cloth material) that maintained the PEMFC temperature. Feed connections were made via feed tubes inserted into the black connections (four connections – inlets and outlets for air and hydrogen). In the schematic, the orange pieces are the aluminum endplates, the gold-colored plates are the current collectors/flow fields, and the black rectangle represents the GDL-PEM-GDL sandwich. It can be seen that serpentine flow channels were machined into the flow fields to distribute the feeds. The materials for this smaller PEMFC were identical to those of the PEMFC utilized in the EIS component of this work. Aluminum endplates, gold-plated current collectors, carbon GDLs, platinum catalyst and a Nafion 117 PEM comprised the layers of this PEMFC. A Nafion 117 membrane is 7 mils thick, equivalent to 178 μm; thus, in the imaging results, the PEM is roughly eight pixels in width since each pixel was nominally 20 μm. The active area of the PEMFC was approximately 2 cm^2. Due to the small size, the power output of this PEMFC was very small, with a maximum of approximately 2 mW for the PEMFC at 75^oC. Such small output limited use of the NIF test stand since it is designed to accommodate kW-scale fuel cells.

The exploration of the effects of operating conditions on water content was guided by previously-obtained EIS results; since cell temperature and humidity had strong effects on internal resistances, these conditions were the focus of neutron imaging experiments. The goal of this component was to attempt to observe whether the changes in internal resistances for varying cell temperature and feed humidity were a result of changes in water content. Thus, effects of temperature ranging from 45^{o}C to 75^{o}C were observed via neutron imaging. Humidification was varied between near-0% to saturation. Saturation of the feed streams was achieved by passing the air stream through temperature-controlled humidification bottles. Humidity probes measured humidity at the outlet of the bottles. The feed lines were heated slightly above the humidification temperature to minimize any condensation of water in the feed lines. The test stand at the NIST NIF did not allow EIS measurements to be taken during imaging experiments. Interference between fuel cell controls prohibited connection of the potentiostat used in work performed prior to the trips to NIST; the test stand at NIST is expected to be able to perform EIS at some point in the future, but this capability was not available at the time of the experiments reported in this work.

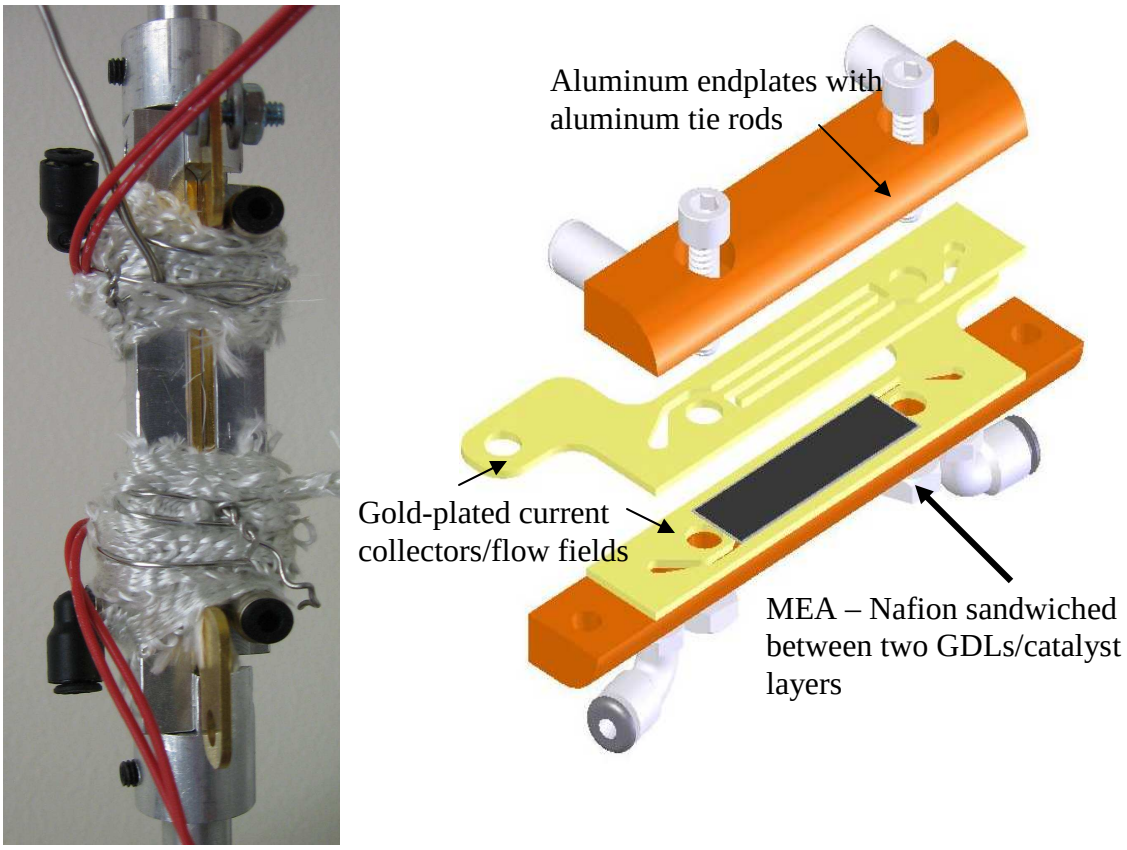

Figure 3.8. Photograph (on left) and schematic (on right) of the smaller PEMFC used for imaging experiments at NIST.

3.4.2 Understanding the neutron imaging results

The primary output obtained via neutron imaging was a gray-scale image of the sample in the beam path. In the case of this work, the sample was a PEMFC oriented edge-on with the beam (see the photograph in Figure 3.8). Figure 3.9 is an example of the raw image that resulted from the neutron intensity measured by the detector. It should be noted that the brightness of any pixel in Figure 3.9 is tied to a "count" of how many neutrons struck the neutron collector during the experiment; brighter sections are related to more neutron "hits" on the detector, which signifies less water content. This is because neutron intensity is inversely proportional to water thickness (see discussion in section 2.4). The low output of the small PEMFC still allowed observation of changes in

water distribution that resulted from varying the operating conditions. Following acquisition of an image such as is shown in Figure 3.9, subtraction of the dry image and background was performed so that only neutron attenuation due to the presence of water was considered. Water content profiles were generated for boxes that spanned from the anode to the cathode (see box in Figure 3.9). Neutron intensity was averaged vertically along the box, generating a horizontal line profile of the water content. Depending on the vertical height of the box, the average neutron intensity could change since more of the image was taken into consideration. In general, the box used for generating a line profile was made tall enough (vertically) to minimize local variations in average neutron intensity. This provided an overall perspective of the neutron intensity and, consequently, water thickness profile between the anode and cathode. An example of the neutron intensity profile can be seen in Figure 3.10. Figure 3.10 shows the neutron intensity profile (a) for the PEMFC at 75^{o}C, as well as the derivative (b) of this profile.

The background in Figure 3.9 is black because the dry image and gamma image were both subtracted out of the wet PEMFC image shown. All neutrons that struck the detector outside of the fuel cell (as well as any neutron attenuation that resulted from non-water-related fuel cell materials) were removed from the neutron intensity used in equation 2.2. Thus, the darker regions in the PEMFC radiograph shown in Figure 3.9 result only from the presence of water in the operating PEMFC.

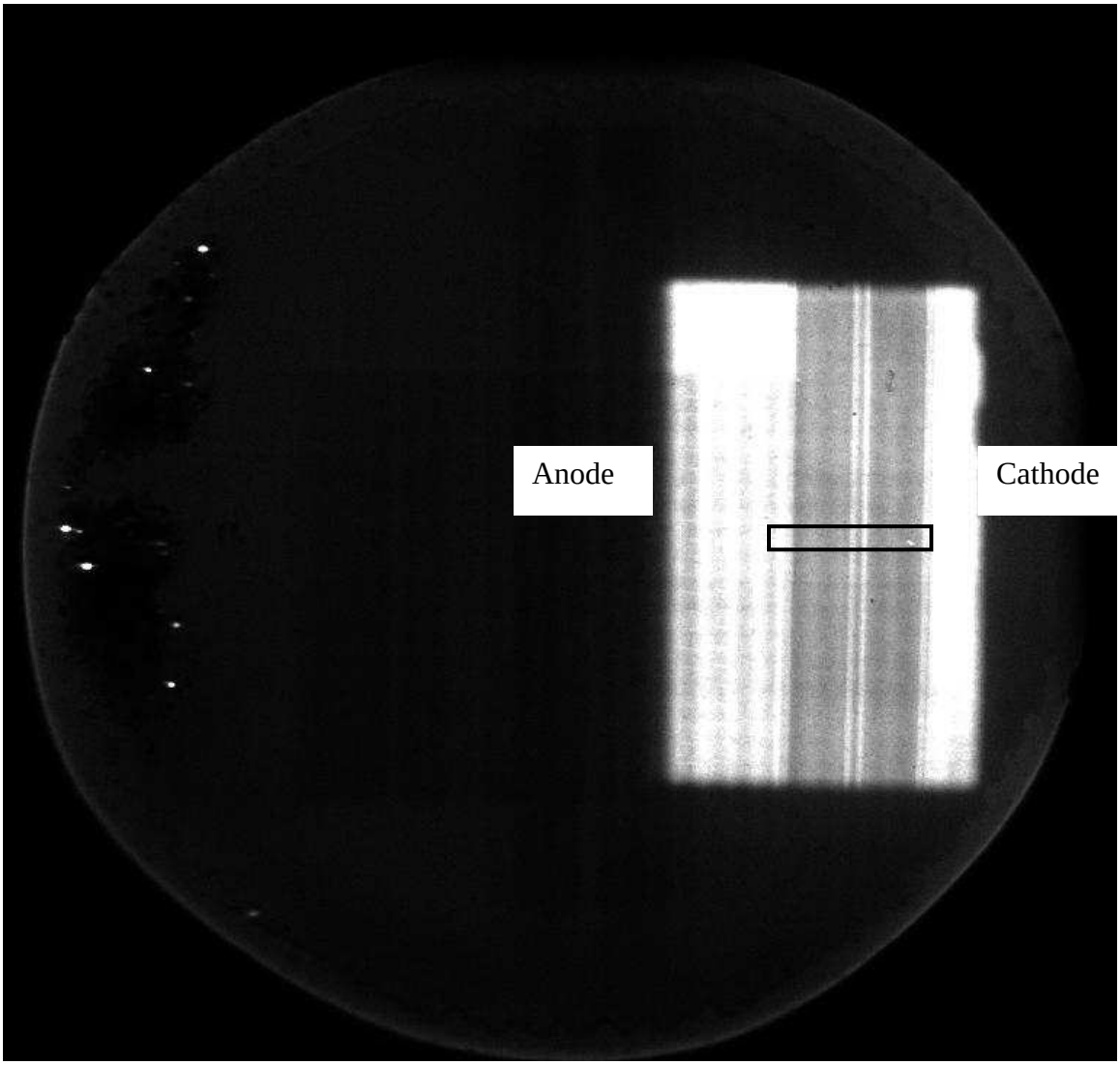

Figure 3.9. Raw neutron radiograph of the operating PEMFC at 75^{o}C. It can be seen that the visible area was larger than the PEMFC used in this work. The orientation of the PEMFC is similar to the photograph in Figure 3.8.

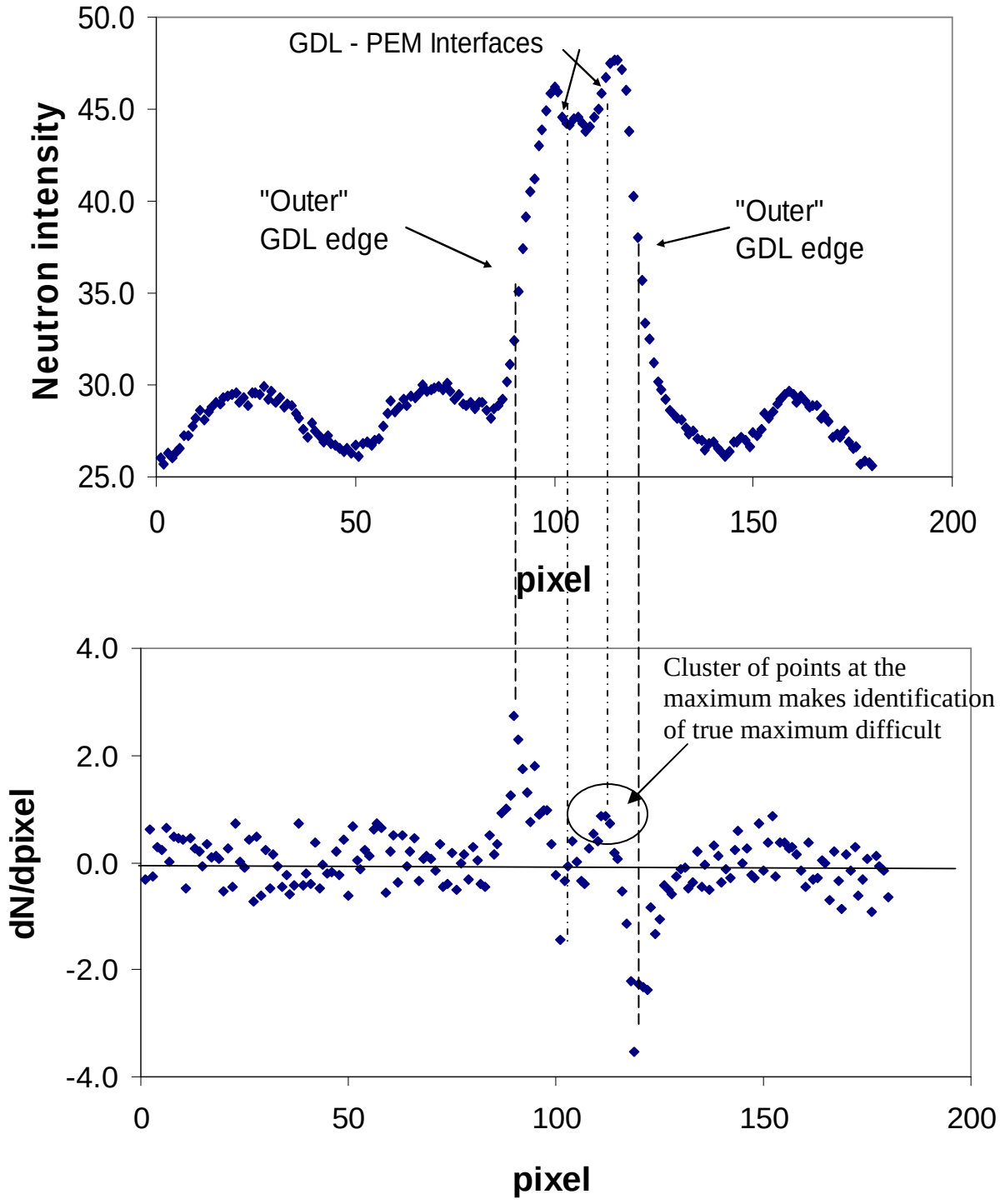

Figure 3.10. (a) Neutron intensity profile of the dry PEMFC at 75°C. Points of greatest slope indicate interfaces between layers of the MEA, as indicated in the Figure.
(b) Derivative of the neutron intensity profile in Figure 3.10a. Such an operation was performed to better locate points of maximum slope to identify layer interfaces.

The neutron intensity profile in Figure 3.10a is for the dry PEMFC. This image was taken so that the interfaces of the MEA could be identified. Were this determination of the interfaces to be attempted when the PEMFC was saturated with water, the interfaces would be much more difficult to distinguish (as will be shown below). The GDLs and catalyst layers are made of Pt and carbon, thus exhibit very little neutron attenuation. The PEM, however, has some hydrogen in it which contributes some neutron attenuation, as well as residual water that could not be removed via drying. In Figure 3.10a it can be seen that two peaks in neutron intensity occur in regions labeled as the GDL. The catalyst layer is actually adjacent to the GDL-PEM interface indicated in Figure 3.10a. Assignment of the layers was made by identifying the points of maximum slope on the neutron intensity profile. The layers of the PEMFC should actually be nearly straight (indicated by the dotted black lines in Figure 3.11), but blurring of the neutron image causes the straight interfaces to appear as sloped lines (the orange line in Figure 3.11). Figure 3.11 is a conceptual representation of how blurring causes the sloped lines observed in Figure 3.10a. The top component is a colorized neutron radiograph of the PEMFC while in the beam line (similar to the box shown in Figure 3.9). It can be seen that the GDLs (two teal bars outside the central blue region) are much thicker than the central PEM. The large blue sections are the flow fields that distribute the feeds. These flow fields are graphite and exhibit greater neutron attenuation than the GDLs, possibly due to the much greater density of graphite plates than the less dense GDLs. It can be seen even in this image that the PEM-GDL interface is blurry in the colorized image. Below this picture is a schematic of the idealized GDL-PEM-GDL

region. Finally, the bottom portion is a qualitative neutron intensity profile corresponding to the region between 43.0 and 50.0 on the y-axis in Figure 3.10a.

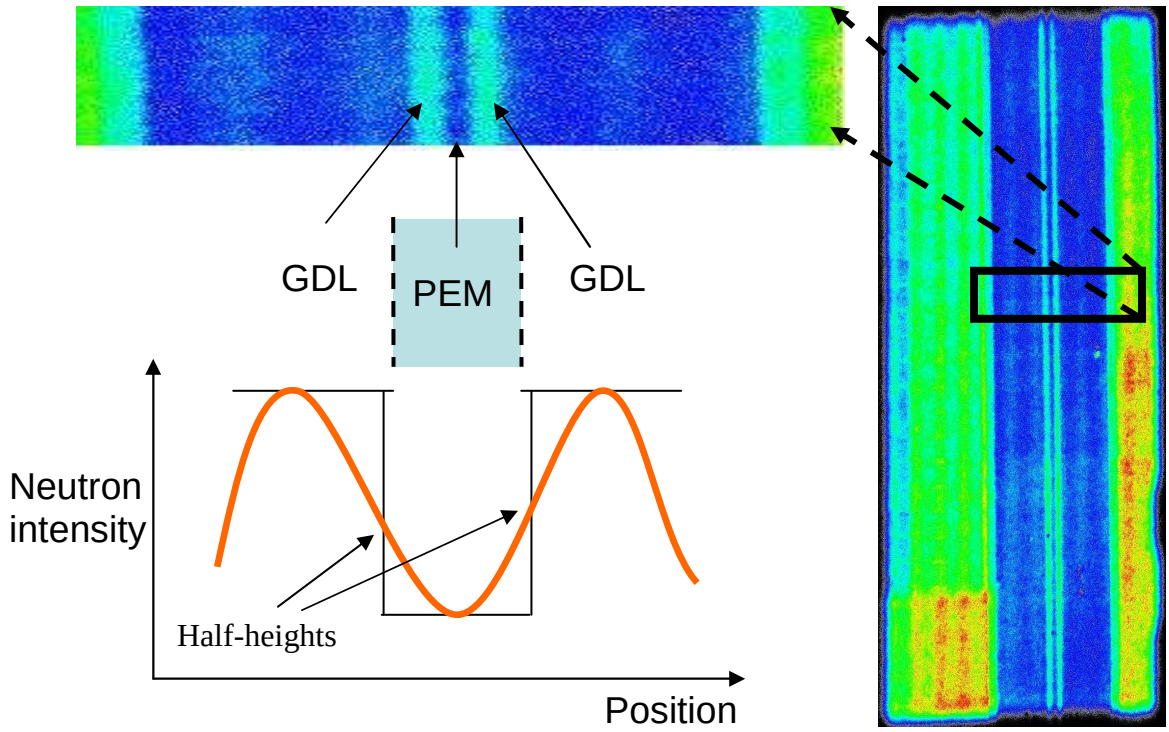

Figure 3.11. The PEM causes more neutron attenuation than the GDLs. The black line on the qualitative neutron intensity profile shows the unblurred profile while the orange line indicates the real, blurred image.

Figure 3.10b shows the derivative of the neutron intensity profile in Figure 3.10a. As explained above, the supposedly linear interfaces between the PEM and GDLs are curved because of blurring that is inherent to the neutron imaging setup. Thus, the interfaces are considered at the half-heights between the local maxima and minima. It is evident in Figure 3.10a that inspecting the half-heights would provide an error-prone, qualitative estimate of the layer interfaces. Thus, the derivative was used to quantitatively define the interfaces. However, this method of assigning the interfaces has

resulted in a questionable peak in water content that occurred inside the PEM, rather than at the PEM-GDL interface, as shown in Figure 3.12 below. This suspect assignment of the PEMFC layers is a result of some ambiguity on where exactly the local maxima and minima occurred in Figure 3.10b. It can be seen in the region near pixel 110 (the maximum near the center of the graph) that the maximum is still somewhat hard to define. As a result, assignment of the peak in water content inside the PEM is only inside by one pixel, still within the error associated with identifying the pixel corresponding to the neutron intensity maximum and minimum in Figure 3.10b.

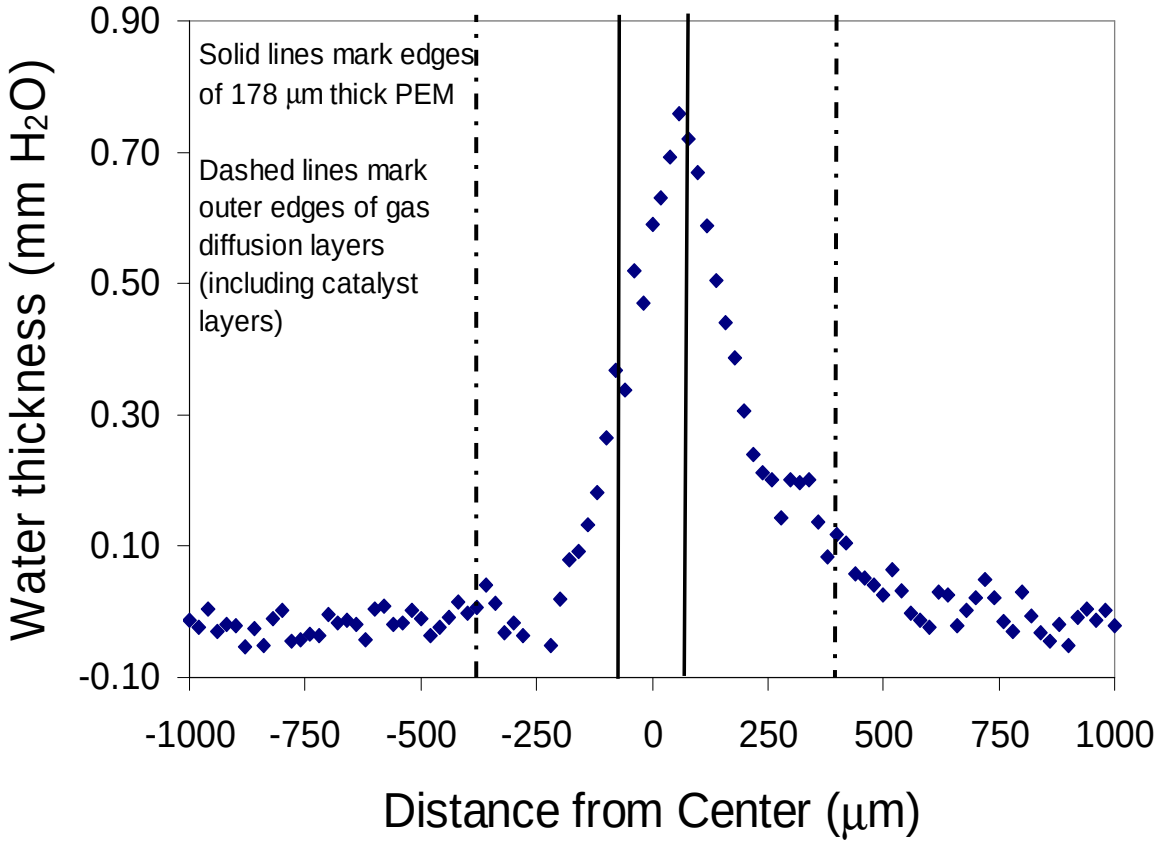

Figure 3.12. Water content distribution for the PEMFC at 75°C, 10 sccm air and hydrogen, 100% RH (at 70°C). Each pixel (or point, in the graph) is 20 μm wide.

The maximum water depth in Figure 3.12 was 0.76 mm deep. This is a composite value along the width of the PEMFC (1 cm) since this was the orientation with respect to the beam. Thus, water depth was equivalent to 7.5% of the width of the PEMFC. It can be seen in Figure 3.12 that the peak in water content actually appears to be just inside the PEM boundary (the solid line on the right) by approximately 20 μm (or one pixel). Fuller and Newman (1993) found that water content should exhibit a maximum at either the PEM-GDL interface or possibly outside the PEM and decrease relatively linearly toward the anode. The linear decrease in water content was observed via neutron imaging, but blurring of the PEM-cathode GDL interface causes the peak in water content to be in question. Skin effects have been proposed as a cause of a water content peak inside the PEM, but are not considered likely. The more likely explanation for the observed water content peak in the PEM is either buckling of the PEM, which would invalidate the assumption that the PEM-GDL interface is straight along the beam line, or blurring of the image resulted in mis-assignment of the PEM-GDL interface. Since the assignment of the peak is only 1 pixel inside the PEM-GDL interface (within reasonable error), it is believed that neutron imaging confirms a peak at the GDL-PEM interface.

Figure 3.13 is the water content profile for a PEMFC operated at 45^{o}C with all other conditions identical to the experiment presented above. It appears that the peak in water density occurred in the PEM, rather than the PEM-GDL interface, as expected. Again, this is not considered to truly be the case, as no explanation for such a maximum inside the PEM is known at this time. If a mass balance were performed on the PEM, a source of water would be present at the cathode, as a result of the production of water in

the cathode and possible condensation of water from the humidified air stream fed to the cathode. At the anode side, possible condensation could occur. Electro-osmotic drag caused by the diffusion of protons could also bring water into the anode side of the PEM. However, no source of water is expected to exist within the PEM, thus a peak in the PEM cannot be explained. It seems more probable that the layers have been assigned inappropriately and that they should be shifted by approximately two pixels. Inspecting Figure 3.10b provides further justification for this conclusion: identification of the points of maximum/minimum slope is still prone to some uncertainty because of uncertainties in the neutron intensity profile.

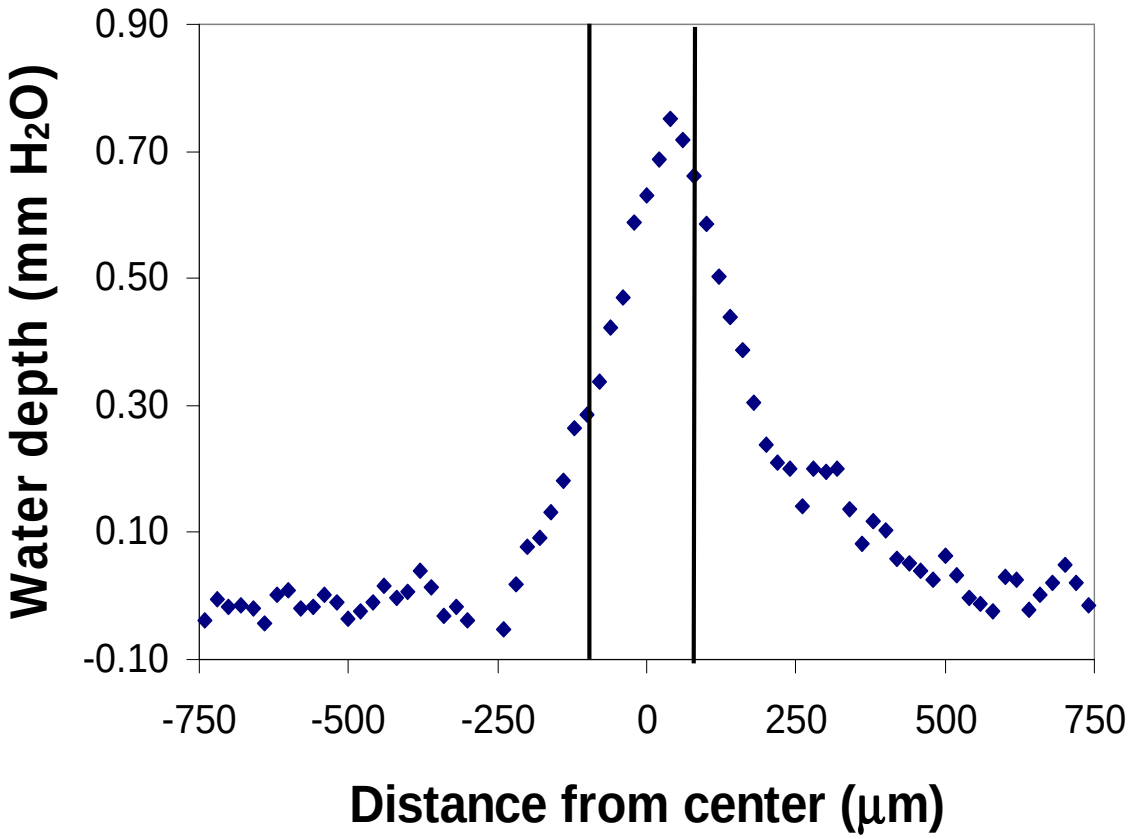

Figure 3.13. Water content distribution for operating PEMFC at 45°C. 10 sccm air and hydrogen, 100% RH (at 45°C).

As a result of this ambiguity in the PEM-GDL interface, modifications to the PEMFC design to include “markers” could help more definitively locate the interfaces. Such markers could be made of cadmium metal since it is an extremely strong neutron attenuator. The presence of cadmium would be indicated by nearly zero neutrons striking the detector, aside from those that result from inevitable blurring. Blurring would still occur, causing the cadmium strips to appear thicker than they really are, but the contribution of blurring would be easily quantified since the width of the metal strips would be known. Still, it is considered that neutron imaging confirms the presence of a peak in water content at the PEM-cathode GDL interface.

3.5 Conclusions

EIS was used to study the effects of cell temperature, air feed humidity, air feed rate, and transient response to a step-wise change in air feed humidity. Anode charge transfer resistance, PEM ionic resistance, and cathode charge transfer resistance all decreased as temperature increased; there was also a corresponding increase in power production. The three resistances also decreased drastically as air feed humidity increased (this is not the case for the transient response, however), which also resulted in increased power production. The air flow rate did not have a large effect on the three charge transfer resistances. In all of the experiments, the greatest resistance was identified in the anode; this resistance was consistently 30-90 mΩ greater than in the cathode and PEM, respectively.

The air-side humidity had the greatest effect on charge transfer resistances in these experiments. Operating temperature also had a significant effect, while the air-side flow rate had relatively little effect, as long as it was maintained at least at a stoichiometric ratio of approximately 1.2. Humidification of both the air and hydrogen feeds and high temperature (below that leading to the degradation of the PEM) are important for optimal power production. Further experiments should focus on investigating resistances at greater temperatures. Greater reactant feed rate is also of interest to explore a wider range of flow rates.

The transient response to a step-wise air humidity increase illustrates an important consideration when performing EIS: charge transfer resistances do not always decrease as power production increases. Even though these resistances increased in both electrodes over time, the power production increased. Charge transfer resistances are often a good indicator of the overall internal impedance, but do not always provide adequate information about the performance a fuel cell. Thus, it is always beneficial to consider power output observations, as well as all ECM impedances, when performing EIS analysis of a PEMFC.

Neutron imaging is useful as a tool for studying the distribution of water within the PEMFC. The results can compare favorably with water distribution models found in the literature, but the current method for assigning the location of the GDL-PEM-GDL interfaces introduces some uncertainty in the locations of those interfaces. Improvements

to PEMFC design to mitigate any buckling of the PEM, as well as inclusion of reference points for the interfaces, could reduce the uncertainty present in assigning the interfaces.

CHAPTER 4

EFFECTS OF ANODE IONIC STRENGTH AND CIRCULATION RATE ON MICROBIAL FUEL CELL INTERNAL RESISTANCES AND POWER DENSITY

4.1 Introduction

Conditions in the MFC anode are expected to significantly influence the output of a MFC. These conditions include carbon source, anode fluid composition, temperature, flow rate, etc. A soluble carbon source compared to a particulate one can significantly change the MFC power output (Borole and Hamilton, 2009). Liu et al. (2005) also studied the effects of temperature and ionic strength on the MFC internal resistance. For example, increasing the anode fluid ionic strength from 100 mM to 400 mM resulted in nearly a 100% increase in power density (from 720 mW/m^2 to 1330 mW/m^2). For the same increase in ionic strength, the internal resistance was observed to have decreased from 161 Ω to 79 Ω. This internal resistance includes all resistive components in the MFC.

MFCs offer a unique benefit in that electricity can be produced simultaneously with the removal of mixed organic contaminants in water, such as those found in municipal and food industry wastewaters (Logan et al., 2006). The application of MFCs is demonstrated by the many studies involving MFC power generation using various wastewaters.

In this work, we utilize EIS to study the effects of the anode fluid circulation rate and ionic strength on the power output and on various resistance mechanisms of an MFC. The design of this MFC has been shown to minimize the internal solution resistance and generate a power density as high as 345 W/m^3 (3650 mW/m^2) (Borole et al., 2009d). The goal of this study is to provide a better understanding of the relationship between the MFC performance and the operating parameters, in order to further improve its performance. For instance, understanding how the biocatalyst in the anode compartment of the MFC responds to various operating conditions can lead to improved operating conditions and also reveal characteristics of the behavior of different components of the MFC (anode, cathode and membrane) that can be further optimized. Stable, optimized operation over a long period of time is important for MFCs; thus an assessment of the MFC subsequent to a four-month period is also included. This work was performed on MFCs developed by Dr. Borole and Mrs. Hamilton at ORNL.

4.2 Materials and methods

4.2.1. MFC design and operation

The inoculum for the MFC used in this work originated from a mature MFC fed with glucose and lactate. This inoculum was used in an effort to minimize startup time, as well as utilize a culture already optimized for exoelectrogenic bacteria. The characterization of the inoculum and the procedure used for its enrichment is described in detail elsewhere (Borole et al., 2009d). Throughout the operation of the MFC, the anode fluid was periodically replaced with fresh fluid to remove planktonic and dead cells. The MFC used in this study was a two-in-one design, comprised of a 4 cm diameter ×

1.27 cm thickness anode chamber, Nafion 115 polymer electrolyte membrane (PEM) and a passive air cathode. The air cathode was made using a 2.54 cm × 2.54 cm carbon cloth deposited with 5 g/m^2 Pt (Fuel Cell Store, San Diego, CA). A perforated carbon foil (to allow airflow to the cathode catalyst layer) was used as a current collector and connected to a gold wire which served as the lead to connect to the external load. The carbon felt (Alfa Aesar, Ward Hill, MA) with a diameter of 4 cm and thickness of 1.27 cm served as a high surface area biofilm support and electrode. This anode had little dead volume and utilized a graphite rod as a current collector. Figure 2.4a is a schematic of the MFC design described here. The total volume of the anode compartment, lines and reservoir was approximately 230 mL. Voltage data were recorded with a 4-port DATAQ DI-158 USB-interface data acquisition system; in addition, power density analysis was performed using a Hewlett-Packard HP 3468B multimeter and variable-load resistor.

(2.4a)

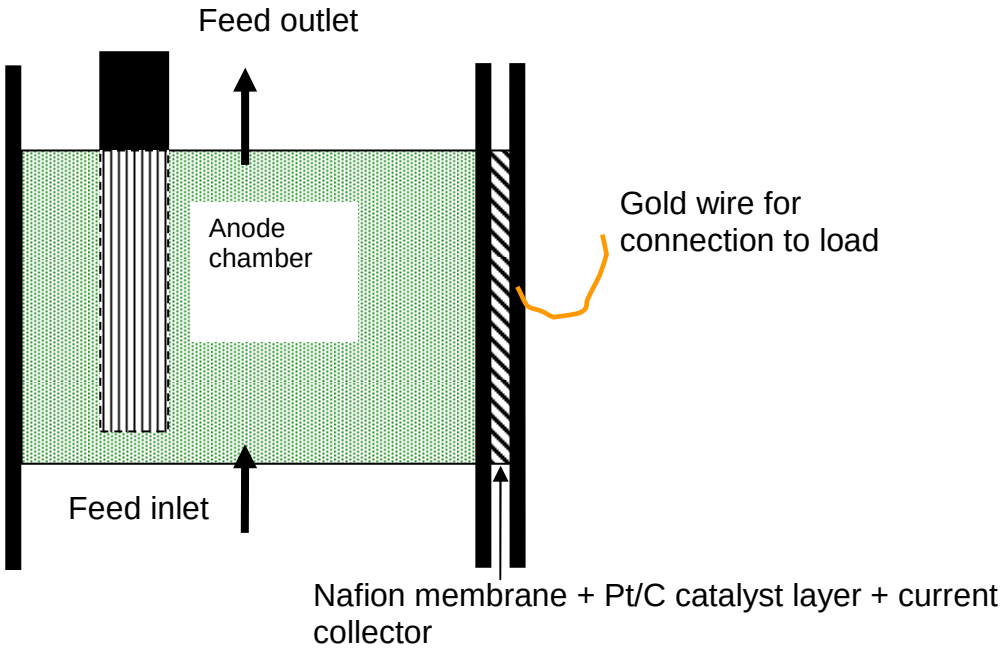

Figure 2.4a. Schematic of single-chamber MFC. Connections between the MFC and circuit are made at the anode carbon electrode and the cathode wire (gold in the above example).

4.2.2. Electrochemical impedance spectroscopy

A Gamry Instruments series G 750 potentiostat/galvanostat/ zero resistance ammeter was used to perform electrochemical impedance spectroscopy (EIS). For a description of EIS and how it is used to measure internal resistances in an electrochemical system see the Gamry Instruments Application Note (Gamry, 2006). All measurements performed in this work were "whole cell" measurements. The EIS analysis was performed between the anode and cathode of the MFC. The cathode served as the working electrode, while the anode functioned as the reference and counter electrodes simultaneously. The applied AC signal for EIS was 0.001 V rms and had a frequency range from 100 kHz to 100 mHz. The signal amplitude was small because greater voltage (i.e., 0.010 V) resulted in the detachment of microbes from the anode. Such detachment disrupted the steady state operation of the MFC. Detachment was observed by the anode medium clouding up rapidly (over the course of a few hours) and a reduction in MFC power output. It was found that a voltage of 0.001 V rms did not result in detachment, thus this value was used for all MFC EIS experiments. Each measurement required approximately 8 minutes to complete. All EIS spectra were recorded when the MFC was generating electricity, thus under a 50-Ω external load. The only exceptions to this operation were the measurements made during the first four days of operation (at a load of 250 Ω). The 50-Ω load resulted in maximum or near-maximum power output for the MFC.

Table 4.1. Summary of components of ECM and associated regions of MFC.

Anode	Resistor	R_{An}
	Constant phase element - coefficient	EDL_{An}
	Constant phase element - exponent	A_{An}
Solution	Resistor	$R_{Solution}$
Cathode	Resistor	R_{Cat}
	Constant phase element – coefficient	EDL_{Cat}
	Constant phase element - exponent	A_{Cat}

Nyquist and Bode plots were used for initial observations of the MFC performance. Nyquist plots allow estimation of $R_{solution}$ as the minimum point at which the data intersect the x-axis; the maximum point at which the data would intersect the x-axis corresponds to an estimate of the total MFC resistance. Figure 2.5 is an example of using the Nyquist plot for these estimations. The Nyquist plot does not, however, provide any indication of the distribution of resistance between the anode and cathode. Equivalent circuit modeling (ECM) was utilized to further explore the EIS results, specifically to determine the distribution of resistive and capacitive features in the operating MFC. Gomadam and Weidner (2005) and He and Mansfeld (2009) provide a description of the ECM technique for fuel cell EIS studies. The Simplex method was employed for fitting to allow delineation of the internal resistances and capacitances.

4.2.4. MFC variables

The variables for MFC operation considered in this work focused on the anode. The effects of the anode fluid circulation rate and ionic strength were both studied. A Masterflex peristaltic pump (Cole-Parmer 7520-00) was used to circulate the anode medium between the anode compartment and a reservoir bottle. The volume of the fluid in the anode compartment was 30 mL and the total volume of the fluid circulating was 230 mL. A calibration of the pump was performed to verify the settings for the desired flow rates. Flow rates ranging from 0 mL/min to 24 mL/min were explored in this work, and the shortest residence time of the fluid in the anode compartment was 1.25 s. The carbon source for the 0 mL/min experiment was the residual carbon in the anode compartment. For all of the flow rate experiments, the anode fluid had a 0.2 g/day loading of glucose as a carbon source. Upon changing the flow rate, a stabilization time of approximately 90 minutes was observed. After this time, if the output voltage for the MFC was stable, EIS measurements were performed. Two EIS spectra were recorded for each flow rate condition to check reproducibility. For the anode fluid strength experiments, the 100% experiment used the 0.2 g/day carbon source loading at a recirculation flow rate of 7 mL/min. The undiluted anode fluid ionic strength was 0.37 M. Fresh fluid was diluted with distilled water to obtain 50%, 25% and 10% strength media, corresponding to ionic strengths of 0.19 M, 0.093 M, and 0.037 M, respectively. The components of this nutrient medium were as follows: 1 mL each of Wolfe's mineral solution and vitamin solution per 100 mL of sterile mineral solution. This sterile mineral solution was comprised of 0.31g NH_4Cl, 0.13g KCl, 4.97g NaH_2PO_4-H_2O and 2.75g Na_2HPO_4-H_2O per liter of nanopure water. Upon completion of recording

two EIS spectra for the 0.37 M condition, the anode fluid was replaced with 0.19 M fluid (50% dilution) and the MFC allowed to equilibrate overnight. The pH was monitored and maintained near 7.0 approximately two hours prior to performing EIS on the day following replacement of the anode fluid. This procedure was repeated for 0.093 M and 0.037 M conditions.

4.3. Results and discussion

4.3.1. Model fitting and justification

The model used in this work consists of two parallel resistor-capacitor elements that represent the MFC electrodes separated by a single resistor that represents a lumped solution resistance (see Figure 2.6). Figure 4.1 includes Bode and Nyquist plots of EIS data taken over the initial four months of MFC operation. These plots provided estimates of solution and total resistance for each measurement day. It can be seen in Figure 4.1a that all of the days had similar high frequency impedances; the highest frequency impedance is a good indicator of solution resistance. The total resistance, indicated by the low frequency impedance, decreased significantly between days 1 and 3. By day 5, the low frequency impedance had mostly stabilized. Over this same period, it can be seen in Figure 4.1b that the phase shift decreased from a peak of -33^{o} to -25^{o} and then further decreased to a minimum of -15^{o} on day 29. This indicates that EDL capacitance decreased during the time period observed here (since resistances do not contribute to phase shift).

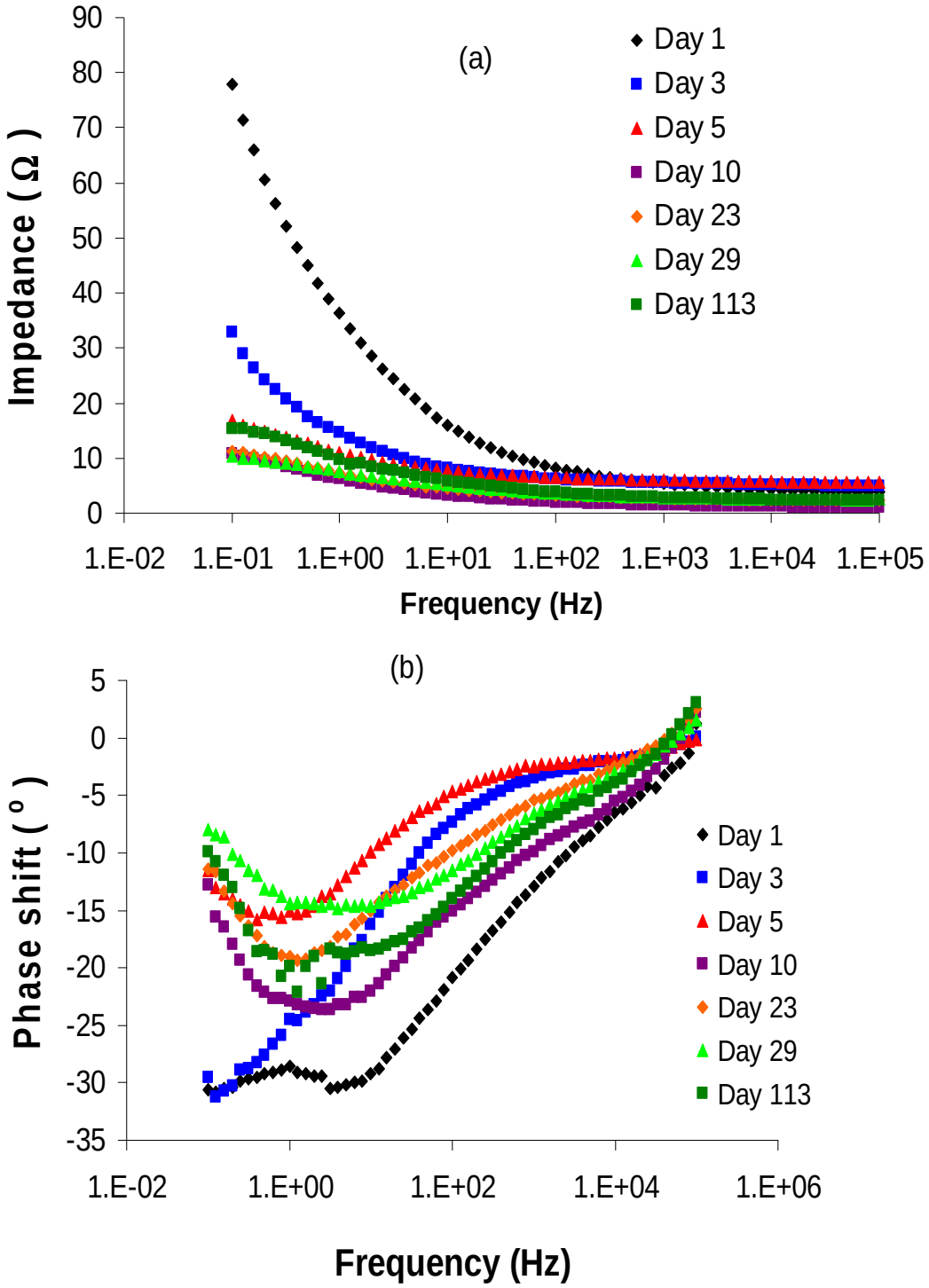

Figure 4.1. (a) Bode plot showing impedance data for EIS scans taken over 113 days. (b) Bode plot showing phase shift data for EIS scans taken over 113 days.

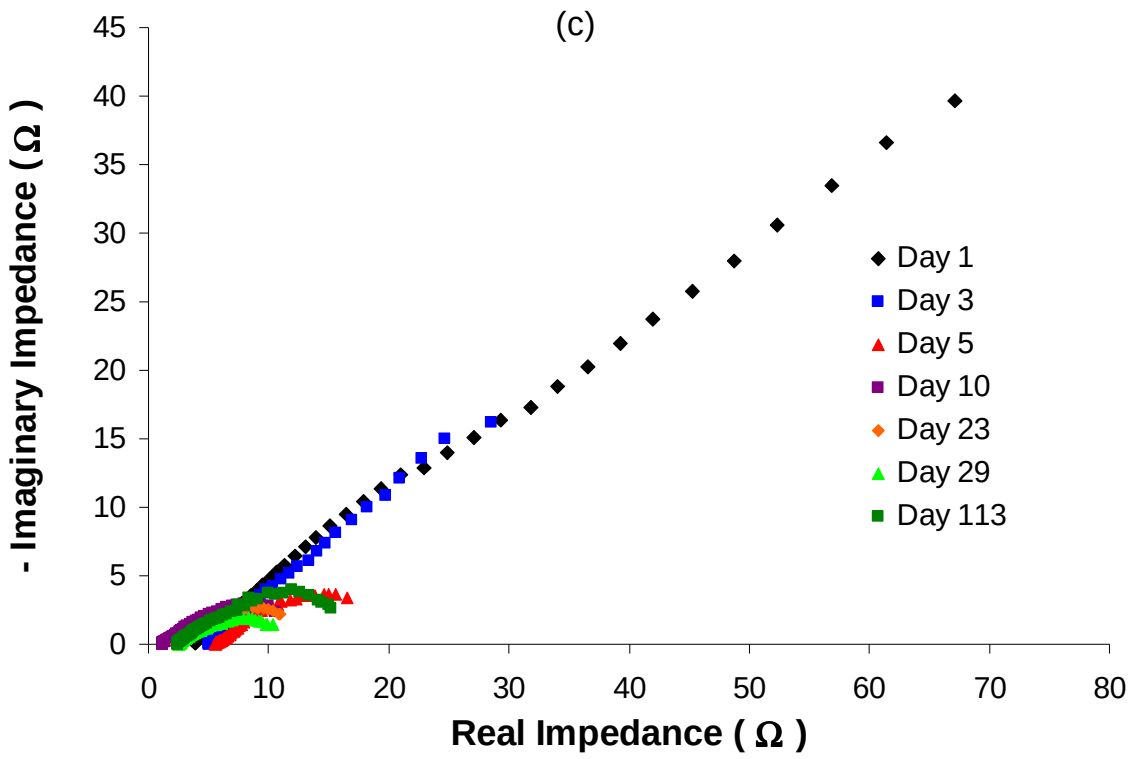

Figure 4.1 (c) Nyquist plot showing superimposition of EIS scans taken over 113 days.

The Nyquist plots in Figure 4.1c clearly exhibit the reduction of total resistance. The measurements on day 1 and day 3 indicate that power density was not high enough to provide good estimates of total resistance. This is reflected in the uncertainty of the ECM fitting for these two days. However, the Nyquist plots do provide good total resistance estimates from day 5 onward. Even without performing equivalent circuit modeling, reductions in total resistance are apparent from the Nyquist plots. Also visible in Figure 4.1c is the effect of periodically replacing the anode fluid. This step was necessary to remove dead and planktonic cells. The solution resistance was observed to vary from approximately 1.3 Ω to as high as 6 Ω on the Nyquist plot.

Figure 4.2 shows the ECM analysis for EIS results collected over nearly four months of MFC operation. The total resistance decreased from 319 Ω on day 1 to a minimum of 13 Ω on day 29; the power output correspondingly increased from 19 mW/m^2 to a maximum of 793 mW/m^2. This corresponds to an increase in coulombic efficiency from 4.2% on day 1 to a maximum of 60.3%. It is apparent in Figure 4.1 that R_{An} dominated the total MFC resistance in the early stages of anode biocatalyst growth. However, R_{An} decreased two orders of magnitude in resistance, from 315 ± 12 Ω to 3.75 ± 0.30 Ω, over the first five days of operation. R_{An} continued to decrease to 2.07 ± 1.01 Ω until day 10, where it remained stable for next 19 days. Analysis after about 4 months of operation indicated that the R_{An} was 3.30 ± 0.01 Ω on day 113. Over the first five days, R_{Cat} increased from 0.28 ± 0.25 Ω to approximately 15 ± 0.36 Ω and then decreased slightly over time until day 29. R_{Cat} increased over time to dominate the total resistance on day five and remained approximately 61% of the total resistance throughout the experiment. $R_{Solution}$ was relatively stable, varying between 0.96 ± 0.15 Ω and 4.66 ± 0.035 Ω; some variation is expected since the anode growth medium was periodically replaced as described above and this would affect time-dependent changes in anode medium ionic strength.

The rapid decrease in R_{An} is attributed to the inoculum for the MFC originating from an already mature MFC. Previous results reported by Ramasamy et al (2008) indicate that anode resistance is initially high and then decreases over time as the biocatalyst acclimates to the MFC environment for exoelectrogenic behavior. The time for such changes to be observed for Ramasamy et al. was approximately three weeks,

likely due to the inoculum originating from an anaerobic sludge. In the case of this study, however, the inoculum was from a previously-enriched MFC. As such, the microbial community did not undergo the period in which the bacteria acclimate and adapt to MFC conditions (Borole et al., 2009d).

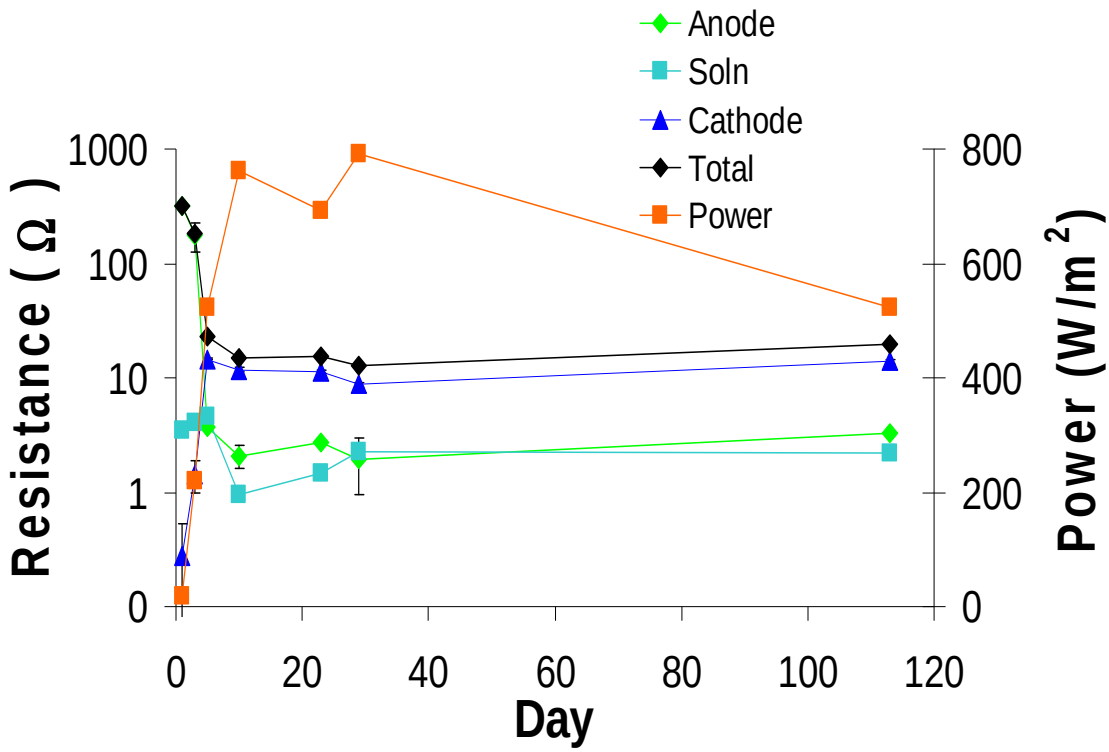

Figure 4.2. ECM analysis results for EIS data collected over 113 days of MFC operation.

Also observed in this experiment was an increase in R_{Cat} rapidly from day 1 to 3, and then a relatively stable value for four months. Such an increase in R_{Cat} is possibly the result of a buildup of cations in the water layer between the PEM and cathode catalyst layer. It was observed over the course of the experiment that dry salt would accumulate on the cathode side, at the air-electrode interface. This salt layer indicated a high salt

concentration in solution near the cathode active area which could impact the cathodic reaction or oxygen mass transfer and may be the reason for the cathodic limitations. The platinum particles in the cathode could have also been physically blocked by precipitated salt. It is expected that the salt was primarily composed of hydroxides since the pH in the cathode was quite high, up to pH 11. This increased pH has implications on long-term operation of the MFC since the Pt catalyst works better at very low pH. The pH in the cathode was not expected to be an issue for the neutral pH bioanode because the anode volume was much larger than the small amount of water in the cathode.

ECM calculations also allowed the delineation of capacitance terms for both the anode and cathode. Electrical double layer capacitance (EDL) forms as charged species in solution form a layer near the charged electrode. Since the capacitive behavior is expected to be non-ideal, a constant phase element (CPE) was used instead; use of a CPE involves addition of an exponent term (A, below) to the impedance response expression for an ideal capacitor. The impedance that results from such EDL behavior is described by equation 4.1 (Gamry, 2006):

$$Z_{EDL} = \frac{1}{Y_o (j\omega)^A} \tag{4.1}$$

In Equation 4.1, Z_{EDL} is the impedance of the capacitor. Y_o is the coefficient, $j\omega$ is the complex frequency term, and A is an empirical factor that describes the degree of non-ideality for the capacitance. A can vary from 0 to 1, with 0 being completely non-

ideal while a value of 1 indicates an ideal capacitance. Table 2 shows Y_o and A data calculated for the anode and cathode over 113 days of operation. Y_0_An refers to the coefficient for the anode, A_An is the exponent factor for the anode; cathode notation is similar.

Table 4.2. EDL factors calculated via ECM for data taken over 113 days.

EDL factor	Day 5	Day 10	Day 23	Day 29	Day 113
Y_o_An	0.181	0.122	0.053	0.225	0.116
A_An	0.124	0.308	0.397	0.667	0.975
Y_o_Cat	0.056	0.068	0.055	0.058	0.038
A_Cat	0.557	0.550	0.683	0.532	0.407

The coefficient for the anode (Y_0_An) was relatively constant throughout the experiment. Y_0_Cat was also relatively constant. Of interest is A_An, the exponent factor for the anode EDL. A_An increased from 0.124 on day 5 to 0.975, approaching unity, over the course of the experiment. This suggests that the anode EDL was highly non-ideal early in the experiment and then gradually approached ideal capacitive behavior. The cathode exponent, A_Cat; however, did not change significantly. The A factor for the anode was the only capacitance-related parameter that changed by any significant degree during the four-month time span. This indicates that the growth of the biofilm affects capacitive impedance of the electrode, in addition to the resistive component. Additionally, the time period over which the A_An changed was much larger than the time period over which the resistive component changes took place. The EDL capacitance in this MFC is expected to have played an important role in how increased

cathode cation concentration affected the cathode resistance as well. Cations aside from protons are expected to have heavily populated the EDL that built up around the cathode since the cation concentration was very high. Especially with smaller ions like sodium, this double layer could have inhibited transport of protons to the cathode. This hypothesis is supported by the observed increase in cathode CTR.

4.3.2. Effect of anode circulation flow rate

The flow rate through the anode chamber varied from 0 ml/min up to 24 mL/min. Figure 4.3 shows ECM results for the EIS measurements performed over the range of anode circulation rates. The total resistance for the MFC decreased from 24.5 Ω to a minimum of 7.51 Ω as the flow rate increased from 0 mL/min to 13 mL/min. The power output correspondingly rose from a minimum of 530 mW/m^2 to 879 mW/m^2. Maximum power and minimum resistance occurred at 13 mL/min, and a slight increase in resistance, with corresponding decrease in power, occurred as the flow rate increased to 24 mL/min. R_{An} over the range of flow rates was relatively stable, varying from 1.74 ± 0.38 Ω at 0 mL/min to a maximum of 3.77 ± 0.78 Ω at 3.9 mL/min. $R_{Solution}$ was observed to remain relatively unchanged throughout the series of flow rates explored here, varying between 0.846 ± 0.005 Ω and 1.48 ± 0.001Ω. R_{Cat} changed the most over the course of flow rates studied here. At 0 mL/min, R_{Cat} was 21.7 ± 0.2 Ω and decreased to a minimum of 7.51 ± 0.061 Ω at 13 mL/min before slightly increasing up to 8.31 ± 0.19 Ω at 24 mL/min.

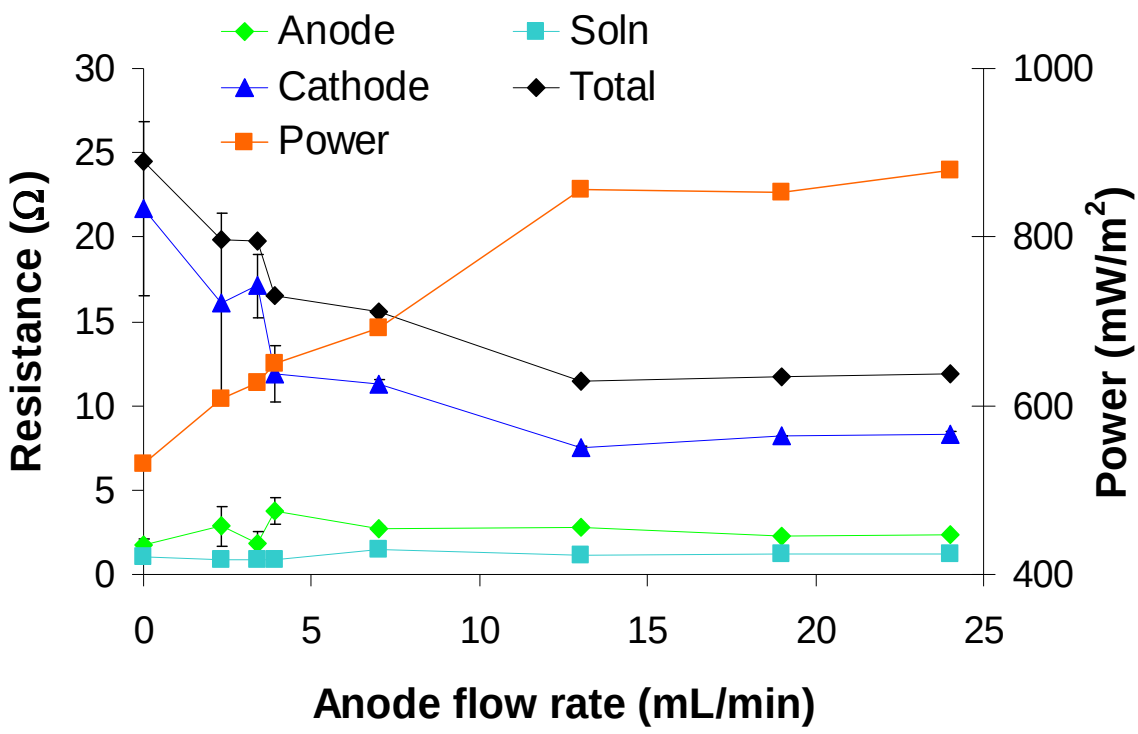

Figure 4.3. ECM analysis results for EIS data collected during variation of anode circulation flow rate.

The experiments investigating the effects of anode medium circulation rate were performed on days 23 and 24 after inoculation of the MFC. The impedance data for the MFC over time also demonstrated that the anode was not the limiting factor. As indicated earlier, the major changes in power density and impedance occurred within the first 10 days. Thus, when the experiments varying flow rate were conducted, the growth of the exoelectrogenic microbial culture in the anode had reached a steady state. R_{Cat} was therefore the dominant resistance among the various MFC components. The anode microbial culture used in this study was enriched under continuous flow conditions and with periodic medium replacement (Liu et al., 2008). As such, the electricity production was potentially dominated by conductive electron transfer mechanisms occurring within

the biofilm. Direct electron transfer via biological nanowires has been suggested as one of the mechanisms for electron transfer within MFCs (He and Mansfeld, 2009) If direct electron transfer is assumed to be taking place within the biofilm, the conditions outside the biofilm would have less effect on the charge transfer between the bacteria and electrode, as opposed to if mediated electron transfer was occurring. The exception to this would be if the flow rate was so great that the biofilm was damaged. However, there was no evidence of biofilm removal under the conditions studied. It should also be noted that even though the anode circulation flow rate was varied, the delivery of glucose to the anode continued at a constant 0.2 g/day. The variation of the anode fluid recirculation rate resulted in a change in the glucose concentration within the anode; however, R_{An} did not change appreciably with changes in flow rate (Figure 4.3), indicating that glucose availability was not a problem.

The cathode resistance, R_{Cat}, was observed to decrease by 63% as the anode flow rate increased from 0 mL/min to 24 mL/min. As flow rate through the anode increased, mixing in the anode is expected to have improved, as well. The half reaction occurring at the cathode consumes protons, which are transported to the cathode from the anode side through the membrane. As the recirculation of the anode medium implies replenishment of protons (or 'protonated species' via the buffer) in the anode chamber, an increasing flow rate would mean higher proton concentration as well as improved mixing, which may have helped reduce pH polarization and improved proton availability at the cathode. With improved proton transport to the cathode, the reaction rate at the cathode can increase, thus resulting in a reduced resistance. The cathode resistance includes charge

transfer resistance, double layer resistance and potentially diffusion resistance. The relationship between charge transfer resistance and reaction rate can be described by equation 4.2, below:

$$R_{Cat} = \frac{RT}{nFI_{Exchange}} \tag{4.2}$$

In equation 4.2, R is the ideal gas constant (J/mol-k), T is temperature (K), n refers to the number of electrons occurring in the charge transfer reaction, F is the Faraday constant (C/mol), and $I_{exchange}$ is the exchange current density. Exchange current density is the rate at which electrons are transferred between an electrode and electrolyte (Orazem and Tribollet, 2008). This is related to the rate at which protons, electrons and oxygen combine to form water, since this is the only sink of electrons present at the cathode. Several studies on the effect of cathode conditions on MFC performance have been reported and it has been shown that the cathodic reaction can be a limiting factor under certain conditions (Manohar and Mansfeld, 2009; He et al., 2008; Ouitrakul et al., 2007). We assume here that the resistance at the cathode is dominated by charge transfer resistance of the reaction occurring at the cathode. Thus, if R_{Cat} is observed to decrease, there is an attendant increase in $I_{Exchange}$, which can result from an increase in the rate at which protons reach the active sites in the cathode.

4.3.3. Effect of anode fluid ionic strength

The experiments focused on anode fluid ionic strength included fluid strengths ranging from 0.37 M (undiluted) to 0.037 M (10% of original concentration). Figure 4.4 is a Nyquist plot including results for EIS spectra for each anode fluid ionic strength. It is apparent that approximate total resistance decreased as anode fluid ionic strength increased. In addition, a reduction in solution resistance is visible as the anode fluid strength increased. It can be seen in Figure 4.5 that a general trend of reduced total resistance and increased power output occurred as the anode fluid ionic strength increased. The total resistance decreased from 22.5 Ω at 0.037 M to 13.0 Ω at 0.37 M. The power output was observed to increase from 378 mW/m^2 to a maximum of 793 mW/m^2 over the same range. R_{An} was 1.96 ± 0.24 Ω at 0.037 M and remained nearly unchanged, increasing only to a maximum of 2.45 ± 1.48 Ω at 0.093 M and then decreasing back down to 1.96 ± 1.01 Ω at 0.37 M. $R_{Solution}$ continuously decreased from 3.79 ± 0.10 Ω at 0.037 M down to 2.27 ± 0.16 Ω at 0.37 M; this is a reduction of approximately one third. R_{Cat} also decreased markedly, from 16.8 ± 0.64 Ω at 0.037 M to 8.72 ± 0.46 Ω at 0.37 M, which is a much larger reduction than the solution resistance in terms of absolute values, indicating the importance of cathode impedance in MFC performance.

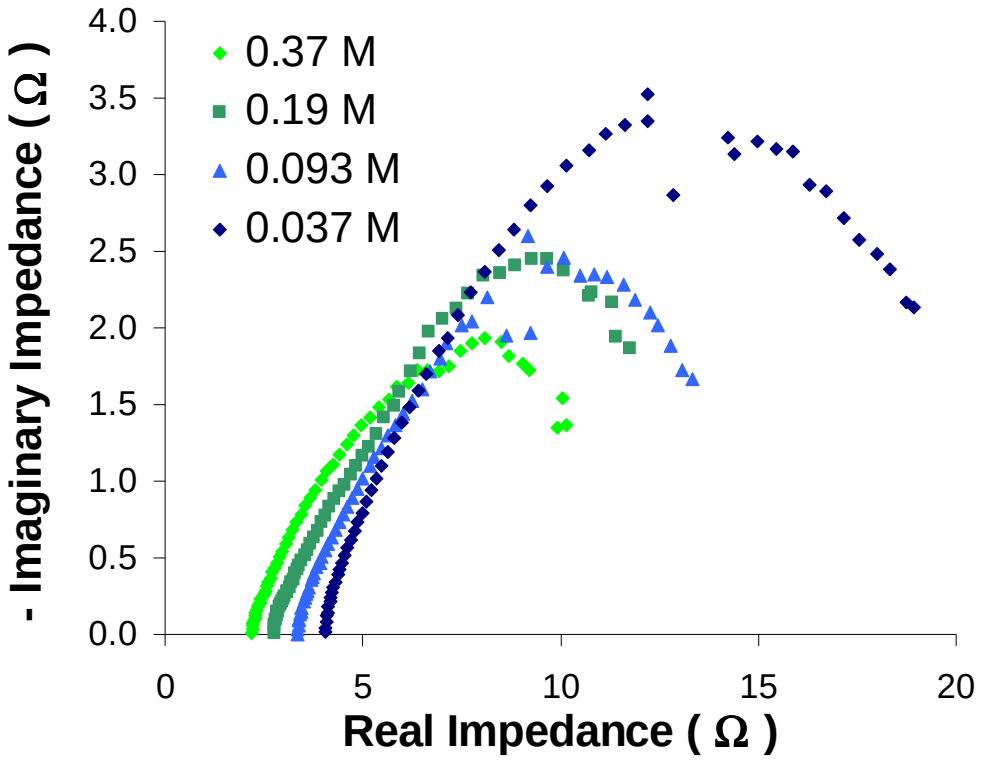

Figure 4.4. Nyquist plot of varying anode fluid strength experiments.

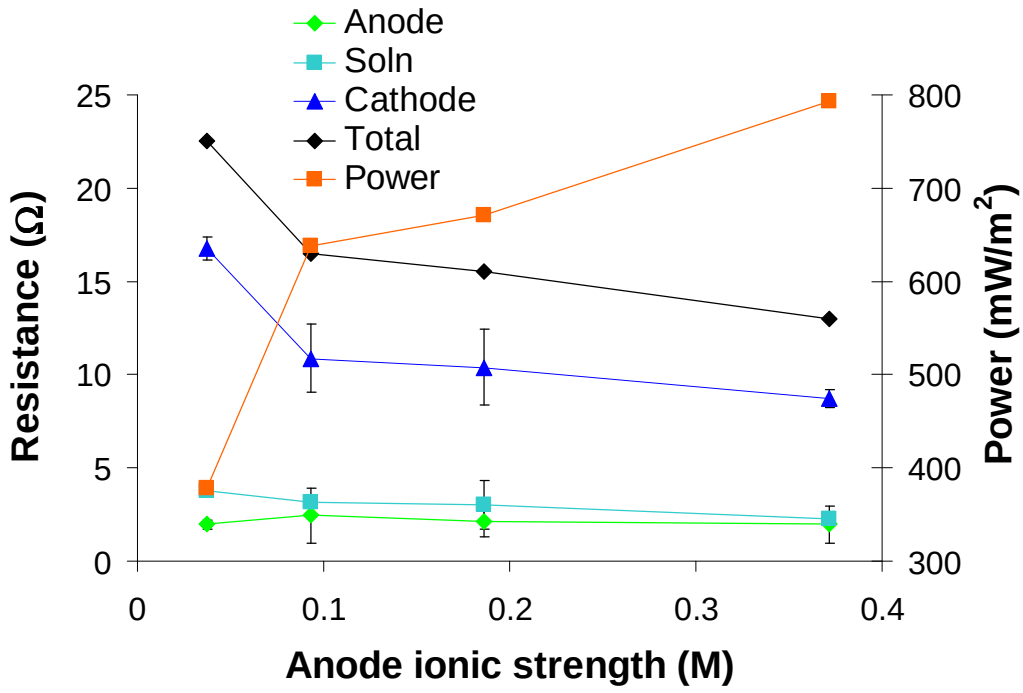

Figure 4.5. ECM analysis results for EIS data while varying anode fluid strength.

The experiments investigating the effect of anode medium ionic strength were performed between days 29 and 36. This, as indicated by Figure 4.2, is in the period when R_{An} has decreased to a steady value below that of R_{Cat}, and similar to $R_{Solution}$. The relatively constant values of R_{An} for varying anode fluid ionic strength indicate that the electron transfer from the microbes to the electrodes is not dependent on any charged species present in the nutrient medium. So long as enough nutrients are present to not limit microbial metabolism, changes to the anode medium will have little effect on the anode behavior. The reduction in $R_{solution}$ is expected, considering increased ionic strength increases conductivity of an electrolyte. Dlugolecki et al (2010) demonstrated that the membrane resistance of a cation-exchange membrane was reduced by up to 93% when the ionic strength was increased by a factor of 20. The salt used in their experiments was NaCl, but similar behavior should be observed for a Nafion membrane with the anode fluid in this work. The reduction in R_{Cat} is likely attributable to increased proton transport to the cathode, similar to that as observed for increasing anode fluid circulation flow rate (described above).

It was demonstrated by Aaron et al. (2008) that changes to one electrode side of a polymer electrolyte membrane fuel cell can have measureable effects on the other side. Thus, the finding that changes to the anode of an MFC can result in effects in the cathode is reasonable. In these experiments, it was observed that R_{Cat} actually responded more strongly to changes in the anode than did R_{An}. Such behavior, observed for changes to both the anode fluid flow rate and strength, is likely due to a combination of a stabilizing effect of the biofilm and a limiting cathode starved for protons.

4.4. Conclusions

Experiments were performed that utilized EIS to investigate internal resistance mechanisms in a MFC. Over the first 10 days of operation, the anode resistance was observed to have decreased below that of the cathode. Such a short startup time is attributed to the inoculum coming from an operating MFC. This is a drastic improvement over MFCs that have inocula derived from anaerobic sludge reactors. The total resistance was dominated in the anode during the first five days, at which time the anode was the limiting step. It was also observed via EIS that the A factor for the anode, which represents the non-ideality of the capacitive behavior changed over time and approached that of an ideal capacitor. Operational parameters included anode fluid circulation flow rate and anode fluid ionic strength. It was observed that increased anode fluid flow rate and ionic strength both contributed to increased power density for the MFC. EIS analysis showed that the power density increased largely due to reductions in cathode impedance. In addition, the anode impedance was observed to be only slightly affected by changes in anode fluid flow rate or ionic strength. This suggests that cathode limitations can be partially mitigated by changes in the anode operating conditions. Such changes are potentially due to an improved rate of proton transport to the cathode, increasing the reaction rate at the cathode. An inter-dependence of each component of the MFC on the other components was also illustrated in this work. Assessment of the EIS parameters of the MFC at the end of one month and four month operational periods indicated that the slight reduction in power output over time co-related with a corresponding increase in the impedance of the MFC components.

CHAPTER 5

USE OF ELECTROCHEMICAL IMPEDANCE SPECTROSCOPY TO MEASURE CHANGES IN MFC INTERNAL RESISTANCE OVER TIME

5.1 Introduction

Current efforts in MFC technology include scaling fuel cells up to provide increased power. Responses of the impedances in the anode, solution and cathode of the MFC to changes in fuel cell conditions, including cell size, materials and geometry should be quantified to better understand how MFC power output can be improved. The current interrupt method (Liang et al., 2007) has been employed to quantify the total internal resistance; however, this method does not differentiate between ohmic, mass transfer and kinetic transport limitations. Electrochemical impedance spectroscopy (EIS) is a technique which delineates the resistive, capacitive and inductive impedances within an MFC when compared to an appropriate equivalent circuit model. The EIS method can be used to quantify charge transfer, electrical double layer, and ohmic limitations for each region or component of the MFC.

Manohar et al. (2008) calculated the individual resistances of an MFC using *Shewanella* in the bioanode of a two-chamber MFC with a power density of approximately 10 mW/m^2. Ramasamy et al. (2008) studied changes in the internal resistances for a similar, two-chamber MFC with improved power density (166 mW/m^2). They found that the solution resistance, comprised of the anode and cathode solutions and the membrane, accounted for approximately 95% of the total internal impedance. He et

al. (2006) studied an upflow MFC with an internal cathode configuration that was capable of reaching a power density of 140 mW/m^2; this fuel cell was also dominated by solution resistance (50.3% of total impedance). The goal in this work is to use EIS to study a MFC with minimized solution resistance. MFCs that are limited by high ohmic or solution resistance can restrict efforts to improve the anode and cathode operation of the MFC, especially in cases where the ohmic resistance greatly dominates the total resistance. However, a low ohmic resistance, while advantageous for improved MFC power density, is only one part of improving MFC power density. While the power density of an MFC is primarily a function of the system architecture (Logan et al., 2006), recent studies utilizing improved MFC designs (resulting in lower ohmic resistance) have indicated that microbes also play a significant role in determining power output (Borole et al., 2009d; Jung et al., 2007; Xing et al., 2008). Ramasamy et al. (2008) have reported the change in the anode impedance during initial biofilm growth (3 weeks) and linked the reduction in anode charge transfer resistance to biofilm growth.

EIS can be a useful tool in obtaining otherwise-inaccessible insight related to the microbial catalyst and its interaction with electrodes. He and Mansfield (2009) suggested the use of EIS for analyzing multiple bio-electro-chemical processes occurring within MFCs. These include electrochemical and biochemical reactions occurring at the electrodes, the effect of mediators and electrode modifications on MFC performance, biofilm formation, biofilm control, effect of substrate and product diffusion through pores e.g., in three-dimensional electrodes and limitations due to design, etc. Thus, the potential

of this technique in understanding MFCs is significant. Recently, Ramasamy et al. (2009) reported the use of EIS for studying the effects of mediators.

Enrichment of anode biocatalysts using various carbon sources has been reported (Borole et al., 2009b; Borole and Hamilton, 2009; Borole et al., 2009c). The enrichment process included a combination of multiple steps including elimination of planktonic cells via media replacement and use of a flow-through system to maximize biofilm formation, as well as a stepwise decrease in load to promote exoelectrogenic microbial growth. Previous studies have employed EIS to study component impedance of H-shaped MFC systems (Ramasamy et al., 2008; Manohar et al., 2008). The total resistance in these systems is typically dominated by ohmic resistance and can be as high as 1000 Ω. The system used in this study was designed to minimize the ohmic resistance to below 10 Ω. Using power density analysis, it was previously shown that the enrichment of anode consortia can take several months instead of weeks (Borole et al., 2010). The MFC design used an electrode with high anode specific surface area, three-dimensional porous structure with minimal dead volume and negligible electrode spacing. Here, we report the characterization of the impedance spectra and quantification of the various resistances for all the components of the MFC. Changes occurring during enrichment of the anode biocatalyst and during subsequent operation for a total period of six months were studied. The MFC development in this chapter was performed under the direction of Dr. Borole (Borole et al., 2010).

5.2 Materials and methods

5.2.1 MFC construction

The MFC was made using a cylindrical anode compartment containing carbon felt and connected to the circuit via a graphite rode. A Nafion-115 membrane separated the anode from the cathode and ensured no oxygen entered the anode. A Pt-deposited carbon air-cathode was utilized for all experiments. The anode volume was 16.0 cm^3 and the projected surface area was 12.6 cm^2.

5.2.2 Inoculation and operation

The anode chamber of the MFC was inoculated with a 1 mL sample of an anaerobic digester slurry collected from the Knoxville, Tennessee, municipal wastewater treatment plant. A nutrient medium was circulated through the MFC anode chamber at 4-7 mL/min. The details of the nutrient medium and the operating procedure are reported elsewhere (Borole et al., 2009d). The conductivity of the nutrient medium was measured to be approximately 6.7 mS (Amber Scientific EC Meter, model 2052). In brief, the biocatalyst growth procedure was targeted to enrich exoelectrogenic biofilm-forming and mediator-less organisms, while removing free-floating cells. The goal was to remove dead cells, as well as all planktonic cells growing in the reservoir and the anode chamber that used alternate electron acceptors or mediators to transfer electrons to the electrode. Such processes as methanogenesis could consume electrons without contributing to electricity production. The external load for the first 42 days was 250 Ω and then was reduced to 100 Ω on day 43 and further reduced to 50 Ω on day 68. The MFC was operated with a constant load of 50 Ω for the remainder of the experiment (ending after 6

months). The details of the voltage and power density measurements were as reported previously (Borole et al., 2009b).

5.2.3 Electrochemical impedance spectroscopy

Electrochemical impedance spectroscopy (EIS) was performed using a Gamry Instruments series G 750 potentiostat/galvanostat/ zero resistance ammeter (Gamry, 2006). Two types of measurements were done, one using a whole cell, two-electrode configuration, and the other using a three-electrode configuration with a reference electrode (Ag/AgCl) inserted near the anode. The whole cell EIS measurements were done using the cathode as the working electrode and the anode as the reference and counter electrodes. EIS has been demonstrated to be able to delineate resistances in the anode, cathode and solution/electrolyte for PEMFC systems via whole cell measurements (Springer et al., 1996; Wagner, 2002; Bard and Faulkner, 2002). These whole cell measurements are often supported by single-electrode measurements to aid in correctly calculating the anode and cathode resistances in a symmetric ECM (see Figure 2.6). The EIS measurements using a three-electrode system were used in this study to support the results from the whole cell measurements.

Whole cell EIS measurements were made in a single MFC on days 24, 43, 61, 68, 130, 136 and 165 to determine the changes in electrochemical parameters as a result of biocatalyst enrichment and operation over a long duration. The frequency for an EIS spectrum ranged from 100 kHz to 100 mHz; the AC amplitude of the perturbation was 1 mV, so as not to disturb steady state operation or cause biofilm detachment. Each

spectrum required approximately 20 minutes to complete, with the bulk of each scan spent in the 0.5 to 0.1 Hz range.

The ECM used in this work is that shown in Figure 2.6. All EIS measurements were conducted in an operational mode of the MFC, i.e., when the MFC was under an external load. The voltage output during the tests varied depending on the MFC performance at the given time. The purpose of doing these tests at the operating load was to examine the EIS resistances during a long term operation of an MFC at a load that gave a power density close to the maximum achievable for the MFC at the given time. The goal was to understand what the limitations of the cell are under conditions which result in the best power output.

Despite operation of the MFC at a constant load instead of a constant voltage, the voltage output between days 61 to day 165 varied only slightly (0.165 V ± 0.006 V). The average cell voltage between day 24 (first EIS measurement) and day 60 was 0.15 ± 0.02 V. The difference in the voltage measured across the anode and cathode or the applied voltage in case of galvanostatic experiments is known to influence the electrochemical parameters (Fan et al., 2007). However, the variation in the voltage in this case was relatively low (from 0.159 to 0.171). Further, the impact of a change in voltage on EIS parameters at high current densities is expected to be relatively low. For example, Ramasamy et al. (2008) reported a very small change in the anode charge transfer resistance (less than 10%) with a change in the anode voltage of 0.049V (representing a change in cell current density from 167 to 267 mA/m^2). Additionally,

their data showed that the change in the resistances decreases with an increase in current density. In the experiments conducted in this study, the current density was above 420 mA/m^2. Manohar et al. (2008) have also shown that changing the applied voltage between the range 0.15 to 0.45 V had a small effect on the impedance of the cell.

5.3 Results

5.3.1 MFC voltage output

During the operation of the MFC at a constant load of 50 ohms, the voltage output between days 61 to day 165 varied only slightly (0.165 V ± 0.006 V). The average cell voltage between day 24 (first EIS measurement) and day 60 was 0.15 ± 0.02 V. The difference in the voltage measured across the anode and cathode or the applied voltage in case of galvanostatic experiments is known to influence the electrochemical parameters (Fan et al., 2007). However, the variation in the voltage in this case was relatively low (from 0.159 to 0.171 V). Further, the impact of a change in voltage on EIS parameters at high current densities is expected to be relatively low. For example, Ramasamy et al. (2008) reported a very small change in the anode charge transfer resistance (less than 10%) with a change in the anode voltage of 0.049 V (representing a change in cell current density from 167 to 267 mA/m^2). Additionally, their data showed that the change in the resistances decreases with an increase in current density. In the experiments conducted in this study, the current density was above 420 mA/m^2. Manohar et al. (2008) have also shown that changing the applied voltage between the range 0.15 to 0.45 V had a small effect on the impedance of the cell.

5.3.2 Equivalent Circuit Model Fitting

The ECM used in this work to represent the MFC consists of three resistances in series, representative of the anode (R_{anode}), the solution + membrane resistance, R_{m+s}, and the cathode R_{cat} (see Figure 2.6). Due to the symmetry of the system and the serial nature of the impedances, it was observed that the fit of the model to the whole cell impedance spectra was reversible between the anode and the cathode. Assessment of the impedance spectra for the individual anode and the cathode compartments was used to determine the relative values of impedance for those components. This analysis was conducted for a mature biofilm (after six months of operation) to ascertain that the model fit for the latter period was correct. Previous reports have clearly indicated how the impedances change during the initial biocatalyst growth period (Ramasamy et al., 2008). Figure 5.1 shows the impedance spectra for the anode, the cathode and the whole cell. The first intersection of the Nyquist plot and the x-axis represents the solution resistance, which also includes the PEM resistance. The plot for the whole cell indicates that the solution + membrane resistance was approximately 7 Ω. The projected point of intersection of the Nyquist curve and x-axis farthest from the origin is representative of the total impedance. The anode Nyquist plot, enlarged in the inset of Figure 5.1, shows that the anode impedance was approximately 1 Ω, while the cathode and the whole cell impedances were 40 and 45 Ω, respectively. This demonstrates that the impedance for the anode compartment was lower than those for the cathode and for the solution + membrane. The EIS spectra for the individual components of the MFC after the first six months were reproducible over multiple experiments carried over several weeks.

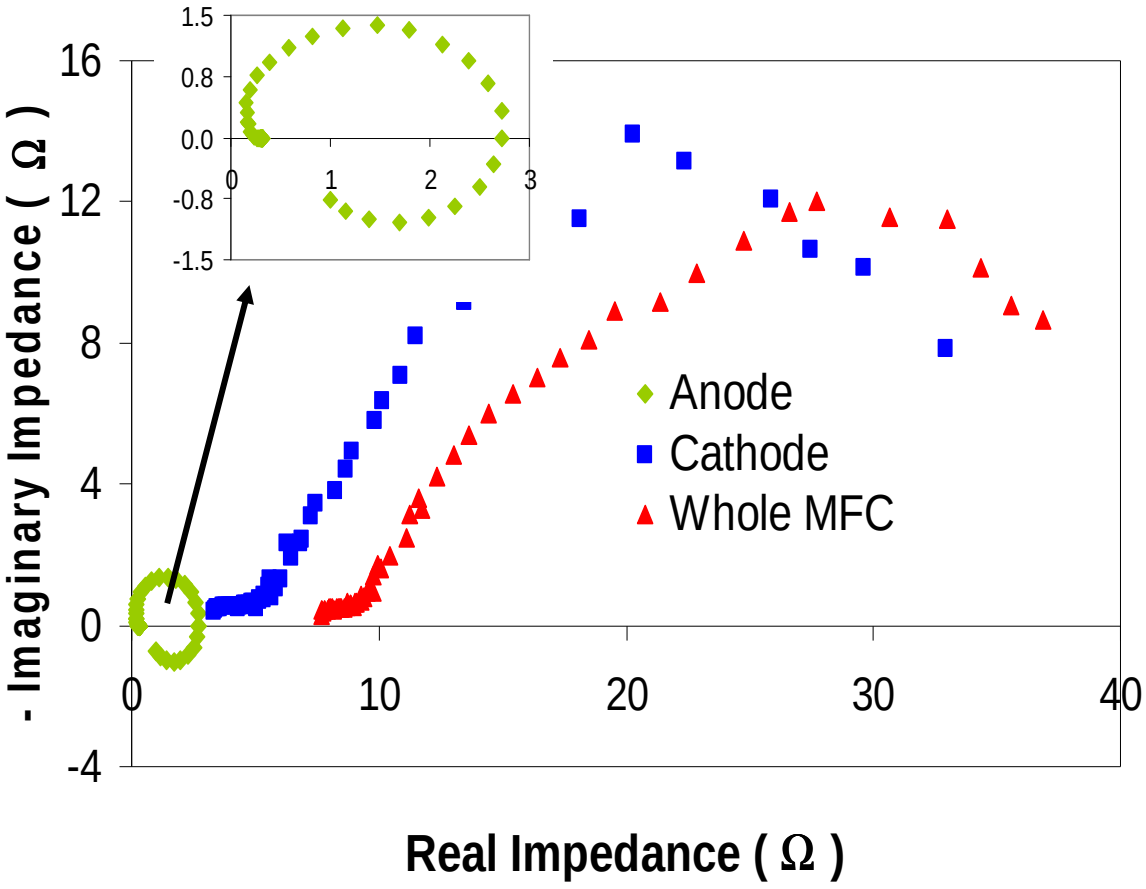

Figure 5.1. Nyquist plot for anode, cathode and the whole cell. The anode response is shown in the inset.

5.3.3 Effect of enrichment on the impedance of the MFC

Electrochemical impedances were determined by fitting the EIS spectra to the model for the whole MFC. Figure 5.2 shows the fitting of the experimental data to the model using a Nyquist plot. In order to assess the impedances under operating conditions, the EIS analysis was conducted at the operational load. The total impedance for the first time event (day 24) was 299.8 Ω (at an external load of 250 Ω and a current density of 420 mA/m^2). This decreased to 48.6 Ω on day 43 (external load of 100 Ω and current density = 1.13 A/m^2). The individual anode and cathode impedances also changed

dramatically as shown in Figure 5.3a. Due to the difference in the current density at which the measurements were made during the initial two time events, the impedances cannot be compared directly. The solution and membrane resistance were modeled together as one parameter, due to the inability to separate them in the model. This resistance changed only slightly over this period. The EIS measurements beginning on day 61 were made at an MFC operational load of 50 Ω. (Voltage output = 0.165 ± 0.02V, current density = 2.63 A/m^2). The total impedance for the MFC on day 61 at this operating voltage and load was 18.2 Ω. This value decreased to 16.6 Ω over the next 70 days (Figure 5.3a). The impedance associated with the anode (R_{anode}), measured at a constant current density (2.63 A/m^2) also decreased from 5.8 ± 0.48 Ω to 1.4 ± 0.14 Ω from day 61 to day 130. These impedances can be compared since they were measured at a constant current density. The decrease in anode impedance can be attributed to establishment of the anodic biofilm on the electrode surface. The cathode impedance denoted by R_{cat} increased from 9.5 ± 0.78 Ω on day 61 to 12.0 ± 0.21 Ω on day 130. It should be noted that the R_{cat} was 1.27 ± 1.13 on day 24. While the impedance measurements made in the first 2 months cannot be compared directly with the latter data, it can be said that there was a significant change in the anode and cathode impedances, primarily resulting from the enrichment of the exoelectrogenic biofilms on the anode. The effect of enrichment on anode impedance has been demonstrated previously by Ramasamy et al. (2008); however, the duration of their study was only 3 weeks. The present study illustrates the changes in the impedance of each of the MFC components over a much longer period, including a period of over two months when the MFC performance was relatively stable.

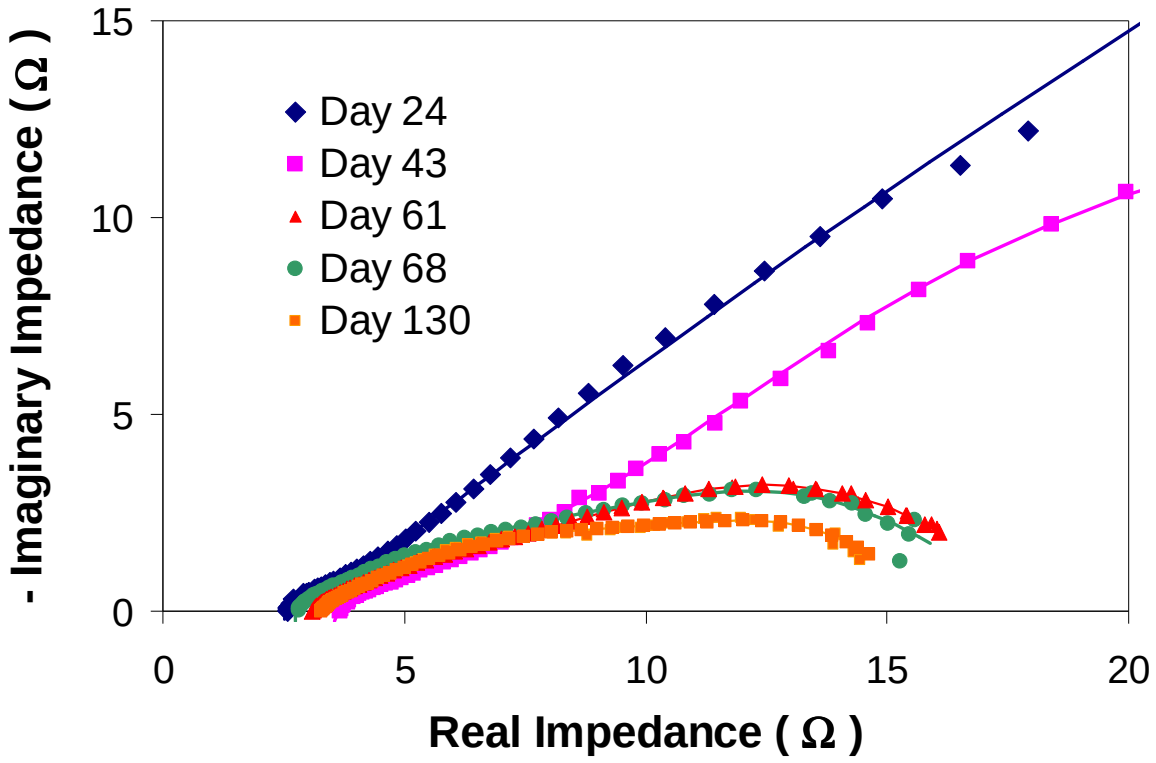

Figure 5.2. Nyquist plot showing fitting of the ECM model to EIS data for days 24, 43, 61, 68 and 130 for the air-cathode MFC.

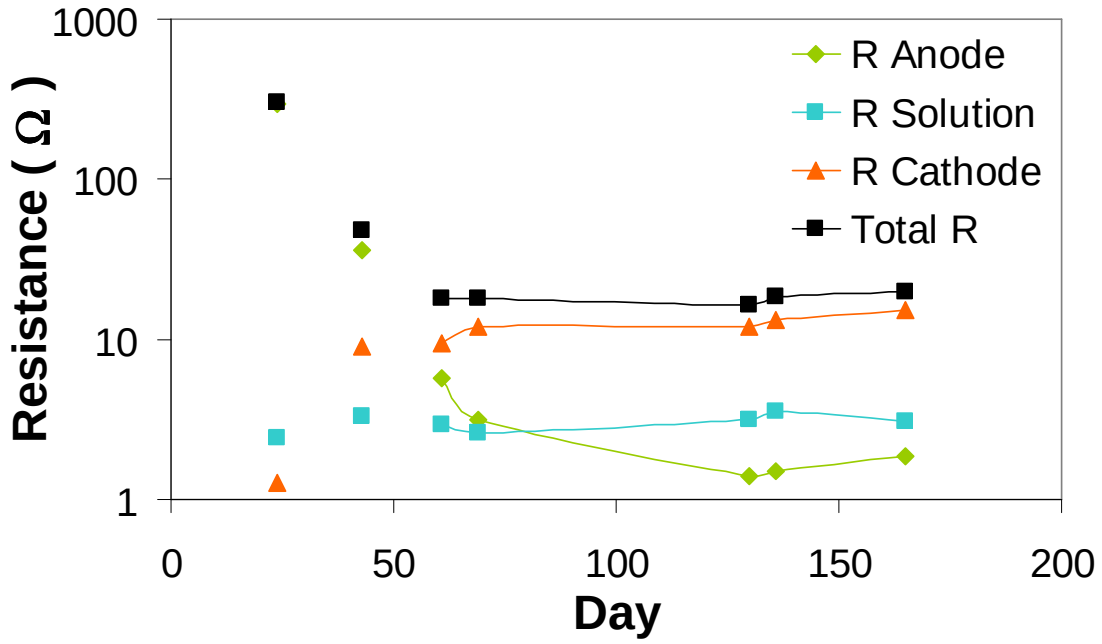

Figure 5.3. (a) Behavior of anode, cathode and solution membrane impedance over time during enrichment of electrogenic microorganisms in MFC. The first three points are not connected, since these data points were taken at different current densities.

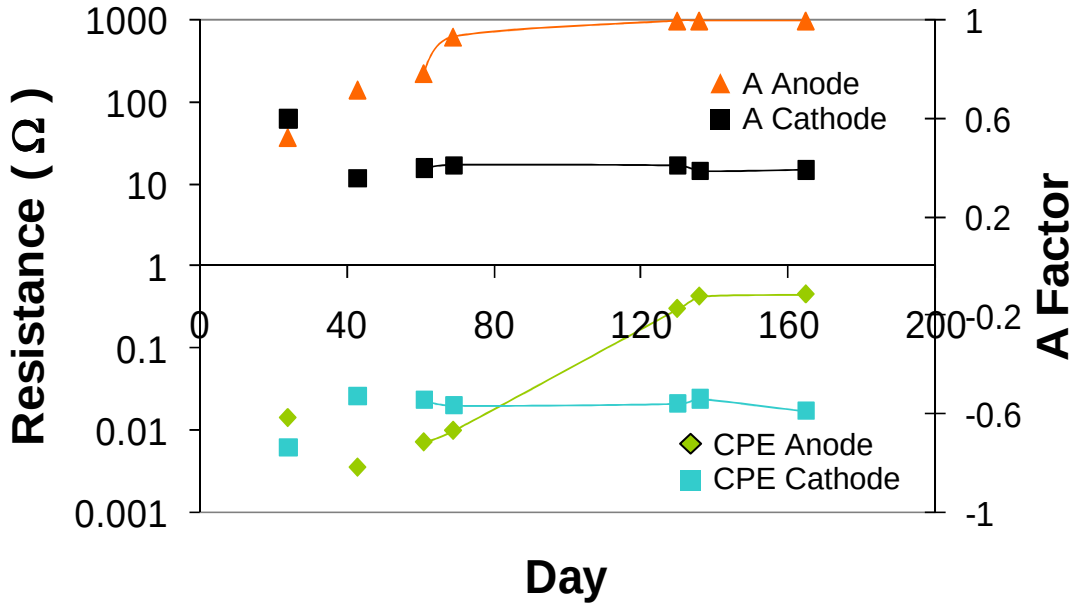

Figure 5.3. (b) Behavior of anode and cathode capacitive elements during enrichment of electrogenic microorganisms in MFC.

The combined impedance of the membrane + solution was relatively constant over the entire measurement period and ranged between 2.4 to 3.6 Ω. Continued measurements of the impedances after day 130 indicated a slow increase in all the impedances (Table 5.1). The increase in cathode and membrane impedances may be due to increase in pH, accumulation of cations in the cathode and fouling of the membrane. Visual observation indicated discoloration of the membrane. Production of dry salts was observed on the outer side of the cathode exposed to air. The increase in the anode impedance during the period from day 130 to day 168 may have been due to degradation of membrane, cathode performance or a change in the operation of the MFC anode from a continuous substrate addition mode to a fed-batch mode of addition (Borole et al., 2009b). However, the change in impedance after day 130 change was relatively minor compared to the changes in impedance leading up to day 130. Further work is needed to better understand the effects of operational conditions on impedance. The R_{anode} increased to 2.96 Ω and the total cell impedance increased to 27.8 Ω. Considering the time span over which the measurements were made, it can be concluded that the major changes in the MFC impedances occurred over the first three months, after which period the changes were relatively slow and attributable to operational changes in the MFC.

5.3.4 Effect of bioanode enrichment on capacitance

The double layer capacitance of the MFC anode and cathode were described by a CPE; this element modifies an ideal capacitor with an empirical A factor that can vary from 0 to 1 (0 being completely non-ideal and 1 being an ideal capacitor). The $CPE_{DL\text{-}an}$ was on the order of 0.01 F during the first two months. It increased by two orders of magnitude between day 61 and day 136, after which it stabilized at 0.42 ± 0.04 F. The A

factor for the anode (A_{anode}) also increased during this period from 0.78 to a value of near-unity (Figure 5.3b). The CPE representing the cathode electrical double did not change much over the course of the experiment.

Table 5.1. Changes in anode, cathode and combined solution + membrane impedances during a 165-day period, including the period for enrichment of the anode consortium.

	Day 24	Day 43	Day 61	Day 68	Day 130	Day 136	Day 165
R_{Anode}	296.1	36.3	5.77	3.15	1.41	1.49	1.88
	± 137	± 2.7	± 0.48	± 0.41	± 0.13	± 0.08	± 0.11
$R_{memb+soln}$	2.40	3.30	2.92	2.59	3.13	3.55	3.10
	± 0.12	± .01	± 0.01	± 0.02	± .01	± 0.01	± 0.01
$R_{Cathode}$	1.27	8.97	9.50	12.1	12.0	13.2	15.1
	± 1.13	± 1.04	± 0.78	± 0.51	± 0.21	± 0.29	± 0.34
$Total_R$	299.8	48.6	18.2	17.9	16.6	18.3	20.1

5.4 Discussion

The measurements performed in this experiment indicate that the total internal resistance changed over the course of months, rather than weeks. A drastic reduction in the anode resistance was observed, as well as an increase in cathode resistance. The long enrichment time is attributed to the inoculum for the MFC coming from an anaerobic digestor. The result of this microbial origin is that many other species of bacteria (besides electrogens and acetate-degraders) were present. The increase in cathode resistance has not been reported previously for MFCs; however, the impact of changes in impedance of one component of a fuel cell on another component has been reported for a

PEMFC (Aaron et al., 2008; Andreaus et al., 2002). For an MFC, the anode impedance can decrease as a result of biofilm formation and, at some point, the anode impedance can presumably be lower than the cathode impedance. This was demonstrated in the present study. In addition to the changes in the anode over time, physical changes can potentially also occur in the cathode. For instance, accumulation of cations and increase in pH has been shown to occur on the cathode side in two-chamber MFCs (Rozendal et al., 2006). The impact of these changes on MFC performance was studied, but not in terms of the EIS parameters. This study documented the changes in the electrochemical parameters of the cathode, which may be related to the physicochemical changes occurring in the cathode. Additionally, this study suggests that as the limiting factors affecting the performance of an MFC change (e.g., the anode biofilm characteristics), they can indirectly affect the impedance of the cathode.

5.4.1 Anode impedance

Ramasamy et al. (2008) demonstrated the positive effect of initial anodic microbial enrichment on anode impedance over time. The impedance reported for the anode (normalized to projected surface area) for a three-week old biofilm was 0.48 kΩ cm^2. It was reported that this impedance was primarily made up of the charge transfer resistance. He et al. reported an anode impedance of 0.45 kΩ cm^2 (2006). For the MFC system developed in this study, the total anode impedance obtained was 0.017 kΩ cm^2 [R_{anode} * projected anode area (12.56 cm^2)]. This represents a minimum of 28-fold lower anode resistive impedance, assuming that the charge transfer resistance reported by Ramasamy et al. (2008) was representative of the total resistive impedance of the anode.

The trend is in agreement with the power densities obtained for MFC systems as well. The power density for the system in this study was 422 ± 42mW/m^2 of projected surface area compared to 166 mW/m^2 (Ramasamy et al., 2008) and 140 mW/m^2 (He et al., 2006). An important difference between this study and the other two studies was the cathode. A ferricyanide cathode was used in the latter study. As indicated above, the use of a different component in the system can potentially affect the anode impedance and may be a reason for the difference in the impedances. Secondly, the scale of the MFC can also make a difference. In the study by He et al. (2006), the anode volume was 90 mL vs. 16 mL in this study. An increase in the volume of the system has been shown to be linked to increase in the internal resistance of the cell (Clauwaert et al., 2008).

If the anode impedance is assumed to be primarily composed of charge transfer resistance, the exchange current density (I_{ex}) can be calculated via the following equation (Ramasamy et al., 2008):

$$R_{Anode} = R_{CT-anode} = \frac{RT}{nFI_{ex}} \quad (5.1)$$

Here R is the gas constant in J/mol/K, T is the temperature in K, n is the number of electrons involved in the charge transfer reaction (n = 8 for acetate oxidation), F is the Faraday constant in Coulombs/mol. If the exchange current density is calculated for an MFC under operation, it can provide the maximum kinetic reaction rate (i.e., Coulombs/second or current) for the electrochemical reaction if anode were the limiting factor. Typically, the exchange current density is calculated under open circuit conditions

to obtain a rate constant; however, its determination under load conditions may provide an alternate parameter to help determine the limits of the anode. The maximum anode exchange current for this study was 1.83 A/m^2, while that calculated using data from the study by Ramasamy et al. (2008) was 0.066 A/m^2. Thus, a 28-fold higher maximum current can be obtained using the MFC system and the biofilm developed in this study.

A second difference between the system used by Ramasamy et al. and our system was the dimensionality of the anode systems. The anode used by Ramasamy et al. was a graphite plate with a planar geometry, while the anode used in this study was a 3-dimensional carbon felt with high porosity. The electrode surface area of the carbon felt electrode was likely much higher than the projected (flat) surface area, which can be considered as a contributing factor to the low impedance and high exchange current density. The ability of three-dimensional systems to support the higher exchange current density suggests the potential ability to increase power output from MFCs by designing the anode as a three-dimensional electrode. The ability to scale the anode in the third dimension (perpendicular to the membrane), while achieving high power densities and high exchange current densities, indicates that these systems can be scaled to develop suitable commercial-scale systems. Potential mass transfer limitations in three-dimensional systems as indicated by modeling studies (Picioreanu et al., 2008; Rozendal et al., 2008) may also be potentially overcome via use of flow-through systems and use of suitable flow and process conditions as described for these 3-dimensional systems (Borole et al., 2008a; Borole et al., 2009d). Three-dimensional anodes, therefore, have potential for use in full-scale systems.

5.4.2 Implications of change in anode capacitance

The capacitance for the anode EDL increased from 0.007 F on day 61 to 0.45 F on day 165. In addition, the A factor also increased from 0.79 to 1.0 during the same period. The change in A factor indicates that the behavior of the anode double layer changed from a non-ideal capacitive behavior to approach that of ideal capacitor over this time frame. Since the anode electrode was three-dimensional, assessment of the capacitance using the electrode surface area versus using the projected surface area reveals that the anode capacitance was 60 μ F/cm^2 (i.e., capacitance per unit surface area of the three-dimensional electrode). This result indicates that the complete electrode surface including the micro- and macro-porous surface was participating in the electrochemical reaction. This is a significant finding because it suggests that three-dimensional electrodes can be effectively used in MFCs for power generation and for increasing the power density per unit projected surface area of the anode.

5.4.3 Implications for long term operation of MFCs

Limitations in MFC power density due to the cathode have been recently documented (Borole et al., 2009d; Rozendal et al., 2006; Zhao et al., 2006). The limitations are suspected to be due to two primary phenomena: low availability of protons and accumulation of cations such as Na+, K+, NH_{4+}, Ca^2+, Mg^{2+}, etc. Due to the high concentration of the cations in the anode compared to protons on the anode side, the rate of cation transport through the membrane can be very high in comparison to proton transport. This would result in accumulation of cations on the cathode side, leading to increased pH and polarization. Also, protons that diffuse to the cathode are consumed in the ORR; salt cations have no comparable mechanism to be consumed. Operation of the

MFC at low pH (anode or cathode) is one potential solution to this problem (Borole et al., 2008b; Erable et al., 2009). This study demonstrates that despite the cathode limitations, a stable power output can be obtained (422 ± 42 mW/m^2) and maintained for several months.

CHAPTER 6

EFFECTS OF CARBON LOADING AND CATHODE CONFIGURATION ON MFC INTERNAL RESISTANCES

6.1 Introduction

Microbial fuel cells (MFCs) have drawn considerable interest due to a demonstrated capacity to degrade various organic compounds while generating electricity (Feng et al., 2008). Early MFCs utilized the potential difference between anaerobic sediment bacteria in the ocean floor and aerobic bacteria living above the sediment. These devices could supply approximately 350 mW/m^2 of graphite electrode or 60 W/m^3 of reactor volume (Lovley, 2006). Advances in MFC design have led to power densities exceeding 50 W/m^3 of liquid volume or 1000 W/m^2 of Nafion membrane surface area (Borole et al., 2008a; Logan and Regan, 2006). Further improvements to MFC materials and designs are expected to continue to increase the power density of these devices.

Electrochemical impedance spectroscopy (EIS) has been used in corrosion, battery and abiotic fuel cell research (Springer et al., 1996) for over a decade. The capacity for this technique to differentiate and quantify the various transport resistance mechanisms at work in an electrochemical system makes it attractive for MFC studies and optimization. Various MFC materials and configurations have been shown to have significant effects on power generation and internal resistance (Min et al., 2005; He et al., 2006; Fan et al., 2007; Fan et al., 2007; Logan et al., 2007). In addition, the effect of biofilm growth on internal resistances was studied by Ramasamy et al. (2008). EIS can

also be used to quantify the electrical double layer (EDL) capacitances that form between the electrode and electrolyte (Barsoukov and Macdonald, 2005). A brief summary of calculated impedances and power densities from published works can be seen in Table 6.1. Thus, incorporation of EIS into MFC analysis adds another dimension to understanding the processes limiting power production.

Table 6.1. Summary of total resistance and power density from other works.

Experiment	Total Impedance (Ω)	Power Density	Feed type	Reference
Bicarbonate buffer	15.0	1550 W/m^3	Continuous	Fan et al., 2007b
Upflow MFCs	17.0	29.2 W/m^3	Continuous	He et al., 2006
J-cloth layers	82-105	55 – 80 W/m^3	Continuous	Fan et al., 2007a
Anode growth	7200	25 mW/m^2	Continuous	Ramaswamy et al., 2008

Acquiring an impedance spectrum (IS) required the fuel cell to be at steady state with minimal drift for the duration of the spectrum scan. Most EIS investigations presented in the literature focus on the anode and cathode charge transfer resistances, as well as the solution resistance. This chapter will include values for the EDL capacitances, as well as the resistances for a single MFC anode compartment that was operated with two different cathode configurations. The objective was to identify, via EIS, internal resistances that could be minimized, thereby allowing higher power production by the MFC. During steady state operation, impedance spectra were recorded and compared to an equivalent circuit model (ECM) formulated to describe the various resistances and capacitances in an MFC developed with Dr. Borole at ORNL.

6.2 Materials and methods

6.2.1 MFC design

Two MFC designs were utilized in this study: a two-chamber design with an aqueous cathode and a one-chamber design with a passive air cathode. The same anode (microbes and housing) was used for both cathode designs; a new cathode was added to the MFC in an anaerobic chamber to minimize exposure of the anode consortium to air. The bacteria are an enriched consortium of anaerobic digester bacteria. The growth medium is described elsewhere (Borole et al., 2008a). In addition to changing the cathode, experiments were performed to explore the effect of varying carbon source load (lactate and glucose) supplied to the bacteria. Carbon source concentrations included 0.4 g/L-day, 0.6 g/L-day and 4.0 g/L-day. The carbon source was a mixture of two substrates: glucose and lactate, each at equal concentrations, e.g. 0.2 g/L-day of each to give a total of 0.4 g/L-day carbon source. Changes to the carbon loading were performed after replacing the anode solution to remove any residual carbon from previous experiments. Following anode medium replacement, sufficient time at the new carbon loading was allowed to reach steady operation. The anode was a 4 cm diameter PVC pipe cut to 1.27 cm length; this volume was filled with carbon felt (Alfa Aesar) as the electrode and microbe support. A Nafion 115 proton exchange membrane (PEM) was used to separate the anode and cathode.

The ferricyanide (abbreviated FeCN) cathode was aqueous; its chamber was a 4-cm diameter PVC pipe cut to a length of 2.54 cm. In addition to FeCN, 100 mM K_4PO_4 buffer was present in the cathode solution. The FeCN cathode electrode was 2.54 x 2.54

x 0.625 cm carbon felt suspended on a graphite rod, such that it was in firm contact with the PEM. FeCN concentrations studied in this paper included 50, 100, and 200 mM. Following FeCN addition to the cathode, the cell output would quickly reach a peak and then decrease quickly. After approximately 10 minutes, the output would decrease very slowly as FeCN was consumed. Since the output never truly reached steady state, EIS measurements were taken during the slow output decrease phase. Each EIS measurement was taken relative to the present output potential of the cell, so drift only became problematic at frequencies below ~5 Hz. The air cathode had a 2.54 x 2.54 cm Pt-impregnated carbon electrode in contact with the PEM. All power densities reported below are normalized with respect to the anode projected surface area (12.6 cm^2). A gold wire was used as a current collector and to connect the Pt electrode to the external circuit. All measurements taken in this work were performed with an external circuit resistance of 49.8 – 50.4 Ω. Lexan endplates, rubber gaskets and steel tie rods were used to hold the MFCs together. Schematics of the MFCs used in this study can be seen in Figure 2.4.

6.2.2 Electrochemical impedance spectroscopy

A frequency spectrum ranging from 0.1 Hz to 10^5 Hz was used in this study. A Gamry Instruments Series 750G potentiostat/galvanostat/zero-resistance ammeter was used to generate the 1 mV AC signal that was passed through the cell. The small AC signal was used because it was observed that a 10 mV AC signal caused bacteria to detach from the anode support (evidenced by rapidly increasing optical density in the anode solution immediately following an IS scan). No DC current was employed in this study because it was also observed to have caused some microbial detachment. A reference electrode was not included because the fuel cell design did not accommodate its

insertion; thus, EIS was performed in a two-electrode mode where the cathode served as the working electrode while the anode was the counter electrode. Also, reference electrodes would not have contributed to the whole-cell EIS measurements that were the goal of this work. Table 2 shows a matrix of the experiments performed. For each condition studied, at least two IS were recorded and analyzed to ensure the resulting model parameters were accurate and consistent. Power densities reported in this study are the result of the potentiostat measurement of the MFC potential just prior to beginning IS recording.

Table 6.2. Matrix of experimental conditions used in this study.

Carbon loading (g/L-day)	**Cathode configuration**
0.4	Pt/C air cathode
0.6	Pt/C air cathode
4.0	Pt/C air cathode
0.6	50 mM FeCN
0.6	100 mM FeCN
0.6	200 mM FeCN
0.2*	Pt/C air cathode

*Note: The final experiment was performed following the various FeCN concentration experiments.

6.2.3 Equivalent circuit model

Despite the fact that two MFC configurations were employed in this work, a single ECM was used to describe both systems. The ECM in this work is shown in

Figure 2.6 (shown below for convenience From an ECM standpoint, the difference between the aqueous cathode and air cathode configurations is the presence of an extra solution resistance in the aqueous cathode setup. In the two-chamber design, the solution resistance is comprised of anode electrolyte, PEM, and cathode electrolyte; the one-chamber design has a solution resistance made up by the anode electrolyte and the PEM (since no cathode electrolyte is present). Since the various solution resistances cannot be isolated without reference electrodes, a single ECM for both cathode configurations is reasonable.

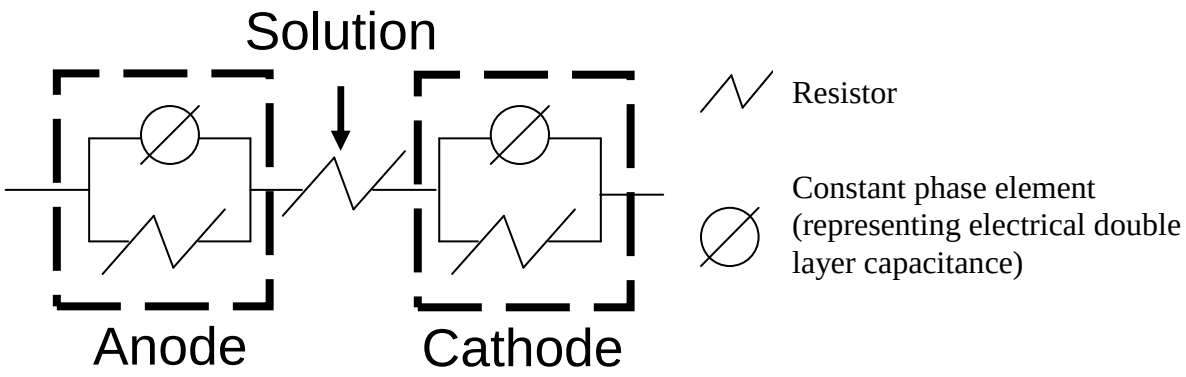

Figure 2.6. Equivalent circuit model (ECM) used to determine internal resistances and capacitances. Note that the resistor separating the two resistor-capacitor components (termed "solution resistance") includes the anode solution, PEM, and cathode solution (present only in the aqueous cathode setup).

6.3 Results

6.3.1 Comparison of air and ferricyanide cathodes

In all experiments, the air cathode MFC had dramatically less power production than that exhibited by the FeCN, aqueous cathode configuration: 0.50 W/m^2 by the air cathode and up to 4.7 W/m^2 by the 200 mM FeCN cathode MFC. The internal resistance did not exhibit as large a range of values, but the air cathode resulted in the greatest total

resistance. The air cathode total resistance was 30.0 Ω while the 50 mM, 100 mM, and 200 mM FeCN cathodes had total resistances of 18.0, 14.8, and 14.0 Ω, respectively. As shown in Figure 6.1a, the bulk of the resistance in all three cathode FeCN concentrations was in the cathode (the cathode made up approximately 70% of the total resistance). As FeCN concentration increased, all of the resistances showed an overall decrease. The increase in cathode resistance corresponding to the increase in FeCN concentration from 100 mM to 200 mM is within the error limits, thus a true minimum in cathode CTR is considered suspect. Even though changes were made only in the cathode, the anode showed improved charge transport since the anode CTR decreased. This anode improvement is likely because the cathode provided less resistance to the electrons that result from the bacterial consortium's metabolism. Thus, the metabolism of the bacteria could speed up, indicated by a reduction in resistance. One important influence on solution resistance is solution ionic strength; higher ionic strength reduces solution resistance. Thus, the reduced solution resistance could mainly occur in the cathode solution (which is a part of the reported solution resistance) as a result of increased ionic strength. In the air cathode configuration, the anode was only 41% of the total resistance; 42% was in the Pt/C cathode and the remaining 17% was located in the solution. This difference in resistance distribution between the two cathode configurations is due to the relatively high charge transfer resistance exhibited in the Pt/C cathode.

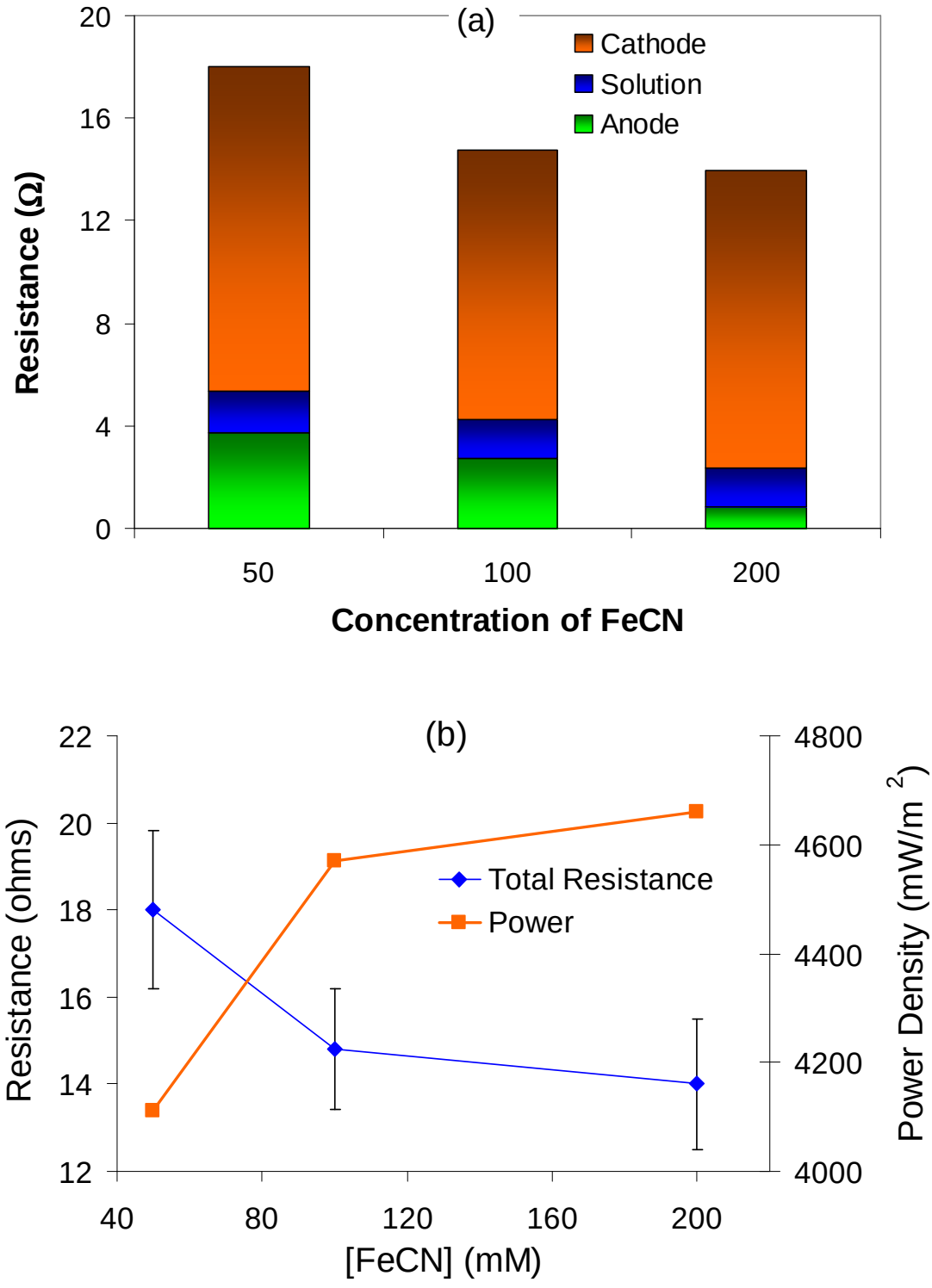

Figures 6.1. (a) Anode and cathode charge transfer resistances, solution resistance, and total resistance for varying ferricyanide cathode solutions. (b) Total resistance and power density for varying ferricyanide cathode solutions. Temperature for experiments was approximately 30°C.

Power densities recorded just prior to performing EIS for aqueous FeCN cathodes are shown in Table 6.3. Table 6.3 also includes values for all resistors, capacitors, and the empirical "A" factor that modifies the capacitance due to its non-ideal nature. These values were calculated using the ECM shown in Figure 2.6. It should be noted that the capacitances reported in Table 6.3 with units of Faradays are determined via Equation 6.1; the A factors in Table 6.3 are shown for reference, but are already included in the calculation for the capacitances in Table 6.3.

$$C = \frac{(EDL * R)^{\frac{1}{A}}}{R} \tag{6.1}$$

In Equation 6.1, *EDL* refers to the coefficient calculated for the CPE at an electrode and has units of Siemens-seconds. *R* refers to the resistor that is in parallel to the CPE for that electrode (see the parallel resistor-CPE elements in the ECM shown in Figure 2.6). Finally, *A* represents the empirical A factor that can vary between 1 (ideal capacitor) and 0 (completely non-ideal capacitor).

Table 6.3. Complete EIS breakdown of resistors and capacitors for ECM representing air cathode and varying ferricyanide, aqueous cathodes.

Element	Units	50 mM FeCN	100 mM FeCN	200 mM FeCN	Pt/C air cathode
CTR anode	**Ω**	**3.73**	**2.74**	**0.825**	**3.81**
EDL anode	F	$1.02E^{-3}$	$8.32E^{-4}$	$4.23E^{-4}$	$2.25E^{-3}$
A anode		0.526	0.514	0.656	0.986
Solution	**Ω**	**1.60**	**1.53**	**1.53**	**2.30**
CTR cathode	**Ω**	**12.7**	**10.5**	**11.6**	**11.1**
EDL cathode	F	0.198	0.116	0.074	25.4E-3
A cathode		0.560	0.579	0.476	0.429
Σ Resists	**Ω**	**18.0**	**14.8**	**14.0**	**18.4**
Power density	**W/m^2**	**4.11**	**4.57**	**4.66**	**0.527**

Notes: Temperature was approximately 29°C. Carbon load for all ferricyanide cathodes and the air cathode was 0.6 g/L-day. The units for the EDLs are Siemens-seconds. The "A" factor for both EDLs is unitless.

6.3.2 Comparison with a proton-exchange membrane fuel cell

Such a high resistance in the cathode is uncharacteristic for a proton-exchange membrane fuel cell (PEMFC), which also uses a similar Pt/C cathode (Aaron et al., 2008). Measured cathode CTR in a PEMFC is on the order of 0.1 Ω; thus, it is expected that further optimization of the Pt/C cathode can result in a much lower charge transfer resistance. Cathode CTR is greatly increased in a PEMFC when the cathode is flooded by water accumulation in the Pt/C catalyst layer; excess water transport through the PEM in the MFC can result in similar flooding conditions for the Pt/C cathode in the MFC, thus causing the high CTR. It should be noted that flooding is an issue for Pt/C air cathode systems; this is because oxygen (in air) must be able to reach the Pt sites in the

catalyst layer on the cathode side of the fuel cell. Transport of oxygen to the Pt particles is inhibited when water covers the particles. The FeCN system generates greater power because the transfer of electrons from the electrode to aqueous FeCN is more effective than the proton-oxygen-electron reaction that takes place on Pt particles. As exhibited by smaller cathode CTR in the FeCN design, charge transport is facilitated by the presence of an aqueous system with FeCN as the electron acceptor. Another factor that can increase CTR in the Pt/C cathode is the buildup of cations in the liquid layer present in the cathode. Steps to minimize the opportunity for flooding should be taken in an attempt to reduce the CTR exhibited in these studies.

6.3.3 Effect of carbon source loading

Increasing the carbon source loading from 0.2 g/L-day to 2.0 g/L-day did not have an appreciable effect on the cell power output; power density varied from 0.516 W/m^2 to 0.527W/m^2 throughout the range of carbon loads explored. This suggested that the bioanode was saturated with carbon source even at a concentration of 0.2 g/L-day. This conclusion is supported by the calculation that coulombic efficiency decreased from 24.9% for 0.4 g/L-day to only 2.49% for the 4.0 g/L-day. It is noted here that these experiments were not designed to maximize coulombic efficiency but to explore whether excess carbon source (resulting in greater availability to the microbes) could improve charge or ion transport in the bioanode. An interesting observation here is that the reduced coulombic efficiency was not tied to any change in any of the internal resistances. Thus, low coulombic efficiency is not necessarily an indicator of poor MFC performance, but can instead signal an excess of carbon source fed to the MFC.

The total resistance showed a small decrease from 18.4 Ω to 16.5 Ω when increasing the carbon source feed from 0.2 g/L-day to 2.0 g/L-d. Most of the total resistance decrease was a result of the anode resistance decreasing as the carbon source concentration increased. The anode CTR showed a slight decrease from 3.81 Ω at 0.2 g/L-day to 2.53 Ω at 2.0 g/L-day. The anode CTR at 0.3 g/L-day was 2.14 Ω, but the error (as high as 30%) in calculating the anode CTR does not support the conclusion that a minimum resistance occurs at 0.3 g/L-day, but rather that increasing carbon loading can cause a small decrease in anode CTR. This suggests that charge transport at the anode was slightly improved when the bacteria had more carbon source to utilize, but that carbon delivery greater than 0.2 g/L-day was in excess of what the bacterial anode could degrade. However, the decrease in the anode resistance was offset by an increase in solution resistance from 2.30 Ω at 0.2 g/L-day to 4.46 Ω at 2.0 g/L-day. A peak in solution resistance occurred at 0.3 g/L-day with a value of 5.15 Ω. The solution resistance for 0.2 g/L-day is lower than expected, but it is consistent for multiple impedance spectra for each setting. Since the electrodes did not move, it is assumed that the solution composition changed during the course of the experiments. In addition, the cathode CTR also decreased over the range of carbon loadings: from 12.3 Ω at 0.2 g/L-day to 9.48 Ω at 2.0 g/L-day. This reduction is likely due to improved proton availability to the cathode.

A summary of all EIS parameters for the various carbon loading experiments can be found in Table 6.4. The solution resistance for the air cathode was usually above 4 Ω, while it was below 2.5 Ω for the aqueous cathodes. Despite the extra resistor in the

aqueous cathode, it is likely that the solution resistance was lower than in the air cathode because the cathode solution had a high ionic strength (which affects the PEM and anode solution as well, due to transport of cations through the Nafion PEM). Calibration experiments in the laboratory have shown that the solution resistance decreases as the ionic strength increases. Figure 6.2 presents the Nyquist plot for each of the three carbon loadings, showing the higher solution resistance for 0.3 g/L-day and 2.0 g/L-day (the projected x-intercept at low values of Z_{Real}) as compared to that for 0.2 g/L-day. The metabolic products of the microbial community in the anode were not analyzed. However, any products present did not exhibit any negative effects on the bacterial output since no loss of power was observed over time in this work.

Figure 6.3a shows each of the three resistances and the total resistance as a function of carbon loading. Figure 6.3b shows total resistance and power density as a function of carbon loading. In all of the varying carbon loading experiments, the MFC was limited by the cathode. The cathode made up 67%, 62% and 54% of the total resistance in the 0.2, 0.3 and 2.0 g/L-day experiments, respectively. It can be seen that carbon loading did not have a significant effect on the internal resistances or MFC power output. This suggests that the microbes had sufficient food, even at 0.4 g/L-day carbon loading, to perform their metabolism.

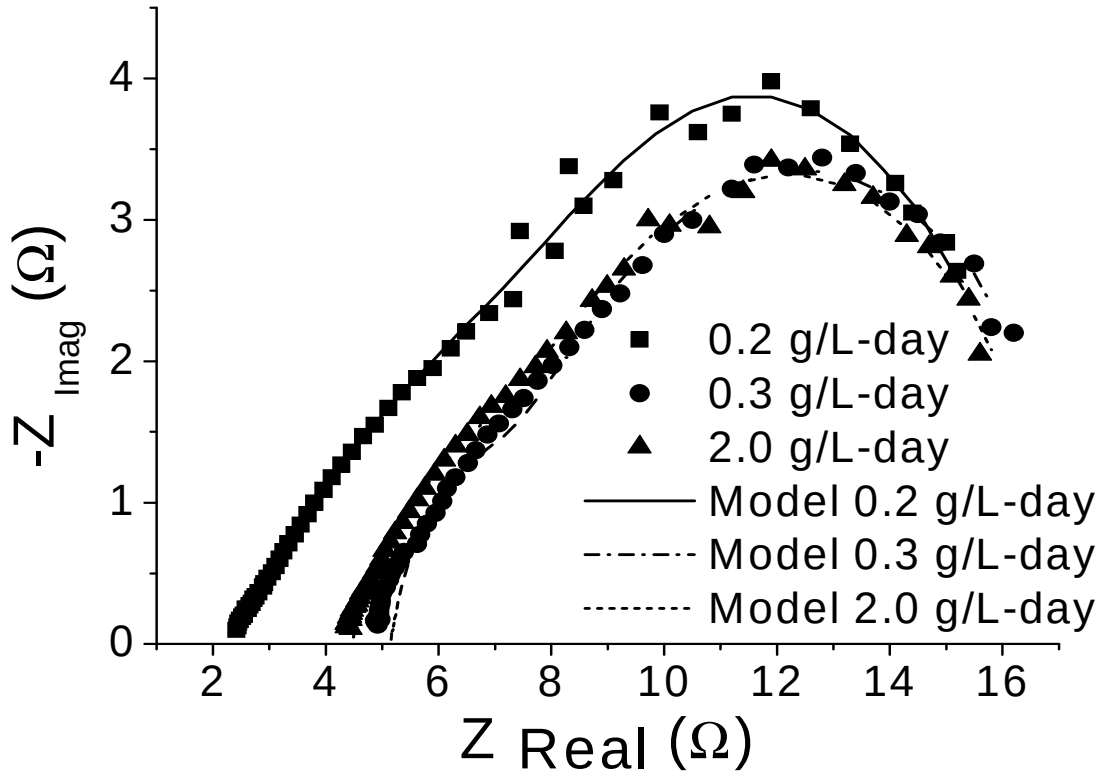

Figure 6.2. Nyquist plot for 0.2, 0.3 and 2.0 g/L-day; note that the high frequency x-intercept for 0.3 and 2.0 g/L-day experiments is much higher than for 0.2 g/L-day.

Table 6.4 Complete EIS breakdown of resistors and capacitors for ECM representing the MFC at varying carbon loads.

Element	Units	0.4 C Source	0.6 C Source	4.0 C Source
CTR anode	**Ω**	**3.81**	**2.14**	**3.53**
EDL anode	F	1.08E-3	2.25E-3	2.22E-3
A anode		0.986	0.823	0.603
Solution	**Ω**	**2.30**	**5.15**	**4.35**
CTR cathode	**Ω**	**12.3**	**11.1**	**9.48**
EDL cathode	F	10.6E-3	25.4E-3	33.4E-2
A cathode		0.429	0.682	0.726
Σ Resists	**Ω**	**18.4**	**18.0**	**17.6**
Power density	**W/m^2**	**0.527**	**0.516**	**0.527**

Notes: Various C source experiments had the Pt/C air cathode at approximately 29^{o}C. The units for the EDLs are Faradays. The "A" factor for both EDLs is unitless.

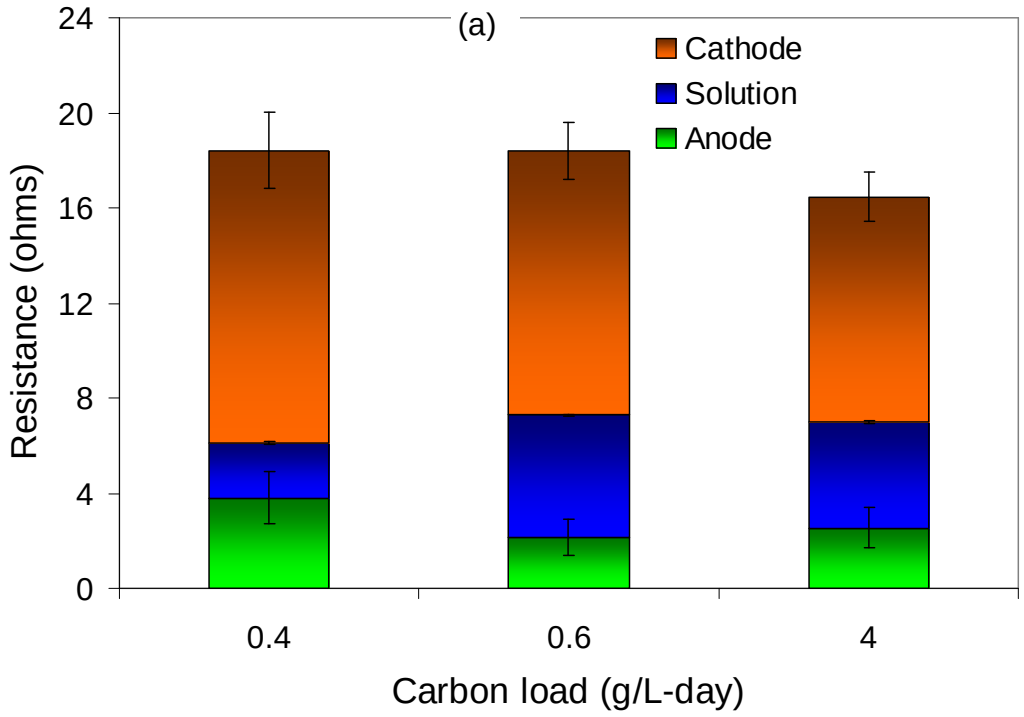

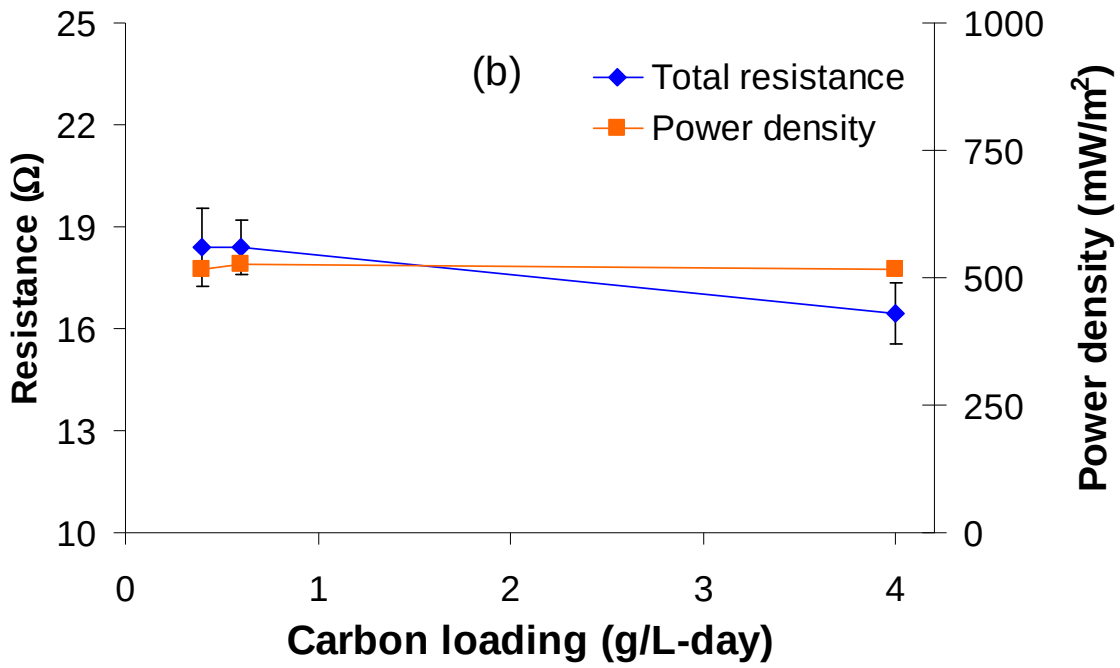

Figure 6.3. (a) Anode and cathode charge transfer resistances, solution resistance and total resistance for various carbon loadings. (b) Power density and total resistance as a function of carbon loading. Pt/C air cathode. It should be noted that the difference in power density is a result in only 1 mV cell potential.

These results show that EIS can be used to quantitatively identify limiting resistance mechanisms in MFCs. Further work can be guided by EIS results, allowing optimization to be focused on the areas that provide the greatest limitations to MFC power production. However, this technique is often impeded by MFC instability; in addition, the response of the microorganisms to changes in feed medium and other environmental factors (including changes in the cathode, as shown above) can present challenges to performing EIS studies. Thus, further refinement of the EIS technique to the special obstacles posed by MFC systems is desirable.

In all of the FeCN cathode experiments, the MFC was limited by the cathode CTR. An air cathode experiment was performed following the FeCN cathode experiments, yielding results similar to the 50 mM FeCN experiment. However, it is noted that the anode resistance was greater for the air cathode than for the FeCN cathode. In the series of carbon loading experiments, the cathode also limited the MFC, though to a lesser degree than in the FeCN experiments. Thus, it can be concluded that the cathode in this MFC provided the greatest resistance, even when the FeCN cathode was employed. As the concentration of FeCN increased, decreased overall resistance and increased power production were observed. Increased carbon loading did not result in any increase in power production and only a slight decrease in internal resistances, indicating that there should be an optimal carbon loading concentration in terms of economic criteria.

This EIS study shows that the different regions of the MFC—anode, solution and cathode—are not independent. Despite only making alterations to the cathode, changes in anode behavior were observed via EIS. This suggests that the anode bacteria respond to changes in the environment outside the anode. High power density in an MFC is often achieved with the use of FeCN in the cathode; based on this EIS study and comparison with a PEMFC with a similar Pt/C cathode, it should be possible to optimize the Pt/C electrode configuration in an MFC to achieve much higher power density without the use of FeCN.

CHAPTER 7

ELECTROCHEMICAL IMPEDANCE SPECTROSCOPY OF AN OPERATING ENZYME FUEL CELL

7.1 Introduction

Enzyme fuel cells are a relatively novel type of fuel cell. The goal with this design is to replace costly precious metal catalysts in regular low-temperature fuel cells with biologically-derived enzymes. Such a replacement can drastically decrease the cost of fuel cell materials (Minteer et al., 2007). Two more benefits stem from the specificity of enzymes: first, multiple fuels (not just hydrogen) can be used if the appropriate enzyme is used (Borole et al., 2009a); second, construction materials can be reduced since enzymes can be specific enough to not require separation materials to chemically isolate the anode and cathode (Zebda et al., 2009). These aspects of EFCs grant them considerable economic potential for providing low-temperature power based on a variety of fuels. However, EFCs are not without obstacles. Hudak et al. (2009) observed that significant power loss is observed over time; contributing causes include enzyme degradation, mediator degradation, and cathode drying. In addition to these longevity issues, even the highest power-density EFCs produce orders of magnitude less power than PEMFCs at similar conditions.

The low power output and short operating time of EFCs are targeted issues being addressed in EFC research. Various electrochemical tools are used to study materials of

construction, effects of operating conditions, and other aspects of EFC operation. Among these tools is EIS, which has been demonstrated in the literature as useful for studying transport in PEMFCs and MFCs, as well as previously in this work. Application of EIS to EFCs, however, is rarer in the open literature, perhaps because EFCs are still a relatively new type of fuel cell.

The common design for EFCs is to have mediated electron transfer between an electrode and a dissolved enzyme (Samukawa et al. 2008, Hudak et al., 2009; Tamaki and Yamaguchi, 2006; Danaee et al., 2008; Katz and Willner, 2003). This design typically benefits from a three-dimensional electrode since this configuration greatly increases electrode surface area for transfer of electrons to the mediator (Minteer et al., 2007). Tamaki and Yamaguchi (2006) utilized EIS to study the effects of immobilizing mediators on the electrode surface. They found that modifications to the electrode did not significantly increase the internal resistance. The modifications in their work actually sped up the oxidation of glucose by utilizing both mediated and direct electron transfer to the enzymes. A study by Katz and Willner (2003) utilized EIS to individually study the anode and cathode of an operating EFC. Since the design of the EFC did not accommodate inclusion of true reference electrodes (such as Ag/AgCl or a standard hydrogen electrode), metal needles were included in the EFC to serve as quasi-reference electrodes. It was found that the cathode resistance was approximately 70% of the total resistance while the anode resistance was approximately 30% of the total. Single-electrode measurements were compared to whole cell measurements. Danaee et al. (2008) included adsorption in the EIS analysis of an glucose oxidation on a Ni-modified,

glassy carbon electrode. It was observed that CTR decreased by nearly an order of magnitude when glucose concentration increased from 1 mM to 7 mM. The resistance to adsorption also decreased by a factor of three over this range of glucose concentration.

The above-mentioned studies are the only examples of EFC EIS measurements we could find in the literature. However, it is apparent from these publications, as well as from the similarity between EFCs and PEMFCs, that EIS can be useful for studying transport phenomena in operating EFCs. In this chapter, internal resistance responses to operating conditions such as enzyme concentration, air humidity, and air flow rate, as well as time-dependent studies are presented. Power density analysis is also included. These experiments were performed with the help of Dr. Borole and Ben Spott at ORNL.

7.2 Materials and methods

7.2.1 EFC materials and design

A three-dimensional cathode EFC (Borole et al., 2009a) was utilized in this work. Two EFCs were constructed. One was made with Lexan endplates and rubber gaskets for experiments performed at ORNL. The other EFC was constructed with aluminum endplates and Teflon gaskets and used in neutron imaging studies performed at NIST (see Chapter 8). Both EFCs had the same geometry; only materials were different. The effect of the materials on EFC performance was found to be negligible. The cathode compartment was 0.43 cm thick with an open internal area of 1.8 cm x 1.3 cm. The anode compartment was approximately 0.075 cm thick with the same open internal area as the cathode. In the Lexan EFC, the current collectors were made of graphite at the

anode and of gold wire at the cathode; in the aluminum EFC, the endplates served as current collectors.

The anode material was 1 cm^2 Pt-deposited carbon cloth (Fuel Cell Store, Inc.). The cathode was made of carbon felt (Alfa Aesar) with an area of 1 cm^2 and thickness of 0.635 cm and 83% porosity. The carbon felt cathode was made hydrophilic via plasma treatment (Harrick Plasma Company). Loosely woven carbon cloth was included in both the anode and cathode to serve as a gas diffusion layer and to aid in contact with the current collectors. The cathode solution included the laccase enzyme from *trametes versicolor*, 100 mM citrate buffer at pH 4, and 2,2'-azinobis(3-ethylbenzothiazoline-6-sulfonate) (ABTS) as the mediator. A schematic of the EFC is found in Figure 7.1.

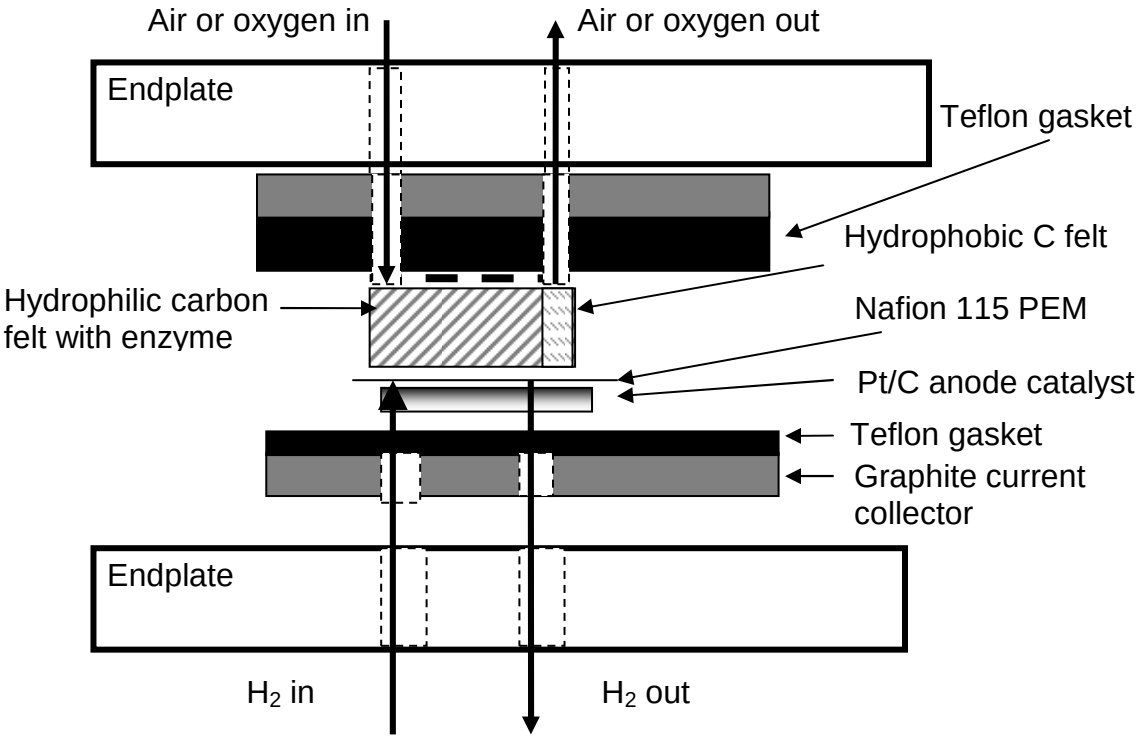

Figure 7.1. Schematic of EFC used for imaging experiments. Only the enzyme solution was a strong neutron attenuator in this setup.

7.2.2 EIS of the EFC

EIS was performed with the same equipment as described earlier in this work. All measurements performed were two-electrode, or whole-cell measurements since the EFC design did not accommodate the inclusion of a reference electrode. The frequency range of the impedance spectra spanned from 100 kHz to 5 mHz with an AC amplitude of 1 mV; the frequency range resulted in scan times of approximately 15 minutes. All measurements were performed while the EFC was under a load of approximately 1000 Ω. Other measurements were taken at high external resistance because these corresponded to greater power density. It was demonstrated by Fan et al. (2007) that fuel cell output greatly influences EIS spectra. Observations in this work included that the EIS spectra were difficult to model at low power density, thus most scans were performed at resistances that resulted in high power density. Because the EFC is very similar in construction to the PEMFC, the same ECM was used for analyzing the EFC spectra. For reference, this ECM is included below (Figure 2.6).

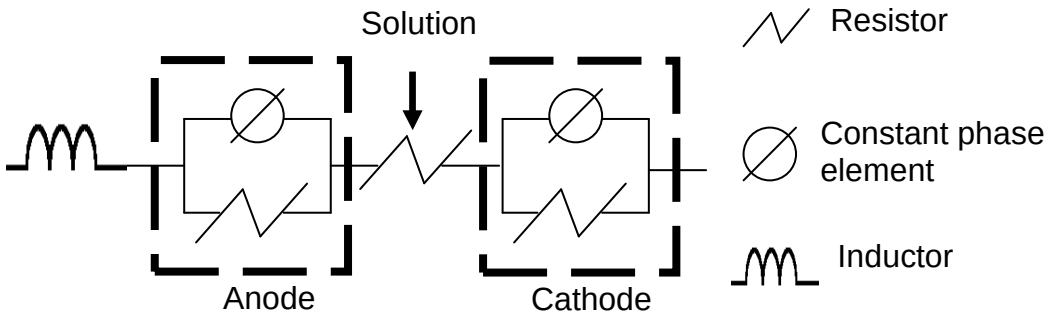

Figure 2.6. Equivalent circuit model representing the fuel cells in this work.

7.2.3 Operating conditions explored with EIS

EIS measurements were intended to be used to study the effects of various operating conditions on the power output and internal resistances of the EFC. In this work, enzyme loading, air saturation temperature, air flow rate, and salt concentration were all varied. Enzyme loadings varied from 0.15 units to 15 units; air humidification temperature varied from 25^{o}C to 50^{o}C; air flow rate was maintained between 10 sccm and 50 sccm; and salt concentration was varied between 100 mM and 800 mM. The air humidification temperature was controlled by placing the humidifier in a thermostatically-controlled hot water bath. It was expected that a combination of conditions would result in improved power density and longevity for the EFC. In general, greater enzyme loading, higher air saturation temperature, reduced air flow rate and increased salt concentration were all expected to contribute to EFC stability and, potentially, power output. Since the enzyme and mediator stability, as well as water content, for any EFC was relatively short-lived (perhaps four hours of stable operation), an EFC with new enzyme solution was constructed for many experimental conditions.

7.3 Results and discussion

EIS measurements were performed at the maximum power density of each EFC. In general, this corresponded to 750 Ω external resistance. Due to drying observed in this work, as well as documented in other studies (Hudak et al., 2009), the EFC output decayed over time. This presented problems with performing multiple scans of the EFC

(for repeat measurements) and then changing conditions for the EFC, allowing it to equilibrate, and obtaining more EIS scans. For example, the measurements performed for varying air-side humidity (via control of saturation temperature) were taken for multiple EFCs, with each temperature measurement being for a different EFC. However, each experimental setting was performed for multiple EFCs to check reproducibility. Output of the EFC was usually stable enough for two sets of measurements since each measurement took approximately 15 minutes to complete. The time between sets of measurements after a change in conditions was approximately two hours. For all experiments, the ratio of ABTS mediator to enzyme was maintained constant at 2:1.

7.3.1 Effects of enzyme loading

Enzyme loading was considered and spanned a range from 0.15 U/cm^2 to 15 U/cm^2. It is noted here that, since the cathode was 1 cm^2, enzyme loading designations will simply be 0.15 U, 15 U, etc. Enzyme loading was expected to have a strong influence on both power density and internal resistance since this determined the amount of catalyst present in the cathode. In Figure 7.2, Nyquist plots are included for enzyme loadings of 1 U, 10 U, and 15 U. Two results are apparent from the Nyquist plot: overall resistance and solution resistance decreased as enzyme loading increased. Lower overall resistance for greater enzyme concentration is reasonable since more catalyst is present to speed up the oxygen reduction reaction (ORR) in the cathode. The solution resistance could have decreased with greater enzyme concentration since proton transport is related to the solution resistance. At increased enzyme loading, protons would have a greater rate of collision with enzymes, thus resulting in a reduced solution resistance. Another

way of understanding is that the average time for protons to diffuse through the cathode water network prior to meeting a laccase enzyme is reduced with greater enzyme loading (more protons would contact enzymes “earlier” in the cathode). Thus, the enzyme concentration is likely to strongly influence the cathode resistance as well as the solution resistance of the EFC.

The ECM shown in Figure 2.6 was utilized to break down the total resistance into its constituent components of anode, solution and cathode. The results for this modeling are included below in Figure 7.3. It is apparent that the resistance was dominated in the cathode even at the highest enzyme loading of 15 U. For the enzyme loadings studied, the cathode made up approximately 80% of the total resistance. Each measurement was performed for three independent EFCs, and the error was never greater than 17% (for the cathode of the 15 U measurement), and often below 5%. Cathode limitation is understandable since Pt was used in the anode and because transport conditions in the cathode have not been optimized, other than to utilize a three-dimensional structure to facilitate airflow through the cathode.

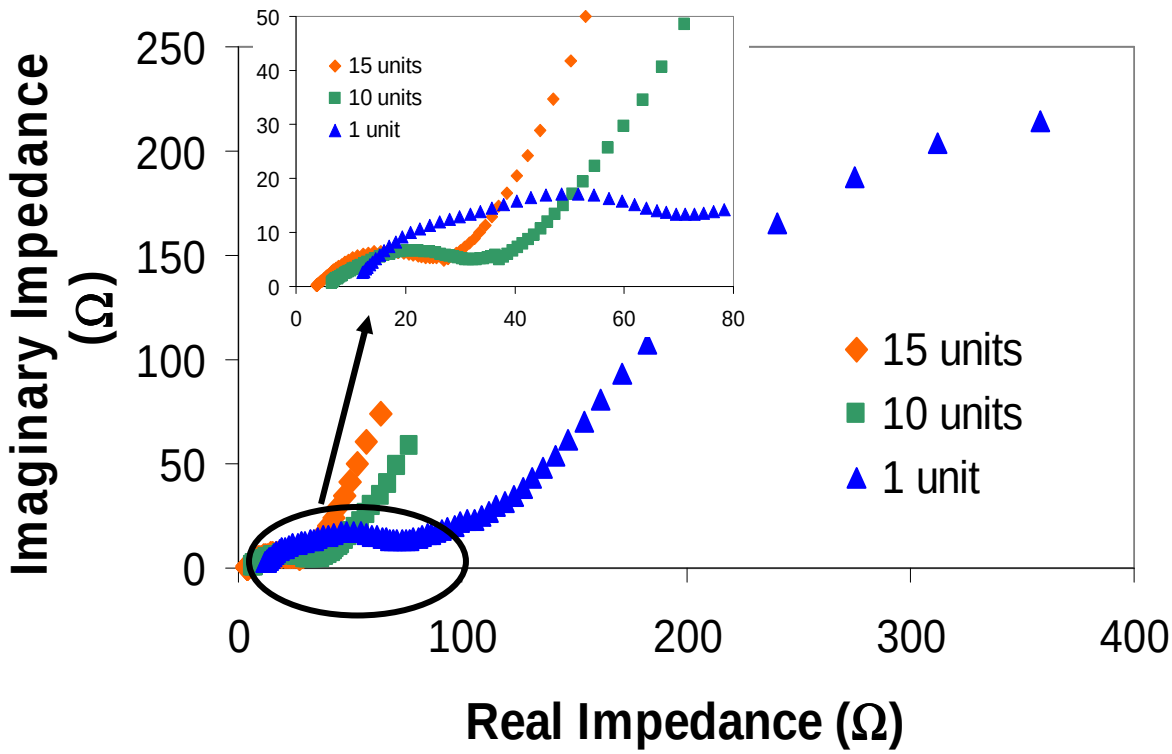

Figure 7.2. Nyquist plots for varying enzyme loading in EFC cathode solution.

It is apparent in Figure 7.3 that most of the reduction in total resistance occurred in the cathode. The cathode decreased from approximately 87 Ω at 1 U loading to 41 Ω at 15 U loading, just over a 50% reduction in resistance. For the same increase in enzyme loading, the anode resistance decreased from 5 Ω to 3 Ω and the solution resistance decreased from 8.5 Ω to 5.1 Ω.

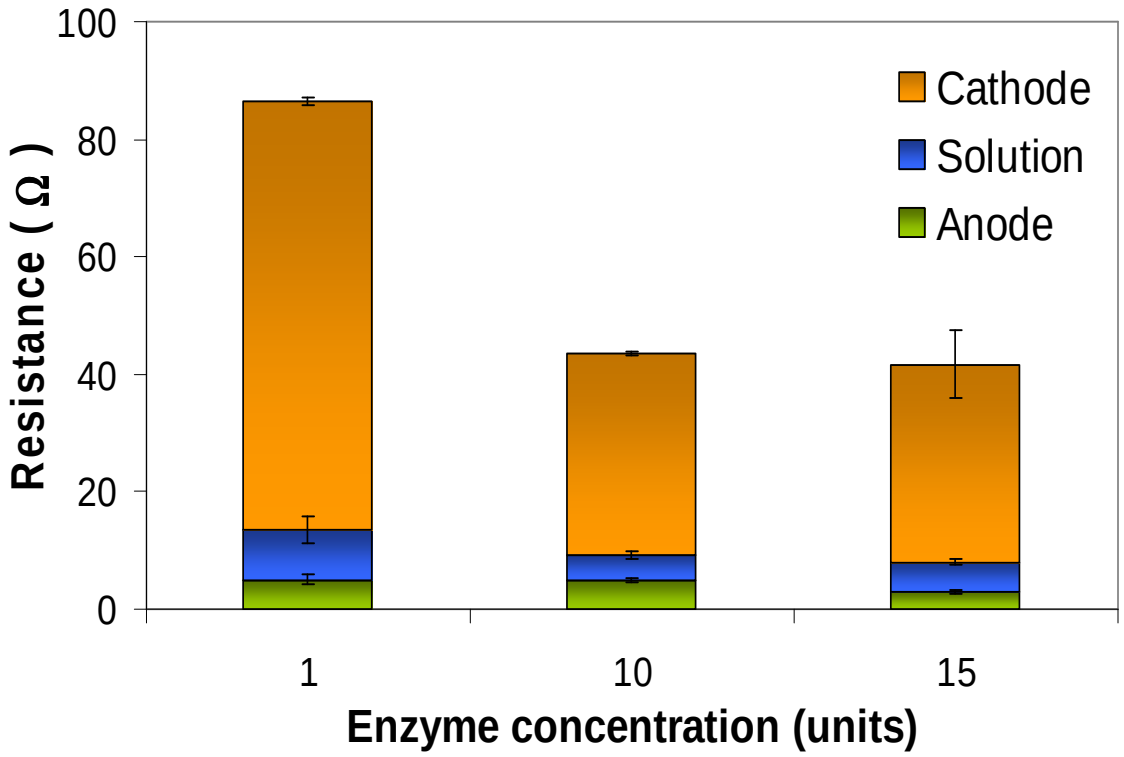

Figure 7.3. ECM results for EFCs of varying enzyme loading in the cathode. The ratio of ABTS:laccase was held constant, as were all other experimental parameters.

The solution resistance did exhibit a minimum of 4.1 Ω at 10 U enzyme loading, but this is believed to be more likely a systemic error rather than a true result of increasing enzyme loading. Error is considered likely because there is no indication in the literature of increased catalyst loading (for enzymes for Pt-based PEMFCs) somehow negatively affecting solution resistance. In addition, the Nyquist plots in Figure 7.2 indicate that the solution resistance did decrease with increasing enzyme loading.

The total resistance shown in Figure 7.3 was 86.5 Ω, 43.6 Ω and 41.7 Ω for enzyme loadings of 1 U, 10 U, and 15 U, respectively. Thus, it appears as though the total resistance was reduced significantly when increasing enzyme concentration from

1 U to 10 U, but did not change much past this point. Power density followed a similar trend: it increased from 2200 W/m^2 to 6710 W/m^2 when enzyme loading increased from 1 U to 10 U. Then, increasing enzyme concentration from 10 U to 15 U only increased the power density to 6900 W/m^2. These trends in total resistance and power density are shown in Figure 7.4. For the system considered in this work, it appears as though little improvements in power density or internal resistance occur when the enzyme concentration is above 10 U. This is believed to be the case because the limitation was no longer in enzyme availability but in some other aspect of the EFC cathode. One example of another cathode limitation could be that mediator transport between enzymes and the cathode was at its peak with 10 U. Borole et al. (2009a) found a similar result but that the maximum useful enzyme concentration was at 15 U/cm^2. Individual values for each of the resistances and enzyme loadings are shown in Table 7.1.

Table 7.1 ECM results for experiments varying enzyme loading.

Enzyme loading (U)	Anode (Ω)	Solution (Ω)	Cathode (Ω)	Total (Ω)	PD (mW/m^2)	Cathode % of total
1	5.0	8.5	73.0	86.5	2200	84.4
10	5.1	4.1	34.4	43.6	6710	79.0
15	2.9	5.1	33.7	41.7	6900	80.7

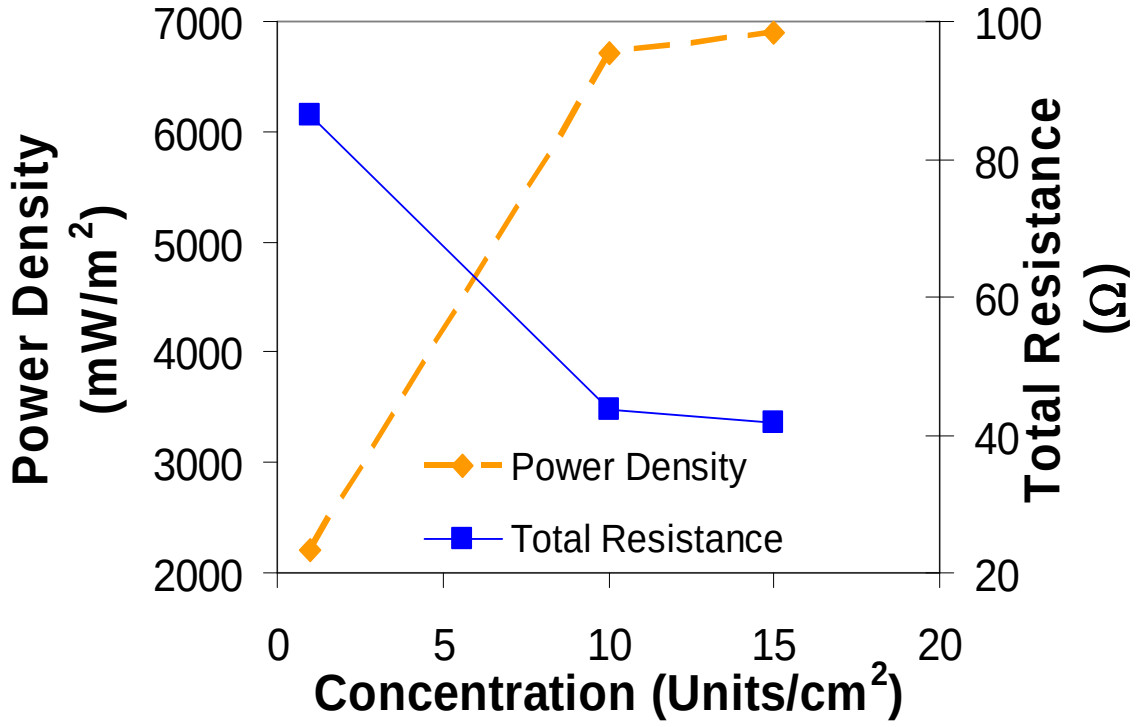

Figure 7.4 Power density and total resistance as functions of enzyme loading. All other experimental parameters were maintained constant between experiments.

7.3.2 Effects of operating resistance

Experiments were also performed for enzyme loadings at multiple resistances. Previous experiments as well as the literature suggest that EIS responses are sensitive to the operating output of the fuel cell (Fan et al., 2007). As explained above, this effect was minimized by performing EIS at the maximum output of the fuel cell. The results from Fan et al. (2007) indicate that the overall impedance of a fuel cell decreased with increasing current density. This is reasonable if one considers that reactions occur more quickly at greater current. However, it was found in this work that minimum total resistance was sometimes achieved at the maximum power density, rather than greatest current. Such behavior is demonstrated in Figures 7.5a and 7.5b. Figure 7.5a qualitatively shows that the minimum resistance occurred at an external resistance setting

of 500 Ω since that Nyquist curve is the smallest. Nyquist curves at 750 Ω and 1000 Ω show increasing total resistance. Other low enzyme loading experiments showed maximum power densities occur at very high external resistance settings (up to 3500 Ω). While the two Nyquist curves in Figure 7.5b are similar, it can be seen that the 1000 Ω spectrum reached its first minimum at a lower impedance than the 750 Ω measurement (approximately 31 Ω compared to 45 Ω, respectively). Additionally, the second part of the 1000 Ω curve began to curve back toward the x-axis before that of the 750 Ω curve. This trend was consistent among repeated spectra. It is possible that enzyme/mediator degradation and water loss contributed to this occurrence; this is considered unlikely, however, since the measurements were all performed within a two-hour period. Such phenomena could be the result of minimized charge transfer resistances at the electrodes, as well as reduction of other losses throughout the EFC.

This brings up an interesting point in studying EIS results across a variety of operating conditions for fuel cells. Varying fuel cell conditions will certainly change the available outputs from a fuel cell. It is apparent in Figures 7.5 that the operating resistance plays a role in the total impedance and resistance of the system; this resistance affects the current and potential of the fuel cell. This makes sense, considering increased current (at low resistance) implies increased reaction rates at the electrodes and increased diffusion through the solution. Thus, resistances are minimized at high current density. Such findings, however, are not relevant to the goal of fuel cells. Power output is the primary aspect of fuel cell operation that will determine whether this technology can be useful for an application. As shown in this work, changing conditions can significantly

affect the output of a fuel cell, as high as an order of magnitude. At first glance, it makes sense to compare all EIS results for identical output, and this occurs in the fuel cell EIS literature. However, by ensuring that the current densities are consistent, one neglects the power output aspect of a fuel cell, and this is arguably the most pertinent consideration for a fuel cell (as is demonstrated by power densities most often being the reported output, rather than current or voltage). Thus, EIS measurements were performed at maximum power densities in this work. The reasoning behind such a decision is that the maximum power density is what characterizes a fuel cell as an improvement over a previous design, operating conditions, etc. Transport limitations at the maximum power density are, therefore, of primary interest.

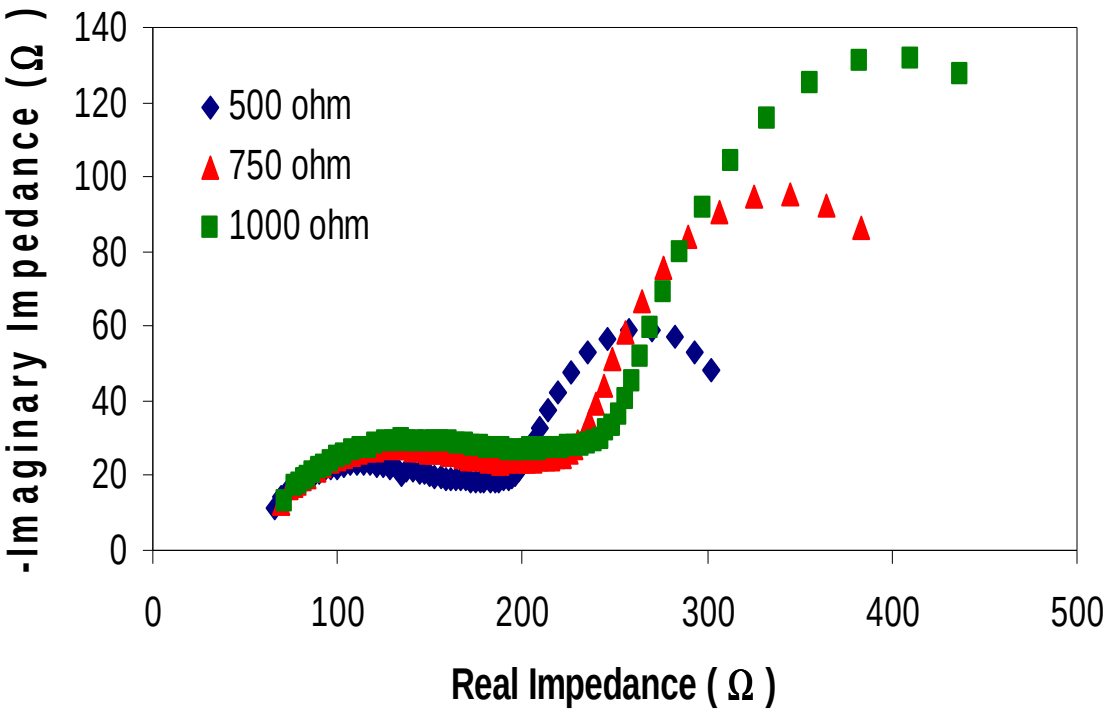

Figure 7.5a Nyquist plots for a 10 U laccase loading EFC at three different external resistances.

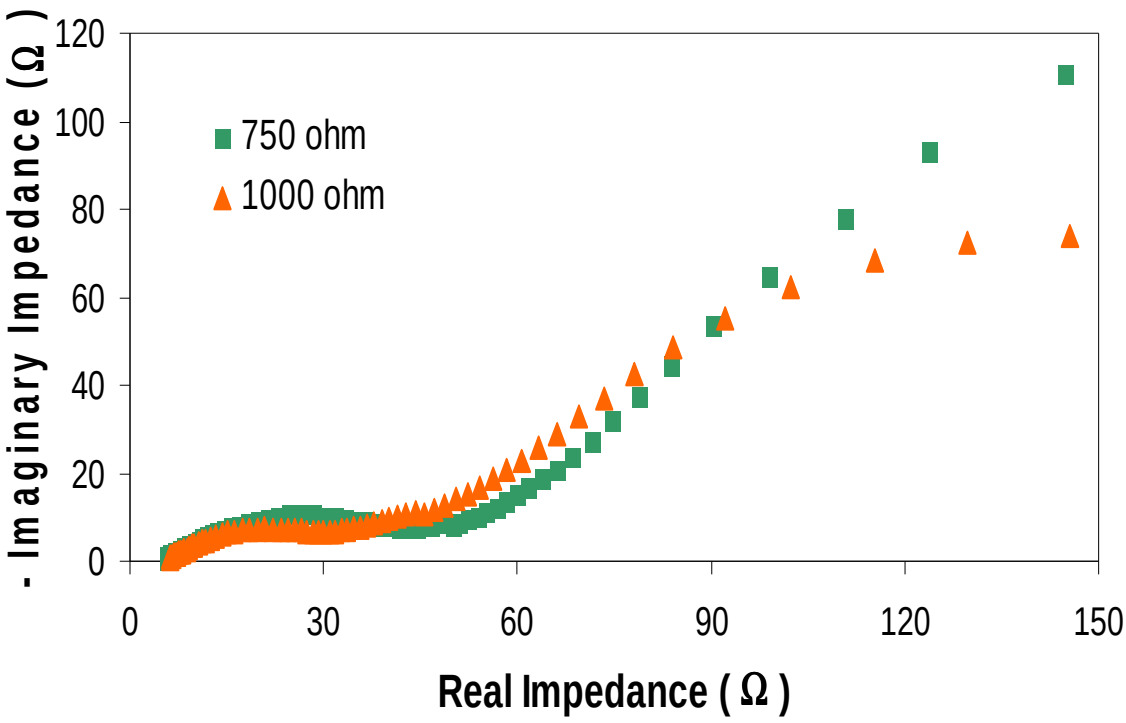

Figure 7.5b Nyquist plots for a 0.30 U laccase loading EFC at two different external resistances.

7.3.3 EFC behavior over time

EIS and power density measurements were performed on EFCs over a time span of approximately 24 hrs and 50 hrs. The EFCs had 10 U and 15 U loadings of laccase with initial enzyme solution volumes of 100 µL. Measurements performed over time are of considerable interest since current EFCs are limited by a relatively short lifetime of less than a day until the enzyme solution (enzyme, mediator, buffer and water) must be refreshed. It has been observed in this work and by others (Hudak et al., 2009) that water loss is a significant problem and has been observed even for supersatured air streams (see Chapter 8 of this work). Water content measurement in these experiments was monitored at the beginning and termination of experiments by weighing the carbon felt; it was consistently found that water loss occurred, even as high as 15% water loss in four hours.

Since water provides the medium for transporting protons from the anode to the cathode, as well as for ABTS to shuttle electrons from the electrodes to the laccase enzyme, loss of water is believed to have contributed to the loss of power output over time. EIS experiments performed by Hudak et el. (2009) observed that the solution resistance in EFCs increased over time, even for a humidified air stream to the cathode. However, humidification did significantly reduce the rate at which the solution resistance increased, indicating a reduction in water loss rate. In addition to water loss, the enzymes and mediator can also degrade over time. All three of these mechanisms contribute to the loss of power for an EFC over time. In general, it is assumed here that increased solution resistance is linked to water loss while all three mechanisms contribute to increased resistance at the electrodes (though enzyme and mediator degradation only occur at the cathode). Thus, if no change in solution resistance were observed, degradation of enzyme and mediator would likely be the primary cause of power loss.

Figure 7.6 shows trends in each individual resistance, as well as overall resistance for a 10 U EFC over 49 hours of operation. It can be seen that, over the course of the experiment, the cathode resistance increased substantially; the anode increased slightly and the solution resistance was relatively unchanged. These results suggest that water loss was primarily in the cathode (as opposed to the PEM or anode) and that enzyme or mediator degradation occurred, as well. In the absence of other methods to independently measure water content or enzyme/mediator degradation, EIS is able to provide information regarding which degradation mechanism is more likely to be causing loss of power.

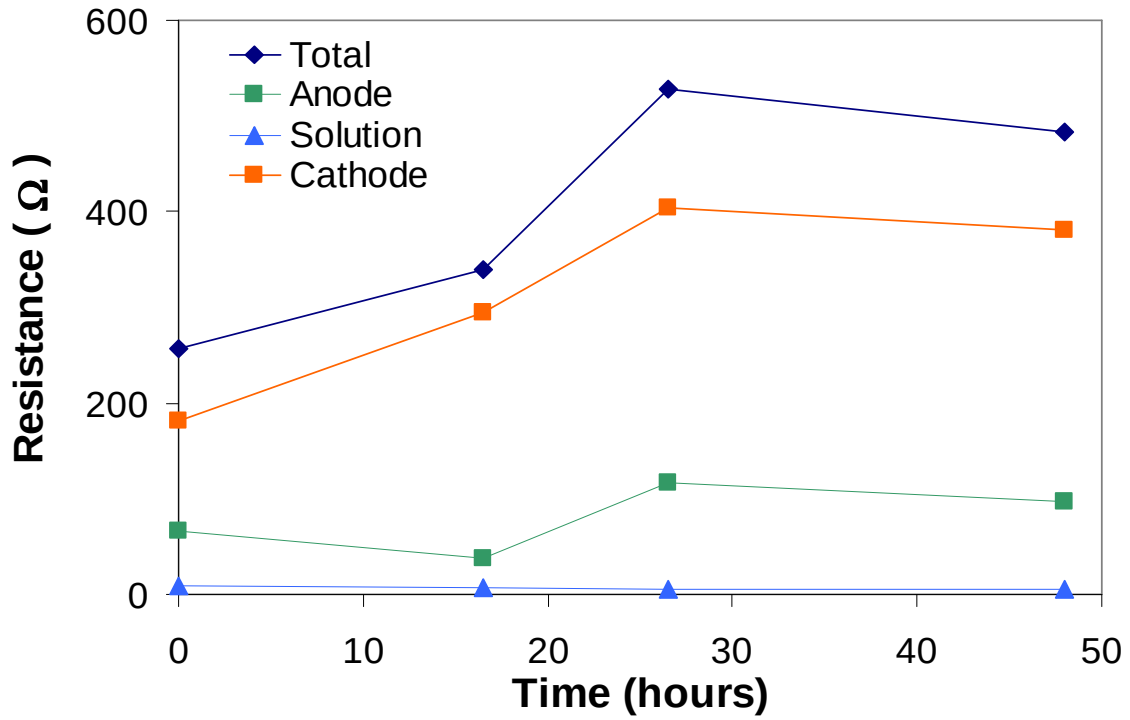

Figure 7.6. ECM results for a 10 U EFC operated for 49 hours at a constant load with fully humidified air and hydrogen streams.

Figure 7.7 shows power density and total resistance over time for the 10 U EFC described via ECM in Figure 7.6. It is apparent that the power density decreased significantly over the first 17 hours to approximately 33% of the initial power output, from 4800 mW/m^2 to 1740 mW/m^2. After 49 hours, power density was only 220 mW/m^2 and the total resistance had increased to 480 Ω. A local maximum in resistance occurred at 27 hours, but this behavior was not reproducible. As can be seen in Chapter 8, however, it is possible that a water droplet entered the cathode sometime after 27 hours. If this occurred, the water content in the cathode would have increased; such an increase in water content can lower the resistance in the EFC as indicated by Hudak et al. (2009). It is expected that drying did continuously occur in the cathode, but entrance of a water droplet would allow for lower total resistance, resulting in a local maximum as seen

below. While the results presented in this section can explain power loss in the EFC over time, it is still difficult to separate the contributions from water loss from those of enzyme and mediator decay.

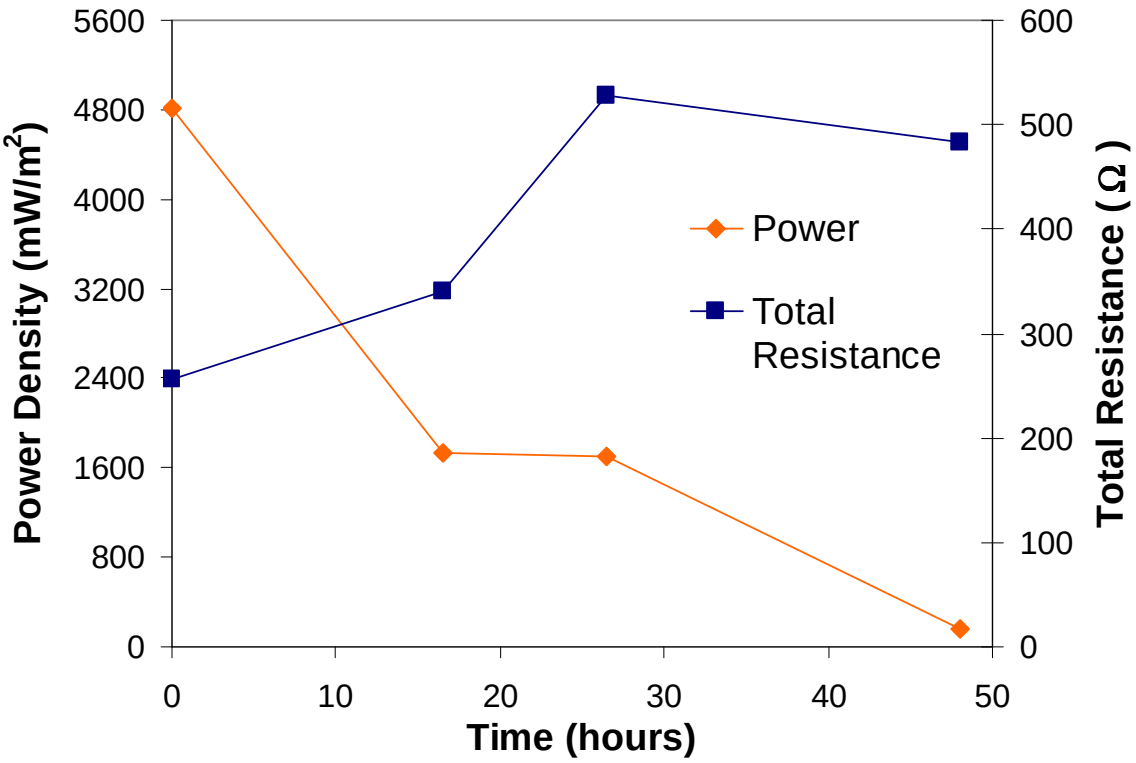

Figure 7.7. Power density and total resistance results for a 10 U EFC operated over 49 hours with a constant load and fully humidified air and hydrogen streams.

Another EFC was built and run overnight. Conditions for this EFC were 15 U enzyme loading, 10 sccm air and hydrogen flows, and saturation of both feed streams. The results from this build were interesting because the changes in total resistance and power density were much greater than that of the 10 U EFC reported above. It can be seen in Figure 7.8 that the total resistance increased from 45 Ω to 965 Ω after 22 hours, a 21-fold increase in resistance. For comparison, the total resistance for the 10 U EFC only increased by a factor of two. In addition, this 15 U EFC exhibited greatly increased anode resistance over the course of the experiment whereas the anode was relatively

stable in the 10 U EFC. As shown in Figure 7.8, the anode resistance increased from 2.6 Ω to 65 Ω over 22 hours. During this same period, the cathode resistance increased from 37 Ω to 865 Ω. The solution resistance for this run varied between 5 Ω and 10 Ω.

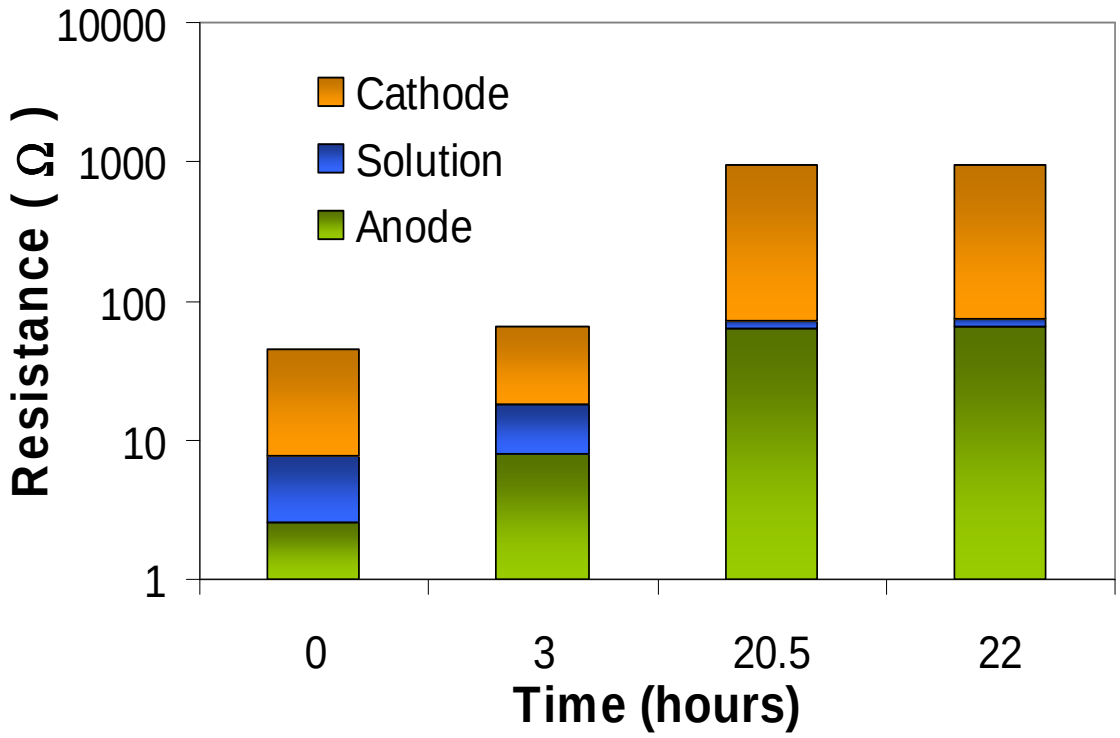

Figure 7.8. ECM results for 15 U EFC operated over 22 hours at a constant load.

Figure 7.9 shows total resistance and power density over the 22 hour experiment with the 15 U EFC. It can be seen that while the resistance increased by a factor of 21, the power density decreased from 6892 mW/m^2 to 1478 mW/m^2, a loss of 79% power output. It should be noted that internal resistance and power density do not always vary in a 1:1 inverse fashion, i.e. twice as much resistance does not result in half the power output. This is because the resistances here do not include all internal impedances, since

the impedance is comprised of resistances, capacitances, inductances and other phenomena. However, impedance and power output are inversely related.

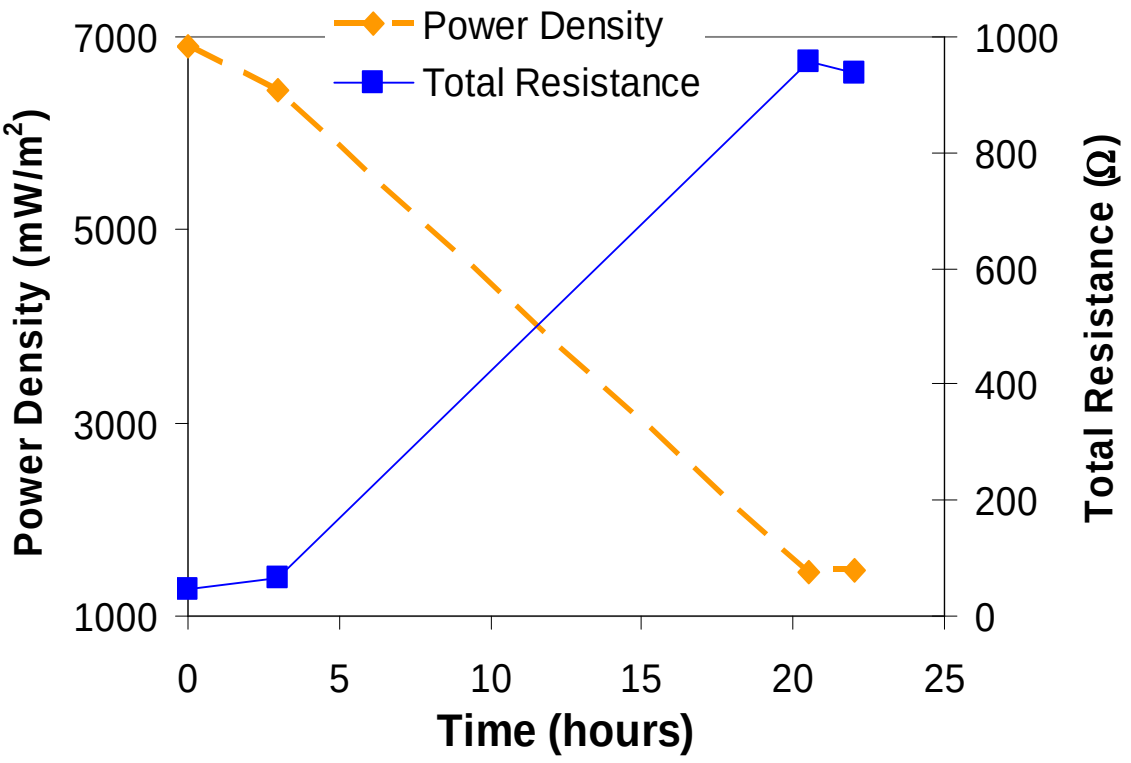

Figure 7.9. Power density and total resistance results for 15 U EFC operated for 22 hours at a constant load with fully humidified air and hydrogen streams.

It is expected that the changes observed in the EFC over time are due to a combination of drying, mediator loss, and enzyme loss. Water loss was measured ex-situ, but such measurements disrupt the EFC operation, making this method undesirable. Measurement of the enzyme and mediator activity at the end of an experiment would prove difficult, as well, since representative samples of the enzyme solution would be difficult to obtain. Since the method of enzyme solution distribution in the cathode carbon felt is not uniform, it is not expected that the drying behavior would be uniform, either. Thus, deposits of enzymes and mediator would be more concentrated in some

places of the carbon felt than in others. Of the three loss mechanisms, water content is the most easily measured ex-situ and is the only feature that can be measured in-situ, based on a current review of the literature. Water content can be measured by neutron imaging, a topic covered in the next chapter.

7.3.4 Effects of air humidification temperature

Water loss has bas been identified as a significant limitation on EFC longevity. One method to slow water loss is to humidify or supersaturate the air stream being fed to the cathode (Hudak et al., 2009). With greater water content in the air stream, the driving force for evaporation from the cathode should be reduced. Improved water retention should then result in more stable power output. Experiments were, therefore, performed at humidifier temperatures ranging from 25^{o}C to 50^{o}C. All other experimental parameters (enzyme loading, feed flow rates, etc) were maintained constant. Measurements were taken approximately 30 – 60 minutes after attaching feeds to the EFC to minimize the effects of degradation between runs.

Figure 7.10 shows ECM results for the 10 U enzyme loading EFC at varying air humidification temperatures. It can be seen that there is a consistent relationship between temperature and total resistance: the total resistance decreased from 51 Ω at 25^{o}C to 43 Ω at 50^{o}C. Little net change occurred in the anode while a slight increase in solution resistance was observed (from 4.10 Ω to 5.95 Ω as temperature increased from 25^{o}C to 50^{o}C). The increase in solution resistance was within the error boundaries, however, thus

it is unclear whether an inverse relationship would exist between humidification temperature and solution resistance.

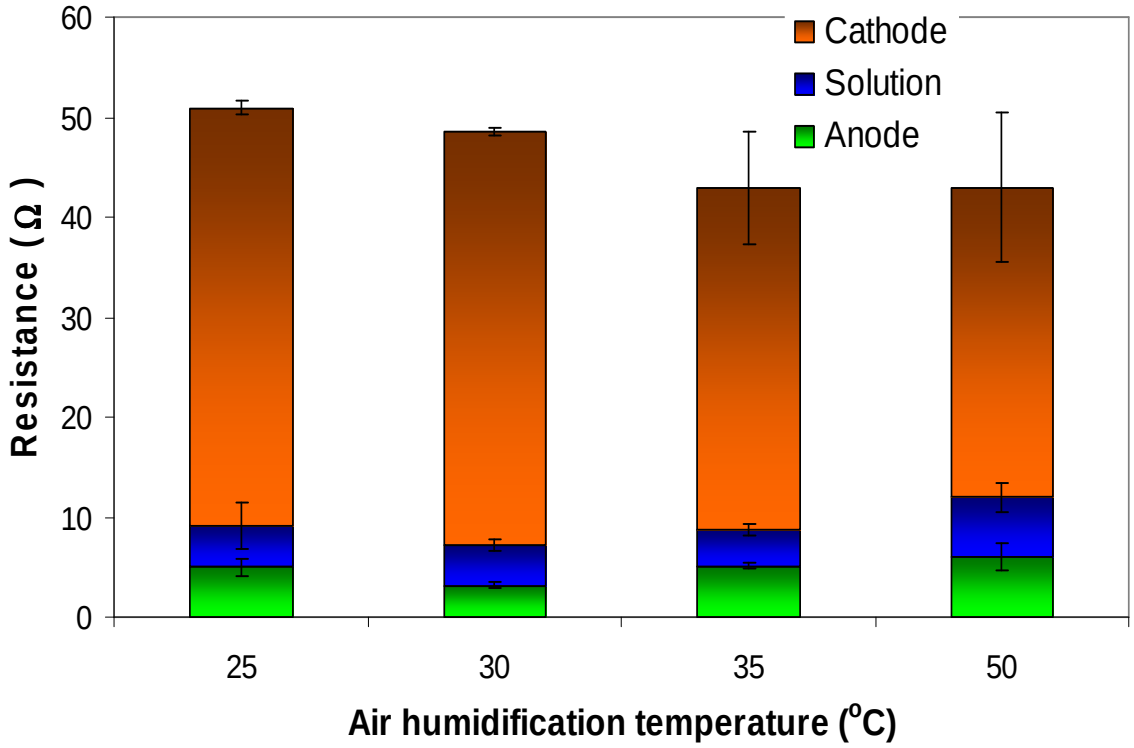

Figure 7.10. ECM analysis results for 10 U EFC at varying air humidification temperatures.

The power output for the EFCs built at the various temperatures did not exhibit a consistent trend, nor did it vary widely, thus power output was expected to have been minimally affected by the humidification temperature. Most catalytic processes occur more rapidly at elevated temperature, on account of more collisions per time between the substrates and catalysts. In this case, enzymes, oxygen, protons and mediators must come together to perform the ORR and form water. It is apparent that the air humidification temperature did not greatly affect power output or internal resistances.

However, the effect of air humidification temperature is expected to have a significant effect on EFC output stability and water retention in the cathode. This will be explored in more detail in Chapter 8, which focuses on neutron imaging of the EFC.

7.4 Conclusions

In this chapter multiple aspects of EFC construction and operation were studied via EIS. Of these conditions, enzyme loading, external resistance (and operating current), air humidification and over-time stability were of interest. It was found that enzyme loading had a very strong influence on both power density and on internal resistances. As enzyme loading increased, the rate at which the ORR proceeded was considered faster, contributing to a significant reduction in cathode resistance. The external resistance, as noted elsewhere, affected the EIS parameters studied in this work. Contrary to some other studies, however, it was found that maximum current density did not always coincide with minimum total internal resistance. Thus, it was decided that EIS would be performed at maximum power density since this is the most pertinent feature of a fuel cell. Air humidification was observed to not strongly affect the resistances or power output of the EFC; however, some reduction in internal resistance was observed as the humidification temperature was elevated. This reduction is attributed to more thermal energy in the cathode speeding up the catalytic reaction occurring in the cathode. Also studied was the EFC stability over time. It was found that significant power loss occurred over the first 16 hours of operation, though power loss was observed as quickly as four hours after connection to the feeds.

CHAPTER 8

IN-SITU NEUTRON IMAGING OF AN ENZYME FUEL CELL

8.1 Introduction

Enzyme fuel cells (EFCs) have emerged as a potentially promising alternative to the more expensive Pt-based polymer electrolyte membrane fuel cells (PEMFCs). EFCs employ biologically-derived enzymes to catalyze the electrode reactions in a fuel cell, replacing precious-metal catalysts as part of an effort to reduce the cost of fuel cells. These fuel cells benefit from being very similar to traditional PEMFCs that run on hydrogen by operating on very similar principles and design (Atanassov et al., 2007). The enzyme laccase from the fungus *trametes versicolor* has been utilized in a three-dimensional cathode design by Borole et al. (2009a) to catalyze the reduction of oxygen to water and provide a relatively high power density. The three-dimensional design facilitates oxygen transport to the cathode and, specifically, the laccase enzyme in solution. As with PEMFCs, water management is a critical issue in EFC operation to ensure optimal power production and longevity. Water serves to provide the medium for proton diffusion from the anode, through the PEM, and into the cathode (Liu et al, 2008). For a mediated-electron-transfer EFC, water also serves to provide a medium for shuttling electrons between the aqueous catalyst and the electrode (Minteer et al., 2007). Hudak et al (2009) observed that long-term EFC activity was unstable due, in part, to water loss in the cathode. Because a proper water balance is critical to EFC operation, a technique to measure the water loss rate in-situ during EFC operation is very desirable.

Neutron imaging has been recently employed to successfully monitor the water content in PEMFCs (in this work and elsewhere). This technique is investigated here for the first time for in-situ measurements of water content and evolution in an operating EFC at varying operating conditions. Efforts are also made to reduce water loss rates and the results are evaluated via neutron imaging.

8.2 Materials and methods

8.2.1 EFC design

Initial experiments were performed at the Oak Ridge National Laboratory to study the power density behavior at a variety of operating conditions. A three-dimensional cathode EFC was constructed with materials that exhibited low neutron attenuation. Teflon endplates (Professional Plastics) were cut to 5 cm × 5 cm to serve as endplates. The cathode compartment was made of Teflon, as well, with a thickness of 0.430 cm and an open internal area of 0.18 cm × 0.13 cm. The anode compartment was 0.075-cm thick Teflon with the same open area as the cathode. This material was used due to its low neutron cross section, as well as ease of handling and shaping. Graphite electrodes were used as current collectors in both the anode and cathode; gold was not used due to its activation in the presence of neutrons.

The anode was an electrode made of carbon cloth impregnated with platinum particles (Fuel Cell Store, Inc.) with an area of 1 cm^2. A loose-weave carbon cloth of the same area as the anode served as a gas diffusion layer and spacer for the anode. The cathode was carbon felt (Alfa Aesar) cut to 1 cm^2 with a thickness of 0.635 cm. The

porosity for this carbon felt was 83% and was made hydrophilic via a 5-minute plasma treatment (Harrick Plasma Company, PDC-32G). The polymer electrolyte membrane (PEM) used was Nafion 115. The cathode solution was composed of enzyme, buffer, and mediator in water. The enzyme was laccase from *Trametes versicolor* with a specific activity of 21.7 units/mg (Sigma, St. Louis, MO). The buffer was citrate at pH 4, and the mediator was 2,2'-azinobis(3-ethylbenzothiazoline-6-sulfonate) (ABTS). Previous experiments performed by Borole et al. (2009a) established that an optimal volume of cathode solution for a similar-geometry EFC was 100 μL, with a 100:1 molar ratio of ABTS:laccase. Figure 7.1 is a schematic of the EFC used in these experiments and is shown again here for convenience.

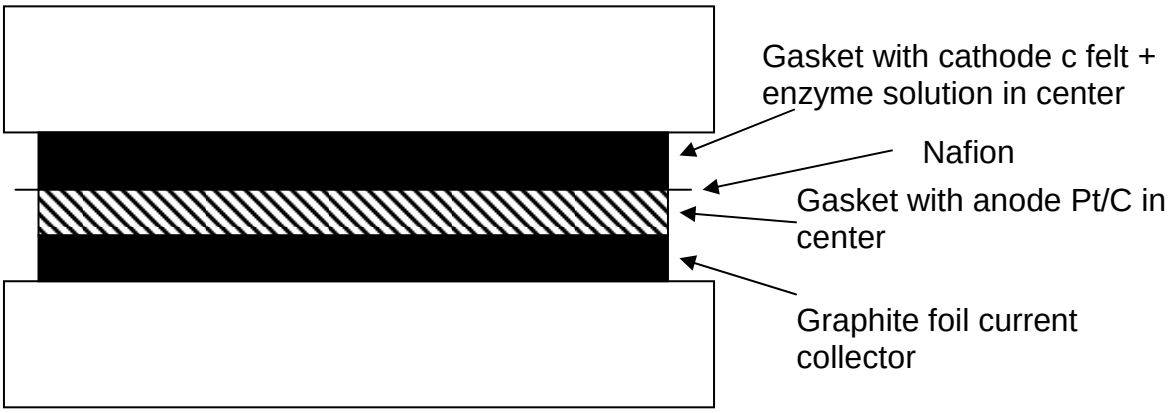

Figure 7.1. Schematic of EFC used for imaging experiments. Only the enzyme solution was a strong neutron attenuator in this setup.

8.2.2 Ex-situ measurement of water content

Previous measurements of water content required dismantling the EFC to measure the mass of the carbon felt and remaining enzyme solution. Thus, water content measurements were only performed at the end of an experiment and calculated via the mass balance shown in Equation 8.1.

$$Loss_{water} = \left(Mass_{CFInitial} + Volume_{SolutionInitial}\right) - Mass_{CFFinal} \quad (8.1)$$

This mass balance assumes that 1 mL of water equals 1 g (reasonable at ambient conditions). The final mass of the carbon felt was a composite of the carbon felt and the remaining enzyme solution. Thus, by dismantling the EFC at the end of an experiment and weighing the wet carbon felt, the mass of water lost due to evaporation could be approximated. However, this method provided no information on the transient water loss profile. In addition, any migration of water from the cathode to the anode could not be verified. With such complications, neutron imaging was identified as an ideal tool to perform in-situ measurements of the water content profile.

8.2.3 Neutron imaging and EFC control

Neutron imaging studies were conducted at the National Institute of Standards and Technology (NIST) Neutron Imaging Facility (NIF), which includes a full suite of equipment for fuel cell operation, control, and analysis, and is integrated with the beam for neutron imaging. A fuel cell test stand was employed to control all operational parameters, including feed flow, feed humidity, and feed composition. The load was controlled via a variable 2-kΩ resistor since the current developed by the 1 cm^2 EFC was too small for the test stand controller. Because the Teflon endplates of the EFC did not allow for good temperature control of the EFC, all experiments were performed at room temperature (approximately 24 ^oC). Supersaturated humidity conditions (i.e., relative humidity above 100%) were achieved by raising the temperatures of the humidifying

bottles above cell temperature. The lines between the humidifiers and EFC were also heated by 5 °C to mitigate condensation in the feed lines. Power density measurements were performed after the EFC achieved steady state output, roughly one hour after enzyme solution injection and initiation of feed flows. The beam had a post-filter fluence rate of approximately 5.1×10^7 neutrons $cm^{-1} s^{-1}$. The detector used in this work was a cross-delay line detector with a 25-μm resolution. Each image had an exposure time of five minutes.

8.2.4 Dry images

It must be noted that "dry images" were taken prior to each experiment to provide the basis for water content measurement. Images of the EFC were taken after flowing dry nitrogen gas through the EFC and prior to injection of the cathode enzyme solution. This was expected to result in a dried-out EFC after a sufficient period of time, with no water present. By this reasoning, any change in neutron attenuation during operation, compared to the dry images, would be due to the presence of water. Calculation of the water content was done by simply subtracting the dry-image neutron intensity from the wet-image neutron intensity and assigning the difference to neutron attenuation by water.

The fuel cell was placed edge-on in the beam, such that the image projected onto the detector was a side view of the EFC (see orientation in Figure 7.1 in previous Chapter). Table 8.1 shows the operating conditions explored in this study. The first experiment utilized low enzyme concentration, low initial liquid volume conditions, oxygen for the cathode, and 105% relative humidity (%RH). It should be noted here that

the %RH reported throughout the manuscript is with respect to the room temperature. The second experiment had greater enzyme concentration, a greater initial liquid volume, and supersaturated air (190% RH) at a lower flow rate. The third experiment had conditions similar to the second, but the air was at 247% RH and the enzyme solution had a greater concentration of citrate buffer.

Table 8.1. Experimental conditions for imaging experiments at NIST.

Experiment	Enzyme loading (units/cm^2)	Initial volume (µL)	Feed flow (sccm)	Cathode feed	Cathode humidity (%RH)	Power density (W/m^2)
1	1	50	50	O_2	105	0.128
2	10	100	10	Air	190	3.49
3	10	100	10	Air	247	4.01

8.3 Results

8.3.1 Interpretation of initial image results

Figure 8.1 is a comparison of an unmodified dry image (left) and unmodified operating image of the wet EFC (right). Qualitatively it can be seen that very little water was in evidence in the dry image, especially in the cathode. This was indicated by the bright white color. Following injection of the enzyme solution, a large, dark area was evident in the cathode region. This indicated that neutron imaging detected the presence of the enzyme solution. Such qualitative visual observations were performed in real time during the experiments to monitor the approximate water content in the cathode. Calculations were performed afterwards to determine the quantitative water content in the cathode region (described below). It was also observed via these images that the graphite current collectors gradually absorbed water over time. This is apparent in the images in

Figure 8.1 since the dark stripe on the left of the cathode was darker in the right image than in the left image, indicating increased water content.

Water loss was observed in all experiments that were performed at NIST and at ORNL. Figure 8.2 is an illustration of the water loss in a colorized format. These images are from the first experiment: 1 unit of enzyme loading (U/cm^2), 50 μL initial volume, 50 sccm oxygen flow rate, and 105%RH for the O_2 stream. The white box illustrates the "region of interest" used to calculate cathode water content. It is apparent that the PEM maintained a high water content, despite drying of the cathode. In addition, a slow uptake of water by the graphite current collector is also evident. A dry image was taken for 30 minutes (to provide a well-developed image) prior to injecting solution for each experiment; this image was subtracted from all "wet" images to yield a change in water content. For all water content results below, the water content was calculated only for the carbon felt region of the cathode (white box in Figure 8.2). Water content in the PEM, anode, and current collectors was excluded. In all plots of water content over time, the uncertainty associated with each measurement never exceeded 0.34 μL, thus uncertainties are not readily visible in the plots.

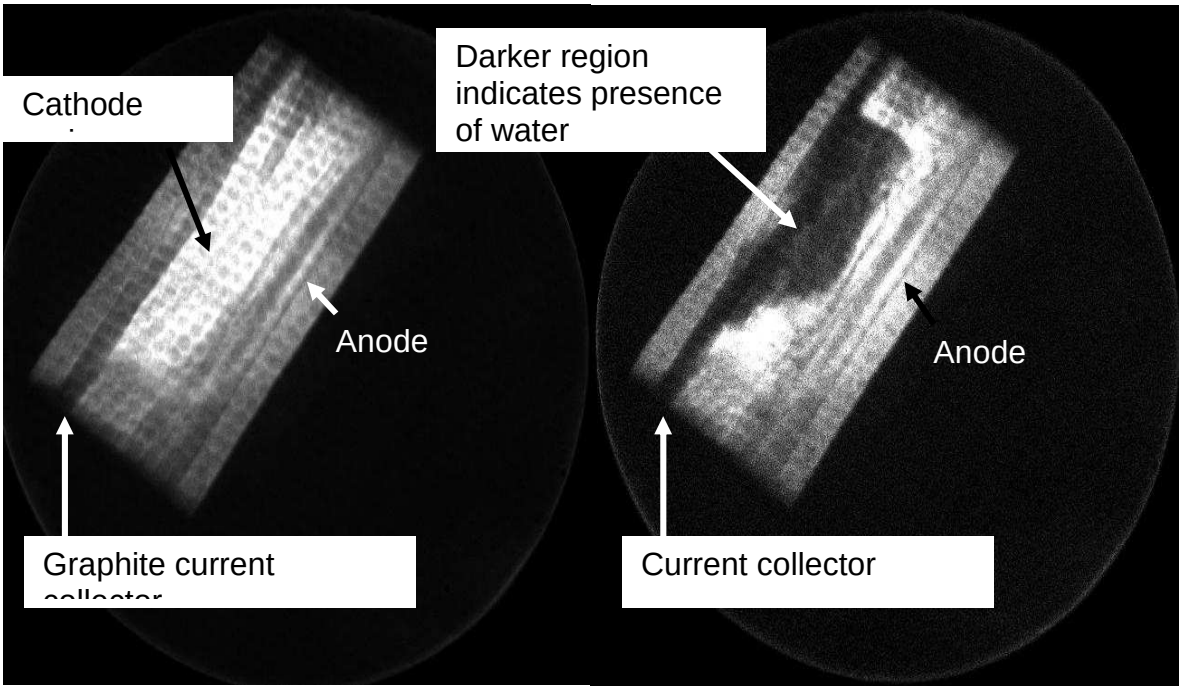

Figure 8.1. Comparison of dry (left) and wet, operating (right) images of the EFC. The dark area present in the cathode signified the presence of the enzyme solution.

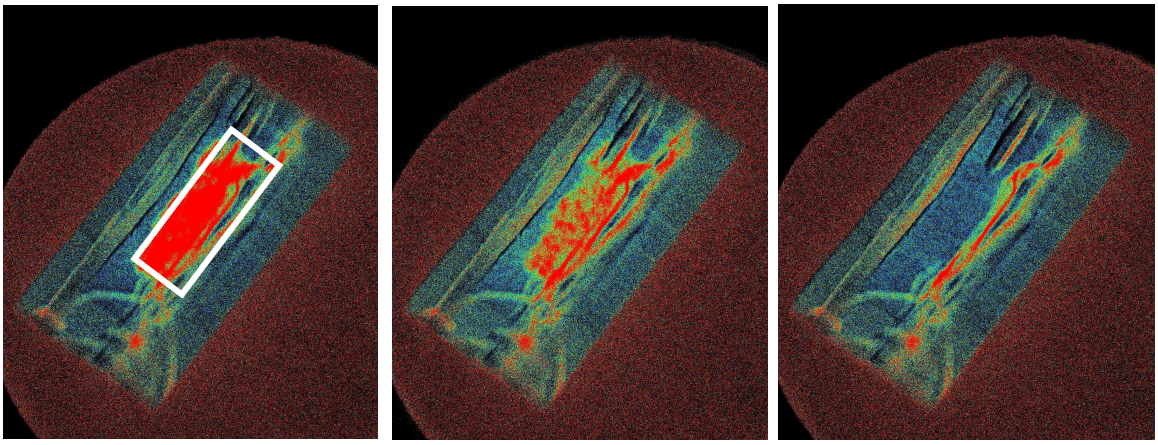

Figure 8.2. Neutron images of the operating EFC. The red region in the first image (5 min) indicates the presence of water; this region thinned out and disappeared entirely by the end of the experiment (545 minutes).

8.3.2 Effects of feed flow rate, feed humidity, enzyme loading and salt concentration

Figure 8.3 shows cathode water content over nine hours of imaging for the 1 U/cm^2, 50-μL initial enzyme-solution volume experiment. The maximum power output during this time was 0.128 W/m^2. A linear fit of the water content profile indicates a water loss rate of 0.051 μL/min. Figure 8.4 shows a similar water content profile for the second experiment, which utilized 10 U/cm^2 enzyme loading, 100 μL initial enzyme-solution volume, 10 sccm air and 190% RH. Linear fits of the two series of images taken during this six-hour period indicate a water loss rate of 0.010 μL/min, representing a five-fold decrease compared to the first experiment. This water loss rate was consistent for the two series of images taken, the second a repeat of the first. The maximum power output during this experiment was 3.49 W/m^2, twenty-seven times greater than that of the first experiment.

Figure 8.5a shows the water content for the final experiment with 10 U/cm^2 enzyme loading, 100 μL initial enzyme solution volume, 10 sscm air and 247% RH. In addition, this experiment utilized the high salt enzyme solution. Over the eight hours of imaging for this experiment, the water loss rate was calculated at 0.005 μL/min, half that of experiment two and one tenth of that of the first experiment. A water droplet had entered the cathode just prior to the 200 minute mark; this droplet is why the original water volume appears to be near 140 μL. Before- and after-droplet images of the EFC are shown as insets in Figure 8.5a. While the entire region of water in the cathode is darker, the blue circles also indicate a region that was wetted by the droplet formation (this region had been relatively dry prior to the droplet condensation). It should be noted

here that, even with a high relative humidity, only once did a water droplet condense in the air line and enter the cathode of the fuel cell. The result was a sudden jump in the water content that was captured by neutron imaging as shown in Figure 8.5a. Figure 8.5b shows the voltage that was measured during the same experiment; also shown is the water content shown in Figure 8.5a. The droplet that entered the cathode corresponding to a large increase in voltage output for the EFC, suggesting that the water loss observed prior to the droplet corresponded to the voltage loss. The maximum power density during this experiment was 4.01 W/m^2, 15% greater than in experiment two and thirty-one times greater than in experiment one.

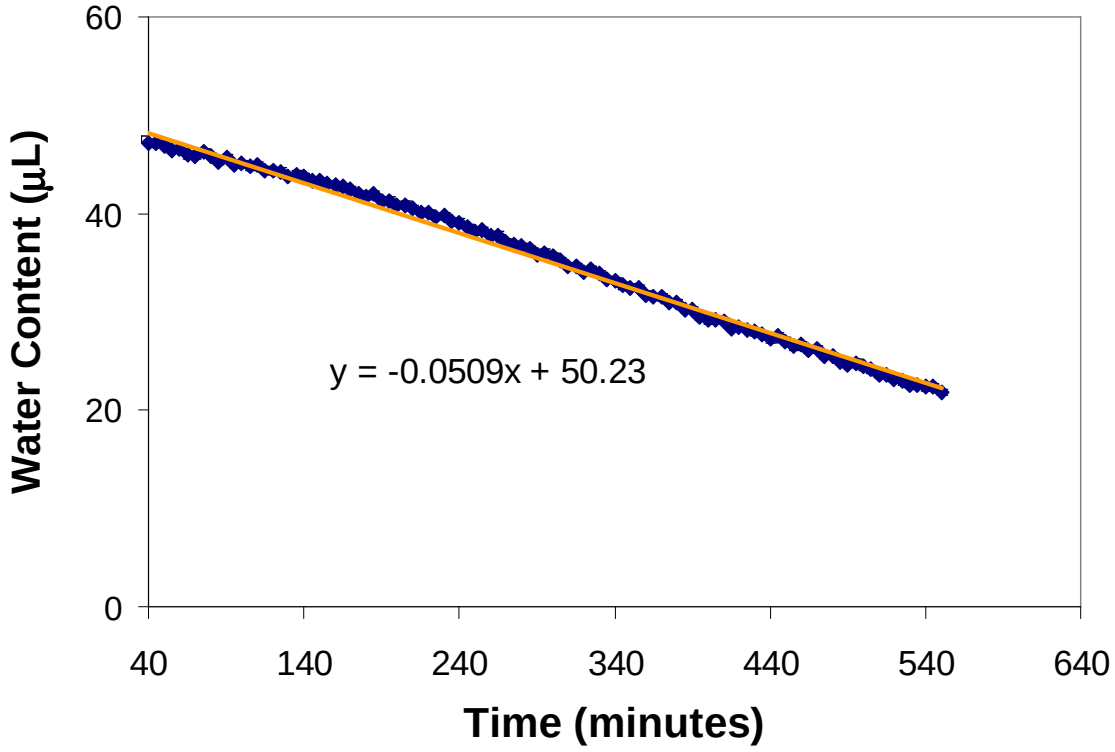

Figure 8.3. Time profile of the EFC-cathode water content. The power output was 0.128 W/m^2; 50 µL enzyme solution initial; 1 U/cm^2 enzyme concentration; 50 sccm oxygen; 105% RH for both feeds. Uncertainty values of 0.32 µL are reported (but not visible) for each data point.

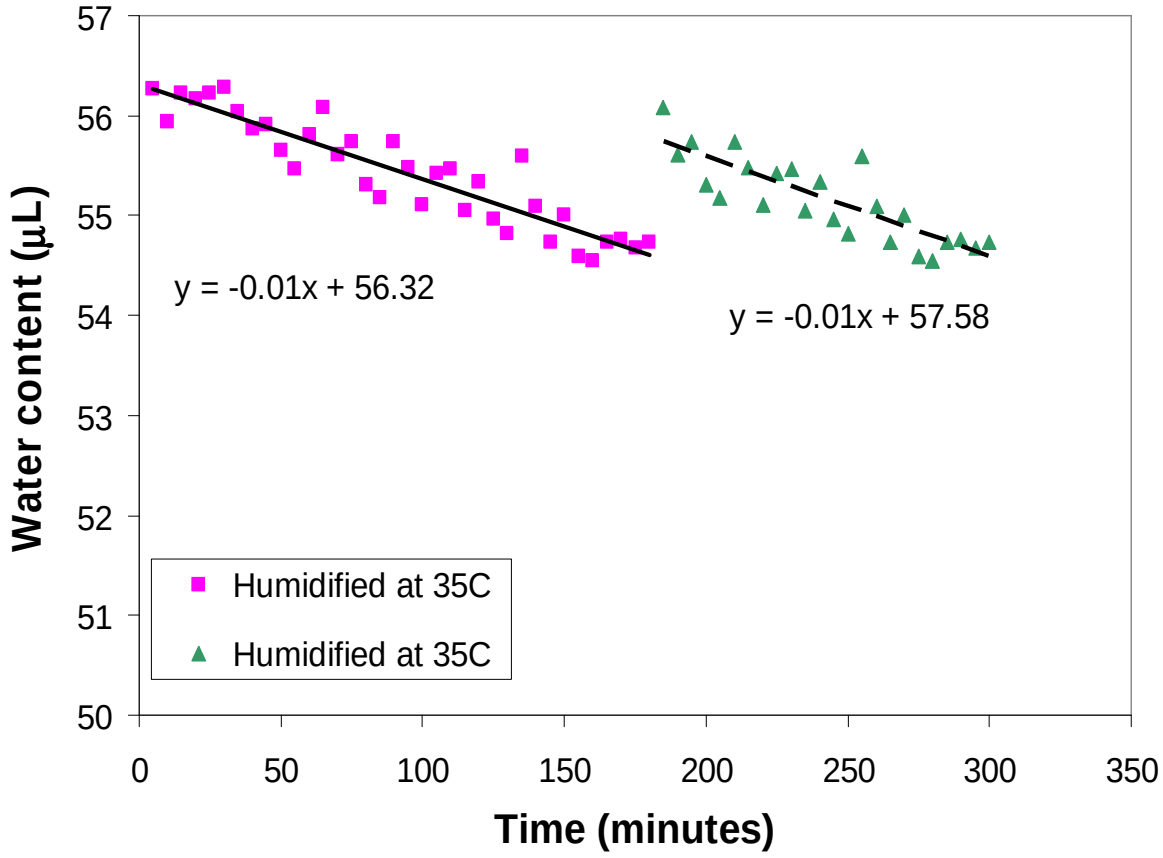

Figure 8.4. Water content over time for supersaturated air condition (190% RH). Enzyme loading was 10 U/cm^2, flow rates were 10 sccm for both H_2 and air. The second line represents a duplicate run performed after three hours of operation.

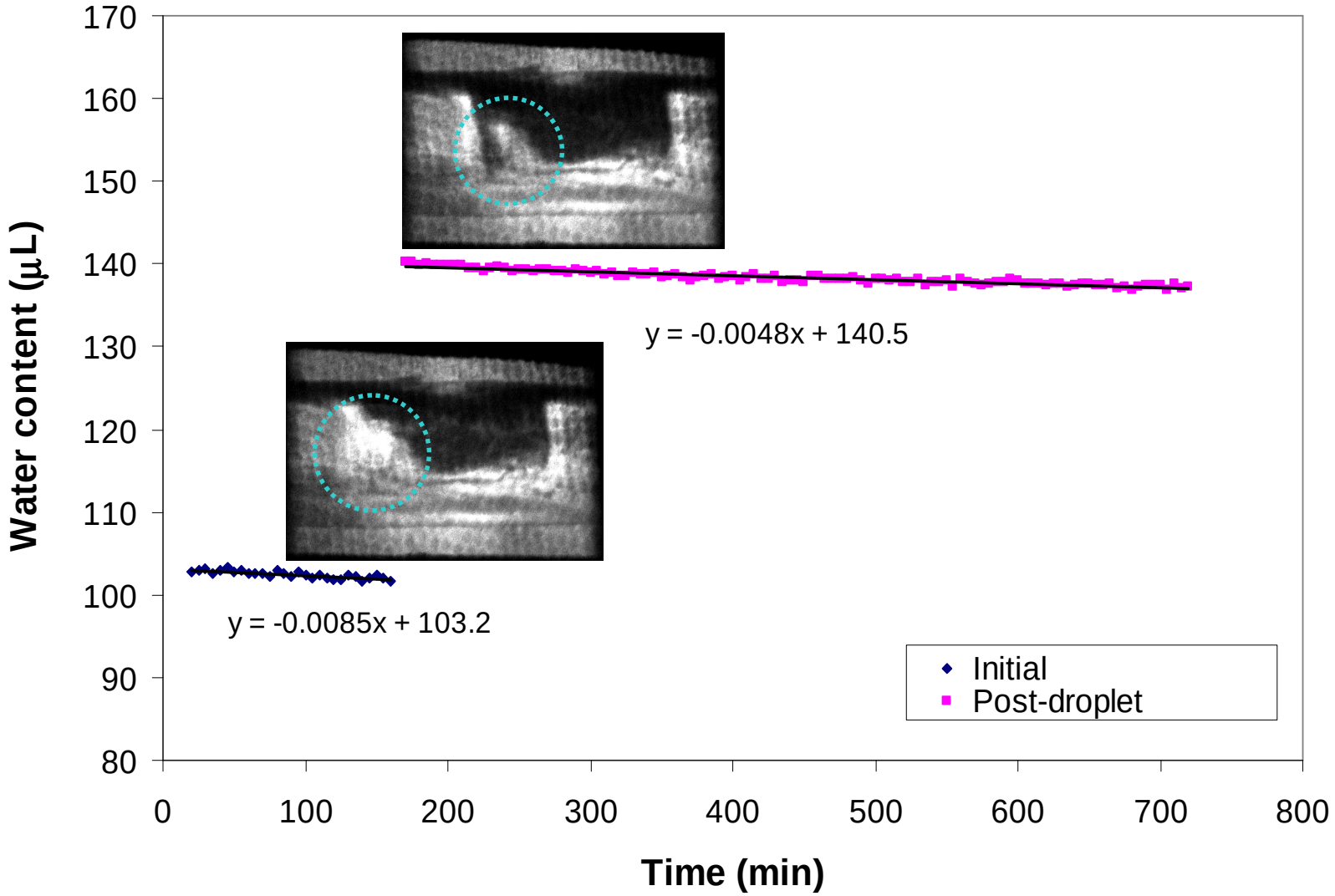

Figure 8.5a. Water content profile over time for experiment 3 with supersaturated air humidity (247%), 10 U/cm^2 enzyme loading, 100 µL enzyme solution volume and increased salt concentration. Inset photographs show a water droplet that was condensed in the cathode input line entrained in the cathode. This event that happened only once was revealed by neutron imaging pictures taken before (160 minutes, bottom picture) and after (165 minutes, top picture) it occurred.

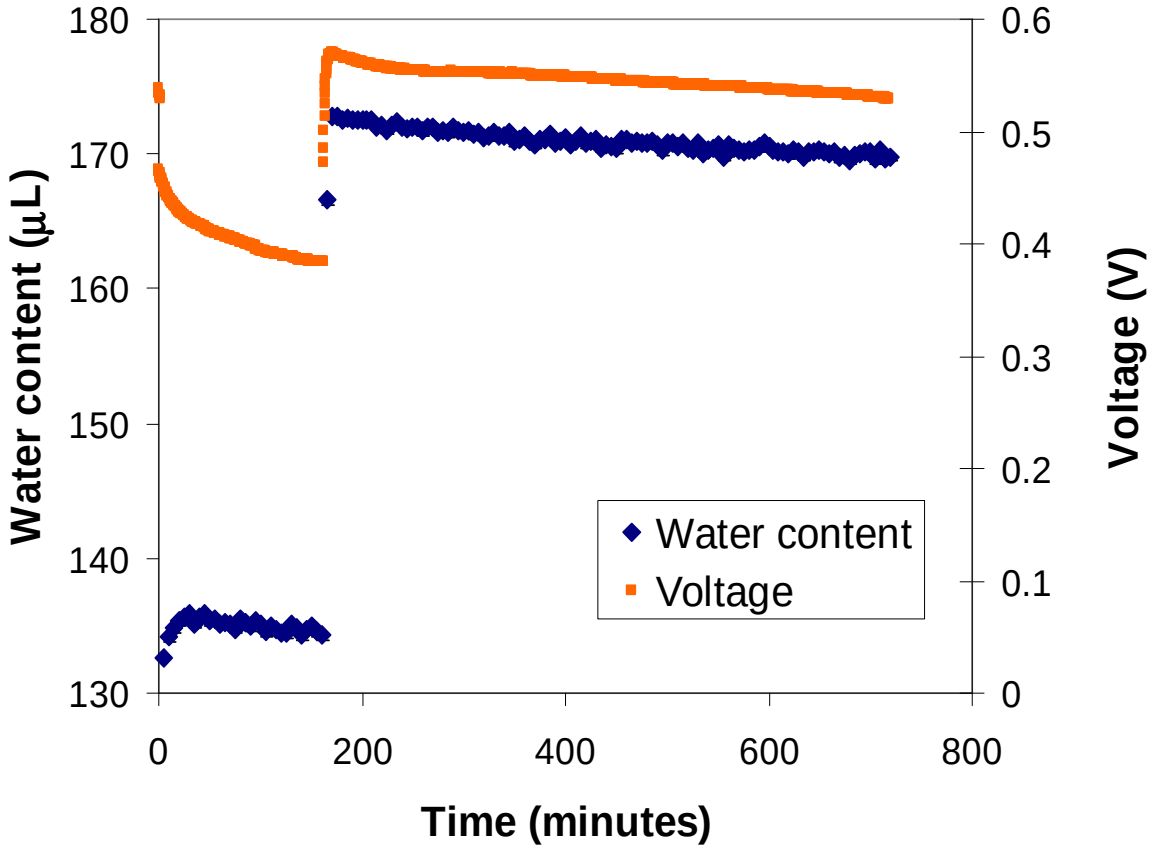

Figure 8.5b. Voltage of the EFC over time for high salt concentration experiment. It is apparent that a large increase in voltage occurred following the droplet entering the cathode.

Two things are noted in Figure 8.5b. First, the increased voltage following the entrance of the droplet suggests that enzyme or mediator utilization improved substantially. Possible explanations include re-dissolution of enzyme or mediator that had been left on dry carbon felt. This explanation is plausible because prior experiments dealing with increased enzyme concentration yielded increased voltage or power. Borole et al. (2009a) also demonstrated that the output of the EFC was not as sensitive to mediator concentration as it was enzyme concentration. In addition, connection of

another water pathway from the PEM to isolated enzyme solution is possible. This would provide another opportunity for protons to come into contact with the enzyme, increasing enzyme utilization or reducing solution resistance. Another feature to note is that the water loss rate was lower by nearly 50% after the droplet entered than before. Such an occurrence could be due to improved stability (i.e. reduced evaporation) of the new water network in the cathode. Increased stability could be achieved if the flow pattern of air through the cathode changed to induce less evaporation (which simultaneously providing more oxygen to the enzymes).

8.4 Discussion

The reduction in water loss rate observed for experiment 2 compared to experiment 1 is likely due to a combination of nearly all operating conditions being optimized for better output and water retention. The air humidity was much higher, the current and power were much greater (resulting in more product water), and the air flow rate was lower. Switching from O_2 to air, and reducing the flow rate, was not expected to have had any adverse effect on the power output, as these parameters were above the minimum values established by Borole et al. (2009a). The reduction in water loss from experiment 2 to experiment 3 is attributed to increased humidity as well as increased salt concentration in the cathode solution. Such an increase in solute concentration would lower the vapor pressure of the cathode solution, inhibiting evaporation.

It is apparent that the initial water content for both runs in Figure 8.4 was approximately 56 μL, rather than the injected 100 μL. This discrepancy is primarily due

to the dry image that was taken as a basis for the series of images used for Figure 8.4. The EFC still had approximately 33 μL of residual water in it for the dry image used in this series, as seen in Figure 8.6. Figure 8.6 shows that the "dry" images taken for experiments two and three reveal some residual water in the cathode; thus, subtraction of the "dry" images from the operating images didn't exactly result in true water content. The remaining 11 μL of water that should have been measured in experiment two is likely due to a droplet of enzyme solution not being in the region of interest used to calculate water content. This region of interest was not changed, however, because inclusion of the membrane and/or cathode current collector would occur.

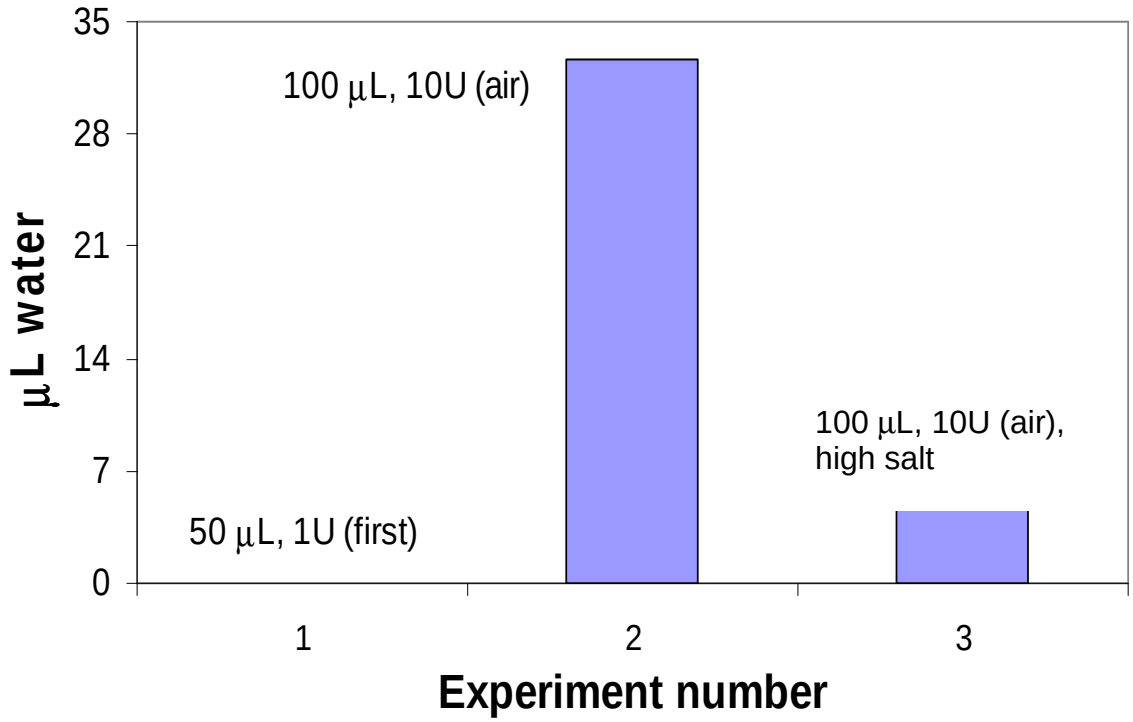

Figure 8.6. Comparison of dry images showing that complete drying was not achieved for either experiment following experiment 1. This explains why initial water volumes for experiments 2 and 3 were not at the expected values (100 μL).

Mechanisms that affect water evaporation rate include relative humidity and flow rate of the cathode stream. The effects of relative humidity and cathode flow rate were observed in this work. As expected, increasing the cathode-stream humidity greatly reduced (by a factor of 10) the water loss rate. However, it is still troubling that water loss was observed for an air stream that was believed to be supersaturated with water as high as 247% RH. Thus, further experiments should be performed that will explore the relationship between water loss rate, air humidity and flow rate in greater detail. Increased salt buffer concentration was also observed to have potentially contributed to a reduced water loss rate (by a factor of two). The salt, in addition to buffering the cathode solution at pH 4, likely contributed to retaining water in the cathode by reducing the vapor pressure of the cathode solution. It is possible that the 5 ^{o}C increased temperature of the gas feed lines, described in the section "*Neutron imaging and EFC control*" of Materials and Methods, contributed to the gas not being saturated while fed into the cathode compartment. Despite the EFC being at room temperature, if not enough cooling of the gas occurred upon entering the cathode, it is possible that evaporation from the cathode water layer into unsaturated air could occur. However, cathode drying was also observed in lines that were not heated above the temperature of the saturation bottles, which implies water loss into a saturated air stream.

Another phenomenon that has been hypothesized to contribute to water loss in the presence of >100% RH air is increased local temperature as a result of the proton-oxygen-electron water formation reaction that releases heat. Many PEMFC models consider the splitting of hydrogen in the anode to be isothermic while the cathode

reaction (production of water from protons, electrons, and oxygen) is exothermic resulting in a net exothermic reaction (Wu et al., 2007). However, electrothermodynamic modeling of a PEMFC performed by Rasmousse et al. (2009) suggests the anode reaction could be highly exothermic, while the cathode reaction is slightly endothermic. These studies indicate that a comprehensive understanding of PEMFC heat sources and sinks is still under debate. However, it can be concluded that, due to electrochemical reactions, overall heat production occurs in a PEMFC system. Since the EFC is analogous to the PEMFC design, such an explanation could prove true here, as well. It should be noted that the above thermodynamic modeling studies focused on Pt-based catalysis in a PEMFC; similar studies involving enzyme-based catalysis in an EFC can provide insight on the magnitude of heating or cooling that occurs in an EFC cathode.

Assuming an overall exothermic reaction system, calculations have been performed to determine the local temperature in the EFC cathode that would cause the loss of water from the cathode via evaporation. This is of interest because elevated local temperature could cause evaporation of water despite a saturated, bulk stream of air, resulting in the observed water loss. Figure 8.7 is a schematic that illustrates the system that was used as the basis for the mass and energy balances considered here. A mass balance was performed for the cathode, where the mass flow of water exiting the cathode compartment was the sum of water vapor entering the cathode, water production via the cathode reaction, and water evaporating from the cathode liquid. A net loss of water from the cathode was considered since neutron imaging experiments showed water loss

from the cathode. This mass balance is described in Equation 8.1. Equation 8.2 shows how the rate of water production was calculated from the EFC current.

$$H_2O_{out} = H_2O_{in} + H_2O_{Lost} \tag{8.1}$$

$$H_2O_{\mathrm{Pr}oduced} = \frac{I}{F} \times \frac{1molH_2O}{2mole^-} \times \frac{18g}{molH_2O} \tag{8.2}$$

In Equation 8.2, *I* is the EFC current measured in Amperes (or C/s) and F is the Faraday constant (mol e^-/C). Since the anode stream was saturated as well, we assumed that the amount of water diffused to or from the anode through the Nafion membrane was insignificant. This assumption was supported by neutron imaging results which showed no appreciable change in anode water content. The entering water flow rate was known since the inlet conditions were experimentally controlled. Water production via the cathode reaction was calculated based on the current at maximum power density (i.e., the condition for which imaging was performed). This calculation was based on the relationship described in equation 8.2; for each two moles of electrons that reach the cathode, one mole of water was formed. These moles of water were converted to a mass flow to coincide with the other water streams considered in these calculations. Finally, water evaporation from the cathode was determined via the slopes calculated in Figures 8.3, 8.4, and 8.5. Addition of these three water streams (feed, product, and evaporation) composed the exit water stream. This stream of water was converted to absolute humidity. Assuming saturated conditions, the exit temperature of the gas stream was determined based on work performed by Lowe and Ficke (Lowe and Ficke, 1974). Table

8.2 includes results from the mass balance analysis described here. Note that the experiment with T = 24.5°C was performed with 100 sccm flow rate while the experiments at 35°C and 40°C were performed at 10 sccm flow rate. In addition, the first experiment was conducted with oxygen fed to the cathode while the second and third experiments utilized air.

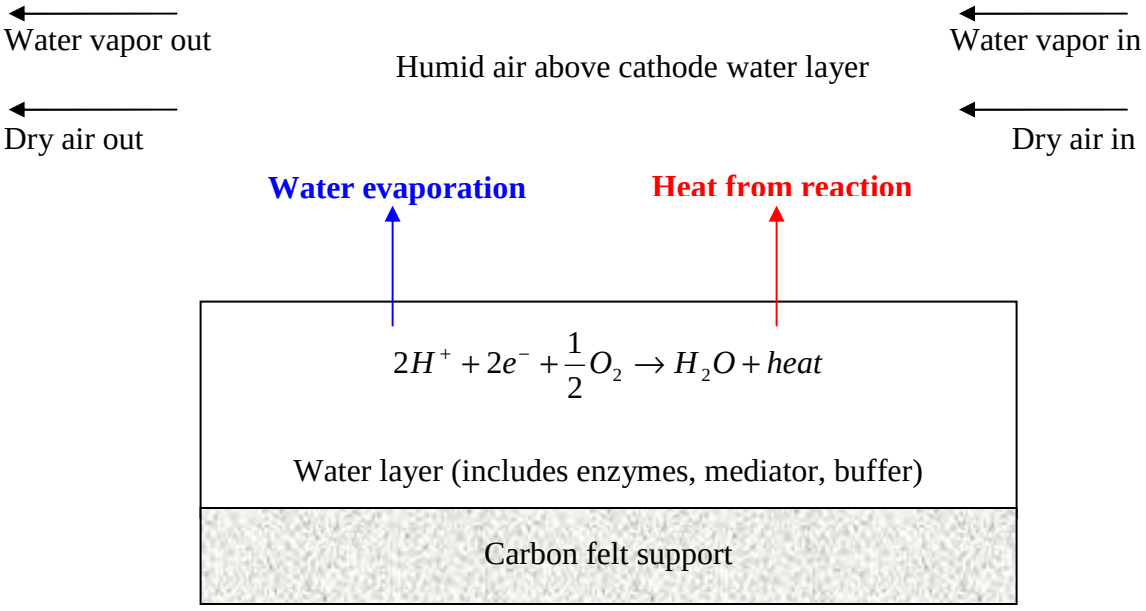

Figure 8.7. Schematic of cathode region for mass and heat balances. Steady state is assumed.

Table 8.2. Mass balance analysis with calculation of local, exit temperature.

T (°C)	Fed water (µL/min)	Product water (µL/min)	Cathode water loss (µL/min)	Evap. water (µL/min)	Exiting water (µL/min)	T exit (°C)
24.5*	2.26	8.96E-04	0.051	0.052	2.31	24.9
35**	0.398	3.16E-03	0.010	0.013	0.408	35.5
40**	0.525	3.86E-03	0.005	0.009	0.530	40.3

*100 sccm O_2; **10 sccm air

It is apparent from Table 8.2 that most of the water flowing through the cathode compartment of the EFC was from the air feed to the cathode, approximately 97%. The product water resulting from the reaction at the cathode was relatively insignificant. The cathode water loss, however, made up approximately 3% of the water leaving the cathode compartment. Increases in temperature of approximately 0.4^{o}C are enough to support such an increase in water flow rate from the cathode due to evaporation. Specifically, increased temperatures of 0.4^{o}C, 0.6^{o}C and 0.3^{o}C for experiments at 24.5^{o}C, 35.0^{o}C and 40.0^{o}C, respectively, can explain the water loss rates observed in the experiments. The void volume of the cathode compartment was approximately 3 mL, thus the corresponding residence time for the 10 sccm experiments was 18s. Such a low flow rate is not suspected of entraining water droplets and removing water in bulk. Furthermore, images of the cathode do not indicate migration of water towards the cathode outlet.

To test whether the EFC could provide enough heating to result in such an increase in temperature in the cathode, we performed an energy balance on the cathode. The system for this energy balance can also be seen in Figure 8.7. The source of heat in this system was assumed to be the exothermic conversion of protons, electrons, and oxygen into water. A steady state was assumed. This assumption is supported by a constant water loss rate throughout the experiment. The rate of the cathode reaction was approximated by converting the current developed into moles of water produced and then to heat evolved by that reaction (see Equation 8.3). Thus, for this heat balance, it was assumed that dry air and water vapor entering the cathode must be heated (Equation 8.4, with appropriate mass flow and heat capacity for dry air or water). The liquid in the

cathode was also a heat sink but was not included since a steady state was assumed. Finally, evaporation of water equal to the rate observed via neutron imaging was considered the final heat sink. Equations 8.3–8.5 describe the energy balance discussed here. Pertinent parameters for this heat balance estimation include the heat capacity of dry air and water (1.004 J g^{-1} K^{-1} and 4.181 J g^{-1} K^{-1}, respectively), enthalpy of vaporization of water (2257 J/g) and enthalpy of formation of water (285.8 kJ/mol). Table 3 below shows the results of this energy balance.

$$Q_{evolved} = \frac{I}{F} \times \frac{1 mol H_2O}{2 mole^-} \times \Delta H_f^{H_2O} \tag{8.3}$$

$$Q_{Heating} = \dot{m} C_p \Delta T \tag{8.4}$$

$$Q_{evolved} \geq Q_{vapor} + Q_{air} + Q_{evaporation} \tag{8.5}$$

$Q_{evolved}$ refers to the heat produced via the cathode reaction. $Q_{Heating}$ refers to the amount of energy needed to heat the dry air stream or water vapor. $Q_{evaporation}$ refers to the heat needed to evaporate water at the rate observed via neutron imaging. The change in temperature (ΔT in Equation 8.4) corresponded to the temperature increase for each experiment shown in Table 8.2. Finally, as shown in Equation 8.5, the heat evolved via the cathode reaction must be greater than the sum of the heat sinks in order for the temperature increases shown in Table 8.2 to be feasible.

Table 3. Heat balance analysis based on calculated temperature increase from Table 8.2.

T (^oC)	Current (A)	Water produced (mol/s)	Heat released from water production (W)		Heat required from Table 8.2 (W)
24.5*	1.60×10^{-4}	8.29×10^{-10}	2.37×10^{-4}	<	2.77×10^{-3}
35**	5.64×10^{-4}	2.92×10^{-9}	8.36×10^{-4}	>	6.58×10^{-4}
40**	6.89×10^{-4}	3.57×10^{-9}	1.02×10^{-3}	>	1.88×10^{-4}

*100 sccm O_2; **10 sccm air

The column titled “Heat released from water production” refers to the enthalpy of formation of water released at a rate based on the current of the EFC. The column titled “Heat required from Table 8.2” refers to the amount of energy input necessary to increase the temperature of the air and water vapor by the temperature increases in Table 8.2. In addition to heating those components of the cathode, heat to cause evaporation at the rate observed via neutron imaging was also considered. It can be seen in Table 8.3 that it was feasible for a slight increase in temperature (~0.4^{o}C) to occur based on the heat released by the reaction that occurred in the cathode. This is indicated by observing that the energy released via the cathode reaction is in excess of the heat required to increase the temperature by the amounts shown in Table 8.2 (for the second and third experiments). It is noted that other heat sources and sinks were likely to exist in the operating EFC. These results, however, indicate that enough heat can be evolved in the cathode to support slightly increased temperature throughout the liquid and gas phases of the cathode.

Additional experiments were planned, where an EFC with aluminum endplates, rather than Teflon, will be utilized. As it is visible in Figure 8.2, the PEM was not flat, but was wavy as a result of being in contact with the tie rods that held the end plates

together. The anode also appears to be at a slight angle compared to the PEM instead of being in parallel to it. The rigid aluminum endplates that will be used in the planned experiments are expected to minimize these effects. A new 40-mm cross-strip detector with an imaging resolution of 10 μm will also be used in the planned experiments. Finally, an effort to accurately measure the temperature in the cathode compartment of the modified EFC will be made to verify the mass balance findings described above.

8.5 Conclusions

The water content in the cathode for an operating EFC was successfully measured and studied in this work. Neutron imaging has been demonstrated as a useful technique for understanding the water-loss behavior and quantifying the rate of water loss; this is important since water balance is an important aspect of EFC operation. The water loss from the cathode, despite a supersaturated air stream, can possibly be explained by a local increase in temperature in the cathode. Thermodynamic studies would be of great interest to understand the general EFC operation as well as commonly-observed water loss. Separation of water loss and enzyme/mediator degradation contributions to EFC power loss can be achieved by implementing neutron imaging as a tool in EFC studies. A better understanding of such contributions to power loss can lead to improvements in the design and operation of EFCs, increasing available power from these devices.

CHAPTER 9

CONCLUSIONS AND RECOMMENDATIONS

This research focused on utilization of electrochemical impedance spectroscopy (EIS) and neutron imaging to study transport in fuel cell systems. Effects of operating conditions, construction, and geometry, as well as temporal effects, have been studied via EIS and neutron imaging. EIS was used to calculate the distribution of transport resistances in three different fuel cell systems. This allowed identification of power output-limiting transport steps occurring in the fuel cells, which led to improved power production and, in the case of the EFC, longevity, as well. Power density studies generally complemented EIS results; however, power density studies cannot indicate which component of a fuel cell is limiting power output. In many experiments, changes in parameters on one side of the fuel cell had greater effects on the other side of the fuel cell. Such an observation is possible only through EIS. Neutron imaging was used to quantify the distribution of water in an operating PEMFC and EFC. Since water plays an important role in dictating transport properties of fuel cells, understanding the water distribution and content was important.

With the results presented in this work, operating conditions, materials and geometry of construction, and other aspects of fuel cells can be identified and further explored to improve the power density of these devices. Based on the results of this work, several specific conclusions can be drawn:

- It was observed in the PEMFC component of this work that multiple conditions contributed to the minimization of internal resistance mechanisms in the fuel cell. Increased temperature and increased feed humidity both improved PEMFC power output and stability. This indicates that both conditions improve the reaction rates at the electrodes and the transport of protons from the anode to the cathode. The flow rate of air to the cathode did not appreciably affect the power output or resistance of the PEMFC, provided the air flow rate did not go below a minimum value for operation. The anode was identified as providing the greatest resistance, which implies that the anode of this fuel cell was poisoned or otherwise damaged. This is because the hydrogen oxidation reaction at the anode generally proceeds more quickly and easily than the oxygen reduction reaction at the cathode.
- Power output for the PEMFC used in this work was observed to be dependent upon the history of the fuel cell operation. For example, power density curves performed for increasing or decreasing external resistance exhibited differing behavior. This was confirmed with EIS measurements. This behavior indicates that temporary microstructures, such as the water network throughout the PEMFC, can change over time. Also, the formation of the microstructures in the PEMFC can have an effect on the fuel cell power output.
- Neutron imaging was performed in an edge-on fashion for an operating PEM fuel cell. A peak in water content at the PEM-catalyst layer interface on the cathode side was observed. However, assignment of this peak was uncertain due to blurring issues with the images. As such, improvements to the assignment of the layers in a fuel cell system are recommended. One method to achieve this improvement would

be the incorporation of neutron markers in the PEMFC. Such markers would definitively indicate the boundaries between fuel cell layers. The imaging results in this work agree with modeling results found in the literature.

- EIS was used to study the response of a MFC operating with inoculum from an anaerobic digester to changes in the flow rate and ionic strength of the anode growth medium. It was found that, despite changes made to the anode side of the MFC, the greatest response was actually in the cathode. Such a result was explained as conditions in the cathode improved when the anode fluid had both higher ionic strength and flow rate. Both parameters in the anode could enhance transport of protons from the anode to the cathode. This transport enhancement allowed the water production rate or the reaction rate at the cathode to increase, resulting in lower cathode resistance. The isolating properties of the anode biofilm are believed to have contributed to the small response of the anode resistance to changes in anode conditions by providing a more stable medium immediately near the bacteria growing in the biofilm.
- It was found that the optimization time for the anode of an MFC could span from days to months, depending upon the inoculum. For an inoculum originating from an anaerobic digestor, it was found that the anode resistance did not stabilize until after approximately two months. However, for an inoculum from an already-mature MFC, the stabilization time for the anode resistance was only five days. Quantification of such bioanode development allowed discernment of when the MFC was limited by the anode (early during enrichment) or the cathode (after maturation of the anode microbial community). This has important implications on

start-up time for MFCs and provided insight into the behavior of the bacterial community as it adjusted to conditions in the MFC.

- The effects of carbon loading and cathode configuration on MFC operation were studied with EIS. Carbon loading had relatively little effect on the MFC output. The implication of this finding is that an MFC used for wastewater treatment can operate at over a wide range of carbon loadings in the wastewater with no loss at high carbon loading. Conversely, a maximum amount of carbon for treatment was identified, suggesting that MFCs have limitations on how much carbon can be treated, even after the bacteria have been optimized for exoelectrogenesis. Coulombic efficiency in various experiments was observed to range from 2.5% (at highly excessive carbon loading) up to 96% for a carbon-lean system. Despite this large range of coulombic efficiency, the anode resistance was often in the range of 2 – 5 Ω, suggesting that low coulombic efficiency was not related to poor bioanode performance.
- It was also found that the concentration of ferricyanide in the cathode strongly influenced output. This agrees well with EFC experiments in which the amount of catalyst was varied. In the case of ferricyanide, greater concentration was analogous to more cathode catalyst, allowing for reduced charge transfer resistance and increased power output.
- EIS was utilized to study the effects of various operating conditions on EFC operation. Specific parameters considered included enzyme loading, air humidification, operating load, and over-time decay. Enzyme loading was the parameter explored that had the greatest effect on total resistance and power output.

Experiments with greater enzyme concentration yielded reduced internal resistances and improved power density. This is attributed to greater enzyme availability and suggests that power output can be limited by enzyme concentration. However, it was observed that the enzyme limitation was removed at high enzyme loading, thus the cathode limitation shifted to another aspect of the cathode such as mediator transport between the electrode and enzymes. Air humidification, while it did not affect the internal resistance or power output appreciably, did have an important impact on water retention and EFC power output stability. Increased salt concentration in the enzyme cathode solution contributed to water retention. It was found that saturation of the air stream (especially at a temperature greater than that of the EFC), along with increased salt content in the cathode solution, reduced the water loss rate from the cathode by a factor of 10. This finding can contribute to the development of more stable EFCs and is of interest since current EFC lifetimes are relatively short.

- Each component of a fuel cell can be strongly dependent upon the other components of the fuel cell. This was observed in all three fuel cell systems wherein changes to the anode had a greater response from the cathode than the anode. The reverse also was observed multiple times in this work. The implication of such an observation is that optimization of one side of the fuel cell (for example, the limiting side) can occur by improving conditions on the non-limiting side of the fuel cell. Viewing a fuel cell as a series of independent unit operations (anode operating independently from the cathode) is therefore inaccurate and will limit efforts to improve the technology.

- PEMFCs exhibit power roughly three orders of magnitude greater than biofuel cells. This greater power coincides with a three orders of magnitude different in internal resistances. It is interesting that the solution or ohmic resistance in biofuel cells is much larger than that of the PEM in a PEMFC, despite the fact that the same material was used and that both the electrodes in the biofuel cells were in close contact with the PEM. The discrepancy in resistance is attributed to the greatly different pH between a PEMFC (suspected to be extremely low, below pH 1) and biofuel cells (pH 7 in the MFC anode, pH 11 in the MFC cathode, and pH 4 in the EFC cathode).
- Neutron imaging has been shown to be useful for quantifying drying conditions in an operating EFC. Prior to this work, neutron imaging had never been employed to study an EFC, but had been utilized in PEMFC studies. Since water loss occurs in the cathode of an EFC despite saturation of the air stream, further improvements to EFC design must be made to improve stability over time and neutron imaging can yield unique insights into the drying behavior of the EFC.
- The oxygen reduction reaction (that forms water) in the cathode of the EFC has been shown to produce enough heat to result in a temperature increase that supports drying of the EFC cathode. The rate of evaporation from the cathode was calculated based on neutron imaging results, while the increased temperature was determined via mass and energy balances. The implication of this result is that conditions in the cathode can force an unsaturated condition, causing evaporation to occur. This is detrimental to EFC longevity since the ORR in the cathode must take place to produce power.

- In the appendix, it is demonstrated that carbon capture and storage (CCS) is a poor choice for the avoidance of CO_2 emissions to the atmosphere from the energy production activities of humans. The cost of CCS is currently high enough that alternative energy technologies are attractive for the avoidance of CO_2 emissions. As examples in this work, wind power was found to be almost twice as effective, nuclear power was nearly five times as effective, and geothermal power was over five times as effective as CCS at avoiding CO_2 emissions on an economic basis. Furthermore, CCS has little to no expected return while these alternative energy technologies have potential for significant profits over their lifetimes. These simulations lay the groundwork for a novel approach to compare alternative energy technologies with CCS on economic and carbon avoidance bases.

In summary, EIS and neutron imaging are employed in this work to provide a better understanding of the transport phenomena that occur in three fuel cell systems. Incorporation of chemical, physical, and biological principles was necessary to perform this work since the types of fuel cells that were investigated incorporated all of these principles. Such studies have implications for the optimization and operation of fuel cells as alternative energy systems.

Regarding the use of EIS and neutron imaging to study a PEMFC, current research activities focus on the development of lower-cost materials of construction, as well as improved materials that can operate at higher temperatures and better eject the heat associated with PEMFC operation. Both thrusts are designed to improve PEMFC

efficiency while scaling up PEMFC designs. Throughout this process, EIS is suggested to be an integral tool used to identify limiting mechanisms that result from new materials, geometries, and operating conditions. EIS can guide further development of PEMFCs in an effort to make this energy conversion system more economically viable. Neutron imaging can also play a role, primarily in verifying water management schemes to establish conditions that avoid both flooding and excessive drying of the PEMFC. It is also suggested that neutron imaging and EIS be used in tandem to better understand how water content influences transport resistances in an operating PEMFC. This will provide verification for models that describe this relationship, as well as provide new insights into how water content affects PEMFC power output.

Further development of MFCs can also benefit greatly from the inclusion of EIS studies. In this work, it was identified that optimization of one electrode of the MFC could occur by changing conditions on the other side. Such an interrelated operation of the two chambers of the fuel cell was discovered with the insight provided by EIS. New materials, configurations, and applications must be explored for MFCs to find the most promising niches for this technology. Microbial diversity causes the spectrum of possible MFC applications to be quite wide since microbes are capable of degrading many carbonaceous compounds. Since MFC limitations were observed in the cathode once the microbial community was established, a design that allows washing of the cathode, without interrupting operation, would be of interest since this can help remove the buildup of cations at the cathode observed in this work. The effects of improved air delivery to the cathode, as well as removal of the cation buildup at the cathode, can be

quantified via EIS and the relative contributions of these improvements to the overall resistance identified. Attendant to the buildup of cations in the cathode was an increase in pH (up to pH 11); experiments to explore the effects of this high pH and ways to minimize its effect would be beneficial to developing more robust MFCs. In addition, it would be interesting to explore the effects of a relatively large EIS voltage (0.015V or higher) on bacterial detachment. Detachment was observed for a perturbation of 0.010V; any dependence upon frequency or whether this detachment was solely a result of the voltage should be determined.

Finally, the relatively new technology of EFCs has considerable development to undergo in order to become economically viable as a distributed power conversion technology. Similarly to PEMFCs, improvements to EFC system architecture, especially to enhance cathode transport, will determine how much the power density of EFCs can improve. It is suggested that immobilizing enzymes on the cathode be performed to reduce the distance between the enzymes and the electrodes; this would reduce or eliminate the reliance of EFCs on electron-shuttling mediators. EIS would be useful in this endeavor since it could be used to quantify enzyme utilization. High resolution neutron imaging (perhaps in three dimensions) should be employed to better understand how water evaporates from the cathode. Evaporation behavior affects whether pockets of enzyme solution become isolated from the bulk cathode solution; when this happens, the enzymes in the isolated pocket can no longer meet with protons. Thus, these enzymes are no longer used in the EFC operation. Neutron imaging can be utilized to understand and guide efforts to mitigate evaporation from the EFC cathode. The main attraction to EFC

technology is that enzymes also can be designed to catalyze a nearly limitless array of reactions, allowing applications of EFCs to span a wide range.

APPENDIX I. CARBON EMISSIONS MANAGEMENT

A.I.1 Introduction

Approximately 30 Gt of CO_2 are emitted to the earth's atmosphere each year as a result of human activity. A large portion of this carbon is in the form of gaseous CO_2, and approximately 30% of this CO_2 comes from fossil fuel power plants. In parallel to rising levels of atmospheric CO_2, the earth's temperature is increasing, and it is believed that the two phenomena are related. Therefore, reduction of CO_2 emissions is currently an important area of research. Separation and sequestration of CO_2 are near-term goals for emission reduction and they are critical and challenging topics for researchers. Many traditional separation processes are being considered for CO_2 capture, including absorption using solvents or solid sorbents, pressure- and temperature-swing adsorption using various solid sorbents, cryogenic distillation, and membrane separation. Several novel technologies are emerging as well. Both traditional and emerging processes are reviewed in this chapter.

A.I.2 Absorption

A.I.2.1 Working principle

The process of CO_2 absorption by a liquid solvent or solid matrix is currently being investigated for scrubbing CO_2 from flue gas streams. Absorption is a process that relies on a solvent's chemical affinity with a solute to preferably dissolve one species over another. In CO_2 absorption processes, a liquid solvent is used that preferentially dissolves CO_2, but not N_2, H_2O, NO_x, SO_x, CO, O_2, or any particulates (Li et al. 2003).

The CO_2-rich solution is typically pumped to a stripping column where the CO_2 is stripped from the solution and the solvent recycled for a new batch of flue gas. Optimal conditions for absorption are low temperature and high pressure. In addition, most solvents are easily degraded or deactivated by compounds such as fly ash, other particulates, SO_x and NO_x, so the absorption step must take place after electrostatic precipitation (ESP) and flue gas desulfurization (FGD). In a typical absorption process, the CO_2-lean exhaust gas is either emitted to the atmosphere or possibly used in other applications (e.g., chemical production). Absorption is often considered a base case for CO_2 separation schemes because it is well known and understood in industrial applications.

A.I.2.2 Use of monoethanolamine as a solvent

An effective, economical, and traditional solvent that can be used for CO_2 absorption is monoethanolamine (MEA). The flue gas from a fossil fuel power plant is passed through a column in which MEA selectively absorbs CO_2 (Figure A.I.1). This CO_2-rich solution is then pumped to a tower in which thermodynamic conditions are manipulated to release the CO_2. High pressure and low temperature favor absorption while low pressure and high temperature result in regeneration of the solvent. Temperature manipulation (specifically, to release the CO_2 and regenerate the MEA) makes up to 70-80% of the operating cost. The main area of improvement for this process is finding new solvents or optimizing the existing method to minimize regeneration costs (Veawab et al. 2001).

In Figure A.I.1, the flue gas is cooled prior to entering the absorption chamber. The minimum temperature of operation should be above the condensation point of the gas and the freezing point of the solvent. After absorption, the CO_2-rich solution is passed through a heat exchanger to recover much of the heat from a hot stream coming from the regenerator. It then goes into the stripper where it is heated to release the CO_2 in solution (if pressure control is involved, the pressure is lowered). The CO_2-lean solution is then pumped back into the absorber for reuse. There are many points where a chilled water stream exchanges heat with the solvent stream, which constitutes a cost-effective method to conserve energy (Yeh and Pennline, 2001).

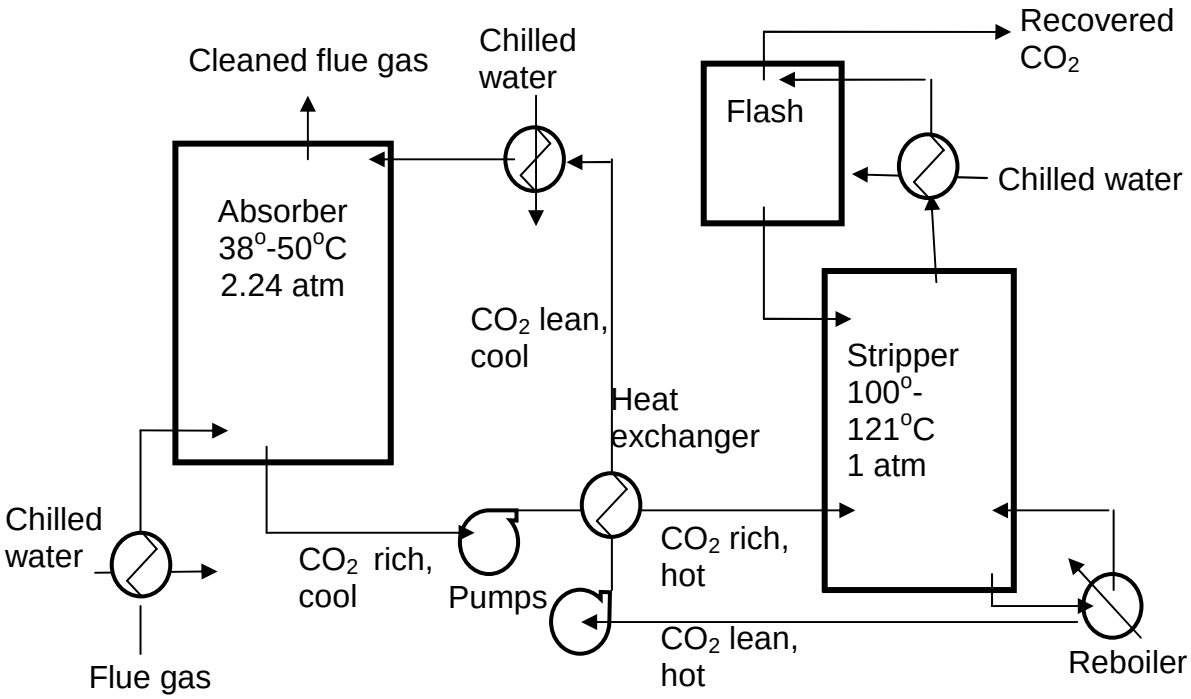

Figure A.I.1. Flow sheet of chemical CO_2 absorption system with MEA solvent (Yeh and Pennline. 2001).

The absorption process has many design issues that must be overcome. The most important issue is the regenerability of the solvent (the regeneration process is the same regardless of the solvent employed). Since it is desirable to carry out the process with as little energy penalty as possible, the solvent activity must have an optimum balance between absorption and desorption rates. Absorption of CO_2 at low temperatures (below 50^oC) and relatively low CO_2 partial pressure (normal flue gas fraction of CO_2 is approximately 0.15) can occur if the solvent is highly attractive to the solute, but this high attraction between the solvent and CO_2 results in significant regeneration energy. If the solvent does not have a high affinity with CO_2, regeneration is simple, but little loading is possible.

Another concern is the oxygen content of the flue gas. A high oxygen concentration can corrode carbon steel facilities and cause excessive amine loss. Hindered amines (organic amine compounds with large attached groups that hinder some solvent-oxygen interactions) offer some resistance against degradation of the solvent. Acidic gases, such as SO_x and NO_x, are also a major concern. It is preferable to keep levels of these acidic gases below 0.001% because they form stable salts with the amines used for absorption. Since typical SO_x scrubbers often remove 90% of the SO_x in the flue gas, solvent degradation can be a major issue if MEA is used. Fly ash and NO_x compounds create the same problems as those presented by SO_x compounds; any amount of these components will cause at least some solvent degradation.

Finally, the high temperature associated with flue gases can degrade the solvents and lower the solubility of CO_2. The maximum ideal temperature for MEA is 45^{o}C. The temperature needs to be decreased to approximately 45^{o}C in the SO_x scrubber, upstream from the separation column (Chapel et al. 1999).

A.I.2.3 Flue gas desulfurization product recycling

One method that has been studied by Taulbee et al. (1997) uses the separated SO_x from flue gas desulfurization (FGD) to form a solvent that absorbs CO_2. Limestone-based compounds are currently used to separate SO_x from flue gas streams prior to absorption. The limestone-SO_x compounds can then be slurried, becoming the liquid solvent for absorption. Laboratory experiments show that up to 0.0257 m^3 CO_2/kg of FGD product can be absorbed. An attractive feature of this design is that many coal power plants are either already equipped with FGD units or are upgrading to include these units in order to comply with tightening environmental standards. Additional transport equipment for the slurry to be moved to the absorber is necessary. The overall cost for an absorption unit using FGD products as the solvent is lower than a conventional absorption process.

A.I.2.4 Advantages and disadvantages for absorption

CO_2 absorption is a well-established method of capturing CO_2 and the mechanisms and involved thermodynamics are well known. The fact that CO_2 absorbers can be regenerated is possibly the most attractive feature that motivates renewed research efforts focused upon improvement of the absorption process. The main advantage of absorption is that there are solvents that can be repeatedly regenerated. MEA has been used for over 60 years in the chemical industry, while new solvents operating on the same

principles are currently being investigated (Herzog, 1999). CO_2 absorption is a well-established method of separating CO_2 and the mechanisms and involved thermodynamics are well known.

When the CO_2-rich solution is sent into the stripper, the solvent can be regenerated, thus reducing the cost of materials. However, different conditions demand different solvents. For low partial pressures of CO_2 (< 15 vol. %), liquid solvents like MEA are preferable. For high partial pressures of CO_2 (> 15 vol. %), solid solvents, such as lithium hydroxide and lithium zirconate, are better because they can absorb more CO_2 and are more easily regenerated (Audus, 1997). Also, the separated CO_2 stream from the stripping column is of high purity, often up to 95%. This is pure enough for most sequestration methods, including aquifer injection, coal bed methane production and enhanced oil recovery (Holloway, 1997).

While absorption does have strong advantages, the total cost (including addition of new solvent and other operating and maintenance (O&M) costs) is relatively high, about \$40 - \$70/ton CO_2 separated, as reported by Chakma and Tontiwachwuthikul (1999). The exact life of a batch of solvent was not reported for MEA or any other solvent, but solvent generally degrades before it is replaced. The energy penalty of the entire absorption process (no O&M costs included) is approximately 0.0764 kWh/kg CO_2 (\$15.14/ton CO_2), as reported by Gottlicher and Pruschek (1997). Note that the cost reported by Gottlicher and Pruschek is only the energy penalty necessary to operate the

process. The cost reported by Chakma includes the cost of purchasing new solvent and other operational costs.

In addition to high regeneration costs, sulfur compounds (SO_x gases) present in flue gases during absorption degrade the solvents currently considered for absorption. Approximately 8.75 kg of solvent are lost for each ton of CO_2 separated (Chapel et al. 1999). The loss of solvent occurs in the form of salts that do not dissociate in solution; they precipitate out. This often requires absorption with MEA to take place after the flue gas desulfurization (FGD) step.

A.I.2.5 Process improvements

A.I.2.5.1 New solvents

Improvement is necessary for absorption to be viable for CO_2 separation in the future. New solvents, such as the new PSR™ solvents reported by Veawab et al (2001), are being investigated. The PSR solvents are a family of solvents, currently under development, that require less heating for regeneration and are able to absorb more CO_2 than MEA. PSR is a trade name for this solvent whose chemical formula is currently unreleased. These solvents absorb 20-80% more CO_2 than MEA per unit volume of solvent, which allows them to be circulated more slowly through the system; this decreases pump costs. PSR solvents are also more resistant to degradation from flue gases and cause less corrosion to equipment.

Possibly the most promising absorption process employs the KS-1, KS-2, and KS-3 solvents being developed by Mitsubishi Heavy Industries (MHI). This family of solvents shows higher CO_2 loading per unit mass of solvent, lower regeneration conditions, and little corrosion, degradation, or amine loss. A novel packing material, KP-1, has also been developed that will further improve this process. Commercial-scale use of the solvent and packing has been in place at a fertilizer plant in Malaysia since 1999 (MHI CO_2 website). The separated CO_2 is used in urea production, mitigating storage costs.

In addition to the Mitsubishi process, the Econamine FG™ process also shows lower overall costs. This process improves upon regular MEA absorption by using hindered amines in solution. Hindered amines are similar to regular amine solvents, but specific functional groups are added to these solvents to diminish or prevent degradation. This also lowers steam costs for regeneration, thereby lowering the overall cost. Audus (1997) reports that the Econamine FG process costs \$18.70/ton CO_2 in O&M costs when CO_2 is 13% of the flue gas by volume. This process is currently being modified to further decrease the cost.

A.I.2.5.2 New equipment configuration

In addition to new solvents and packing configurations, alterations of the equipment used in the absorption process are being investigated. Fisher et al. (2005) have performed rigorous simulations of a MEA absorption system with various equipment configurations. The base case setup is illustrated in Figure A.I.2, but includes

compression after CO_2 exits the stripping column. This compression is included in all of the process configurations explored as a necessary prerequisite for transport of the separated CO_2. In addition to the base case, heat recovery from the exiting CO_2 and multistage compression in the stripping column were considered. Four scenarios were actually simulated: base case, heat recovery, multistage compression, and multistage compression combined with heat recovery. Figure A.I.2 is an illustration of multistage compression combined with heat recovery used in the simulations.

In these simulations, the goal of 90% CO_2 recovery was met, and the associated cost for each configuration was calculated using costing software and simulations. It was determined that multipressure stripping with heat recovery reduced the cost of MEA absorption by 9.8% compared to simple stripping and compression. The implementation of this process would cause the cost of electricity to be $0.0599/kW-hr, while the base cost without any CO_2 capture was $0.025/kW-hr. Despite this increase, this modification shows great promise, especially if the configuration changes are coupled with better solvents.

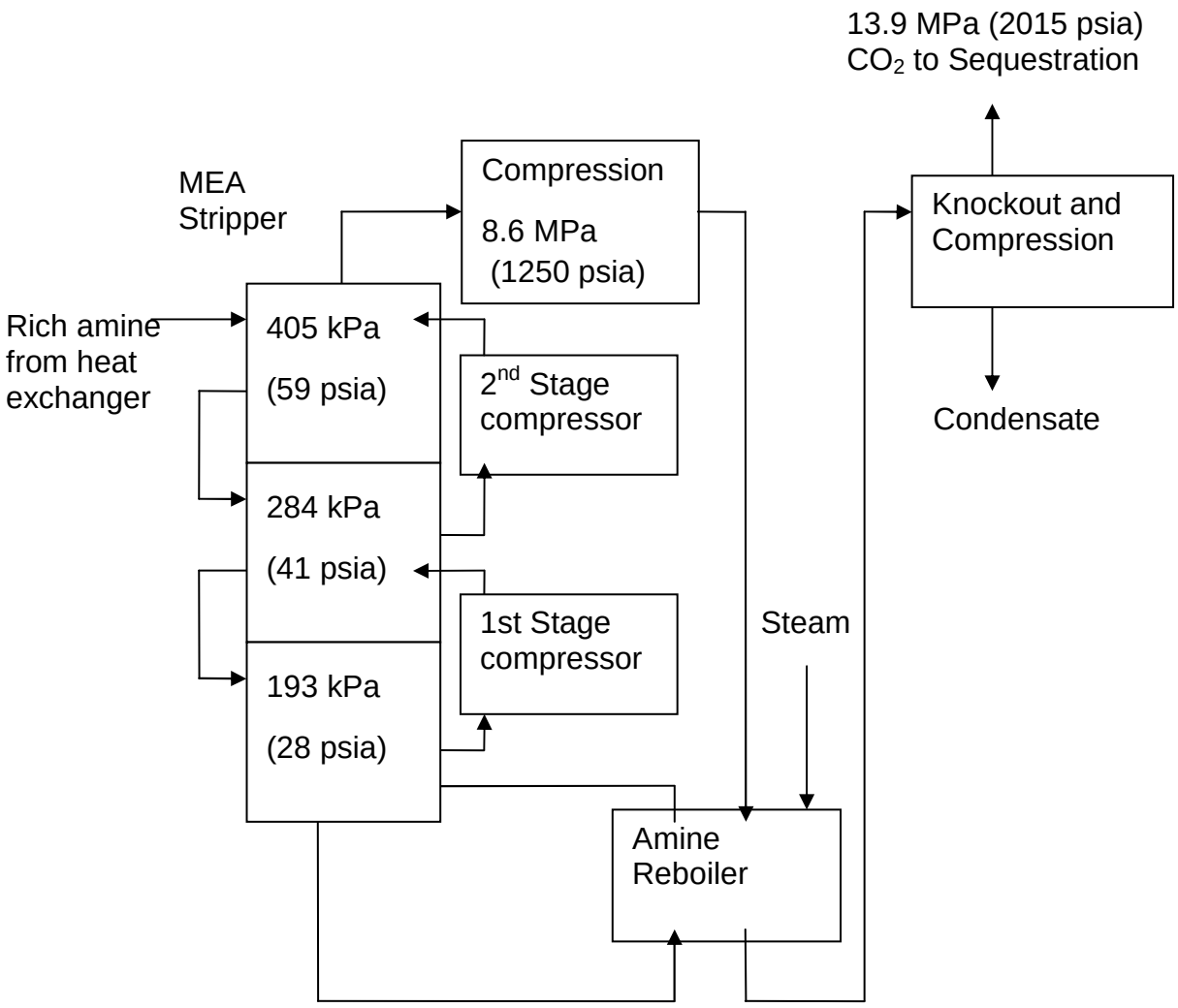

Figure A.I.2. Multistage compression and heat recovery in the simulations by Fisher et al. (2005).

A.I.2.5.3 Other possible improvements to absorption

Another approach to improve absorption is to increase contact between the solvent and the flue gases in the absorption column. The addition of packing is used to maximize flue gas-solvent contact as well as decrease residence time. In a recent experiment performed by Yeh and Pennline (2001), a column with gases and conditions typical of flue gases entering an absorption chamber was packed with different materials such as BX gauze, Flexipac, and intalox saddle (made by Norton Chemical Process

Products). The saddle packing was tested with both random and structured configurations. Absorption took place at approximately 50^{o}C for the MEA, regardless of which packing was used. Regeneration took place at 120^{o}C. This process is often used in current applications at most plants with MEA scrubbers. The structured packing showed the greatest solvent utilization at 43.9 ±0.5 % (fraction of solvent that absorbed CO_2), while the random packing achieved only 28.6% solvent utilization.

In summary, different packing materials and organic solvents have various effects on the absorption rate and regeneration energy for the system. The right combination of solvent, packing, and operating conditions could yield a process that cleans flue gases for a fraction of the current costs. A list of materials and conditions reported thus far for the separation of CO_2 by absorption is given in Table A.I.1.

Table A.I.1 Selection of materials and conditions in CO_2 absorption.

Absorbent	Absorption Temp. (^{o}C)	Absorption Pressure (atm)	Desorption Temp. (^{o}C)	Desorption Pressure (atm)
MEA	50	2.24	120	1
PSR	50	2.24	110	1

A.I.3 Adsorption

A.I.3.1 Working principle

Adsorption is another method that can be used to separate CO_2 from flue gases generated by fossil fuel power plants. Due to the interaction energy between adsorbent

and guest molecules, CO_2 molecules are attracted to and trapped by surface groups of the adsorbent. Conditions can be manipulated to facilitate adsorption or desorption. Many solids have the capability to selectively adsorb CO_2 into small cracks, pores, or onto their external surfaces under specific temperature and pressure conditions. Adsorbents such as activated carbon, molecular sieves, and zeolites have all been considered for adsorption processes.

The two traditional methods for adsorption are pressure swing adsorption (PSA) and temperature swing adsorption (TSA). In either case, adsorption rates depend on temperature, partial pressures of CO_2, surface forces (interaction energy between adsorbent and CO_2), and pore size or available surface area of the adsorbent (Meisen and Shuai, 1997). Riemer et al. (1994) report that PSA is superior to TSA due to its lower energy demand and faster regeneration rate.

Figure A.I.3 shows a pressure swing adsorber where two chambers pass the pressure back and forth in a continuous cycle. Flue gases are sent into one of the two chambers and pressure is applied, allowing adsorption of CO_2. The pressure is then transferred to the other chamber where a new volume of waste gas has been introduced. As that chamber is pressurized, the first chamber is depressurized and the CO_2 is collected. The cycle then continues in a switching mode as waste gases are sequentially injected into the two chambers. The lines and valves shown beneath the tanks in Figure A.I.3 control the flow of the CO_2 out of one tank (line 1) and the flow of untreated flue gases to the other (line 2).

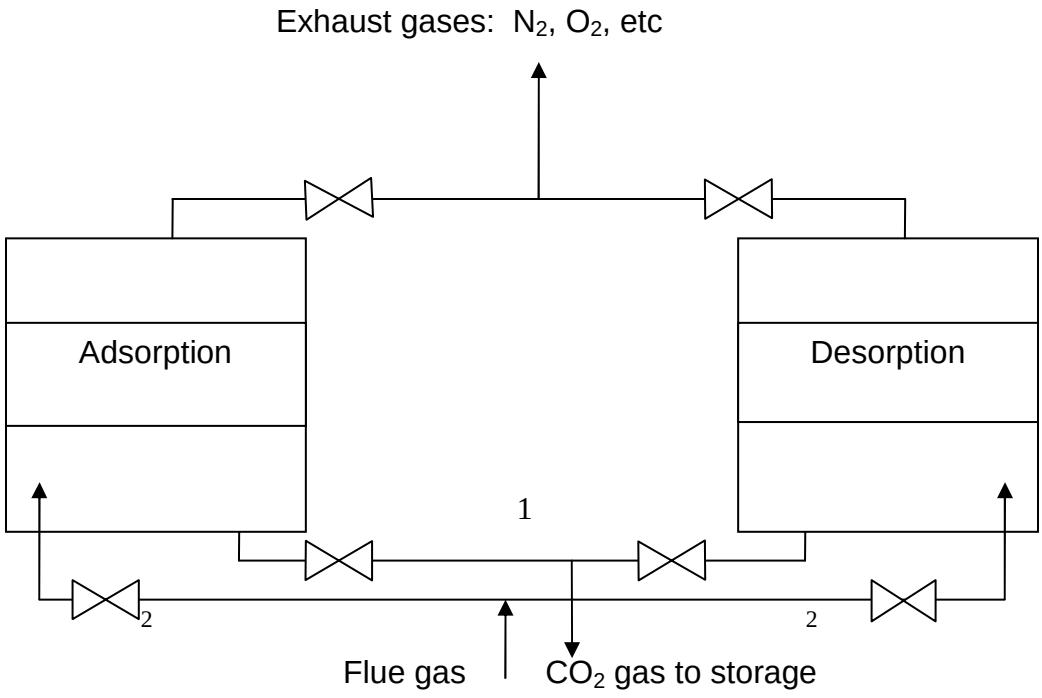

Figure A.I.3. Flow chart of a pressure swing adsorption (PSA) system.

A.I.3.2 Process improvements

A.I.3.2.1 Electrical desorption

A new class of adsorbents, based on a carbon fiber composite molecular sieve (CFCMS), can adsorb CO_2 and then release it when an electric current is applied across the adsorbent. Similar to PSA or TSA, electricity is the means to liberate the CO_2 trapped in the adsorbent. The adsorbent used is electrically conductive; electric current passed through the CFCMS raises the temperature, allowing for CO_2 desorption. Desorption was achieved on a CFCMS (2.5 cm diameter, 7.5 cm length cylinder) using 1 V direct-current potential and 5 amps. The carbon CFCMS proposed for this process is carbon-based

because of the high electrical conductivity and high specific surface area of carbon (Judkins and Burchell, 1997).

A.I.3.2.2 Hydrotalcite and water-gas shift

Perhaps the most promising use of adsorption is in conjunction with the water-gas shift process. Water-gas shift is a catalytic process that yields decarbonized H_2 fuel gas to a boiler for combustion (Allam et al. 2004). In this process, CO and steam are fed to a reactor where CO_2 and hydrogen gas form according to the following reaction: $CO + H_2O \leftrightarrow CO_2 + H_2$. Hydrotalcite (HTC) adsorbs CO_2, pushing equilibrium to favor H_2 and CO_2. The advantage is two-fold: less CO and more H_2 are present in the boiler feed.

This sorbent-enhanced water-gas shift (SEWGS) process shows exceptional promise for future power generation. The adsorption step proceeds as the pressure swing adsorption described above, but is operated simultaneously to the water-gas shift process. Allam et al. (2004) have performed ASPEN simulations to determine the efficiency and net power output of a plant operating with the SEWGS process, using HTC as the adsorbent. Experiments were performed to determine the properties of HTC under high temperature conditions (>400^{o}C). Based on these experiments and simulations, it was concluded that a plant employing air for combustion could achieve 48% efficiency, while the use of pure O_2 in combustion could achieve a plant efficiency of 47%. The air combustion is more efficient, but also uses more fuel for duct heating of the incoming air and has larger equipment sizes to accommodate N_2 in the system. Additionally, air combustion removes more CO_2 per year than O_2 combustion, but this is at least partially attributed to capturing CO_2 from the increased fuel usage. Further design modifications

and simulations are being performed to characterize design parameters of this process at an industrial scale.

A.I.3.3 Advantages and disadvantages for adsorption

Unlike liquid absorption where the solvent can form corrosive solutions with flue gases, physical adsorption only requires vessels capable of withstanding small pressure changes. PSA, like chemical absorption, is based on regenerability of the adsorbent. As shown in Figure A.I.3, the adsorbent can be reused many times for CO_2 separation. Gottlicher and Pruschek (1997) report that the energy cost for adsorption is projected to be \$6.94/ton CO_2 removed at CO_2 concentrations of 28-34 mole %. The energy cost associated with the treatment of gas with CO_2 concentrations of 10-11.5 mol% (the most common CO_2 concentration in flue gas) is expected to be four times greater than that at 28-34 mol%.

There are three significant drawbacks that make adsorption currently unfavorable as a stand-alone process. The first is that the system cannot easily process high concentrations of CO_2; good separation is achieved at low percentages of CO_2 (1-2 mol%). Most power plants have much higher concentrations of CO_2 in flue gases, approximately 12%. The second is that available adsorbents are not selective enough for CO_2 separation from flue gases. The adsorbents' ability is usually based on pore size. When CO_2 is the target to be selectively adsorbed, gases smaller than CO_2 can also penetrate the pores. N_2 is the gas that most commonly fills up pore space in adsorbents. This makes the process less efficient as a lower degree of CO_2 separation can be achieved

in each cycle. The purity of the CO_2 stream is consequently also affected by the adsorbent used, since various adsorbents will adsorb varying amounts of N_2 (the most common impurity). A third drawback is that adsorption is slow. For typical materials, the residence time for maximum adsorption depends on the adsorbent, but 20 min is a reasonable estimate (Satyapal et al. 2001). When dealing with large volumes of flue gas, as in a power plant, this is just too slow to be practical.

Despite these disadvantages, physical adsorption can play a satisfactory role in a hybrid system. Since it requires a low concentration of CO_2 for optimum performance, it could be placed after another separation process. Research is currently being conducted to find more selective adsorbents, adsorbents with higher capacities, better operating conditions, and more efficient packing structures. If these goals can be met, adsorption can become a viable method for separating CO_2 in the future.

A.I.4 Cryogenic Distillation

A.I.4.1 Working principle

Another separation process that has received some attention is cryogenic distillation. In this process, flue gas is sent to equipment designed to cool and compress the stream to conditions that will cause CO_2 to liquefy and leave the other components in the gaseous state [the triple point (point where solid, liquid and gas all coexist) for CO_2 is 5.1 atm and -57.6^{o}C]. Pressure and temperature can be varied, but cryogenic separation operates at low temperature and high pressure.

After leaving the boiler, flue gas enters a chamber cooled by a refrigerant stream. Water is condensed to avoid chemical corrosion and particulate matter is removed by appropriate traps. CO_2, O_2, and N_2 are then directed to the column for cryogenic fractionation/distillation. Some of the CO_2-lean gases (mostly O_2) are recycled to the boiler while the high purity liquid CO_2 is stored (Meratla, 1997).

A.I.4.2 Advantages and disadvantages for cryogenic distillation

Cryogenic distillation has one advantage over most other separation processes: its product is liquid CO_2, which is ready for transport via pipeline or tanker for sequestration. In addition to being ready for transport, the CO_2 recovery is very high (CO_2 purity after distillation can exceed 95%). The cryogenic process, however, is extremely energy intensive. The energy required to keep the system cool makes the current process cost ineffective. If H_2O is in the stream when the gases enter the chamber, it can freeze and clog the pipes (the water could also corrode the equipment). The cost for cryogenic distillation is predicted by lab-scale experiments performed by Gottlicher and Pruschek (1997) to be approximately \$32.7/ton CO_2 separated. This can be compared to the absorption cost of \$15.14/ton CO_2 removed and the adsorption cost of \$27.8/ton CO_2.

Refrigeration under pressure offers similar benefits to cryogenic separation, with similar drawbacks. While the cost for cooling under pressure is lower than that for cryogenic separation, more energy is required to pressurize the gases. To reduce the cost, a heat exchanger may be introduced to assist in cooling entering gases and heating exiting gases. The exiting gases may also power a turbine to generate energy, offering some repayment for the energy required in the rest of the process. The energy penalty for this

process depends on the degree of separation. If 90% of the CO_2 is captured, the overall efficiency of the plant is decreased from 38% (before any CO_2 removal) to 26%; the efficiency is 31% when 50% of the CO_2 is removed. The base-case efficiency of 38% was an arbitrary decision by Schussler and Kummel (1989).

A.I.5 Membrane separations

A.I.5.1 Working principle

The use of membranes has been established as a means of separating CO_2 from light hydrocarbons in the fuel and chemical industries. Membranes are also traditionally used to separate hydrogen gas from various other gases. Ceramic, metallic, polymeric, and solid-liquid are all forms of membranes used today (Audus, 1997). A list of membranes and their operating conditions is shown in Table A.I.2.

Table A.I.2. Materials and conditions for membrane diffusion.

Material	Type	Temperature (^oC)	Pressure (atm)
Organic	Solid polymer	25	1.01
Glycerine Carbonate	Gas absorption	23	Transmembrane pressure = 0.4 atm
Ideal metallic or ceramic	Solid inorganic	350	1.00

The selectivity of polymeric membranes is based on their ability to interact with the target molecule. Whatever molecule is to be separated interacts with the membrane and is allowed to diffuse across, either by solution-diffusion or absorption-diffusion mechanisms. The principle of ceramic and metallic membranes, which are porous, is that only gases of a certain size are able to pass through the pores of the membrane. So, these membranes act as a sieve to separate CO_2 from larger gas molecules. The flue gases from a fossil fuel power plant are sent at atmospheric pressure into a vessel that is divided by a

membrane; the CO_2 passes through the membrane into another part of the chamber where it is collected at a lower pressure (typically 10% of the feed pressure).

In Figure A.I.4, the flue gases simply enter the separation tank and the CO_2 diffuses across the membrane. The pressure on the permeate side is approximately 10% of the feed side; this pressure difference, established by a vacuum pump, will continually pull CO_2 across the membrane. Sometimes SO_x, NO_x, H_2O, O_2, CO and particulates are separated prior to entering the membrane unit because they can harm the membrane. If this is the case, the membrane primarily has to separate CO_2 from N_2.

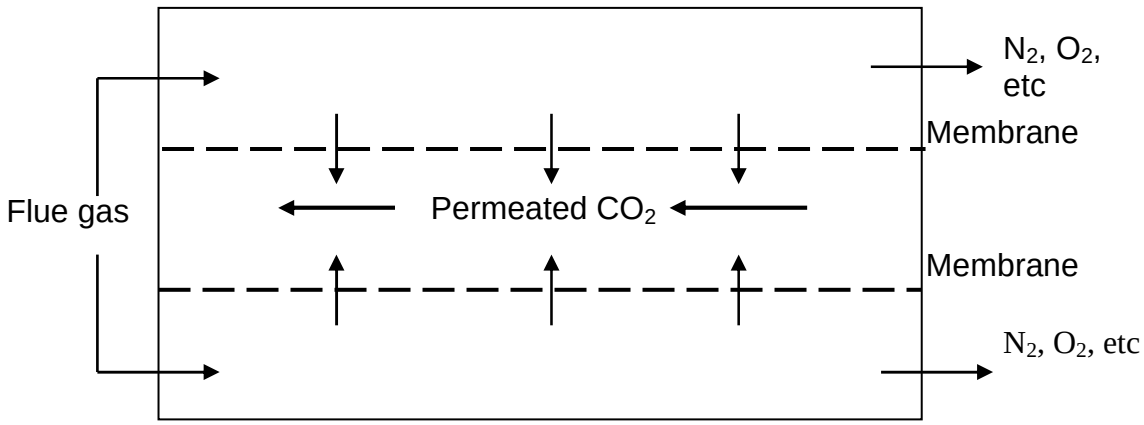

Figure A.I.4. Simple membrane separation tube for selective permeation of CO_2.

With a two-stage membrane system, the same process takes place, but the gases that permeate the membrane in the first chamber are again separated in a second separation vessel. This approach provides greater separation and a gas stream that is more suitable for carbon sequestration. The unpermeated gases from both units are sent to the same receiver for further treatment. Tokuda et al. (1997) report that double separation

yields a much higher purity stream of CO_2: 89.1% instead of 46.4% at 25^oC with a single stage. However, it generally costs twice as much as the traditional amine separation processes (Tam et al. 2001).

In addition to the membranes mentioned above, gas absorption membranes are being investigated. These consist of microporous solid membranes impregnated with a liquid absorbent. Thus, gas absorption membranes are a hybrid of a solid membrane and liquid absorbent. In this arrangement, CO_2 selectively diffuses across the membrane and is captured and removed by the liquid absorbent. This allows for individual control of gas and liquid flows and minimizes complications such as flooding, channeling, and foaming. The gas absorption membrane system is a hybrid of solid membranes and liquid absorption. Research performed by Kovvali and Sirkar (2002) shows that the thickness of the gas absorption membrane plays an integral role in the effective permeance of the system. A membrane that is 10 μm thick would be 20 times more permeable than a membrane that is 200 μm thick. However, Kovvali and Sirkar have found that membrane thickness does not significantly influence selectivity. These experiments used glycerin carbonate as the liquid and either Celgard or poly(vinylidene fluoride) as the polymeric solid.

A.I.5.2 Advantages and disadvantages for membrane diffusion

The greatest asset to membrane separation is simplicity. While pressure swing adsorption (PSA) requires special equipment for swinging the pressure and cryogenic distillation must endure extreme temperatures, the only equipment necessary for membrane separation is the membrane and fans. The flue gases must be compressed

somewhat before separation (the ideal pressure is approximately 1.01 atm) but this compression is much smaller than that necessary for PSA. Membrane separators do suffer from a trade-off between selectivity and permeability to CO_2. Also, many organic membranes do not perform well at the high temperatures typical of flue gases exiting the boiler. Boiler exit temperature is approximately 370^{o}C while the temperature following electrostatic precipitation (particle removal) and FGD is approximately 150^{o}C. The difference between the pressure of the flue gases and the permeated gases (a factor of 10) also causes problems for membranes that are not structurally stable.

Gas absorption membranes suffer the same drawbacks that absorption does: the incoming gases may contain chemicals that foul or otherwise damage the liquid component of the membrane (Meisen and Shuai, 1997). Gas absorption membranes are also less structurally stable than what metal or ceramic membranes are predicted to be.

Research is being done to find new metallic, ceramic, and alumina membranes. These membranes would withstand better the high temperature of the entering gases and the pressure changes associated with the gas flow through the chamber. Mowbray (1997) considers 350^{o}C a reasonable temperature for testing these membranes. Since gas absorption membranes have higher permeability and selectivity for CO_2, methods of making the solvent stage of the membrane more chemically stable are being investigated. The presence of water vapor in the pores of membranes has also been studied by Park and Lee (1995). It was found that, when water vapor clogs micropores, permeability decreases for both N_2 and CO_2. However, the decrease of N_2 permeability was so great

that its permeability was immeasurable while CO_2 permeability decreased by only a factor of 10 (small decrease compared to the decrease in N_2). Additionally, the membranes in development must be able to withstand the presence of SO_x and other compounds that typically pose problems for CO_2 separation units, since they are located before the FGD unit. Development of more stable solid and gas absorption membranes will determine whether membrane separation can stand alone as a CO_2 capture process or whether it may have to be part of a hybrid separation system.

A.I.6 CO_2 precipitation

A.I.6.1 Hydrate formation and dissociation

A.I.6.1.1 Working principle

One method for separating CO_2 from flue gases is to use hydrate formation. Hydrates are ice-like structures in which water forms a cage with cavities where small gases such as CO_2 can be trapped. While other gases can get trapped in these cavities, CO_2 is often the most likely occupant (a better hydrate former than other gases, under induced conditions). The maximum weight fraction of CO_2 in a unit of hydrate is 0.31 g CO_2/g H_2O (Pruschek et al. 1997).

Since water readily forms hydrates with CO_2, this process can capture CO_2 and allow the waste gases to escape. Hydrates do not form above 10^oC or much below 4 atm. Conditions on the ocean seafloor where CO_2 hydrates are being researched for sequestration are approximately 2-4^oC and pressure varying with depth (Brewer et al. 1999). In the case of syngas separation (Figure A.I.5), the CO_2 hydrate slurry goes to the

slurry separator where the H_2 is removed. This is a highly pure stream and can be used for future hydrogen cells or chemical reactions. This process is most likely to be used in an integrated gasification combined cycle (IGCC) application, but a similar process could be adapted for a standalone CO_2 hydrate separator at a pulverized coal plant. Using heat from the ammonia cooling exchangers, the hydrates are melted and the CO_2-rich stream is collected for sequestration or utilization. This process is also known as the SIMTECHE process (Deppe, 2004).

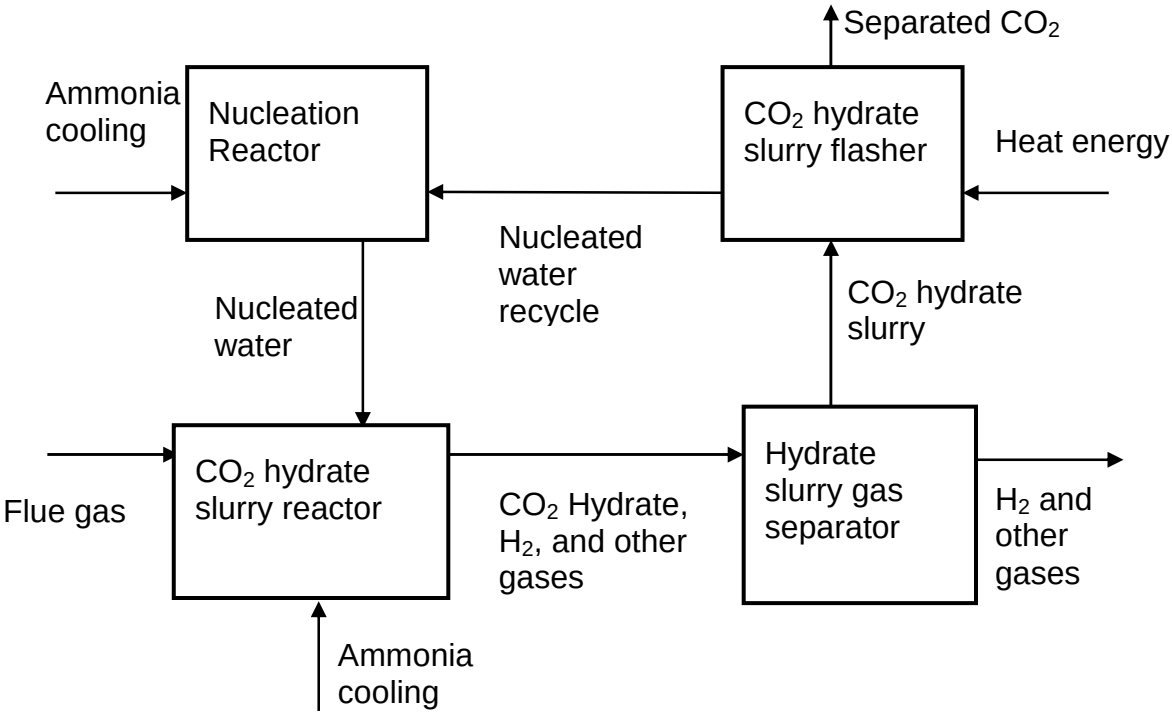

Figure A.I.5. Flow diagram of a CO_2 hydrate separation process.

A.I.6.1.2 Addition of tetrahydrofuran for hydrate formation

Investigations, performed by Kang and Lee (2000), sought to maximize CO_2 hydrate formation. One barrier to the use of hydrate formation is the high pressure

involved. It was found that the addition of 1mol% tetrahydrofuran (THF) lowered the pressure necessary for hydrate formation from 82.4 atm to 4.69 atm. In addition, it was found that lowering the temperature in the presence of THF by only 6 K increased the mol% of CO_2 in hydrate form from 39% to 61%. THF is used only in small quantities (1-3 mol% solution in water) and it can be recycled easily with the water after CO_2 has been liberated. The optimum conditions determined in this experiment were approximately 2^oC and 3.95 atm, 70 mol % CO_2 + 30 mol% N_2 gas mixture, and 3 mol% THF (3% when THF is added to water). Further research is being conducted to determine the effect of varying concentrations of THF and other hydrate promoters.

A.I.6.1.3 Advantages and disadvantages of hydrate formation

The advantage of using hydrate formation for separating CO_2 from flue gas or syngas in an IGCC reactor is that it may not be more energy-intensive than traditional processes (chemical absorption, PSA, etc) and the product can be easier transported than CO_2 gas. Conventional amine scrubbers, pressure swing adsorption (PSA), and other methods impose energy penalties of up to 35% for coal-fired plants. Hydrate formation, while not actually performed in a plant, is believed to impose an energy penalty of only 4.4% in an IGCC system (Ubis et al, 2000).

Hydrate formation is limited for current separation applications because it requires high pressures (~88 atm). While PSA requires high pressure, it is not as high as that for hydrate formation. In addition, the temperature for hydrate formation is quite low, ~4^oC, especially when compared to the temperature of flue gases from coal plants. A

significant amount of energy would be required to cool the flue gases to a suitable temperature, and then more energy would be required for pressurization.

While some conversion rates were as high as 35% (that is, 35% of the CO_2 that entered the reactor was captured in the hydrate form), better phase contacting could increase the efficiency of hydrate separation. Other major areas of improvement include the removal of the heat liberated during hydrate formation and the achievement of steady flow despite multiple phases (liquid CO_2, hydrate, liquid water, and ice) present in the process.

A.I.6.2 Ammonium carbonation

A.I.6.2.1 Working Principle

Separation of CO_2 from flue gas streams can be achieved by reacting the CO_2 with ammonia gas and water vapor in a gas-phase reaction (Figure A.I.6). The reaction proceeds according to the following equation:

$$CO_2 + NH_3 + H_2O \rightarrow NH_4HCO_3\ (s) \qquad \text{(A.I.1)}$$

This reaction can be achieved by bubbling raw flue gas through an aqueous ammonia solution. The NH_4HCO_3 forms a stable solid while the N_2 and other gases present in the flue gas stream continue through for release or treatment. It should be noted here that the solid product is to be used as a soil fertilizer, instead of being regenerated to recover the CO_2. In experiments done by Li et al. (2003), the flue gas was bubbled through a water

bath kept at 40°C and then sent to the reactor to be bubbled through the ammonia solution. In bench-scale testing, the reaction proceeded at room temperature and ambient pressure, indicating that the energy penalty for this method would be lower than most current methods (such as amine scrubbing, adsorption, etc.). Maximum CO_2 removal percentages were reached after approximately 400 min of residence time. The flow rate ratio (NH_3: flue gas) that yielded the highest CO_2 conversion percentage (48%) was 0.12; lower flow rate ratios yielded lower conversion rates. While a higher NH_3 to flue gas ratio yields a higher conversion rate, computer modeling suggests that 20-60% conversion would be the best balance between conversion and cost. Another promising result of this study is that the residence time in the reactor can be cut from 188 s to 47 s if the flow rate of the gas mixture is quadrupled (these times correspond to the 20-60% conversion, which takes less time than the 100% conversion). Decreasing residence time had no measurable effect on the conversion rate. This shows that, if a large-scale version of this process is used, large volumes of flue gas can be efficiently cleaned.

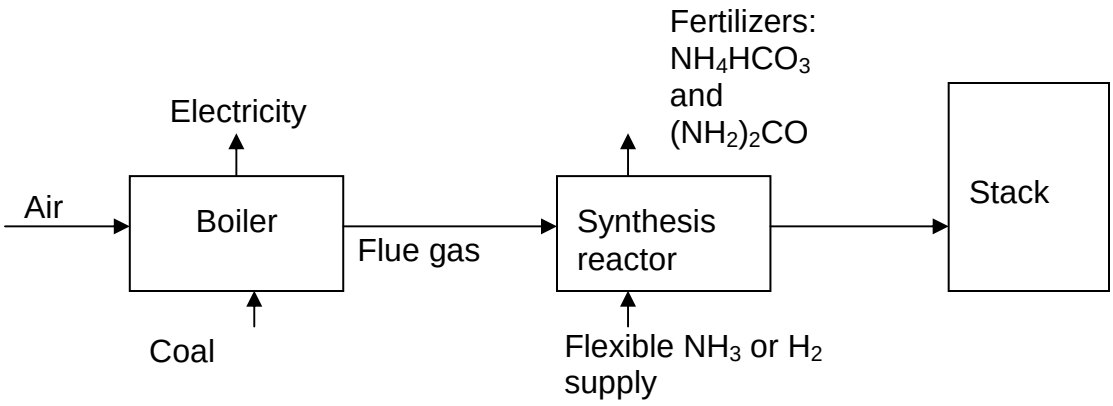

Figure A.I.6. Flow diagram of ammonium carbonation to produce fertilizer.

A.I.7 Summary of development status

Absorption using chemical solvents is already in commercial application. The solvents currently used are not as efficient as the next generation being developed. These new solvents are in the pilot plant testing stage. Physical adsorption is used in some chemical commercial applications, but not for CO_2 separation. Development of an adsorbent that can function despite the high CO_2 concentration and is selective enough to be economically viable is still in lab testing. Cryogenic distillation is also used in industry to produce pure CO_2, but not on the scale involved in flue gas separations. The energy requirements and other costs associated with this method inhibit progress. Membrane diffusion is also used in some chemical applications, but not for CO_2 separation yet. Development of membranes capable of surviving and functioning well at pre-FGD conditions is necessary before testing can get out of the lab test phase. In all of the processes mentioned above, trace constituents of the flue gas are emitted to the atmosphere or treated further in some other process. Hydrate formation, electrical desorption, and ammonium carbonation separations are promising novel concepts still in laboratory testing. More details are discussed elsewhere (Aaron and Tsouris, 2005).

A.I.8 Virtual Carbon Capture and Storage

The high risks of excessive cost and environmental consequences prompted us to propose the adoption of "virtual[1] CCS" by directing the resources that would have been

[1] The term "virtual" is used here because the concept described in this work satisfies the Merriam-Webster Dictionary definition of virtual: "being such in essence or effect though not formally recognized or admitted."

spent on CCS to alternative energy technologies (Tsouris et al., 2010). Here, we consider wind and nuclear power as an example and use the funds that would have been required by CCS to invest in installation and operation of either of these technologies. Many other options exist in addition to wind and nuclear power including solar, biomass, geothermal, and others. These additional energy technologies can be considered in future studies. While CCS involves spending resources to concentrate CO_2 in sinks, such as underground reservoirs, low-carbon alternative energy produces power, which will displace fossil fuel use while simultaneously generating revenues. Thus, these alternative energy technologies achieve the same objective as that of CCS, namely the avoidance of atmospheric CO_2 emissions.

A.I.8.1 Carbon capture and storage

The Intergovernmental Panel on Climate Change released a report in 2005 summarizing the technologies available for CCS. The most promising of multiple options for capture is currently liquid absorption with a regenerable solvent. Advantages of this technology include high treatment capacity, high CO_2 stream purity (because of solvent selectivity for CO_2), and capacity for retrofit with older coal power plants (Aaron and Tsouris, 2005). However, this method imposes a significant energy penalty for regeneration of the solvent, as well as solvent replacement cost, because the solvent degrades in the presence of acid gases. Also, retrofitting a coal power plant is more expensive than integrating a capture system into a newly built plant, thus adding to the cost (IPCC Report, 2005). The retrofit cost factor is important since 785 GW of coal and natural gas plants were operational in the U.S. in 2007, with planned additions of 10.9 to 16.8 GW each year until 2012 (EIA, 2009). Thus, retrofit may be more common in the

U.S. in the coming years than building coal power plants integrated with CCS. Capture methods including adsorption, membranes, and other novel approaches are currently less optimal than liquid absorption (Aaron and Tsouris, 2005) for a variety of reasons. In addition to the costs associated with capturing CO_2, equipment must also be in place to transport the captured stream. The most popular method for transporting CO_2 is via pipeline in a liquid state, a technique requiring significant compression and pumping energy, further increasing the cost (IPCC Report, 2005).

Following capture and transport, storage must be performed. Multiple storage options exist, including mid- and deep-ocean injection (Tsouris et al., 2004; Tsouris et al., 2007), mineralization, coal seam injection, enhanced oil recovery, and aquifer injection (Lackner, 2003). Of these traditional options, aquifer injection is the most cost-effective and technologically feasible (IPCC Report, 2005). A suitable site for aquifer injection must meet stringent criteria regarding seal integrity to prevent leakage, geological stability to minimize seismic activity risks, and groundwater dynamics to ensure millennia-scale storage time, as well as sociopolitical and jurisdictional issues (Bachu, 2000). Currently, cost and environmental risks are the main obstacles to performing deep aquifer injection. This scenario leads to the question: “Why is CCS such a popular component of the CO_2 mitigation strategy?” Perhaps because it would allow us to maintain our dependence on a source of energy with which we have considerable experience.

A.I.8.2 Virtual CCS

Objections to alternative energy generally focus on the high cost of these technologies, relative to coal and natural gas, for baseload and peaking capacities, respectively. Other obstacles including intermittency, an unprepared grid, and site specificity impede the implementation of alternative forms of energy. Nuclear energy must also deal with waste and security issues. Because fossil technologies are well-known and established, it is reasonable that efforts are being made to allow further use of these energy strategies while cautiously developing alternatives. Thus, CCS can be considered an effort to shield us from taking a large step away from fossil fuels for electricity production. The concept of virtual CCS is to take the resources that are being or expected to be directed to CCS efforts and, instead, direct them to alternative energy technologies. This activity would achieve the same goal as CCS, but by a different method. While transitioning to these alternatives seems a daunting task, the costs associated with CCS are so great that enormous progress can be made if we simply redirect our efforts and resources.

The mass basis for our calculations was the "stabilization wedges" concept of Pacala and Socolow (Pacala and Socolow, 2004): atmospheric CO_2 emissions can be stabilized by splitting carbon emissions mitigation among various technologies, including CCS, nuclear power, and wind power. A "wedge" is defined as the avoidance of 1/8 of increased CO_2 emissions over 50 years. Even though there is a high probability that economic realities will change substantially over a period of 50 years, this time scale was adopted in our analysis because it is of the same order as the lifetime of alternative

energy installations that are proposed as an alternative to CCS. The CO_2 emission rate in 2010 is estimated at 30 Gt/year (~8 GtC/year) and was projected to approximately double over the next 50 years. This projection represents an increase in emissions of 0.64 $GtCO_2$ each year, or 0.08 $GtCO_2$/year for a single wedge. Thus, a "wedge" of emissions totals 100 $GtCO_2$ over 50 years. We assumed that approximately 0.95 kg CO_2 is emitted per kilowatt-hour of electricity production from fossil fuels (U.S. DoE, 2000). The cost of capturing, transporting, and storing CO_2 was assumed to be $51/ton (IPCC Report, 2005) with an optimal combination of capture and storage technologies for a new pulverized-coal power plant. We note that the cost for retrofitting capture technology to an existing plant is higher than the new-plant cost—$59/ton rather than $41/ton (a 44% increase), resulting in a total CCS cost of approximately $69/ton (a 17% increase) (IPCC Report, 2005). A CCS cost of $51/ton is considered current best-case, as higher costs can be found in the current literature. For example, Hamilton et al. *(2009*) estimate the cost of CCS to be $62/ton for a supercritical pulverized coal plant; such increase in cost is partially attributed to recent increases in materials and fuel costs. Bukhteeva et al (2009) estimate the total cost of CCS to be $75.1/ton$CO_2$ ($56.2/ton of which is due to separation and extra power required for separation). It should be noted that these costs are presented in constant 2010 dollars. Since the timescale of this project spans generations, constant dollar values accurately convey the cost of CCS (and revenues of alternative energy) to future generations. Discounting of these costs would eventually cause the cost of CCS to be negligible while compounding for inflation would introduce further uncertainty to these estimates. Thus, the constant dollar value offers a consistent, common comparison between CCS and alternative energy technologies.

The average installation cost for wind power is $1700/kW with an average capacity factor of 30%, leading to an overall installation cost of $5667/kW (Wiser and Bolinger, 2007). Net revenue over the lifetime of a windmill (25 years) was estimated at $394/year per kilowatt (busbar price) after adjustment for operation and maintenance, land use, and other operating costs (Wiser and Bolinger, 2007). The installed cost for a nuclear plant was initially estimated at $4000/kW (EMWG, 2007; Shropshire et al., 2009), but adjustment for interest during construction was made, assuming a 5-year construction period. Assuming quarterly compounding of a 5% interest rate, a total interest adjustment of 13.52% was made, increasing the installed cost to $4541/kW. Finally, considering the 90% capacity factor resulted in a "true" installed cost of $5046/kW. Adjustment for CO_2 emissions associated with steel and concrete production for both wind and nuclear power was made (though these CO_2 emissions are negligible compared to the CO_2 avoided by using non-fossil energy). The recurring costs used in this study have been levelized over the lifetimes of the alternative energy installations. It is recognized here that all of the costs utilized in this study are volatile and subject to change. However, these calculations are designed to provide perspective on the economic efficiency with which CCS and alternative energy avoid CO_2 emissions.

A.I.8.3 Virtual CCS for wind and nuclear power

With these assumptions, as well as the assumption that alternative energy technologies can be readily deployed on a large scale, the total cost to perform CCS on a single wedge of CO_2 emissions was estimated to be $5.10 trillion over 50 years. However, if $5.10 trillion was spent to build windmills on an annual basis over the same

period, 1.91 wedges' worth of CO_2 would be avoided over the lifetime of the windmills. Thus, wind power is roughly twice as effective at avoiding atmospheric CO_2 emissions as CCS on a per-dollar basis. In addition, a net pre-state incentive income of $9.05 trillion in electricity sales would be earned over the lifetime of the windmills. Part of this income can then be spent on further developing wind power and supporting systems, a topic not considered here. The total useful wind power capacity for the world has been estimated at 72 TW (Archer and Jacobson, 2005); in our simulation, the maximum amount of one wedge of wind power employed at any time was 738 GW, 2 orders of magnitude below the total estimated capacity.

The results for nuclear power, instead of wind power or CCS, were even more impressive. For the same $5.10 trillion investment over 50 years, a sufficient number of nuclear power plants could be installed to avoid 4.31 wedges' worth of CO_2 over the lifetime of the project. In addition to this CO_2 avoidance, approximately $22.3 trillion would be generated via electricity sales during the lifetime of the nuclear plants. The attractive cost efficiency of nuclear plants stems from the competitive capital cost of $5046/kW, high capacity factor (90%), and long lifetime (50 years). A maximum nuclear capacity of 1033 GW would be developed over the course of 50 years of virtual CCS.

Figure A.I.7 illustrates carbon emissions after one to five wedges' worth of CCS have been used to develop wind (solid lines) and nuclear (diamonds) power. It is interesting to note that Figure A.I.7 shows an initial increase in fossil energy for both cases because the alternative energy generated when CCS resources were first redirected

was inadequate to offset energy demands. The fact that fossil energy will keep increasing for several years is expected to give adequate time for the development of alternative uses of coal. Fossil energy decreases (indicated by reduced CO_2 emissions) after sufficient alternative energy has been established, as a result of the cumulative effect of the alternative energy capacity. The light grey lines in Figure A.I.7 correspond to the eight Pacala-Socolow wedges.

Figure A.I.8 shows the constant value cost of CCS and revenue of wind and nuclear power from a $5.1 trillion investment (i.e., 1 wedge) over the period of 50 years. While CCS provides practically no revenue, wind and nuclear power will lead to revenues of $9.05 trillion and $22.3 trillion, respectively. The CCS cost is projected to increase over the 50-year period because of the expected increase in CO_2 emissions (Figure A.I.7). This simulation does not reflect concurrent use of CCS and renewable energy. Rather, we propose to completely replace CCS efforts with the use of alternative energy. The alternative power revenue was found to initially increase exponentially and then follow a linear trend. This behavior is a result of the cumulative effect of alternative power establishment until the initial lifetime (25 years for wind, 50 years for nuclear) of the installations is exhausted. At this point, increases in alternative energy are tempered by loss of installations that have reached end of life. If virtual CCS were abandoned in 2060, wind power would continue to provide a revenue stream until all of the windmills reached 25 years of operation, while nuclear power would do the same until all nuclear plants reached 50 years of operation.

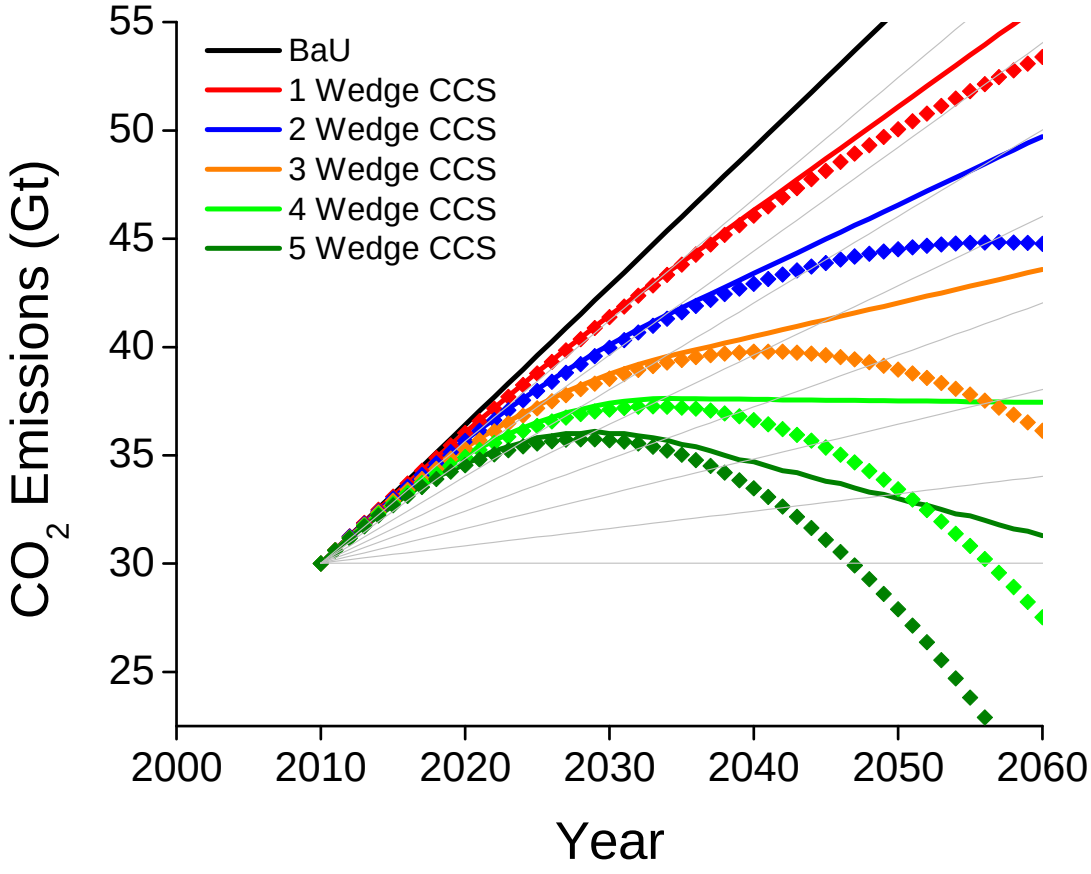

Figure A.I.7. CO_2 emissions without virtual CCS (Business as Usual—BaU) and with investment in wind power (solid lines) or nuclear power (diamonds) in place of one to five wedges' worth of CCS. The light-grey lines correspond to the eight Pacala and Socolow wedges.

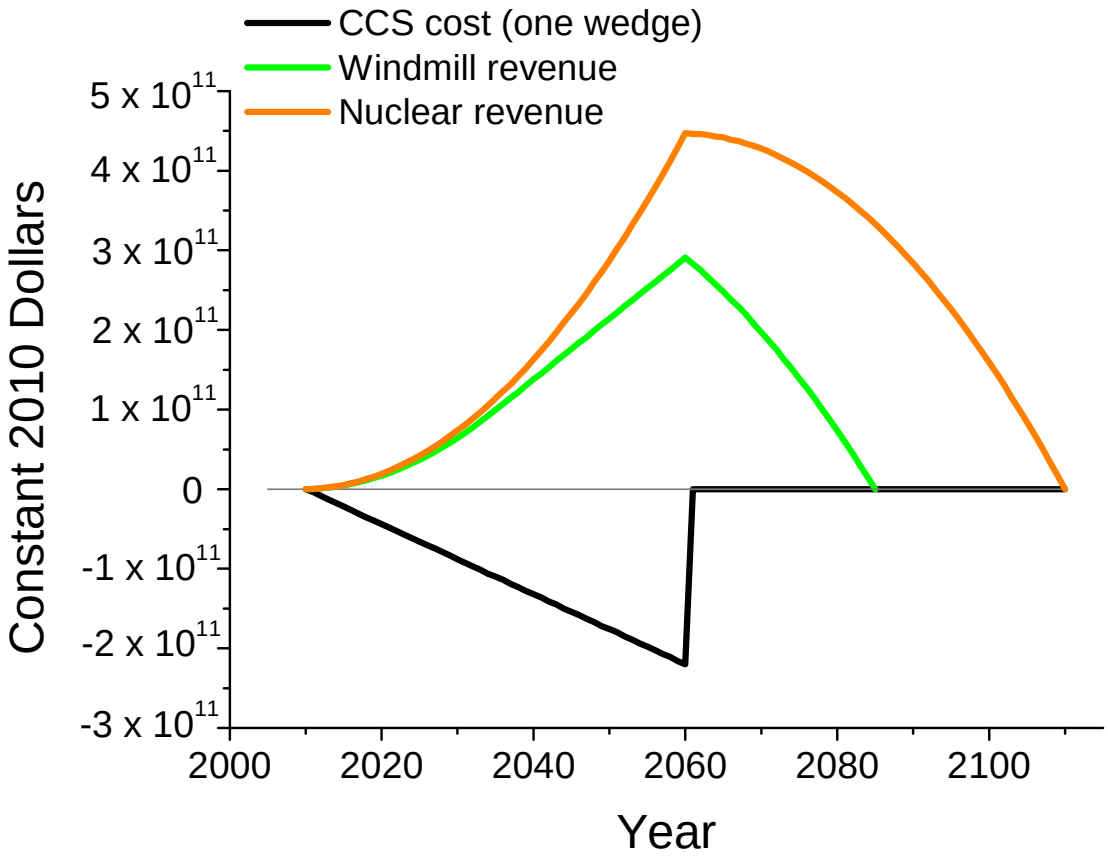

Figure A.I.8**.** Comparison of wind power revenue (green line), nuclear revenue (orange line) and cost of CCS (black line) for one Pacala-Socolow wedge for a 50-year investment. Wind and nuclear power provide income beyond the 50-year investment because windmills have a lifetime of 25 years and nuclear plants have a lifetime of 50 years. Overall, $9.05 trillion for wind and $22.3 trillion for nuclear in revenue are realized from an investment of $5.1 trillion for one wedge.

It is recognized here that the most productive wind sites will be developed first, as they should exhibit the highest capacity factors. As wind is developed, it is possible that a capacity factor lower than 30% can be observed in some areas. Table A.I.3 illustrates the dependence of carbon avoidance ratio on wind power capacity factor and cost of CCS for both wind and nuclear power; specifically, it shows how much CO_2 could be avoided by wind or nuclear power in place of CCS. It is apparent that, even as low as 15% capacity

factor, wind is still competitive with CCS at avoiding CO_2 emissions. However, the wind power development in this model does not exceed 2% of the expected world capacity for one Pacala-Socolow wedge. A similar effect is not considered for nuclear power since nuclear installations are typically operated at a 90% capacity factor for their lifetimes. It can also be seen in Table A.I.4 that both wind and nuclear power become increasingly more attractive than CCS as higher estimates of CCS cost are utilized. A CCS cost of \$27/ton CO_2 was estimated as the cost at which the wind power carbon avoidance ratio is equivalent to 1, meaning wind and CCS are equally cost efficient at avoiding CO_2 emissions. It should be noted that wind and nuclear power are expected to be components of a diverse energy portfolio. Also, since discounting would affect the cost of CCS and alternative energy technologies equally, the carbon avoidance ratio would be unchanged if discounting were applied.

Table A.I.3. Dependence of carbon avoidance ratio (wind power:CCS) on wind capacity factor
(wind power:CCS) and cost of CCS (wind power:CCS and nuclear power:CCS).

Wind Capacity Factor	30%	25%	20%	15%
WP:CCS (1 wedge)	1.95	1.59	1.27	0.95

Table A.I.4. Dependence of carbon avoidance ratio on cost of CCS.

Cost of CCS (\$/ton)	27.0[a]	51.0 *(2)*	62.0 *(10)*	75.1 *(11)*
WP:CCS (1 wedge)	1.01	1.95	2.32	2.80
NP:CCS (1 wedge)	2.28	4.31	5.24	6.35

[a] The cost of \$27.0/tCO_2 was included to show the cost at which wind and CCS are equivalent for carbon avoidance.

A.I.8.4 Potential implications of "externalities" on CCS cost

The cost of CCS is largely based on modeling since few large-scale CCS projects are operational worldwide to provide observational data. As such, small, "negligible" costs associated with CCS have not been included in the total CCS cost. For example, treatment of produced water from CCS applications in aquifers is considered an appreciable cost, which has been estimated at \$1.50/ton CO_2. For reference, monitoring and verification of an underground CO_2 plume has been estimated at approximately \$0.3/ton CO_2 and is often included in CCS cost estimates (*2*). The cost of produced-water treatment has not been included in the total cost of CCS of \$51/ton (*2*). Although this cost is somewhat small compared with the overall CCS cost, it would result in an additional \$0.14 trillion over 50 years for one wedge of CCS. Small, negligible costs such as this can add up to further increase the real cost of CCS. It is acknowledged that such externalities can also apply to alternative energy, but the wind and nuclear data used here are based on real-world observations of operational installations.

A.I.8.5 Conclusion

The calculations presented here should instill some caution in a decision to place emphasis on CCS. CCS consumes resources and provides no benefits other than CO_2 avoidance —a finding that should cause us to consider redirecting our efforts. Alternative energy technologies can avoid carbon emissions more efficiently than CCS and also produce profits. As we move forward in developing low-carbon energy production strategies, those strategies that have single benefits, with nothing else to offer, must be considered critically before substantial investments are made. The main difference

between CCS and alternative energy technologies is that CCS is not an investment with expected revenue. If, instead of CCS, we focus on problems associated with sustainable solutions, we can go directly to solutions that simultaneously address both our current and future energy needs and the problem of atmospheric carbon emissions.

REFERENCES

Aaron, D., Tsouris, C. Separation of CO_2 from Flue Gas: A Review. *Separation Science and Technology*, **2005**, *40*, 321-348

Aaron, D., Yiacoumi, S., Tsouris, C. Effects of proton-exchange membrane fuel-cell operating conditions on charge transfer resistances measured by electrochemical impedance spectroscopy. *Separation Science and Technology*, **2008**, *43*, 2397 – 2320.

Aaron, D.; Tsouris, C.; Hamilton, C.Y.; Borole, A.P. Assessment of the Effects of Flow Rate and Ionic Strength on the Performance of an Air-Cathode Microbial Fuel Cell Using Electrochemical Impedance Spectroscopy. *Energies*, **2010**, *3*, 592-606.

Aelterman, P.; Rabaey, K.; Pham, H. T.; Boon, N.; Verstraete, W. Continuous electricity generation at high voltages and currents uding stacked microbial fuel cells. *Environmental Science and Technology*, **2006**, *40*, 3388 – 3394.

Allam, R., Chiang, R., Hufton, J., Weist, E., White, V., Middleton, P. Power Generation with Reduced CO_2 Emissions via the Sorption Enhance Water Gas Shift Process. Presented at the Third Annual Conference on Carbon Capture and Sequestration, May 3-6, **2004** Alexandria, VA

Allen, R. M.; Bennetto, H. P. Microbial fuel cells – electricity production from carbohydrates. *Applied Biochemistry and Biotechnology*, **1993**, *39*, 27 – 40.

Amir, L.; Tam, T. K.; Pita, M.; Meijler, M. M.; Alfonta, L.; Katz, E. Biofuel cell controlled by enzyme logic systems. *Journal of the American Chemical Society*, **2001**, *131*, 826 – 832.

Andreaus, B.; McEvoy, A.; Scherer, G. Analysis of performance losses in polymer electrolyte fuel cells at high current densities by impedance spectroscopy. *Electrochimica Acta*, **2002**, *4*, 2223-2229.

Archer, C.; Jacobson, M. Evaluation of global wind power. *Journal of Geophysical Research*, **2005**, *110*, D12110.

Arning, M. D.; True, B. L.; Minteer, S. D. Citric acid cycle biomimic in an ammonium salt modified Nafion membrane for fuel cell applications. *Polymeric Materials Science and Engineering*, **2004**, *90*, 566 – 569.

Atanassov, P.; C. Apblett, S. Banta, S. Brozik, S.C. Barton, M. Cooney, B.Y. Liaw, S. Mukerjee, S. D. Minteer. Enzymatic biofuel cells. *Electrochemical Society Interface*, 16 (2007) 28 – 31.

Audus, H. Greenhouse Gas Mitigation Technology: An Overview of the CO_2 Capture and Sequestration Studies and Further Activities of the IEA Greenhouse Gas R&D Programme. *Energy,* **1997**, *22,* 217-221.

Bachu, S. Sequestration of CO_2 in geological media: criteria and approach for site selection in response to climate change. *Energy Conversion and Management,* **2000**, *41*, 953–970.

Bard, A., Faulkner, L. (2001) *Electrochemical Methods: Fundamentals and applications, 2nd ed*. John Wiley and Sons, New York.

Barsoukov, E., Macdonald, J. (2005) *Impedance spectroscopy: Theory, experiment, and applications*, 2nd ed. John Wiley and Sons, New Jersey.

Biyikoglu, A. Review of proton exchange membrane fuel cell models. *International Journal of Hydrogen Energy,* **2005**, *30*, 1181 – 1212.

Borole, A. P.; Aaron, D. S.; Hamilton, C.Y.; Tsouris, C. Understanding Long-term Changes in Microbial Fuel Cell Performance Using Electrochemical Impedance Spectroscopy. *Environmental Science and Technology*, **2010**, *44*, 2740 – 2745.

Borole, A.P.; S. LaBarge, B. A. Spott, Three-dimensional, gas phase fuel cell with a laccase biocathode. *Journal of Power Sources*, **2009a**, *188*, 421 – 426.

Borole, A. P.; Hamilton, C. Y.; Vishnivetskaya, T. A.; Leak, D.; Andreas., C. Improving power production from acetate-fed microbial fuel cells via enrichment of exoelectrogenic organisms in continuous flow systems. *Biochemical Engineering Journal*, **2009b,** *48*, 71-80.

Borole, A. P. and Hamilton, C. Y. (2009) Energy production from food industry wastewaters using bioelectrochemical cells. *Emerging Environmental Technologies*, Vol. 2; Shah, V., Ed.

Borole, A., Hamilton, C., Vishnivetskaya, T., Leak, D., Andras, C., Morrell-Falvey, J., Keller, M., Davison, B. Integrating engineering design improvements with exoelectrogen enrichment process to increase power output form microbial fuel cells. *Journal of Power Sources*, **2008a**, *191,* 520 - 527.

Borole, A. P.; O'Neill, H.; Tsouris, C.; Cesar, S., A microbial fuel cell operating at low pH, using an acidophile, *Acidiphilium cryptum*. *Biotechnology Letters,* **2008b,** *30*, 1367-1372.

Borole, A. P.; Mielenz, J.; Vishnivetskaya, T. A.; Hamilton, C. Y. Controlling accumulation of fermentation inhibitors in biorefinery water recycle using microbial fuel cells. *Biotechnology for Biofuels,* **2009c,** *2*:7.

Borole, A. P.; Hamilton, C. Y.; Aaron, D. S.; Tsouris, C. Investigating microbial fuel cell bioanode performance under different cathode conditions. *Biotechnology Progress*, **2009d,** *25*, 1630-1636.

Brewer, P. G., Friederich, G., Peltzer, E., Orr, F. M. Jr. Direct Experiments on the Ocean Disposal of Fossil Fuel CO_2. *Science*, **1999**, *284*, 943 – 945.

Bukhteeva, O.; Neal, P.; Allinson, S. Optimisation economics for CO_2 Capture and Storage in Central Queensland (Australia). *Energy Procedia*, **2009**, *1*, 3969 – 3976.

Carbon Dioxide Emissions from the Generation of Electric Power in the United States; U.S. Department of Energy and U.S. Environmental Protection Agency: Washington, DC, July 2000.

Carrette, L.; Friedrich, K. A.; Stimming, U. Fuel Cells – Fundamentals and Applications. *Fuel Cells*, **2001**, *1*, 5 – 39.

Chakma, A., Tontiwachwuthikul, P. (1999) CO_2 Separation from Combustion Gas Streams by Chemical Reactive Solvents. Online Library: Combustion Canada.

Chapel, D., Ernest, J., Mariz, C. Recovery of CO_2 from Flue Gases: Commercial Trends. Presented at the Canadian Society of Chemical Engineers Annual Meeting, Saskatchewan, Canada, October 4-6, 1999.

Chen, Y. S.; H. Peng, D. S. Hussey, D. L. Jacobson, D. T. Tran, T. Abdel-Baset, M. Biernacki Water distribution measurement for a PEMFC through neutron radiography. *Journal of Power Sources*, **2007**, *170*, 376 – 386.

Cheng, X.l; Yi, B.L.; Han, M.; Zhang, J.X.; Qiao, Y.G.; Yu, J.R. Investigation of platinum utilization and morphology in catalyst layer of polymer electrolyte fuel cells. *Journal of Power Sources*, **1999**, *79*, 75 – 81.

Choi, J. H.; Kim, M. H.; Kim, Y. J. Fabrication of 316L stainless steel having low contact resistance for PEMFC separator using power metallurgy. *Journal of the Korean Institute of Metals and Materials*, **2008**, *46*, 817 – 822.

Clauwaert, P.; Aelterman, P.; Pham, T. H.; De Schamphelaire, L.; Carballa, M.; Rabaey, K.; Verstraete, W., Minimizing losses in bio-electrochemical systems: the road to applications. *Applied Microbiology and Biotechnology* **2008,** *79*, 901-913.

Cui, S.T.; Liu, J.; Esai Selvan, M.; Keffer, D.J.; Edwards, B.J.; Steele, W.V. A molecular dynamics study of a Nafion polyelectrolyte membrane and the aqueous phase structure for proton transport. *Journal of Physical Chemistry B.*, **2002**, *111*, 3469-3475.

Danaee, I.; Jafarian, M.; Forouzandeh, F.; Gobal, F.; Mahjani, M. G. Impedance spectroscopy analysis of glucose electro-oxidation on Ni-modified glassy carbon electrode. *Electrochimica Acta*, **2008**, *53*, 6602 – 6609.

Deppe, G. Development in the SIMTECHE Process – CO_2 capture by Formation of Hydrates. Presented to the 3rd Annual Conference on Carbon Capture and Sequestration, Washington D.C., May, 2004.

Djilali, N.; Lu, D. Influence of heat transfer on gas and water transport in fuel cells. *International Journal of Heat and Mass Transfer*, **2005**, *41*, 29 – 40.

Dlugolecki, P.; Anet, B.; Metz, S. J.; Nijmeijer, K.; Wessling, M., Transport limitations in ion exchange membranes at low salt concentrations. *Journal of Membrane Science*, **2010**, *346*, 163-171.

Economic Modeling Working Group of the Generation IV International Forum. Cost estimating guidelines for generation IV nuclear energy systems; Revision 4.2. Printed by the OECD Nuclear Energy Agency, September 26, 2007. GIF/EMWG/2007/004

EG&G Technical Services, Inc. *Fuel Cell Handbook (Seventh Edition)*. For the U.S. Department of Energy, contract number DE-AM26-99FT40575. November, 2004.

Energy Information Administration online database: Existing Generating Capacity and Planned Generating Capacity sections; http://www.eia.doe.gov/fuelelectric.html.

Erable, B.; Etcheverry, L.; Bergel, A., Increased power from a two-chamber microbial fuel cell with a low-pH air-cathode compartment. *Electrochemistry Communications*, **2009,** *11*, 619-622.

Fan, Y., Hu, H., Liu, H. Sustainable power generation in microbial fuel cells using bicarbonate buffer and proton transfer mechanisms. *Environmental Science and Technology*, **2007**, *41*, 8154 – 8158.

Fan, Y.; Hu, H.; Liu, H., Enhanced coulombic efficiency and power density of air-cathode microbial fuel cells with an improved cell configuration. *Journal of Power Sources*, **2007**, *171*, 348-354.

Feng, Y.; Wang, X.; Logan, B. E.; Lee, H. Brewery wastewater treatment using air-cathode microbial fuel cells. *Environmental Biotechnology*, **2008**, *78*, 873 – 880.

Fisher, K.S., Beitler, C., Curtis, R., Searcy, K., Rochelle, G., Jassim, M., Figueroa, J.D. Integrating MEA Regeneration with CO_2 Compression to Reduce CO_2 Capture Costs. Presented at the Fourth Annual Conference on Carbon Capture and Sequestration, May 2–5, 2005, Alexandria, VA.

Fuller, T. and Newman, J. Water and thermal management in solid-polymer-electrolyte fuel cells. *Journal of the Electrochemical Society*, **1993**, *140(5)*, 1218 – 1225.

Gamry Instruments. Basics of Electrochemical Impedance Spectroscopy." Application Note, www.gamry.com/App_Notes/Index.htm. 2006

Gerteisen, D.; Hakenjos, A.; Schumacher, J. O. AC impedance modelling study on porous electrodes of proton exchange membrane fuel cells using an agglomerate model. *Journal of Power Sources*, **2007**, *173*, 346 – 356.

Gottlicher, G., Pruschek, R. Comparison of CO_2 Removal Systems for Fossil-Fuel Power Plant Processes. *Energy Conversion and Management*, **1997**, *38*, S173 - S178.

Gomadam, P.; Weidener, J. Analysis of electrochemical impedance spectroscopy in proton exchange membrane fuel cells. *International Journal of Energy Research*, **2005**, *29*, 1133-1151.

Grove, W. R. On Voltaic Series and the Combination of Gases by Platinum. *Philosophical Magazine and Journal of Science*, **1839**, *14*, 127 – 130.

Hamilton, M. R.; Herzog, H. J.; Parsons, J. E. Cost and U.S. public policy for new coal power plants with carbon capture and sequestration. *Energy Procedia,* **2009**, *1*, 4487 – 4494.

He, Z.; Mansfeld, F., Exploring the use of electrochemical impedance spectroscopy (EIS) in microbial fuel cell studies. *Energy and Environmental Science,* **2009,** *2*, 215-219.

He, Z.; Huang, Y. L.; Manohar, A. K.; Mansfeld, F., Effect of electrolyte pH on the rate of the anodic and cathodic reactions in an air-cathode microbial fuel cell. *Bioelectrochemistry* **2008,** *74*, 78-82.

He, Z.; Wagner, N.; Minteer, S. D.; Angenent, L. T., An upflow microbial fuel cell with an interior cathode: Assessment of the internal resistance by impedance spectroscopy. *Environmental Science and Technology* **2006,** *40*, 5212-5217.

Herzog, H. An Introduction to CO_2 Separation and Capture Technologies. MIT Energy Laboratory, August, 1999.

Hickner, M. A.; N. P. Siegel, K. S. Chen, D. S. Hussey, D. L. Jacobson, M. Arif, In situ high-resolution neutron radiography of cross-sectional liquid water profiles in proton exchange membrane fuel cells. *Journal of the Electrochemical Society*, **2008**, *155*, B427 – B434.

Holloway, S. An Overview of the Underground Disposal of Carbon Dioxide. *Energy Conversion and Management*, **1997**, *38*, S193 - S198.

Hudak, N. S.; J.W. Gallaway, S.C. Barton. Mediated biocatalytic cathodes operating on gas-phase air and oxygen in fuel cells. *Journal of the Electrochemical Society*, **2009**, *156*, B9 – B15.

Hussey, D. S.; D.L. Jacobson, M. Arif, J.P. Owejan, J.J. Gagliardo, T.A. Trabold, Neutron imaging of the through-plane water distribution of an operating PEM fuel cell. *Journal of Power Sources*, **2007**, 172, 225 – 228.

Ivanov, I.; Vidakovic-Koch, T.; Sundmacher, K. Recent advances in enzymatic fuel cells: experiments and modeling. *Energies*, **2010**, *3*, 803 – 846.

Jinnouchi, R.; Okazaki, K. Molecular dynamics study of transport phenomena in perfluorosulfonate ionomer membranes for polymer electrolyte fuel cells. *Journal of the Electrochemical Society*, **2003**, *150*, E66 – E73.

Johnston, W.; Cooney, M. J.; Liaw, B. Y.; Sapra, R.; Adams, M. W. W. Design and characterization of redox enzyme electrodes: new perspectives on established techniques with application to an extremeophilic hydrogenase. *Enzyme and Microbial Technology*, **2005**, *36*, 540 – 549.

Judkins, R. R., Burchell, T. D. A Novel Carbon Fiber Based Material and Separation Technology. *Energy Conversion and Management*, **1997**, *38*, S99-S104.

Jung, S.; Regan, J. M., Comparison of anode bacterial communities and performance in microbial fuel cells with different electron donors. *Applied Microbiology and Biotechnology* **2007,** *77*, 393-402.

Kang, S.P., Lee, H. Recovery of CO_2 from Flue Gas Using Gas Hydrate: Thermodynamic Verification through Phase Equilibrium Measurements. *Environmental Science and Technology* **2000**, ***34***, 4397 – 4400.

Katz, E.; Willner, I. A biofuel cell with electrochemically switchable and tunable power output. *Journal of the American Chemical Society*, **2003**, *125*, 6803 – 6813.

Kim, C., Pyun, S., Kim, J. An investigation of the capacitance dispersion on the fractal carbon electrode with edge and basal orientations. *Electrochimica Acta*, **2003**, *48*, 3455 – 3463.

Kovvali, A. S., Sirkar, K. K. Carbon Dioxide Separation with Novel Solvents as Liquid Membranes. *Industrial Engineering Chemistry Research*, **2002**, *41*, 2287-2295.

Kreuer, K. D. On the development of proton conducting polymer membranes for hydrogen and methanol fuel cells. *Journal of Membrane Science*, **2001**, *185*, 29 – 39.

Lackner, K. S. Climate change: a guide to CO_2 sequestration. *Science,* **2003**, *300*, 1677–1678.

Le Canut, J.; Abouatallah, R.; Harrington, D. Detection of membrane drying, fuel cell flooding, and anode catalyst poisoning on PEMFC stacks by electrochemical impedance spectroscopy. *Journal of the Electrochemical Society*, **2006**, *153*, A857-A864.

Li, X., Hagaman, E., Tsouris, C., Lee, J. W. Removal of Carbon Dioxide from Flue Gas by Ammonia Carbonation in the Gas Phase. *Energy and Fuels*, **2003**, *17*, 69-74.

Liang, P.; Huang, X.; Fan, M. Z.; Cao, X. X.; Wang, C. Composition and distribution of internal resistance in three types of microbial fuel cells. *Applied Microbiology and Biotechnology*, **2007**, *77*, 551-558.

Litster, S.; McLean, G. PEM fuel cell electrodes. *Journal of Power Sources*, **2004**, *130*, 61 – 76.

Liu, J.; Esai Selvan, M.; Cui, S.; Edwards, B.J.; Keffer, D.J.; Steele, W.V. Molecular-level modeling of the structure and wetting of electrode/electrolyte interfaces in hydrogen fuel cells. *Journal of Physical Chemistry C*, **2008**, *112*, 1985-1993.

Liu, H.; Cheng, S. A.; Logan, B. E., Power generation in fed-batch microbial fuel cells as a function of ionic strength, temperature, and reactor configuration. *Environmental Science and Technology*, **2005,** *39*, 5488-5493.

Liu, H.; Cheng, S.; Huang, L. P.; Logan, B. E., Scale-up of membrane-free single-chamber microbial fuel cells. *Journal of Power Sources*, **2008,** *179*, 274-279.

Logan, B., Cheng, S., Watson, V., Estadt, G. Graphite fiber brush anodes for increased power production in air-cathode microbial fuel cells. *Environmental Science and Technology*, **2007**, *41*, 3341 – 3346.

Logan, B. E.; Hamelers, B.; Rozendal, R.; Schroder, U.; Keller, J.; Freguia, S.; Aelterman, P.; Verstraete, W.; Rabaey, K. Microbial Fuel Cells: Methodology and Technology. *Environmental Science and Technology*, **2006**, *40*, 5181 – 5192.

Logan, B. E.; Regan, J. M., Microbial fuel cells, challenges and applications. *Environmental Science and Technology*, **2006,** *40*, 5172-5180.

Logan, B. E.; Regan, J. M. Electricity-producting bacterial communities in microbial fuel cells. *Trends in Microbiology*, **2006**, *14*, 512 – 518.

Lovley, D. Bug juice: harvesting electricity with microoganisms. *Nature Reviews: Microbiology*, **2006**, *4*, 497 – 508.

Lowe, P. R.; J.M. Ficke, The computation of saturation vapor pressure. Tech.Paper No. 4-74 Environmental Prediction Research Facility, Naval Postgraduate School, Monterey, CA., 1974

Manohar, A. K.; Mansfeld, F., The internal resistance of a microbial fuel cell and its dependence on cell design and operating conditions. *Electrochimica Acta,* **2009,** *54*, 1664-1670.

Manohar, A. K.; Bretschger, O.; Nealson, K. H.; Mansfeld, F., The use of electrochemical impedance spectroscopy (EIS) in the evaluation of the electrochemical properties of a microbial fuel cell. *Bioelectrochemistry,* **2008,** *72*, 149-154.

Manohar, A. K.; Bretschger, O.; Nealson, K. H.; Mansfeld, F., The polarization behavior of the anode in a microbial fuel cell. *Electrochimica Acta,* **2008,** *53*, 3508-3513.

Meisen, A., Shuai, X. Research and Development Issues in CO_2 Capture. *Energy Conversion and Management,* **1997**, *38*, S37 – S42.

Meratla, Z. Combining Cryogenic Flue Gas Emission Remediation with a CO_2/O_2 Combustion Cycle. *Energy Conversion and Management,* **1997**, *38*, S147-S152.

Min, B., Cheng, S., Logan, B. Electricity generation using membrane and salt bridge microbial fuel cells. *Water Research*, **2005**, *39*, 1675 – 1686.

Minteer, S. D.; B. Y. Liaw, M.J. Cooney. Enzyme-based biofuel cells. *Current Opinion in Biotechnology*, **2007**, *18*, 1 – 7.

Mitsubishi Heavy Industries Research. http://www.mhi.co.jp/en/products/category/co2_recovery_plants.html

Mowbray, J. Ceramic Membrane to Combat Global Warming. *Membrane Technology,* **1997**, *92*, 11 –12.

Orazem M. E.; Tribollet, B. (2008) *Electrochemical Impedance Spectroscopy*; John Wiley and Sons, Inc.: Hoboken, New Jersey, USA.

Ostwald, W. Electrochemistry: history and theory (2 volumes). Written 1896. Translated by N.P. Date, published for the Smithsonian Institution and National Science Foundation, Washington, DC, by Amerind Publ. Co., New Delhi, 1980.

Ouitrakul, S.; Sriyudthsak, M.; Charojrochkul, S.; Kakizono, T., Impedance analysis of bio-fuel cell electrodes. *Biosensors and Bioelectronics,* **2007,** *23*, 721-727.

Pacala, S.; Socolow, R. Stabilization wedges: solving the climate problem for the next 50 years with current technologies. *Science,* **2004**, 305, 968-972.

Page, S.; Anbuky, A.; Krumdieck, S.; Brouwer, J. Test method and equivalent circuit modeling of a PEM fuel cell in a passive state. *IEE Transactions on Energy Conversion*, **2007**, *22*, 764-773.

Park, Y.I., Lee, K.H. The Permeation of CO_2 and N_2 Through Asymmetric Polyetherimide Membrane. *Energy Conversion and Management,* **1995**, *36*, 423 – 426.

Perry, M. L.; Fuller, T. F. A Historical Perspective of Fuel Cell Technology in the 20th Century. *Journal of the Electrochemical Society*, **2002**, *149*, S59 – S67.

Picioreanu, C.; Katuri, K. P.; Head, I. M.; van Loosdrecht, M. C. M.; Scott, K., Mathematical model for microbial fuel cells with anodic biofilms and anaerobic digestion. *Water Science and Technology,* **2008,** *57*, 965-971.

Pruschek, R., Oeljeklaus, G., Haupt, G., Zimmermann, G., Jansen, D., Ribberink, J. S. The Role of IGCC in CO_2 Abatement. *Energy Conversion and Management,* **1997**, *38*, S153 – S 158.

Ramasamy, R. P.; Ren, Z. Y.; Mench, M. M.; Regan, J. M., Impact of initial biofilm growth on the anode impedance of microbial fuel cells. *Biotechnology and Bioengineering*, **2008**, *101*, 101-108.

Ramasamy, R. P.; Gadhamshetty, V.; Nadeau, L.; Johnson, G. R., Impedance spectroscopy as a tool for non-intrusive detection of extracellular mediators in microbial fuel cells. *Biotechnology and Bioengineering,* **2009**, *104*, 882 – 891.

Rasmousse, J.; O. Lottin, S. Didierjean, D. Maillet, Heat sources in proton exchange membrane (PEM) fuel cells, *Journal of Power Sources*, **2009**, *192*, 435 – 441.

Riemer, P.W.F., Webster, I.C., Omerod, W.G., Audus, H. Results and full fuel cycle study plans from the IEA greenhouse gas research and development programme. *Fuel*, **1994**, *73*, 1151 – 1158.

Rikukawi, M.; Sanui, K. Proton-conducting polymer electrolyte membranes based on hydrocarbon polymers. *Progress in Polymer Science*, **2000**, *25*, 1463 – 1502.

Rosenbaum, M.; Zhao F.; Quaas, M.; Wulff, H.; Shroder, U.; Scholz, F. Evaluation of catalytic properties of tungsten carbide for the anode of microbial fuel cells. *Applied Catalysis B,* **2007**, *74*, 262 – 270.

Rowe, A.; Li, X. Mathematical modeling of proton exchange membrane fuel cells. *Journal of Power Sources*, **2001**, *102*, 82 – 96.

Rozendal, R. A.; Hamelers, H. V. M.; Buisman, C. J. N., Effects of membrane cation transport on pH and microbial fuel cell performance. *Environmental Science and Technology,* **2006,** *40*, 5206-5211.

Rozendal, R. A.; Hamelers, H. V. M.; Rabaey, K.; Keller, J.; Buisman, C. J. N., Towards practical implementation of bioelectrochemical wastewater treatment. *Trends in Biotechnology*, **2008,** *26*, 450-459.

Samukawa, T.; Tsujimura, S.; Kana, K. AC impedance analysis of enzyme-functional electrodes. *Bunseki Kagaku*, **2008**, *57*, 625 – 629.

Satija, R.; D. L. Jacobson, M. Arif, S. A. Werner, In situ neutron imaging technique for evaluation of water management systems in operating PEM fuel cells. *Journal of Power Sources*, **2004**, *129*, 238-245

Satyapal, S.; Filburn, T.; Trela, J.; Strange, J. Performance and Properties of a Solid Amine Sorbent for Carbon Dioxide Removal in Space Life Support Applications. *Energy & Fuels*, **2001**, *15*, 250-255.

Schussler, U.; Kummel, R. Carbon Dioxide Removal from Fossil Fuel Power Plants by Refrigeration Under Pressure. *Proceedings of the 24th Intersociety*, **1989**, *4*, 1789-1794.

Secanell, M.; Songprakorp, R.; Suleman, A.; Djilali, N. Multi-objective optimization of a polymer electrolyte fuel cell membrane electrode assembly. *Energy and Environmental Science*, **2008**, *1*, 378 – 388.

Shropshire, D. E.; Williams, K. A.; Smith, J. D.; Dixon, B. W.; Dunzik-Gougar, M.; Adams, R. D.; Gombert, D.; Carter, J. T.; Schneider, E.; Hebditch, D. Advanced Fuel Cycle Cost Basis. Idaho National Laboratory report, December, 2009. INL/EXT-07-12107

Special Report on Carbon Dioxide Capture and Storage; Intergovernmental Panel on Climate Change: Geneva, Switzerland, 2005, Chapters 3 and 8.

Springer, T.E.; Zawodzinski, T.A.; Wilson, M.S.; Gottesfeld, S. Characterization of polymer electrolyte fuel cells using AC impedance spectroscopy. *Journal of the Electrochemical Society*, **1996**, *143*, 587-599.

Srinivasan, S. (2006) *Fuel Cells: From Fundamentals to Applications*. Springer Science, New York, NY.

Tam, S.S., Stanton, M.E., Ghose, S., Deppe, G., Spencer, D.F., Currier, R.P., Young, J.S., Anderson, G.K., Le, L.A., Devlin, D.J. A High Pressure Carbon Dioxide Separation Process for IGCC Plants. Presented at the First National Conference on Carbon Sequestration, May 14 – 17, 2001.

Tamaki, T.; Yamaguchi, T. High surface area three-dimensional biofuel cell electrode using redox-polyer-grafted carbon. *Industrial & Engineering Chemistry Research*, **2006**, *45*, 3050 – 3058.

Taulbee, D. N., Graham, U., Rathbone, R. F., Robl, T. L. Removal of CO_2 from Multi-component Gas Streams Using Dry-FGD Wastes. *Fuel*, **1997**, *76*, 781 – 786.

Tokuda, Y., Fujisawa, E., Okabayashi, N., Matsumiya, M., Takagi, K., Mano, H., Haraya, K., Sato, M. Development of Hollow Fiber Membranes for CO_2 Separation. *Energy Conversion and Management*, **1997**, *38*, S111 - S116.

Torres, C. I.; Lee, H. S.; Rittmann, B. E., Carbonate Species as OH- Carriers for Decreasing the pH Gradient between Cathode and Anode in Biological Fuel Cells. *Environmental Science & Technology*, **2008,** *42*, 8773-8777.

Tsouris, C.; Brewer, P.; Peltzer, E.; Walz, P.; Riestenberg, D. A.; Liang, L.; West, O. R. Hydrate composite particles for ocean carbon sequestration: field verification. *Environmental Science and Technology*, **2004**, *38*, 2470–2475.

Tsouris, C.; Szymcek, P.; Taboada-Serrano, P.; McCallum, S. D.; Brewer, P.; Peltzer, E.; Walz, P.; Adams, E.; Chow, A.; Johnson, W. K.; Summers, J. Scaled-up ocean injection of CO_2-hydrate composite particles. *Energy and Fuels*, **2007**, *21*, 3300–3309.

Tsouris, C., Aaron, D., Williams, K. Is carbon capture and storage really necessary? *Environmental Science and Technology*, to be published June 1, **2010**.

Ubis, T., Bressan, L., O'Keefe, L. The 800MW PIEMSA IGCC Project. Presented at 2000 Gasification Technologies Conference, Oct. 8-11, 2000.

Wagner, N., Characterization of membrane electrode assemblies in polymer electrolyte fuel cells using a.c. impedance spectroscopy. *Journal of Applied Electrochemistry*, **2002,** *32*, 859-863.

Wagner, N.; Schnurnberger, W.; Muller, B.; Lang, M., Electrochemical impedance spectra of solid-oxide fuel cells and polymer membrane fuel cells. *Electrochimica Acta*, **1998,** *43*, 3785-3793.

Veawab A., Aroonwilas A., Chakma A., Tontiwachwuthikul P. Solvent Formulation for CO_2 Separation from Flue Gas Streams. Presented at the First National Conference on Carbon Sequestration, May 14-17, 2001.

Watson, V. J.; Logan, B. E. Power production in MFCs inoculated with Shewanella oneidensis MR-1 or mixed cultures. *Biotechnology and Bioengineering*, **2010**, *105*, 489 – 498.

Wiezell, K.; Gode, P.; Lindbergh, G. Steady-state and EIS investigations of hydrogen electrodes and membranes in polymer electrolyte fuel cells: I. Modeling. *Journal of the Electrochemical Society*, **2006**, *153*, A749-A758.

Wiezell, K.; Gode, P.; Lindbergh, G. Steady-state and EIS investigations of hydrogen electrodes and membranes in polymer electrolyte fuel cells: II. Experimental. *Journal of the Electrochemical Society*, **2006**, *153*, A759-A764.

Willner, I.; Yan, Y. M.; Willner, B.; Tel-Vered, R. Integrated enzyme-based biofuel cells – A Review. *Fuel Cells*, **2009**, *9*, 7 – 24.

Wiser, R.; Bolinger, M. *Annual Report on U.S. Wind Power Installation, Cost, and Performance Trends: 2007*; U.S. Department of Energy, Energy Efficiency and Renewable Energy: Washington, DC, 2007.

Wu, H.; P. Berg, X. Li, Non-isothermal transient modeling of water transport in PEM fuel cells. *Journal of Power Sources*, **2007**, *165*, 232–243.

Xing, D. F.; Zuo, Y.; Cheng, S. A.; Regan, J. M.; Logan, B. E., Electricity generation by Rhodopseudomonas palustris DX-1. *Environmental Science and Technology*, **2008,** *42*, 4146-4151.

Yeh J.T., Pennline H.W. Study of CO_2 Absorption and Desorption in a Packed Column. *Energy and Fuels*, **2001**, *15*, 274-278.

You, S. J.; Zhao, Q. L.; Zhang, J.; Liu, H.; Jiang, J. Q.; Zhao, S. Q., Increased sustainable electricity generation in up-flow air-cathode microbial fuel cells. *Biosensors and Bioelectronics*, **2008**, *23*, 1157-1160.

Zebda, A.; Renaud, L.; Tingry, S.; Cretin, M.; Pichot, F.; Ferrigno, R.; Innocent, C. Microfluidic biofuel cell for energy production. *Sensor Letters*, **2009**, *7*, 824 – 828.

Zhao, F.; Harnisch, F.; Schrorder, U.; Scholz, F.; Bogdanoff, P.; Herrmann, I., Challenges and constraints of using oxygen cathodes in microbial fuel cells. *Environmental Science and Technology*, **2006,** *40*, 5193-5199.

Zhao, X. Y.; Jia, H. F.; Kim, J.; Wang, P. Kinetic limitations of a bioelectrochemical electrode using carbon nanotube-attached glucose oxidase for biofuel cells. *Biotechnology and Bioengineering*, **2009**, *104*, 1068 – 1074.

VITA

Douglas Scott Aaron was born in Oak Ridge, Tennessee on April 15, 1983. He attended the University of Tennessee at Knoxville and received a Bachelor of Science degree in Chemical Engineering in May, 2005. He then entered the School of Civil and Environmental Engineering at the Georgia Institute of Technology in the fall of 2005 and joined the research group of Dr. Sotira Yiacoumi and Dr. Costas Tsouris investigating transport phenomena in fuel cells. In May, 2007 he received a Master of Science degree and continued in pursuit of a doctorate degree in Environmental Engineering which he successfully defended in May, 2010.